Flow behaviour over rough riverbeds

By Shahla Abdulqader Nassrullah

Hydro-Environment and Research Centre
School of Engineering
Cardiff University

A thesis submitted in candidature for the degree of Doctor of Philosophy at Cardiff University

August 2022

Dedication

To the memory of my late mother, father, and brother

With love and eternal appreciation

And to my brothers and sisters for their continuing love and encouragement

Acknowledgements

The undertaking of this thesis has taken four years of full-time study. During this journey I have received a wonderful amount of help and support; without such assistance this work would not be complete.

Firstly, my thanks go to my supervisors Dr. Catherine Wilson, and Professor Shunqi Pan, without whose assistance and work this thesis would never have been possible to finish. I would like to offer a warm and special thanks to Professor Thorsten Stoesser, who is an associate partner (external advisor) for his invaluable guidance, without whose suggestion this work would not be where it is today. I would like to thank Dr Alex Stubbs who offered me opinion of critical necessity. I am grateful to Dr. Bettina Bockelmann-Evans for providing valuable remarks and consultations from my first two annual reviews which assisted me in improving my thesis at the outset. My sincere thanks go to all of them.

Great appreciativeness goes to my sponsor the Iraqi Ministry of Higher Education and Scientific Research and the University of Middle Technical, Institute of Technology Bagdad-Iraq for funding my study and giving me this opportunity. I also appreciate the Iraqi Cultural Attaché in London for their continued advice and assistance in achieving my academic aims.

I would like to thank the technical staff and students of the Hydro Environmental Research Centre at Cardiff University for their support during my PhD journey; particularly Elizabeth Follett, Valentine Muhawenimana, Stephanie Muller, Harry Lane, Paul Leach and Amanda Kitching for their services in building and achieving my experimental setup.

I am grateful to all staff members in IT, the finance and research offices and especially Aderyn Reid and Jeanette Whyte in the school of engineering for their help during my period of research.

Last but not least, deep appreciation and special thanks are expressed to my brothers, sisters and all my family and friends in my beloved country Iraq for their support throughout my journey in completing this work and during the COVID-19 lockdown.

Shahla Nassrullah

Abstract

Over the past several decades, many studies have investigated turbulent flows over natural, hydraulically rough-beds to identify behaviour similar to flows over smooth beds. Such studies have made a substantial contribution to our understanding of flows above impermeable and permeable rough-beds, but the effect of permeable beds on specific turbulent flow characteristics, such as bursting and sweep events, remains elusive. Therefore, this study investigates the flow over permeable natural gravel-bed and artificial beds in terms of the velocity profile, turbulence intensity, turbulent kinetic energy, and Reynolds stresses, which are investigated in part utilising quadrant analysis.

Various beds are explored in this study and are comprised of natural gravel with median diameters of 20 mm and 35 mm, as well as an artificial bed with particles nominally 28 mm in diameter. Measurements of instantaneous velocities in the three-component directions for six experiments were collected under uniform flow conditions in intermediate and high relative submergence scenarios using an Acoustic Doppler Velocimeter positioned above the beds within a narrow flume. Endoscopes were also used to track dye flow paths within the various beds themselves. The first- and second-order velocity statistics were investigated by applying a time-space averaging methodology to the Navier-Stokes equations.

The experimental results were compared against the logarithmic equation and show that a logarithmic velocity profile is valid for rough-bed flows where von Karman's constant is within the range of 0.38 to 0.41. Additionally, the Nikuradse equivalent sand roughness was found to range from 5 mm to 61 mm for the different beds. The results showed that κ increases with increasing porosity, and decreases with increasing Re_k for flow above natural gravel-beds. Turbulence intensity in the vertical direction was found to notably differ in this study compared to the literature, likely due to the high porosity of the beds used here. Additionally, it was found that relative submergence affects the streamwise turbulence intensity more than in the vertical direction. The distribution of double averaged Reynolds shear stress, Reynolds normal stress, and turbulent kinetic energy were found to decrease linearly from the bed towards the water surface. While the influence of K^+ on second-order statistics was found to be insignificant, relative submergence and porosity were found to have a significant effect. Quadrant analysis show ejection and sweep events dominate more than inward and outward interaction events. Interstitial flow results show that numerous turbulent upwelling and downwelling events were observed within all the experiments that were conducted.

Publications

1. Conference articles

Nassrullah, S., Stubbs, A., Stoesser, T. and Wilson, C.A.M.E. 2019. The Validation of the Logarithmic Velocity Profiles Above Rough-Bed Flows. *E-proceedings of 38th IAHR World Congress 38*, pp. 5072–5079. doi: 10.3850/38wc092019-0421.

2. An extended conference abstract

Nassrullah, S., Bockelmann-Evans, B. and Stoesser, T. 2018. Velocity profiles of flow measurements over a laboratory gravel bed. *Proceedings of the 5th IAHR Europe Congress — New Challenges in Hydraulic Research and Engineering*, pp. 453–454. doi: 10.3850/978-981-11-2731-1.

Table of Contents

List of Figures

List of Tables

Nomenclature

$-\rho\langle\overline{u'v'}\rangle$	Double average Reynolds shear stress in (x-y) plane
d_{84}	84th percentile size distribution of the surface material
K^+	Roughness Reynolds number
U_{bulk}	Average bulk velocity
$(B_1\text{-}C_1)$	Mass of water displaced by the SSD sample
$\lvert\langle\overline{S_{1,H}}\rangle\rvert$	Double average of Reynolds shear stress
$\langle\overline{U_{RMS}}\rangle$	Double average of root means square fluctuation streamwise velocity
$\langle\overline{V_{RMS}}\rangle$	Double average of root means square fluctuation cross-streamwise velocity
$\langle\overline{W_{RMS}}\rangle$	Double average of root means square fluctuation vertical velocity
$\langle\overline{RNS}\rangle$	Double average of Reynolds normal stress
$\langle\overline{RSS}\rangle$	Double average of Reynolds shear stress
$\langle\overline{TKE}\rangle$	Double average Turbulence Kinetic Energy
$\langle\bar{u}\rangle$	Double average velocity in the streamwise direction
$\lvert\overline{u'w'}\rvert$	Time-averaged stress
$\lvert u'w'\rvert$	Horizontal and vertical velocity fluctuations
$\overline{w}$	Mean velocity in the z-direction
$\bar{z}$	Mean bed surface elevation
$\bar{v}$	Mean velocity in the y-direction
$\langle\ \rangle$	Spatial area average (double average)
$A(z_b')$	Roughness geometry function
B	Flume width
B_1	Mass of SSD sample in the air
C	Integration constant
C_1	Mass of SSD sample in water
D/S	Downstream of the test section

D_1	Experimental constant
D_2	Experimental constant
d_{20}	20th percentile size distribution of the surface material
D_3	Experimental constant
d_{50}	50th percentile size distribution of the surface material
d_{90}	90th percentile size distribution of the surface material
e	Void ratio
ET	Thickness of loose bed material
Fr	Froud number
g	Gravitational acceleration
G_{SSD}	Bulk Saturated Surface Dry Specific Gravity
γ_w	Unit weight of the water
H	Hyperbolic hole size
H	Water flow depth
H_{max}	Maximum flow depth, from the water surface to roughness troughs
$H_{measurement}$	Flow depth measured using gauge point
i	Hydraulic gradient
i	ith quadrant
$I_{i, H, t}$	Conditional sampling function
k	Permeability of the bed
k	Roughness height
K'	Friction factor
k_s	Equivalent sand roughness of Nikuradse
Ku_z	Kurtosis coefficient
N	Total record length
n	Manning number

N	Total number of measurements points of bed elevation in a longitudinal direction
n_p	Porosity
Q	Discharge
Q1	First quadrant outward interaction
Q2	Second quadrant ejection event
Q3	Third quadrant inward interaction
Q4	Fourth quadrant sweep event
Qi	Q the quadrants, (i=1–4)
Q_{sub}	Flow rate through gravel
Q_{sup}	Flow rate above the gravel
Q_{total}	Total flow rate
Re	Reynolds number
Re_H	Reynolds number calculated using flow depth
Re_k	Permeability Reynolds number
Re_R	Reynolds number calculated using the hydraulic radius
RMS	Root Mean Square
RSS	Reynolds shear stress
S	Slope of bed
$S_{i,H}$	Reynolds shear stress
Sk_z	Skewness coefficient
t	Time
T	Sampling period
TKE	Turbulent Kinetic Energy
u	Instantaneous velocity in the x-direction
$\bar{u}$	Time average velocity in the streamwise direction
u_*	Shear velocity

U/S	Upstream of the test section
u'	Velocity fluctuations in the streamwise direction
$u'v'$	Reynolds shear stress in (x-y) plane
$u'w'$	Reynolds shear stress in (x-z) plane
U_{RMS}	Time average Root Means Square of streamwise velocity fluctuation
U_{sub}	Velocity through gravel
v	Instantaneous velocity in the y-direction
v'	Velocity fluctuations in the cross-streamwise direction
V_{RMS}	Time average Root Means Square of cross-streamwise velocity fluctuation
Vs	Solid volume
V_t	Total volume
V_v	Void volume
w	Instantaneous velocity in the z-direction
w'	Velocity fluctuations toward flow depth
W_{RMS}	Time average Root Means Square of vertical velocity fluctuation
W_s	Weight of the gravel
x	Streamwise coordinate
y	Cross-sectional coordinate
z	Vertical coordinate
Z	Vertical measurement with the flow depth direction
Z^+	Zu_{*}/ν
z_0	Zero-displacement distance
z_b	Fluctuations in surface elevation
zi	Bed surface elevation
Z_{max}	Distance from the bed when maximum velocity occurs
Δ	Roughness scale

κ	Von Karman constant
λ_1	Experimental constant
λ_2	Experimental constant
λ_3	Experimental constant
ν	Water viscosity
$-\rho\langle\overline{\mathrm{U_{RMS}W_{RMS}}}\rangle$	Double average Reynolds shear stress, as Root Mean Square of both streamwise and vertical velocity fluctuation
$\rho\langle\overline{\mathrm{U}_{\mathrm{RMS}}^2}\rangle$	Double average streamwise Reynolds normal stress, as Root Mean Square of streamwise velocity fluctuation
$\rho\langle\overline{\mathrm{V}_{\mathrm{RMS}}^2}\rangle$	Double average cross-streamwise Reynolds normal stress, as Root Mean Square of transverse velocity fluctuation
$\rho\langle\overline{\mathrm{W}_{\mathrm{RMS}}^2}\rangle$	Double average vertical Reynolds normal stress, as Root Mean Square of vertical velocity fluctuation
$-\rho\overline{v'^2}$	Time average cross-streamwise Reynolds normal stress
$-\rho\langle\overline{v'w'}\rangle$	Double average Reynolds shear stress in (y-z) plane
$-\rho\overline{w'^2}$	Time average vertical Reynolds normal stress
$-\rho\overline{u'v'}$	Time average Reynolds shear stress in (x-y) plane
$-\rho\overline{u'w'}$	Time average Reynolds shear stress in (x-z) plane
$-\rho\overline{v'w'}$	Time average Reynolds shear stress in (y-z) plane
σ_b	Standard deviation of bed elevations

Chapter 1
Introduction

CHAPTER 1
Introduction

1.1 Background

Rivers are essential for habitats, which deliver water, solutes, and fine materials from the natural landscape, together with contaminants from urban and rural regions to rivers and eventually the ocean. They supply valuable and distinctive environmental habitats, whose enhancement and protection are now enshrined in the United Kingdom and European Union legislation through the Water Framework Directive (Cooper 2006).

Good water quality for the river is fundamental for human life, as well as the survival of animal and organism's species in both the aquatic and terrestrial environment. Water quality is impacted by both anthropologic activities from societal development and 'natural' events, which are driven by climatic, hydrological and geological systems which influence the abundance of water and its quality both on the earth's surface as well as in its surrounding atmospheric layers (Bartram et al. 1996). Natural meteorological events such as storms and high rainfall and flow events bring large volumes of runoff and surface water to the river basin. Anthropological activities such as urbanisation increase runoff entering watercourses by reducing ground infiltration. Furthermore, human activities such as timber harvesting, land clearance and agricultural practices lead to an increase in the sediment yield in the upper landscape, while dam construction reduces sediment supply and leads to a sediment discontinuity in the lower landscape (Nilsson et al. 2005; Hupp et al. 2009; Kondolf and Schmitt 2018). Both anthropological activities and 'natural' events change riverbed material size and elevation of the bed leading to changes in the riverbed pattern with time (Williams and Wolman 1984). Further deposition of fine materials on the surface of the riverbed over a long period creates hydrologic alterations in these regions (Hupp et al. 2008). In addition, the water quality of a river basin is also linked to anthropological activity and the magnitude of water input and as well as the sediment input (Raven et al. 1998; Soulsby et al. 2001). It is important that these activities are managed using a catchment-wide approach (Raven et al. 1998; Soulsby et al. 2001).

1.2 Alluvial River Characteristics

The physical formation and structure of a river system are dependent on the grain size diameter of the bed sediment; it is this property that governs whether a river is defined as having a sand- or gravel-bed (Barila et al. 1981; Dade and Friend 1998; Gilvear 1999). A river is characterised as a sand-bed river when the characteristic size of the surface sediment is in the range of 0.0625–2 mm, and as a gravel-bed river is classified as very fine, fine, medium, coarse and very coarse gravel-bed, when the characteristic size of the surface bed sediment is 2-4 mm, 4-8 mm, 8-16 mm, 16-32 mm, and 32-64 mm, respectively (Buffington and Montgomery 1999a). The work presented in the thesis is focused on rough-bed rivers which are typically gravel-bed rivers.

The bed of a gravel river is typically poorly sorted with vertical segregation of grain size. Typically there is an upper surface layer containing coarser material overlying a finer subsurface layer (Parker et al. 1982; Carling 1989; Powell 1998; Buffington and Montgomery 1999b). In a gravel-bed river, the geomorphological changes are controlled typically by bedload transport, with bedload being the main mode of sediment transport (Gomez 1991; Dade and Friend 1998; Powell 1998; Noack et al. 2016). The upper layer is typically transported by bedload during peak flows (Gomez 1983; Powell et al. 2001; Robert 2003).

In general, the grain size distribution in a sand-bed river is assumed to be well-sorted (Haschenburger 2016), however, this is not always the case (Haschenburger 2016). For example, the Beberibe river, located in the state of Pernambuco in the Northeast of Brazil, is a sand-bed river ($0.0625\ \text{mm}<d_{50}<2\ \text{mm}$), and bed sample analysis has revealed a heterogeneous grain size distribution, with vertical segregation present (Veras et al. 2016). Similar to a gravel-bed river, coarse particles were found in the upper layer and the subsurface layer was poorly sorted and contained a higher proportion of fine particles (Veras et al. 2016). Fine particles move faster than coarse particles in sand-bed rivers, similar to gravel-bed rivers (Frings 2008), where a similar alteration in bed roughness occurs when subject to flow fluctuations (Gaeuman et al. 2005). However, a material derived from a gravel-bed river transports at a slower rate than sand-bed rivers under the same flow conditions. Therefore, adjustments and variations in gravel-bed rivers will take longer to be reflected in river morphology and exhibit lower shear stress compared to sand-bed rivers (Parker and Klingeman 1982; Grant 2012). Gravel-bed rivers are comparatively common and provide a great environment for aquatic ecosystems (Neave

2014). Sand-bed rivers predominate in lowland regions due to the narrow size distribution of the bed particles and various geographical settings, whilst gravel-bed rivers predominate in upland regions (Frings 2008). Thus, steep gradient sand-bed rivers are rarely observed in nature (Crowley 1983).

A gravel-bed river, has a different physical structure compared to a sand-bed river with the macro bedforms including riffles and pools, as shown in Figure 1.1a, as well as bars. However, the bedforms of the sand-bed river comprise ripple, dune, and bar bedforms (Hey and Thorne 1986; Whiting et al. 1988; Kirchner et al. 1990; Thorne et al. 1996; Montgomery and Buffington 1997; Singh et al. 2011).

Bedforms develop due to erosion, deposition, and sediment transport, and frequently supply the bulk of the particles to be transported within the river, and though they are relatively simple structures, the resulting hydrodynamics arising due to their existence are highly complex in nature (Dinehart 1992; Radecki-pawlik et al. 2006; Robert 2003). Often such bedforms, which vary greatly in both length and height, greatly influence the overall hydraulic conditions of the rivers in which they exist (Carling and Orr 2000; Radecki-pawlik et al. 2006). Bedform was widely defined in different types of rivers that it is multi-layered in the sand-bed river, laterally oscillatory in the gravel-bed river, vertically oscillatory in a cobble-boulder-bed river, featureless in a gravel-cobble-bed river, random in a boulder-bed river, irregular in a rock-bed river and variable in a variable-bed river (Montgomery and Buffington 1997). The gravel bedform is larger than the sand bedform and analysis of both bedforms gives insight concerning their individual statistical characteristics (Singh et al. 2011).

In gravel-bed rivers, the pool-riffle bedform results in an undulating bed where a reach is composed of a sequence of pools, riffles and bars (Montgomery and Buffington 1997; Thompson 2018). Pool-riffle bedforms are heterogeneous features that display a range of sorting and packing involving coarse particles in the surface region and finer particles in the subsurface (Leopold et al. 1964; Milhous 1973). A riverbed will become relatively stable, with a certain periodicity, when numerous bars are formed along a reach. (Lanzoni 2000a; Lanzoni 2000b). Riffles and bars are considered topographic with a high elevation within gravel-bed rivers, and riffles are the downstream term for bars begun by pool scour. However, pools are considered topographic with low elevations within gravel-bed rivers (Clifford 1993; Robert 2003; Wilkinson et al. 2004; Thompson 2018). Pool-riffle bedforms generate changes in depth and width along the river reach (Gregory et al. 1994; Thompson and Hoffman 2001; Wilkinson et al. 2004; Sear and Newson 2004).

Such bedforms are likely altered with changes in the distribution of surface bed particles as the result of changes in the discharge of the river (Keller 1971). Thus, pool-riffle bedforms are associated with local flow and particle transport conditions such that when the near riffle bed average velocity equals that in the near pool bed with increasing discharge, particles can be moved across both the riffle and pool features (Keller 1971; Thompson et al. 1998; Robert 2003). However, when the near riffle bed average velocity is faster than that in the near pool, coarse particles are transported across the riffle and then trapped in the pool (Keller 1971).

In sand-bed rivers, dunes are classified by their form in terms of two or three-dimensionality, as well as their length in terms of being a small dune 0.6-5 m, medium dune 5-10 m, large dune 10-100 m or very large dune more than 100 m. Dunes are also related to flow depth (Baas 1978; Ashley 1990; Robert 2003). Ripples in sand-bed rivers, on the other hand, are small-scale bedforms, which have a height less than 0.1 m and a length less than 0.5 m. Ripples are ridges of sand or silt that run transversely to the flow direction and are generated by fluid shear at the interface between an erodible sediment bed and the overlying water (Baas 1978; Ashley 1990; Robert 2003). As the flow depth is larger than the ripple wavelength, ripples are not related to flow depth so their influence is only exerted near the bed, but they play a role in the flow far away from the bed surface when bed roughness increases (Maddux et al. 2003). In general, dunes are large-scale bedforms sharing similar characteristics to their small-scale equivalents, i.e.: ripples. Dunes are commonly created under steady flow and low flow conditions such as in subcritical flow (Kennedy 1969; Singh et al. 2011).

Ripples and dunes in sand-bed rivers have a gentle upstream face, or stoss side, slope and a steep slope downstream face, or lee side, which causes flow separation. Just downstream of the crest, the flow separates into two regions, namely an upper region of free flow, and a lower region of backflow with a separation vortex in the lee of the ripple (Baas 1978). The two regions are separated by a shear layer and mixing region (Baas 1978). The main flow re-attaches to the bed downstream of the bedform due to the shear layer slowly tending towards a downward direction, as shown in Figure 1.1b (Baas 1978; Nelson et al. 1993). Though dunes are observed in both sand- and gravel-bed-rivers, they are the most commonly associated with sand-bed rivers, where small-scale dunes tend to develop maximum steepness achieving equilibrium geometry (Carling et al. 2000; Singh et al. 2011).

Bars are observed in both sand- and gravel-bed-rivers (Lanzoni 2000b; Singh et al. 2011). Bars for both bed types can be characterised by radial flow distributions, downstream decreases in velocity, physical dimensions, and particle size (Smith 1971; Smith 1974).

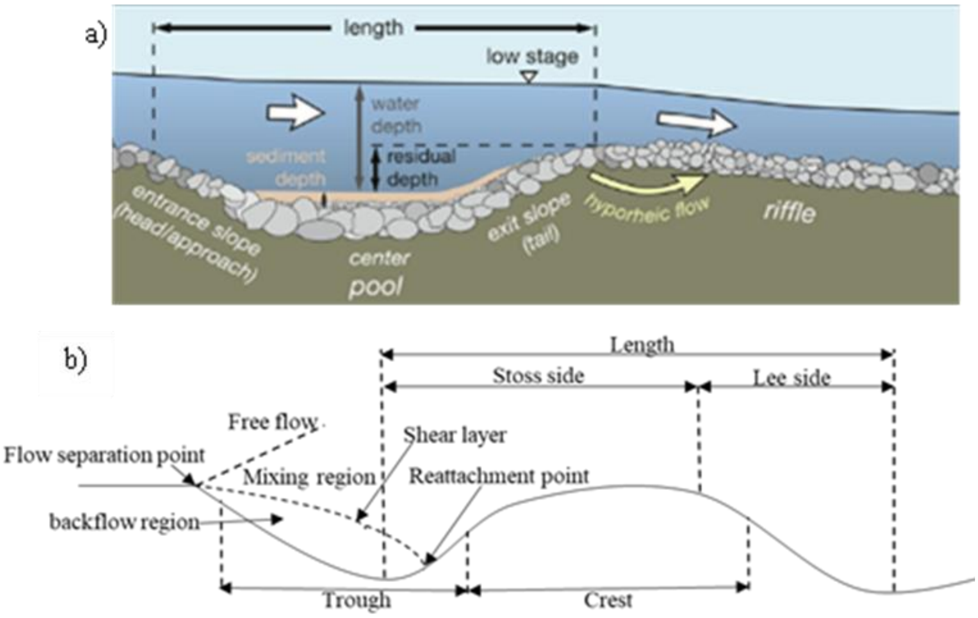

Figure 1.1. A schematic of the river bed a) the gravel-bed river, b) processes which occur in riffle and pool adapted from Thompson (2018, P. 2) and c) the sand-bed river based on Baas (1978, P. 2).

A narrow region close to the river centreline is where the maximum bedload can be transported for any bed type (Wilson 1973; Gomez 1991). Form drag can cause total boundary shear stress to be higher than bed shear stress in either sand- or gravel-bed-rivers (Parker and Peterson 1980; Prestegaard 1983; Dietrich et al. 1984; Hey 1988).

The supply of fine particles (e.g., clays, silts, and sand) into the river is affected by two types of events: the first event is a relatively low-velocity event which results in fine sediment depositing and infiltrating into the gravel-bed matrix; and the second event is a high flow event (e.g. flood), where elevated bed shear stresses cause bank and bed erosion, and the re-mobilisation of particles as well as soil erosion from overland flow (Dietrich et al. 1984; Powell 1998; Buffington and Montgomery 1999b; Maddock and Hill 2007; Verheijen et al. 2009; Simpson and Meixner 2012; Wilkes et al. 2019). Such processes lead to changes in riverbed elevation and grain size composition which in turn, can alter the form drag resistance the bed exerts on the overlying flow.

1.3 Riverine Hydrodynamics

Fluid hydraulics traditionally considers flow in rivers as one-dimensional, while many emerging cases require an understanding of two- or even three-dimensional flow, particularly those flow phenomena associated with turbulence (Cooper 2006). This is because within a turbulent flow, fluid elements act randomly and always in three dimensions with instabilities and uneven fluctuations, i.e. the velocity of fluid elements alters in magnitude and direction with time at a particular point in space (Nezu and Nakagawa 1993; Versteeg and Malalasekra 1995; Nguyen 2012). From this study's point of view, the turbulent flow occurs at a high Reynold number and fast flow in the rivers. it is a result of extreme kinetic energy in the fluid element that overcomes the damping consequence of the fluid’s viscosity. Therefore, turbulent flow leads to reduce fluid viscosity. Turbulent flow has long been identified as coherent structures at a wide range of space and time scales (Matthes 1947; Jackson 1976). Large-scale coherent flow structures seem to exist everywhere in gravel-bed rivers (Kirkbride and Ferguson 1995; Roy et al. 1996; Roy et al. 2004). The large-scale coherent flow structures play a role in the near-bed region of a river, such as driving particle transport and the formation of bed roughness features that affect river ecology (Jackson 1976; Wharton et al. 2017). These coherent flow structures occur due to the movement of low momentum fluid away from the bed, which is associated with low streamwise velocity, and the movement of high momentum fluid towards the bed surface, which is associated with high streamwise velocity (Grass 1971).

In addition, the near-bed area is significant for the generation and maintenance of turbulent flow (Corino and Brodkey 1969). For example, due to sudden variations in the bed geometry and existing obstacle elements (coarse sediments or vegetation) in natural rivers, flow separation occurs near the bed. Flow separation leads to the generation of local areas of high bed shear stress (see Figure 1.2a) (Best and Brayshaw 1985; Robert 2003). Therefore, vortices occur above the surface of roughness particles, individual large particles, or bedforms and cause laminar sublayer disruption and enhance the dominant coherent flow structures above these types of bed surfaces (Kirkbride 1993; Kirkbride and McLelland 1994; Bennett and Bridge 1995; Roy et al. 1999; Robert 2003).

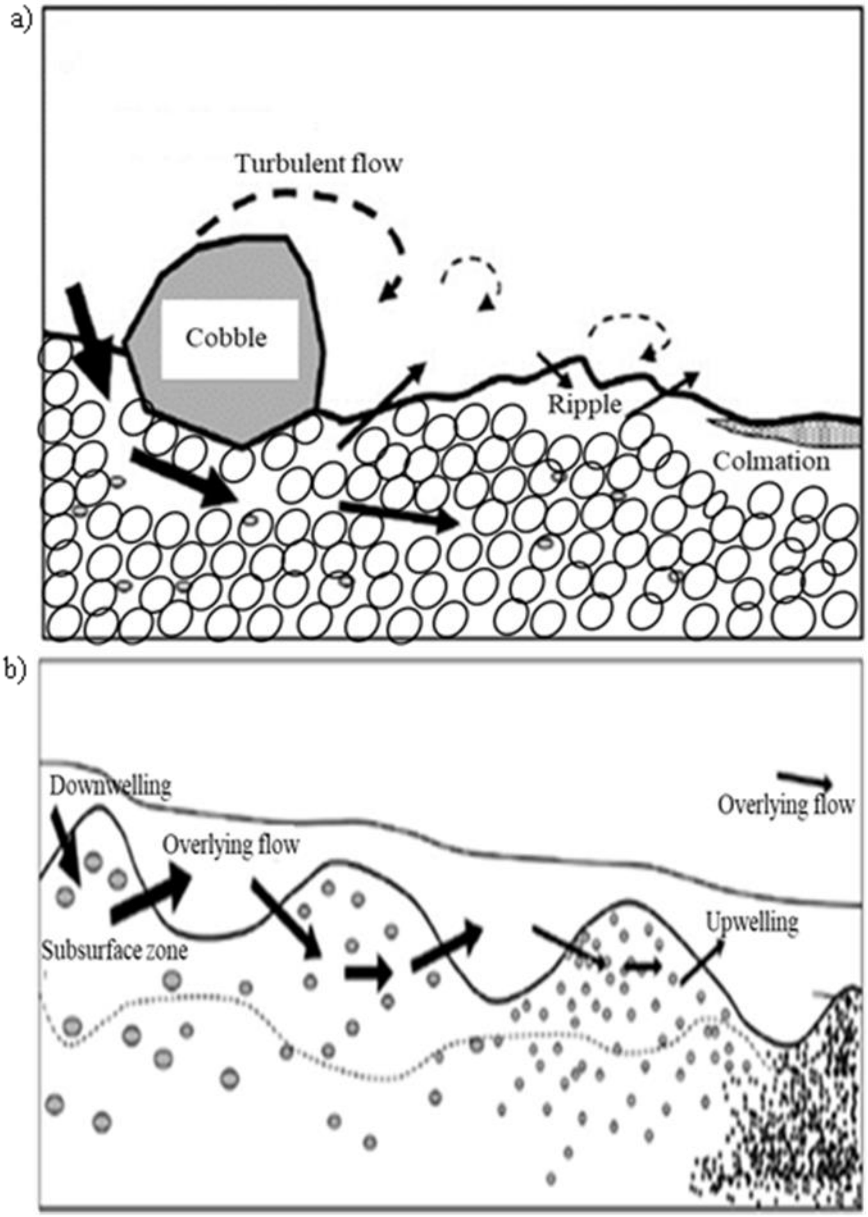

Figure 1.2. a) A schematic of the flow separation due to obstacle element and interactions between the water column and interstitial flow b) a schematic of the upwelling and downwelling flow near the gravel-bed river, adapted from Boulton et al. (2010, p. 32).

These vortices above rough-beds have the same shape as above smooth beds, yet are formed differently from that within the turbulent boundary region above smooth beds (Robert 2003). Structures of coherent flow occur as eddies shed off from the lee side of large protruding particles or downstream of the highest level of the bed surface (Robert 2003). Such turbulent flow processes drive the exchange of oxygen, nutrients, and pollutants between the bed and overlying flow and are often characterised as upwelling or downwelling flow. These upwelling and downwelling flows are directly related to the turbulent kinetic energy of the flow within the near-bed and the wider water column, see Figure 1.2b (Lorke et al. 2003; Packman et al. 2004).

A secondary current consists of time-averaged cross-streamwise and vertical velocity directions (Nezu 2005). Secondary currents occur in straight channels of non-circular cross-section due to the result of turbulence anisotropy (Naot and Rodi 1982; Nezu and Nakagawa 1984). However, a secondary flow of helical nature is generated in meandering rivers due to the centrifugal force (Nezu 2005). Secondary flows are generated near the bed by variations in the sediment size and fluctuations in bed topography which cause some degree of amplification of spanwise flow features (Barros and Christensen 2014). Secondary flows share several similarities with very large-scale coherent flow structures or superstructures (Kim and Adrian 1999; Hutchins and Marusic 2007; Monty et al. 2009). Both secondary and very large-scale coherent flow structures appear as large, counter-rotating eddies characterised by elongated streaks of varying low- and high-momentum flow. Both flow structures contribute to momentum exchange and mixing irrespective of their origin, and they adjust hydraulic resistance, turbulence formation, and sediment transfer (Nikora and Roy 2012; Zampiron et al. 2020). However, very large-scale coherent flow structures meander laterally in time and are related to the Reynolds number (Adrian and Marusic 2012). The direction of secondary flow structures is principally governed by the turbulent conveyance of turbulent kinetic energy, which itself might considerably rely on bed roughness characteristics in addition to the flow conditions (Hwang and Lee 2018).

1.4 Hyporheic Region and Aquatic Organisms

There are many factors that affect the quality of water in a river, such as biological, physical, and chemical properties. When these properties exceed the ranges suggested by the WHO (World Health Organization), the water can be considered polluted and could be harmful to humans, aquatic organisms, and cattle. The physical parameters that affect water quality include light penetration, water temperature, pH, the particle size of suspended and deposited sediments, conductivity, dimensions of the water body, hydrological balance, and flow velocity (Bartram et al. 1996). The region between the overlying surface flows of a permeable river bed and the groundwater flow is called the hyporheic zone see Figure 1.3. There are several flow processes that occur within this zone that directly influence water quality for the whole water column.

The hyporheic zone is a dynamic boundary region distinguished by steep gradients of pressure and velocity (Boulton et al. 1998; Harvey and Fuller 1998; Salehin et al. 2004; Cooper et al 2018). There are significant nutrient and chemical exchanges in this region (Brunke and Gonser 1997; Boulton et al. 1998) which include two key physical processes. Firstly, the upwelling of subsurface water into the benthic and surface flow layers provides river organisms with nutrients. Secondly, the downwelling of river water into the subsurface zone supplies dissolved oxygen and organic matter to microbes and invertebrates (Boulton et al. 1998).

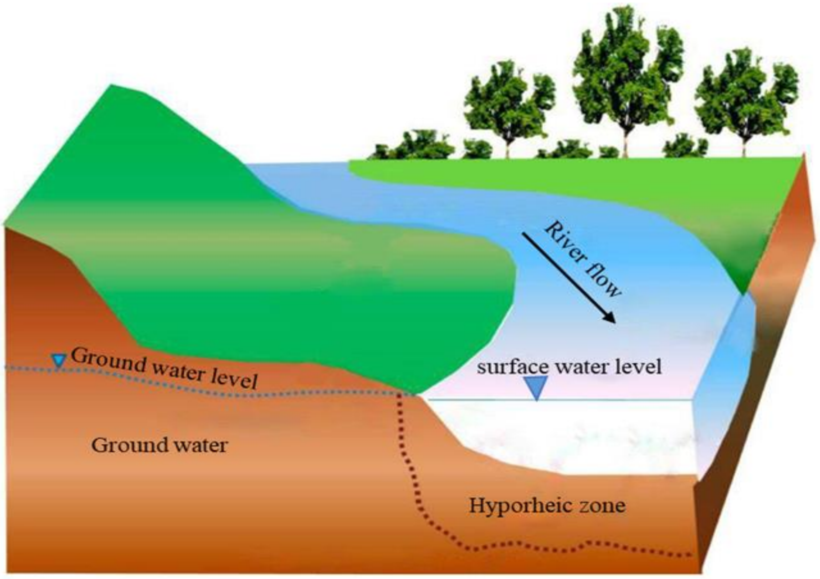

Figure 1.3. A schematic of the hydrogeology of the hyporheic zone and mixing zone and transition between surface water and groundwater, based on Kim and Lee (2018, p. 3).

In a gravel-bed river's hyporheic zone, fluctuations in water flows occur due to the hydraulic gradient and affect the ecology and biogeochemistry of the bed. These fluctuations increase interactions between the water surface and pore water flow and so increase the dissolved oxygen rate (Triska et al. 1989; Boulton et al. 1998). Without such interactions, the hyporheic zone would become anoxic (Boulton et al. 1998). This can occur during the colmation process, which typically reduces the exchange of river water between the surface, bed and sub-surface layers, and can negatively affect aquatic organisms as it reduces dissolved oxygen levels in gravel-bed rivers (Heywood and Walling 2007). Colmation is the deposition of fine sediments onto the surface of a gravel-bed river as well as deeper into the bed itself which results in a reduction in the porosity of the bed. This is especially true under low flow conditions (Schalchli 1992; Brunke and

Gonser 1997; Blaschke et al. 2003). Colmated particles can be beneficial to biota as they bring with them many nutrients, however, excessive quantities of fines can have a significant adverse environmental impact, particularly on anadromous fish species (Mohajeri 2014). Therefore, understanding the mechanics of fine particle infiltration into gravel-bed rivers is vital for evaluating the economic and biological effects on river ecosystems (Wooster et al. 2008). Also, there are potentially critical socio-economic ramifications related to the increased deposition of fine particles within gravel-bed rivers. This is because the majority of people in the world depend on aquatic animals for food and many fish, such as salmonids, breed exclusively in the upper-reaches of rivers. Therefore, an appreciation of the hydrodynamics of rough gravel-bed rivers, where for example female salmonids spawn (Kondolf and Wolman 1993), is key for hydraulic engineers, environmental and ecological scientists when evaluating river restoration projects (Harper et al. 1992; Thomson et al. 2001; Navaratnam and Aberle 2017; Tenzin et al. 2019). Colmation also affects groundwater recharge. The deposition of fines, particularly cohesive sediment such as clays, can decrease the circulation of interstitial flow and consolidate the bed, reducing the flushing effects of the fine particles during high flow events. Under such conditions the exchange between groundwater and the river is reduced and can severely limit groundwater recharge and supply (Schälchli 1995; Peloutier 1998).

Due to the deposition and infiltration of fine sediments into the pores of gravel-bed rivers, the overall roughness of the bed can gradually reduce (Iseya and Ikeda 1987). The degree of deposition can be directly influenced by anthropogenic activities. For example, flushing, or hydro-peaking, from dams in response to a request for peak power or due to a storm event can lead to the flushing of fines from the bed through so-called decolmation or declogging (Schälchli 1995; Flodmark et al. 2002; Thompson 2011). The hydraulic fluctuations resulting from hydro-peaking are typically frequent and rapid (Harby and Halleraker 2001; Harby and Noack 2013). Hydro-peaking can cause serious disruption to the ecology of a river, the hydrological system in general, and river morphology (Harby and Halleraker 2001; Thompson 2011; Tuhtan et al. 2012; Harby and Noack 2013).

Dewatering events, largely due to agricultural processes such as abstraction for irrigation, can also cause fish stranding and migration leading to high mortality rates of juvenile fish which are critical to sustaining the population overall (Saltveit et al. 2001; Harby and Halleraker 2001; Thompson 2011; Tuhtan et al. 2012).

Colmation, decolmation, and dewatering processes can all lead to alterations in the roughness of the river bed (Madej 2001). The roughness of gravel-bed rivers is significant for fish populations as they prefer a certain velocity, depth, quantity of woody debris, and roughness to spawn (Lamouroux et al. 1999; Rifflart et al. 2009; Capra et al. 2017; Judes et al. 2020). It should be noted that this preferential region in water depth and the streamwise plane is also named the boundary layer (Nikora et al. 2001; Franca et al. 2008). Fish performance, in terms of swimming, is affected by local velocity and turbulence stresses such as turbulent intensity (Richmond et al. 2007), Reynolds shear stress (Silva et al. 2011), and turbulent kinetic energy (Smith et al. 2006). For example, juvenile graylings prefer slow water velocities and low flow depths (Tuhtan et al. 2012; Harby and Noack 2013).

In summary, gravel-bed rivers are essential for salmonids and other aquatic organisms, and therefore, it is of critical importance to understand and quantify the physical mechanisms by which the transport of nutrients, pollutants, sediment, and other influences on their habitat are driven.

1.5 Thesis Objectives

This thesis focuses on the velocity and turbulent flow structures above a gravel-bed to understand the impact of gravel characteristics, porosity, and relative submergence on velocity profiles and turbulent stresses. Specifically, it investigates turbulent flow over permeable, hydraulically rough-beds to understand the complexities of open channel flows over rough surfaces. The following key objectives addressed in this study are:

1. To compare the mean and turbulent flow fields for the flow over a highly porous natural gravel-bed and an idealised rough-bed under intermediate and high relative submergence conditions.
2. To characterise the porosity and distribution of bed surface elevations for both the naturalistic and idealised rough-beds within the experimental sampling area.
3. To validate the theoretical logarithmic velocity law equation for a hydrodynamically rough boundary for a natural gravel-bed and an idealised rough-bed.
4. To validate and compare the distribution of turbulent intensity with pertinent equations for rough-beds for both natural gravel and idealised beds.

5. To investigate average velocity distributions within the voids of the gravel-bed layer of different rough-beds.

To achieve these objectives, an acoustic Doppler velocimeter (ADV, Nortek Vectrino; Nortek 2004) was used to measure the three-dimensional velocity field above a hydrodynamically rough-bed in an open channel flume. In addition, ten endoscopes were used to measure the velocity distributions within the voids of the gravel medium of the channel bed. The investigation was conducted for two ‘natural’ unworked gravel-beds composed of different particle sizes and one idealised artificial bed. A range of flow conditions was examined in the fully turbulent flow regime ($13{,}448 < Re_H < 30{,}208$), with a focus on the pore-particle layer and the intermediate and high region of the velocity profile.

A double-averaging methodology was used to analyse the turbulent flow above various gravel-beds and to quantify the turbulent ejection and sweep events. The image analysis code developed by Forughi (2014) was also used to study velocity distribution through the voids in different gravel-beds themselves.

1.6 Outline of the Thesis

Chapter two presents a literature review on turbulent flow above and within the gravel-bed river. This chapter examines pertinent literature involving the logarithmic velocity profile, exponential decay equations for turbulent intensities, Reynolds shear stress distribution, Reynolds normal stress, turbulent kinetic energy, and quadrant analysis. The chapter also explores literature focused on interstitial flows within gravel-beds themselves as well as possible instrumentations to measure velocity profiles both above and within the pores of a gravel-bed.

Chapter three presents the methods and materials used in this study and includes details about how the flume bed was covered with natural gravel-bed and artificial beds. The determination of the standard deviation of the surface elevations as well as the porosity of the different beds is also presented. The method for gathering velocity measurements using an Acoustic Doppler Velocimeter (ADV) and endoscopes above and below the bed surface is also presented.

Chapter four reports on the experimental results gathered using an ADV in the near-bed region and beyond and determines the applicability of the logarithmic velocity profile. This chapter also presents turbulence stresses such as turbulent intensity, Reynolds shear stress, Reynolds normal stress, and turbulent kinetic energy.

Chapter five presents a quadrant analysis conducted for flows above a gravel-bed, which is key to understanding the upwelling and downwelling flow in the subsurface region. In addition, this chapter reports on the experimental results obtained using endoscopes within the sediment bed layer including the average velocity distribution in this region.

Finally, chapter six presents the conclusions and key findings of this research and outlines the contribution made by this study to the bigger picture of science on this topic. Suggestions for further research work are proposed at the end of this chapter.

Chapter 2
Literature Review

CHAPTER 2
Literature Review

2.1 Introduction

This chapter will review relevant previous and current theories on the hydrodynamics of gravel-bed flows, with specific reference to the determination of the logarithmic law following measurements in the field and the laboratory under intermediate and high relative submergence types of flow above different rough-beds. As such, the impact of relative submergence will be explored. The concept and determination of the zero-displacement distance are also presented. The characteristics of turbulent flows are highlighted with particular reference to the second-order velocity statistics. Velocity measurement methods are also reviewed as well as subsurface flow phenomena. Finally, areas for further research are highlighted

2.2 Velocity Profile

Although much research has recently focused on flows above gravel-bed rivers, such as velocity flow profiles and turbulent flow characteristics, there is a need for further investigation to fully understand the behaviour within the hydraulically rough flow regime. The vertical profile of the streamwise velocity in the inner layer of open channel flow is described by Prandtl's logarithmic law (Prandtl 1925). The logarithmic region of the flow depth above both smooth and rough-bed surfaces can be described by the following equation (Nezu and Nakagawa 1993; Nikora et al. 2001):

$$\frac{\bar{u}}{u_*} = \frac{1}{\kappa}\ln\left(\frac{Z}{k_s}\right) + C \tag{2.1}$$

where, $\bar{u}$ is mean velocity, u_* is shear velocity, κ is von Karman constant, Z is the distance from the bed, k_s is the equivalent sand roughness of Nikuradse, and C is a constant integration (5.5 for a smooth bed and 8.5 for a rough-bed). These parameters will be discussed in more detail later in this section.

The constant of integration was found to be 7.1 and the Nikuradse equivalent sand grain roughness was found to be $1.5d_{50}$, which is approximately $4\sigma_b$, where d_{50} is the 50th percentile grain size distribution of the surface material and σ_b is the standard deviation of bed elevations, above a bed covered with 1.2 mm thick styrene sheets with a thin 0.3–0.4 mm flocked coating with spherical segments of 21 mm in height (Nikora et al. 2001). The velocities were 0.483 m/s and 0.674 m/s, where experiments were carried out under uniform flow conditions fitted to the logarithmic law Eq. (2.1). The von Karman constant was assumed to be a constant of 0.4 (Nikora et al. 2001).

Nezu and Nakagawa (1993) examined a range of datasets above the smooth bed from Steffler et al. (1985), Nezu and Rodi (1986) under numerous flow conditions corresponding to Reynolds number (Re) in the range 23,000 to 440,000; Froude number (Fr) in the range 0.077 to 1.240; and velocities in the range 0.076 m/s to 1.185 m/s. They found by using κ and C values of 0.41 and 5.29, respectively, velocity profile measurements could be fitted to the theoretical logarithmic equation irrespective of the Fr and Re numbers (Nezu and Nakagawa 1993). However, the von Karman constant is now understood to not always be constant with different Re number values (Huffman and Bradshaw 1972; Zagarola and Smits 1998; Marusic et al. 2010). This is particularly the case for permeable beds when boundary resistance increases with Re and can lead to a decrease in κ down to 0.28. This was observed during experiments above a permeable bed with median uniform gravel of diameter 9.8 mm and an overall bed thickness of approximately 5.50 cm (Gupta and Paudyal 1985).

The constant of integration has been found to be 8.5 for a rough-bed (Nezu and Nakagawa 1993). However, Kironoto and Graf (1994) found that it varies somewhat (8.47±0.90) depending on the degree of roughness. In this thesis, a constant of integration of 8.5 will be applied for all cases in a similar fashion to that found by Nezu and Nakagawa (1993). However, it should be noted that others (Mendoza and Zhou 1992; Prinos et al. 2003) suggest that the constant of integration is actually a function of the interfacial velocity and thus, cannot be identified a priori. Clearly, the application of the logarithmic law to rough-bed conditions is highly challenging.

When the hydraulic roughness number $K^+ > 70$, the flow can be considered hydraulically rough and, thus, within the fully rough, turbulent flow regime (Nikuradse 1933; Nezu and Nakagawa 1993; Bomminayuni and Stoesser 2011). K^+ is defined as the roughness Reynolds number by $K^+ = u_* k_s/\nu$ in which, k_s is the Nikuradse equivalent sand roughness, and ν is kinematic viscosity. k_s is expressed in terms of uniform sand particle diameters and will be applied in this thesis in a similar fashion to Nikuradse (1933), Grass (1971), and Bomminayuni and Stoesser (2011).

In general, the logarithmic equation is applicable to approximately 20% of the water depth in the so-called logarithmic layer (Nezu and Nakagawa 1993). It is assumed that with increasing distance from the bed surface, the mixing length increases whilst the shear stress remains constant resulting in the logarithmic law only being applicable within this region (Koll 2006).

Averaging of the governing Navier-Stokes equations in time and space within a plane parallel to the bed, so named Double Average equations (DA), are used in the study of atmospheric sciences and river dynamics to explore heterogeneous flows over roughness elements (Finnigan 2000; Nikora et al. 2001; Nikora et al. 2007). The main disadvantage of the DA method is that it leads to a loss of information about the local variation of flow variables (Nikora and Rowiński 2008). However, the advantages of the DA method have been highlighted to outweigh any such disadvantages (Nikora et al. 2001). Firstly, double averaged flow variables are associated with spatially averaged roughness factors (Nikora et al. 2001), thus, associating the water column with the pore bed interstitial flow (Hsu et al. 2002; Nikora et al. 2004). Secondly, due to the derivation and integration of the DA equations, form-induced stresses and form drag terms appear in the momentum equation directly. Finally, double averaged variables are likely to cover the whole flow layer as well as the interfacial sublayer (Nikora et al. 2001).

However, as Nikora et al. (2001) highlight, the spatial resolution of velocity measurements must be high for the DA method to be applicable, this is especially true above irregular rough-beds. The investigation in this thesis will use the double average method to analyse turbulent characteristics above rough-beds under uniform conditions.

Eq. (2.2) was determined to characterise the double averaged velocity within the logarithmic layer (Nikora et al. 2001).

$$\frac{\langle \bar{u} \rangle}{u_*} = \frac{1}{\kappa} \ln\left(\frac{Z}{k_s}\right) + C \tag{2.2}$$

in which $\langle \bar{u} \rangle$ is the double averaged streamwise velocity, where $\bar{\cdot}$ signifies the time-average and $\langle \cdot \rangle$ signifies the spatial area average.

In the last two decades, researchers (e.g. Nikora et al. 2001; Nikora; et al. 2007) have identified different types of flow above permeable and impermeable beds in open channels. These flow types are classified based upon the relative submergence of the flow depth to the bed roughness length (H_{max}/Δ) where, H_{max} is the maximum flow depth from the water surface to roughness troughs, and Δ is the roughness scale (Nikora et al. 2001; Nikora; et al. 2007).

Flow type I is the high relative submergence flow condition and includes the outer layer, the logarithmic layer, and roughness layer (e.g. the form-induced sublayer and the interfacial sublayer) above the impermeable rough-bed, as shown in Figure 2.1a, and when in reference to permeable beds, also includes the subsurface layer (Nikora et al. 2001; Nikora 2007), as shown in Figure 2.1b.

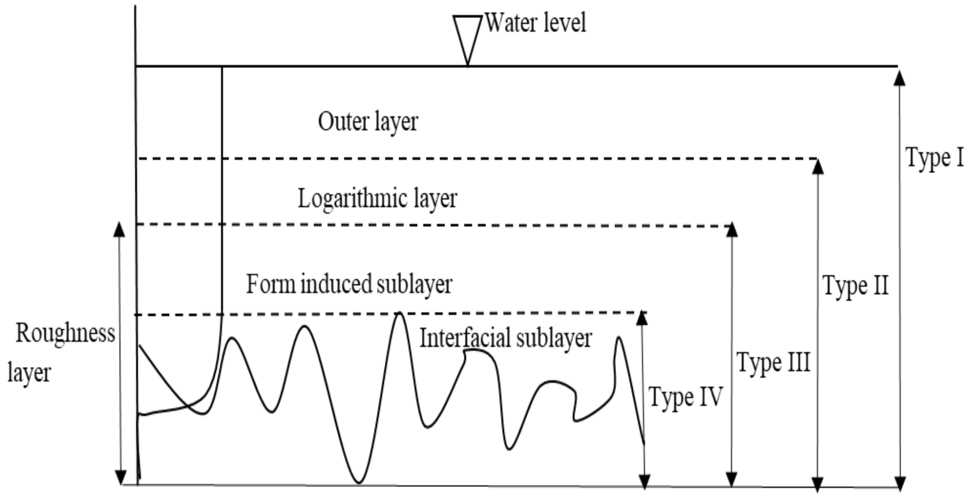

a) impermeable rough-bed

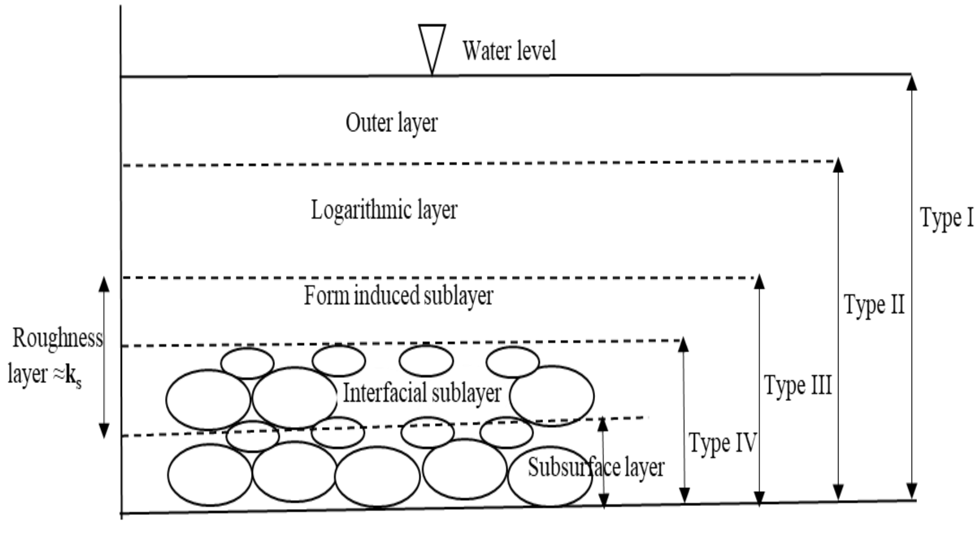

a) permeable rough-bed

Figure 2.1. Schematic shows different layers and types of flow above porous rough-bed defined by Nikora et al. (2001).

Flow type II is the intermediate relative submergence flow condition and includes the subsurface layer, a roughness layer, and an upper flow zone in which it has been reported (Nikora et al. 2007) that there is not a universal logarithmic velocity distribution as this ratio is not large enough. Flow type III is the low relative submergence flow condition, and the maximum flow depth extends to an upper elevation of the roughness layer including the subsurface layer and the roughness layer. The ratio range for this type of flow is $(2\text{-}5)\Delta > H \geq \Delta$, where H is flow depth. Finally, flow type IV is the flow condition whereby the bed is only partially inundated and maximum flow depth extends to the upper interfacial sublayer including the subsurface layer and interfacial sublayer. The ratio range for this type of flow is ($H<\Delta$) (Nikora et al. 2001; Nikora et al. 2007).

Flow type II has been extensively experimentally investigated (e.g. Nikora 2007; Afzalimehr 2010; Mohajeri 2014; Cameron et al. 2017; Yanda et al. 2018). Mohajeri et al. (2015), investigated flow structures above an immobile gravel-bed in an open channel with relative submergence between 7.5 and 10.8 and found that the governing parameters of the logarithmic law depend upon the submergence (Mohajeri et al. 2015). Interestingly, it was suggested that the logarithmic law may still apply under intermediate relative submergence flow conditions but requires further investigation (Mohajeri et al. 2015) and remains debatable (Nikora et al. 2001; Pokrajac et al. 2006; Mohajeri 2014). Although much research has been conducted under flow type II conditions, few relate to the spatial organisation of near-bed velocity profiles and those that do, have contradictory conclusions (e.g. Nikora 2007; Afzalimehr 2010; Mohajeri et al. 2015; Cameron et al. 2017; Yanda et al. 2018). In addition, the shape of the velocity profiles above the interfacial sublayer for flows with high relative submergence (type I), as well as within the form-induced sublayer for flows with intermediate relative submergence (type II), is not yet determined (Nikora; et al. 2007).

Von Karman's constant (κ) is a dimensionless constant in the logarithmic law, which describes the distribution of the average streamwise velocity near the bed of a channel (Frenzen and Vogel 1995). It was defined originally by von Karman (1930 cited in Frenzen and Vogel 1995), who proposed a similarity hypothesis whereby turbulent velocity variations can be considered statistically similar from point to point. This allowed von Karman to express mean characteristics in terms of length and time scales. In general, von Karman's constant can be defined as the relationship between mixing length (Gaudio et al. 2010; Zeng et al. 2015) and distance from the bed (Lo et al. 2005; Gaudio et al. 2010; Zeng et al. 2015), and links the time-averaged streamwise velocity distribution within the bed bounded shear flow to the shear stress at the bed in the flow depth direction. The mixing length is a function of the velocity gradient and the Reynolds shear stress.

Numerous different ways of calculating κ, as well as varying values, have been expressed in the literature. For example, it was found to be within the range of 0.17 to 0.38 under uniform conditions (Franca et al. 2008) using the relationship between mixing length and distance from the bed. Equally, κ was found for a mobile bed to equal 0.29 (Nikora and Goring 2000), 0.37 by applying regression analysis to the logarithmic law fitting until the maximize regression coefficient was found for a given value of zero-displacement distance (z_0) (Dey et al. 2012) and 0.27 by shifting the logarithmic law profile downwards from a known smooth wall distribution until a fit with the measured data was obtained (Hanmaiahgari et al. 2017). Von Karman's constant is likely less than the traditional value (0.41) for a mobile bed due to variations in the roughness length (Heathershaw 1981; Hanmaiahgari et al. 2017) resulting in reduced effects of drag (Nikora and Goring 2000).

Different scenarios were used to determine other logarithmic parameters using an assumed κ value of 0.40, which causes non-physical values of k_s and would mean the expansion of the inner region up approximately 50% of the water depth that is physically hard to interpret (Antico et al. 2019).

Von Karman's constant was also found to range between 0.305 and 0.355 due to differences in experimental conditions, while it was found to not vary due to differences in bedload (Antico et al. 2019), and decrease due to unknown hydrodynamic causes (Ferreira et al. 2012). In addition, some researchers found a κ value of 0.4 and 0.41 (Nikora and Goring 2000) and 0.41 (Dey et al. 2012; Hanmaiahgari et al. 2017) for an immobile bed. However, other researchers found κ lesser or higher than the traditional value. For example, the double averaged velocity distributions fit well with the logarithmic equation when κ values range between 0.2 and 0.51 above two different types of gravel-beds by applying the best fit measurements velocity profiles with logarithmic law above the immobile bed (e.g. Zeng et al. 2015) and above the water worked for bed (e.g. Cooper 2006), as shown in Table 2.1. Increasing concentrations of suspended sediment lead to decrease values of κ (Best et al. 1997) and κ equalled 0.27 due to the porosity used by Nakagawa and Nezu 1980 cited in Gupta and Paudyal 1985.

Table 2.1. Previous studies investigating von Karman's constant.

Reference	κ	Fr	Re	Type of bed
Nezu and Nakagawa (1993)	0.41	0.08-1.24	23,000-440,000	Smooth beds
Gupta and Paudyal (1985)	0.28 0.4	0.15-0.81 0.48-1.01	4,870-58,340 10,780-53,180	Permeable beds an impermeable bed
(Vanoni 1946 cited in Gupta and Paudyal 1985)	0.31			Unclear water condition
(Nakagawa and Nezu 1980 cited in Gupta and Paudyal 1985)	0.27			Permeable beds
Bailey et al. (2014)	0.40		80,000-10,000,000	Hydraulically smooth pipe
Franca et al. (2008)	0.17 0.38	0.42 0.19	126,000 95,000	Venoge river Chamberonne river
Nikora and Goring (2000)	0.29 0.4 0.41	0.38 0.29 0.16	780,000 430,000 200,000	Mobile bed Immobile bed Immobile bed
Dey et al. (2012)	In average 0.37 0.41	0.55-0.77	238,000-551,000	Mobile bed Immobile bed
Hanmaiahgari et al. (2017)	0.26 -0.27 0.40-0.42 0.35 0.33	0.37- 0.38 0.24- 0.28 0.30 0.34	26,713- 27,687 16,696- 19,200 21,565 24,000	Mobile bed Immobile bed Incipient motion minor bedforms
Antico et al. (2019)	0.305-0.355	0.62- 0.92	41,405- 58,999	Immobile and mobile bed, where flume bed was divided to bed large boulders, smooth bottom, one layer of glued spherical glass beads and mobile reach
Zeng et al. (2015)	0.2- 0.5	0.37- 0.68	111,000-256,000	Immobile bed
Cooper (2006)	0.21-0.51	0.40- 0.83	2,171- 42,618	Water worked bed
Koll (2006)	0.40	0.41-0.60	41,333-242,000	Glass beads, PVC cubes and gravel

There are also other, inconclusive factors that have been noted in the literature to cause variations in κ. For example, the submergence ratio has been shown to affect both κ and the zero-displacement distance by influencing the scale of coherent turbulent structures whereby, κ increases with increasing relative flow submergence as well as the velocity distribution gradient (Kirkbride 1993; Sirovlch and Karlsson 1997; Koll 2006). Additionally, as z_0 reduces with increasing relative submergence (Koll 2006), the existence and upper bounds of the logarithmic region are inconclusive (Gaudio et al. 2010; Rouzes et al. 2019).

There is also contradictory evidence that von Karman's constant is affected by the Nikuradse equivalent sand roughness and the friction factors alike, as well as by the nature of the roughness and the roughness Reynolds number (K^+) (Vanoni 1953; Mortensen et al. 1987; Frenzen and Vogel 1995).

Velocity profiles have also been noted to decrease with increasing κ values (Jain and Ghoshal 2020), and a small value of κ perhaps due to a relationship between the size of turbulent eddies (McLean et al. 2008).

The value of von Karman's constant found in the literature varies by up to 60% compared to the traditional value of 0.41. However, the physical mechanisms for such variation are unclear with numerous reasons given from bed mobility, unclear water, experimental conditions, porosity, etc raising many contradictory conclusions which cast doubt over any perceived cause. Clearly then, von Karman's constant and the displacement height need more investigation to cover the ambiguity in the applicability of the logarithmic velocity profile (Ferreira 2015).

The Nikuradse equivalent sand grain roughness (k_s) was originally introduced by Nikuradse (1933), who created a rough-bed using pipes covered with uniform sand grains, 0.8 mm in diameter. Pipe diameter varied from 25 mm to 100 mm and total length ranged from 1800 mm to 7050 mm. At the time, this was the easiest way to create geometrically similar roughness elements (Nikuradse 1933).

Nikuradse (1933) hypothesised that any deviation in the observed velocity profile from the logarithmic law was simply a function of the Nikuradse equivalent sand grain roughness. This equivalent roughness is representative of one dimension (a theoretical roughness length) of complicated three-dimensional bed topography and particle composition (Nikuradse 1933; Weill et al. 2010). As such, the Nikuradse equivalent sand grain roughness varies with the size and shape of bed particles, as well as the space between the particles themselves and their arrangement (Schlichting 1936; Morris 1955; Sayre and Albertson 1963; Gomez 1993; Dey and Ali 2019). Additionally, k_s has been determined as not only a geometric factor, but also a hydraulic factor dependent on the flow conditions (Jimenez 2004; Camenen et al. 2006; Liu et al. 2016; Dey and Ali 2019), as well as particle transport near the bed (Liu et al. 2016) and bed mobility.

However, Aberle and Smart (2003) used the standard deviation of the bed elevations as k_s. They assert that simply using the bed particle diameter is not representative of the surface geometry composition and thus, is inadequate for use as k_s in this way. Experiments were undertaken by Aberle and Smart (2003), in conjunction with data sets from Rosport (1997) and Koll (2002) to demonstrate this. Above the roughness crests, the standard deviation of the bed surface was applied and found that k_s is 8.053 mm when double averaged velocity profile measurements follow the logarithmic law under uniform conditions (Adak 2018), as shown in Table 2.2.

In contrast, a double average of the velocity profile below the crests obeys a polynomial relationship (Adak 2018). The bed of gravel-bed is three-dimensional, so it is the best for more bed characteristics including to describe its effect on overlying turbulence flow.

Table 2.2. Previous studies exploring Nikuradse equivalent sand roughness.

Reference	k_s	Type of bed
Adak (2018)	$0.20d_{50}$	Water-worked-bed
Ferguson (2007)	$4d_{85}$	Rough-bed
Weill et al. (2010)	$2.56d_{50}$	Rough-bed
Van Rijn (1993)	$2\ d_{90}$-$3d_{90}$	Immobile-bed

Nikuradse's (1933) experiment was carried out with uniformly sized, well-sorted sand and regular particle arrangement. However, gravel-beds found in open-channel flows, such as rivers, are made up of particles of irregular size and packing, often with a single large particle, or clusters of particles, protruding into the flow creating microtopography and bedforms which resist the flow (Ferguson 2007; Jay Lacey and Roy 2007; Jay Lacey and Roy 2008). Thus, the determination of k_s has been adjusted to better fit velocity measurements to the logarithmic law profile by using values such as $4d_{84}$ instead, where d_{84} is the 84th percentage of the particles size distribution uniform flow conditions (Ferguson 2007). For instance, the Nikuradse equivalent sand roughness was found to be approximately $2.56d_{50}$ under steady flow conditions, close to the finding of other experiments, even with different shaped bed materials (Weill et al. 2010).

From the literature, it is clear that the value of k_s varies, even by as much as 50%, but the causal relationship between any number of physical characteristics, such as bed topography, bed mobility, Froude number, Reynolds number etc, is highly debatable.

The zero-displacement distance (z_0), which is another parameter in the equation for the logarithmic law velocity profile, was introduced as the height where the logarithmic velocity distribution computed using Eq. (2.1) and Eq. (2.2) theoretically becomes zero above a rough-bed, as shown in Figure 2.2. In the case of a smooth bed, such a parameter is not required (Clauser 1956; Smart 1999). The coordinate of the zero-displacement distance may be anywhere between the highest crest and the deepest valley of the surface of a rough-bed depending on the penetration of large eddies into the rough wall, as shown in Figure 2.2 (Clauser 1956; Nikora et al. 2001; Nikora et al. 2002). A physical basis for the zero-displacement distance is highly controversial and often misrepresented in the literature by providing quantification without a full explanation.

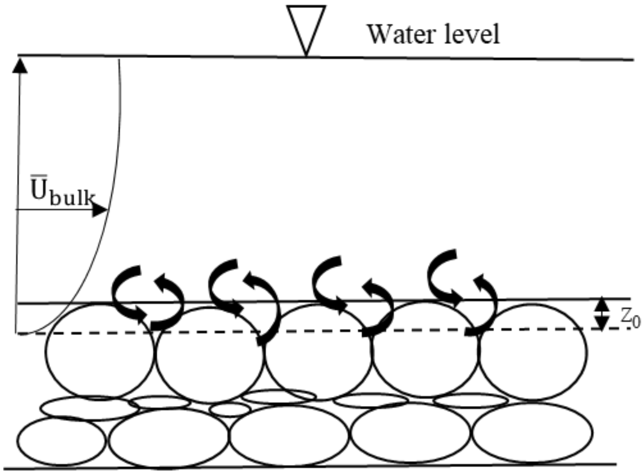

Figure 2.2. The schematic shows the zero-displacement distance (z_0) and eddies that occur near the bed.

The zero-displacement distance varies from one experiment to another depending on the experimental conditions, specifically, the bed topography. For example, it was found to be $0.2d_{50}$, where d_{50} equalled 25.4 mm, below the gravel crest when Re was in the range of 230,000 to 490,000 (Afzalimehr and Anctil 2000). Similarly, it was found to range between 0.15 and $0.3d_{50}$ by Nezu and Nakagawa (1993) who compared the data set of Grass (1971), where Re was 6,620 and gravel diameter was 9 mm, against Nakagawa et al. (1975), where Re ranged from 8,600 to 9,800 above uniform glass spheres. Mohajeri et al. (2016) equated the standard deviation of the bed elevations to the zero-displacement distance giving z_0 equal to 6.1 mm ($0.28d_{50}$) above an immobile gravel-bed with a median diameter of d_{50}=22 mm and d_{90}= 29 mm and a flow where Re ranged from 12,750 to 23,320. The zero-displacement distance found for these, and similar studies are summarised in Table 2.3.

However, the zero-displacement distance equals 0.7 times the height of roughness, where drag force acts on the elements, and it depends on the density of elements in the case of k-type roughness (Jackson 1981), who used rod as roughness elements. It was theoretically verified the rod roughness that z_0, where drag force acts. Therefore, the correct estimation of zero-displacement distance above complex beds such as gravel-bed rivers is considerably challenging.

Table 2.3. Previous studies on zero-displacement distance.

Reference	z_0	Fr	Re	Type of bed
Afzalimehr and Anctil (2000)	$0.2d_{50}$	0.14-0.36	230,000-490,000	Gravel-bed
Nezu and Nakagawa (1993)	$0.15d_{50}$-$0.3d_{50}$	0.15-0.18	6,620- 9,800	Rough-bed
Mohajeri et al. (2016)	$0.28d_{50}$	0.47- 0.51	12,750-23,320	Gravel-bed
Jackson (1981)	0.7k			Theoretically above k-type bed
Singh et al. (2007)	$0.19d_{50}$		3112	Rough-bed
Bomminayuni and Stoesser (2011)	$0.1d_{50}$	0.17	13,680	Rough-bed
Hanmaiahgari et al. (2017)	$0.35d_{50}$	0.24-0.38	16,696-27,687	Mobile and immobile bed
Kim et al. (2019)	$0.11d_{50}$-$0.13d_{50}$	0.58-0.90	18,621-40,921	Rough-bed

More recently, the so-called modified Clauser method has been used to find a value for z_0 that allows for the best fit between measured velocity data and the logarithmic law (Perry and Li 1990; Kim et al. 2019). This method has a higher resolution (Chan et al. 2015) compared to the method based on the centroid of the drag forces (Jackson 1981).

The zero-displacement distance was found to be 0.19 times the diameter of the hexagonally packed spheres ($0.19d_{50}$) used by Singh et al. (2007) to create a bed; 0.2 times the roughness height for a bed of hemispheres ($0.1d_{50}$) (Bomminayuni and Stoesser 2011); $0.35d_{50}$ for a rough sand bed (Hanmaiahgari et al. 2017); as well as 0.21 and 0.25 times the roughness height for beds of cubically and hexagonally packed large hemispheres, respectively ($0.11d_{50}$-$0.13d_{50}$) (Kim et al. 2019). The modified Clauser method will also be used in this study to find the best fit between the measured velocity data with the logarithmic law and parameters of logarithmic law.

A great deal of debate surrounding the zero-displacement distance for gravel-beds remains. This is because of the challenge in measuring velocities near complex bed topography which hampers efforts to fit measured data with the logarithmic law in this region (Ferguson 1993; Singh et al. 2007; Afzalimehr and Rennie 2009). Many more experiments with complex bed geometries and under various flow conditions and relative submergences are required to add clarification to velocity profiles and the applicability of the logarithmic law above rough-beds (Nikora et al. 2004). Thus, the present study will explore the applicability of the logarithmic law and its parameters for turbulent velocities above highly porous gravel-beds.

2.3 Turbulent Flows in a Gravel-Bed River Channel

Riverbeds are crucial for sustaining aquatic organisms which need a high quantity of dissolved oxygen. Turbulent flows lead to sediment suspension and increased voids within a gravel-bed river leading to increased dissolved oxygen exchange. Therefore, turbulent flows are the focus of this section of the literature review.

Bursts of turbulent flow from the bed occur with a high Reynolds number, which leads to an increase in the frequency and duration of turbulent bursts (Kline et al. 1967; Nguyen 2012). In the laminar sublayer, spatially and temporally motions occur and are well organized. These motions cause the generation of low-speed streaks near the bed. These streaks interact with the outer region of flow during a process of slow ‘lift-up’ and then bursting, sudden oscillation and ejection occur. These processes are significant in the generation of new turbulence and the transfer of turbulence into the boundary layer on smooth beds (Kline et al. 1967). The concept of a turbulent burst is that it is a sequence of ejections that occur due to the passage of a packet of hairpin vortices, the lowest hairpin producing the most vigorous ejection velocity (Adrian et al. 2000).

Turbulence was found to be a considerable contributor to the exchange of momentum and mass between the water column and subsurface flow when turbulence structures were investigated in the subsurface under different permeability Reynolds numbers Re_k (Voermans et al. 2016). The behaviour of flow above a permeable bed with low permeability Reynolds number is likely to be similar to an impermeable bed due to lesser exchange between the water column and interstitial flow. This is observed when suspended particles do not penetrate the subsurface layer and instead recirculate between individual roughness particles, moving continually back and forth, likely due to the turbulent pressure fluctuations above the roughness particles (Voermans et al. 2016). Otherwise, suspended particles penetrate the subsurface layer at high Re_k (Voermans et al. 2016).

In this study, Reynolds permeability was calculated in a similar fashion to Breugem et al. (2006), where $Re_k = \frac{\sqrt{k}u_*}{v}$, k is the permeability of the bed defined as $k = \frac{d_{50}^2 n_p^3}{180(1-n_p)^2}$. If Re_k is greater than one the bed can be considered permeable, where viscous impacts are insignificant on the bed surface, and if less than one the bed can be considered impermeable (Breugem et al. 2006).

An understanding of both near-wall and interstitial turbulent flows is required to further explore the exchange of flows between the water column and a porous gravel-bed river. Recently, many researchers have conducted experimental studies focusing on the flow in the outer, or logarithmic region, using measuring techniques such as Laser Doppler Velocimeter (LDV) (Balachandar and Bhuiyan 2007) or Particle Image Velocimetry (PIV) (Spiller et al. 2015). Additionally, Ultra-sound Velocity Profiler (UVP) and an Acoustic Doppler Velocimeter (ADV) have also been used to study the flow in the logarithmic region (Zeng et al. 2015). In contrast, relatively few experimental investigations have concentrated on turbulent flow within the near-bed area. This is probably due to the complexities of measuring such flow fields (Adrian and Marusic 2012). Consequently, available experimental data for flow in the near-bed area above a rough-bed river is relatively limited (Knopp et al. 2009).

Turbulent flow and turbulent characteristics will be studied, as part of the research presented here, through statistical analysis of the flow above rough-beds to find the effect of bed roughness particles on the flow inside and near voids within a gravel-bed river. To understand turbulence flow behaviour above rough-beds, this study will focus on the analysis of second-order statistics of turbulent flow near the bed and its interface with the water column. A review of the literature focused on turbulent stresses will be presented in the following sections as turbulence intensity (see Section 2.3.1), Reynolds shear stress (see Section 2.3.2), Reynolds normal stress (see Section 2.3.3), turbulent kinetic energy (see Section 2.3.4) and quadrant analysis (see Section 2.3.5).

2.3.1 Turbulence Intensity

This section outlines the behaviour of turbulence intensity above rough-beds. The horizontal turbulence intensity distribution is larger than the vertical turbulence intensity distribution, while cross-streamwise turbulence intensity is somewhere in-between, as defined by the following exponential decay equations (Nezu and Nakagawa 1993):

$$\frac{\sqrt{u'^2}}{u_*} = D_1 e^{-\lambda_1 (Z/H)} \tag{2.3}$$

$$\frac{\sqrt{v'^2}}{u_*} = D_2 e^{-\lambda_2 (Z/H)} \tag{2.4}$$

$$\frac{\sqrt{w'^2}}{u_*} = D_3 e^{-\lambda_3 (Z/H)} \tag{2.5}$$

where, u′, v′ and w′ are the velocity fluctuations in streamwise, cross-streamwise and vertical directions, respectively, H is water depth, and λ_1, λ_2, λ_3, D_1, D_2 and D_3 are experimental constants. All λ are equal to 1 and D_1, D_2 and D_3 are 2.3, 1.63 and 1.27, respectively. These equations will be used to compare with measurements of the Root Mean Square (RMS), of the velocity fluctuations above natural gravel-beds and artificial bed in this study.

Determining the standard deviation, or (RMS), of the velocity fluctuations, gives the turbulent strength as:

$$U_{RMS} = \sqrt{\frac{\sum_{i=1}^{i=N} u'^2}{N}} \tag{2.6}$$

where, U_{RMS} is the RMS of velocity fluctuation, and N is the total record length in time steps.

Progress in understanding the distribution of turbulent intensity inflows with hydraulically rough-beds was made by Kironoto and Graf (1994), who studied the turbulent characteristics above a gravel-bed with large relative roughness, where the Nikuradse equivalent sand roughness to flow depth ratio was approximately 0.1, subject to uniform flow. The turbulence intensity distribution was compared with previous studies and two data sets from their own experiments; no distinct difference between flow over smooth and rough-beds was found (Kironoto and Graf 1994). The experimental constants were found to be D_1 = 2.04, D_2 =1.14 for and λ_1 = 0.97 and λ_2 =0.76 by Kironoto and Graf

(1994). Their study was focused on two-dimensional flow above a gravel-bed that was glued to a plate (an impermeable bed) as well as a bed covered in loosely arranged gravel (a permeable bed).

The parameters of the turbulence intensity exponential equation, ie: D_1, D_2, D_3, λ_1, λ_2 and λ_3, were found to be 2.50, 1.60, 1.50, 1.50, 1.30 and 1.10, respectively for uniform flow conditions above a smooth bed (Pu et al. 2018). Such values are higher compared to Kironoto and Graf's (1994) results due to the difference in shear velocity between the experiments arising from the differing bed roughness applied.

On the other hand, only a small difference was found in both D_1 and λ_1 in the streamwise direction between flow above a rough and a smooth bed, equal to 2.14 and 0.8, respectively for a rough-bed (Wang et al. 1993) and 2.26 and 0.88, respectively for a smooth bed (Nezu and Rodi 1986). The empirical constants of the exponential decay equation such as D_1 and λ_1 appear to vary with H/k_s (Wang et al. 1993).

More recently, in the logarithmic layer, turbulent intensity and turbulent statistics have been shown to be dependent on roughness and decrease linearly from the bed above highly porous beds. This means that such stress is a function of frictional stress and the distance from the bed, as well as the velocity in the subsurface layer when non-zero (Pan et al. 2018). Thus, highlighting that the effects of subsurface flow on overlying flow must be considered and remain unclear.

Turbulent intensities in both the cross-streamwise and vertical component directions are weakly affected by roughness particles, whilst the turbulent intensity in the streamwise component direction is strongly affected by roughness particles (Nakagawa et al. 1975), ie: $U_{RMS}>V_{RMS}>W_{RMS}$. The effects of bed permeability and topography on turbulent intensities remain somewhat questionable, requiring additional research to be fully understood and quantified (Nakagawa et al. 1975; Hosseini and Hajibabaei 2020; Cao et al. 2020).

Recently, Cooper et al. (2018) found that there is a considerable difference in turbulence intensities above permeable beds compared with that above impermeable beds. This is due to the effectiveness of the momentum transfer since vortices are more coherent (Cooper et al. 2018). Similarly, Stoesser et al. (2007), who carried out Large-Eddy Simulations (LES) of turbulent flows above and within three layers of spheres in an open channel, showed that due to the high permeability of the wall significant momentum is transferred between the water column and subsurface which creates extra shear stresses (Stoesser et al. 2007; Albayrak and Lemmin 2011). Such shear stresses result in velocity and turbulence intensity profiles differing significantly from those above impermeable beds (Stoesser et al. 2007).

Turbulent energy re-distribution has been found to tend towards being isotropic as macro-scale eddies decay due to the porosity (Nezu 1977). Consequently, some universality in turbulent features may occur, and the turbulent intensity may be independent of Reynolds and Froude numbers (Nezu 1977). The anisotropy of turbulence intensity also becomes stronger close to the free surface (Albayrak and Lemmin 2011) and flow velocities, pressure variations, and turbulent intensities are dampened exponentially below the roughness interface.

Streamwise turbulence intensity shifts down from the exponential decay equation in the near-bed region under supercritical flow conditions above rough (sandpaper) and smooth beds. This decrease in turbulent intensity occurs near the bed due to the increase in shear velocity and reduction in energy generation within the buffer layer (Tominaga and Nezu 1992). The reason for measurements of turbulence intensity to be shifted down from equations (2.3), (2.4) and (2.5) remains unclear for supercritical flows.

Thus far, this section has shown that the effect a highly porous gravel-bed has on the overlying flow, specifically the distribution of turbulence intensity, remains unclear and requires further investigation. Therefore, this study will present turbulence intensity profiles as the double average of the root mean square of the velocity fluctuations in the three component directions above highly permeable beds and will compare this with the exponential decay equations reported by Nezu and Nakagawa (1993).

2.3.2 Reynolds Shear Stress

The governing continuity and Navier-Stokes equations assume that flow is incompressible with constant viscosity. These equations can be utilised to explain the influence turbulent fluctuations have on the average flow of the channel. The result of derivatives and integrals leads to the derivation of terms such as the Reynolds shear stresses, which are related by the correlation between the different velocity components $-\rho\overline{u'v'}$, $-\rho\overline{u'w'}$ and $-\rho\overline{v'w'}$, further details in Versteeg and Malalasekra (1995). If, for example, u' and v' were statistically independent, fluctuations in time would result in the average of their product $\overline{u'v'}$ being zero. However, turbulent shear stresses are non-zero and very large, compared to the viscous stresses in turbulent flow (Versteeg and Malalasekra, 1995).

One approach to the evaluation of the mean shear stress distribution arising from velocity fluctuations is to use the spatially averaged open channel flow method as suggested by Nikora et al. (2001) and Nikora et al. (2004). The double average method was derived from the double averaged Navier-Stokes equations by Nikora et al. (2001) and Nikora et al. (2007). The double averaged stresses $-\rho\ \langle\overline{u'v'}\rangle$ and $-\ \rho\langle\overline{v'w'}\rangle$ should be equivalent to zero if the double averaged flow is uniform and 2D, though the local shear stresses $-\ \overline{\rho u'v'}$ and $-\ \rho\overline{v'w'}$ might deviate from zero considerably because of local flow heterogeneity close to the bed area (Nikora et al. 2001). This thesis aims to report the results of an experimental study for turbulent flow above a rough-bed and bases its approach on the double average method whereby the root mean squared velocity fluctuation in both the streamwise and vertical component directions can be used to calculate the double averaged Reynolds shear stress $\langle\overline{RSS}\rangle$ as $\rho\langle\overline{U_{RMS}W_{RMS}}\rangle$ scaled with shear velocity.

The turbulent flow properties above gravel-beds have been examined experimentally using PIV to find the effects of turbulent flow on sediment transport (Mohajeri et al. 2016). The profiles of spatially averaged Reynolds shear stress were shown to be scaled with shear velocity and increase linearly toward the bed and reach a peak value at approximately the gravel crest (i.e: above the zero-displacement distance) (McLean et al. 2008; Mignot et al. 2009b; Bomminayuni and Stoesser 2011; Mohajeri et al. 2016; Cameron et al. 2017). It should be pointed out that the Reynolds shear stress is approximately zero at the water surface and maximum near the bed surface. The shear stress is generally assumed constant in the logarithmic layer, which causes a linearly increasing eddy viscosity in this regain. Therefore, the trend for eddy viscosity is similar to the Reynolds shear stress, where both of them vary linearly above bed particles resulting in the linear velocity profile (McLean et al. 2008). However, below the gravel particle (i.e.: below the zero-displacement distance), Reynolds shear stress decreases rapidly within the bed (Mohajeri et al. 2016). This was also found in an experimental study above a gravel-bed (Mignot et al. 2009b), however, there was some uncertainty in measurements gathered in the near-bed region. Although various experiments have been performed, the effect of relative submergence on Reynolds shear stress remains unclear in open channel flow and further experimentation is required to expand our understanding (Cameron et al. 2017).

In general, turbulent stresses scaled with shear velocity have been shown to not be affected by the roughening of the bed surface outside the roughness sublayer (Raupach et al. 1991; Jimenez 2004). In contrast, the contribution to the RSS depends significantly on the wall roughness in the near-bed zone (Keirsbulck et al. 2002).

Recently, the dynamics of large-scale coherent structures were examined above permeable, immobile gravel-beds in an open channel (Bagherimiyab and Lemmin 2018). A peak value in the Reynolds stress profile was detected near the bed. The profile of Reynolds shear stress was found to obey, as close as possible, a linear fit. It was confirmed that flow is two-dimensional when the shear boundary layers are fully developed. Reynolds shear stress is related to the roughness of the bed and coherent structures above a permeable bed (Bagherimiyab and Lemmin 2018), however, further experiments are required to fully understand the effects of permeability.

This section has attempted to provide a summary of the literature relating to Reynolds shear stress behaviour above gravel-beds. Furthering our understanding of the Reynolds shear stress characteristics above highly porous beds is an aim of this study.

2.3.3 Reynolds Normal Stresses

Moving on now to consider Reynolds normal stresses in the streamwise, cross-streamwise, and vertical component directions that occur in turbulent flows in an open channel. To explain the effect of turbulent fluctuations on the mean velocity, the governing Navier-Stokes and continuity equations were considered. From the derivation and integration of these equations, the additional stress terms can be obtained and are called the Reynolds stresses. For turbulent flows, the normal stresses $-\rho\overline{u'^2}$, $-\rho\overline{v'^2}$, $-\rho\overline{w'^2}$ are always non-zero since these stresses include squared velocity fluctuations (Versteeg and Malalasekra 1995). In this study, the streamwise, cross-streamwise and vertical Reynolds normal stresses $\langle\overline{RNS}\rangle$, scaled with shear stress, are expressed as $\rho\langle\overline{U_{RMS}}\rangle^2/u_*^2$, $\rho\langle\overline{V_{RMS}}\rangle^2/u_*^2$and $\rho\langle\overline{W_{RMS}}\rangle^2/u_*^2$.

Researchers have found that the double averaged Reynolds normal stresses in each of the three component directions increase quickly within the interfacial sublayer as Z/H increases, reaching a maximum at the crest of the bed particles. However, beyond the crests of the bed particles, the profiles of Reynolds normal stress decrease with increasing Z/H with an order of magnitude of $\rho\langle\overline{U_{RMS}}\rangle^2/u_*^2 > \rho\langle\overline{V_{RMS}}\rangle^2/u_*^2 > \rho\langle\overline{W_{RMS}}\rangle^2/u_*^2$. This appears to confirm that when particles protrude to flow, both Reynolds normal stresses and magnitude in turbulence increase as the result of increased mixing of flows in proximity to bed particles (Dey and Das 2012). However, it should be noted that there are some unexplained dissimilarities in the double average of Reynolds normal stresses between the results of the experiments performed by Dey and Das (2012) and Nikora et al. (2001) and Mignot et al. (2009a). For example, $\rho\langle\overline{U_{RMS}}\rangle^2/u_*^2$is less than $\rho\langle\overline{U_{RMS}}\rangle^2/u_*^2$found in Nikora et al. (2001) and Mignot et al. (2009a) near the bed, and then it tends to be higher than in both studies. However, $\rho\langle\overline{V_{RMS}}\rangle^2/u_*^2$is higher than $\rho\langle\overline{V_{RMS}}\rangle^2/u_*^2$found in both studies. In addition, $\rho\langle\overline{W_{RMS}}\rangle^2/u_*^2$is higher than $\rho\langle\overline{W_{RMS}}\rangle^2/u_*^2$found in Nikora et al. (2001), but it is less than Mignot et al. (2009a) in interfacial sublayer and then it tends to be approximately similar to Mignot et al. (2009a) results and it remains less than Nikora et al. (2001) results until the water surface. It was explained that it is due to the difference in characteristics of roughness particles such as shape, size and space in each study.

Nevertheless, there is a substantial decline in the double average of Reynolds normal stresses within the interfacial sublayer toward the bed (Nezu and Nakagawa 1993; Dey and Das 2012). The anisotropic nature of turbulence is likely the reason for the order of magnitude of $\rho\langle\overline{U_{RMS}}\rangle^2/u_*^2 > \rho\langle\overline{V_{RMS}}\rangle^2/u_*^2 > \rho\langle\overline{W_{RMS}}\rangle^2/u_*^2$ present for flows in open channels (Nezu and Nakagawa 1993; Dey and Das 2012). It was interpreted that Reynolds normal stresses are impossible to be constant in three components because instantaneous velocity fluctuations are a directional preferred in the anisotropic turbulence. However, under idealized conditions, flow is considered isotropic and thus, the velocity fluctuations do not alter irrespective of the component direction (Sarkar et al. 2019).

At present, there is something of a gap in the literature surrounding Reynolds normal stresses above rough gravel-beds, in particular, beds with porosity, regarding quantification in all three component directions. Therefore, this study will focus on the quantification of the Reynolds normal stresses in all three component directions above highly porous gravel-beds which at present, remain ambiguous at best.

2.3.4 Turbulent Kinetic Energy

This section presents a review of the characteristics of Turbulence Kinetic Energy (TKE). TKE is the average kinetic energy per unit mass of fluid related to the vortices in a turbulent flow and can be calculated using Eq. (2.7) as reported by Versteeg and Malalasekra (1995):

$$\mathrm{TKE} = \frac{1}{2}\left(u'^2 + v'^2 + w'^2\right) \qquad (2.7)$$

The Root Mean Square (RMS) of the three velocity components can easily be measured with existing velocity instruments and is of particular importance in determining turbulent fluctuations (Versteeg and Malalasekra 1995). Here, to calculate the normalised $\langle\overline{\mathrm{TKE}}\rangle$ or the scaled double averaged TKE, Eq. (2.7) was modified similar fashion to (Buffin-Bélanger et al. 2006) to be:

$$\langle\overline{\mathrm{TKE}}\rangle = \frac{1}{2u_*^2}\left(\langle\overline{\mathrm{U_{RMS}}}\rangle^2 + \langle\overline{\mathrm{V_{RMS}}}\rangle^2 + \langle\overline{\mathrm{W_{RMS}}}\rangle^2\right) \tag{2.8}$$

Many studies that consider the TKE of flows above rough-beds have been conducted. For example, the double averaged turbulent flow properties above a permeable gravel-bed with obstacles on top of the top bed were explored by Sarkar et al. (2016). Analysis of the experimental results showed that the double averaged TKE profiles increase from the bed towards the bed particle crests and then decrease linearly towards the water surface (Sarkar et al. 2016). The bedforms applied by Sarkar et al. (2016) were made-up of large, regularly spaced spheres placed on top of a gravel-bed. Such bedforms led to a decrease in the roughness geometry function in the upper part of the interfacial sublayer and an increase below (Dey and Das 2012; Sarkar et al. 2016). Protruding roughness particles generate considerable TKE (Campbell et al. 2005). The TKE profiles reported by Sarkar et al. (2016) are therefore quite different to that reported more widely in the literature.

Experiments were also conducted to study the influence of roughness elements and relative submergence on TKE in near-bed flows (Monsalve et al. 2017). It was found that reach-averaged TKE reduced with increasing relative submergence and was dominated by the plunging flow degree. The hydrodynamics of near-bed flows above immobile gravel-beds requires further investigation with different beds under different relative submergence conditions (Monsalve et al. 2017). Experimental studies have shown that turbulent flow above permeable beds is less intense and that less energy is extracted from the average turbulent flow due to increased coherency of vortices above such beds. These processes result in less turbulent kinetic energy in the water column overall, lower bulk flow resistance and higher velocity (Cooper et al. 2018).

The effect of subsurface flow on overlaying flow needs more investigation to create a fuller picture of river hydrodynamics (Buffin-Bélanger et al. 2006; Cooper et al. 2018).

Recent experiments for flows above water-worked gravel-beds and a unworked gravel-bed using PIV systems to study the impact of K^+ on the double averaged TKE (Padhi et al. 2018b). The double averaged TKE in the water-worked gravel-beds is greater than that in the unworked gravel-bed due to near-bed mixing flow occurs resulting from higher roughness of the water-worked gravel-bed, and leads to higher instantaneous velocity fluctuations near the bed (Nezu and Nakagawa 1993; Dey and Das 2012; Ferraro et al. 2016; Sarkar et al. 2016; Padhi et al. 2018a; Padhi et al. 2018b). Thus, the value of double averaged TKE near the bed is greater than the water surface (Padhi et al. 2018b). The double averaged TKE is also related to the roughness Reynolds number (Padhi et al. 2018b). However, increased TKE is related to large-scale eddies produced in the wake area downstream of a boulder (Buffin-Bélanger et al. 2006; Xu et al. 2020). This is because the boulder results in flow separation and increases recirculated flow, resulting in increased TKE when the flow re-attaches downstream of the boulder (Tan and Curran 2012).

In summary, the effects of rough gravel-beds on TKE that are presented in the literature are, at present, somewhat limited by the contradiction between different studies as well as a lack of directly comparable studies.

2.3.5 Quadrant Analysis

The concept of quadrant analysis and its use goes back approximately 50 years ago when it was applied in investigations for the visualisation of turbulent flows (Wallace 2016). This field has been started by introducing two types of investigations for turbulent flow visualisation. These investigations are interesting to look at the turbulence topic by supplying insight into this physics (Wallace 2016). Quadrant analysis is important to distinguish bursting events, which are the low-momentum streaks, (i.e. the bubbles coalesce and intermittently blow up away from the bed in a chaotic process (Wallace 2016). These events can be seen in the quadrant analysis as ejection and sweep events, so it should be highlighted to understand the hydrodynamic mechanisms that take place near the riverbed.

Quadrant analysis has been used as the standard method for the analysis of turbulence and the study of bursting phenomena in the near-bed area (Wallace 2016). The contribution of Reynolds shear stress ($u'w'$) is classified into four eddies events by quadrants. Quadrant 1 (Q1) represents outward interactions (u' and $w' > 0$), Quadrant 2 (Q2) represents ejections ($u' < 0$ and $w' > 0$), Quadrant 3 (Q3) represents inward interactions ((u′ and w′<0) and Quadrant 4 (Q4) represents sweep events (u′> 0 and w′<0) (Sulaiman et al. 2013; Wallace 2016; Padhi et al. 2020).

Sweep events carry high-momentum fluid with relatively fast fluid motions downward towards the bed often causing the dislodging of fine sediments from the bed. However, ejection events carry low-momentum fluid with relatively slow fluid motions upward away from the bed leading to traction and re-suspension of fine bed sediment (Sutherland 1967; Drake et al. 1988; Thorne et al. 1989; Robinson 1991; Lapointe 1992; Cellino and Lemmin 2004; Mohajeri et al. 2016; Fang et al. 2018). Consequently, these events also contribute to the generation of TKE in the boundary layer (Kline et al. 1967; Wallace 2016).

Sweep events contribute positively to the average bed shear stress events and interact with sediment motions. Outward interactions contribute negatively to bed shear stress. When the magnitude of the outward interactions grows relative to other events, the sediment flux rises, and the bed shear stress reduces (Nelson et al. 1995). Quadrant analysis is a method for quantifying the part of a structure that primarily causes the entrainment and deposition of sediments, which are associated with coherent structures in the boundary layer as a bursting cycle (Grass 1971; Cecchetto et al. 2017). Quadrant analysis can therefore be used in the present study as an indicator for furthering our understanding of the interaction between the water column and pore water, as well as the hydrodynamic drivers behind them.

Quadrant analysis may be applied to the mean stress values above a specified threshold or the whole Reynolds shear stress signal. Such a threshold gives an indication of the hyperbolic hole size (H) and can be found by comparing the product of the horizontal and vertical velocity fluctuations $|u'w'|$ against the time-averaged shear stress $|\overline{u'w'}|$ (Yue et al. 2007) as such:

$$H = {|u'w'|}\big/{|\overline{u'w'}|} \tag{2.9}$$

Reynolds shear stress ($S_{i,H}$) can also be expressed as a function of H giving (Yue et al. 2007):

$$S_{i,H} = \frac{1}{T}\int_0^T u'(x,z,t)\, w'(x,z,t) I_{i,H,t}(u'w')dt \tag{2.10}$$

where, i is the ith quadrant, t is time, T is the sampling time, x and z are the streamwise and vertical coordinate directions, respectively, and $I_{i,H,t}$ is a conditional sampling function for which (Yue et al. 2007):

$$I_{i,H,t} = \begin{cases} 1 \text{ if } (u', w') \text{ is in quadrant i and } |u'w'| \geq \left|\overline{u'w'}\right| \\ 0, \text{otherwise} \end{cases} \tag{2.11}$$

Reynolds shear stress ($S_{i,H}$) in double averaged form is symbolised as $\left|\langle\overline{S_{i,H}}\rangle\right|$. As bed particles begin to move, the occurrence rate of ejection events decreases, and the resulting eddies break up into small coherent structures.

The type of rough-beds leads to a change in the role of ejection and sweep events in the near-bed region. For example, the ejection occurrence above an immobile bed decreases rapidly less than above the mobile bed. However, the sweep occurrence above immobile increases slower than above the mobile bed. It was explained that the sweep bursts initiate from the outer flow zone, and as a result, the bed load plays a less significant role in adjusting their occurrence. In contrast, the ejection bursts originate from the bed, and therefore, the bed load has a considerably larger effect on their occurrence (Liu et al. 2016). The effects of rough-beds and such events warrant further investigation to better understand turbulent interactions between sediment and flow (Jay Lacey and Roy 2008; Liu et al. 2016; Cooper et al. 2018).

This section has shown that quadrant analysis is a key analysis tool that aids our understanding of the role coherent turbulent structures play in open-channel flows.

2.4 Interstitial Flows Through a Gravel-Bed

This section considers the interstitial flow characteristics within the gravel-beds themselves. Many researchers have focused on interstitial flows experimentally and numerically (Breugem et al. 2006; Pokrajac et al. 2007; Blois et al. 2012; Kim et al. 2018; Leonardi et al. 2018). Interstitial flows are related to pressure fluctuations arising from coherent turbulent movements (Vollmer et al. 2002; Detert et al. 2010; Higashino and Stefan 2011). One way to measure the flow field in complex porous beds experimentally is to use Refractive Index Matching (RIM) techniques. RIM provides optical access to the interstices of porous beds by matching, as closely as possible, the refractive index of bed particles to the surrounding fluid (Huang et al. 2008; Blois et al. 2012; Dijksman et al. 2012). However, there are some disadvantages in terms of measurement accuracy as maintaining a perfect matching between solid and fluid is very difficult, and many velocity measurement techniques rely on the interaction between light and a seeding material to obtain readings. Naturally, if the degree of refraction changes at the fluid-bed particle interface, any such velocity measurements could be somewhat misleading. In addition, the cost of using RIM techniques is often high due to the volume of specialist bed materials and viscosity-changing chemicals that are required to fill a flume of appropriate size to perform any experiments. Moreover, the best work of the RIM technique occurs when fluids have high viscosity. In this case work of (RIM) techniques to measure velocity with high Reynolds number flows is very challenging (Blois et al. 2012). Some issues remain unfixed such as bounded experiment duration and flow seeding density with RIM techniques (Huang et al. 2008).

Interstitial velocity can be calculated based on the methods applied by Stephenson (1979) and Pagliara et al. (2008):

$$\mathrm{U_{sub}} = \mathrm{n_p}\left(\frac{\mathrm{igd_{50}}}{\mathrm{K'}}\right)^{0.5} \tag{2.12}$$

where, U_{sub} is the average velocity within the gravel-bed, i is the hydraulic gradient equal to the bed slope under uniform flow conditions, d_{50} is median particle diameter, K′ is the friction parameter which may vary from 1 for a smooth spherical particle, to 2 for gravel particles, and 4 for sharp-crested particles, and g is the gravitational acceleration.

The flow in an open-channel above a permeable rough-bed is considered turbulent whilst flow within the bed itself is considered laminar (Kim et al. 2018). Flow in the subsurface region is governed by Darcy's law and the balance of viscous and pressure forces. It was also observed that flow within three dimensions of the pore bed that turbulent flow in porous bed is microscopic turbulence. The ‘microscopic’ indicates the dimension of the single pore space. In another word, non-Darcian macro-scale events, such as provided by the pressure decline law. It cannot recognise the move from one regime to another (Hlushkou and Tallarek 2006).

Kim et al. (2018) carried out experiments in a 2.5 m long flume filled with an aqueous solution of sodium iodide (as opposed to water) measurement interstitial velocity collected in either two or five layers of acrylic spheres bed. Velocity measurements were obtained using PIV techniques. The results showed that increasing the bed thickness led to increasing momentum losses in the bed pore spaces compared to the shallow thickness and is associated with low momentum for overlying flow due to the thin boundary sublayer (Kim et al. 2018). The shallow thickness bed restricts the interaction of overlying and pore flow near the bed due to the thick boundary sublayer. However, these types of experiments do not represent natural gravel-bed rivers because the viscosity of the fluid, the shape and the roughness of the bed particles differ from natural riverbeds. The length of the flume is also inadequate for open-channel flow investigations, which could affect achieving uniform and fully developed flow in the overlying flow.

The upwelling and downwelling of interstitial flows were measured indirectly by measuring solute concentrations by using recirculating flume, which was covered with either sand, sand with a top layer of gravel, or sand/gravel with a top layer of cobbles (Reidenbach et al. 2010). Increasing the roughness height resulted in an increase in solute concentrations found in the subsurface flow. This is the result of increased mass flux within the pore bed due to increased turbulent mixing (Reidenbach et al. 2010). Increasing the overlying flow velocity led to a decrease in the solute concentrations found in the interstitial flow. This is because more downstream transport of the solute above the bed occurs, as well as increased dispersion of the solute within the bed pores themselves (Reidenbach et al. 2010). Contrarily to Reidenbach et al. (2010), Packman et al. (2004) found that the overlying flow velocity and bed particle diameter influenced the exchange between the water column and subsurface flow irrespective of the roughness height (Packman et al. 2004).

Interstitial velocity measurements were obtained by Pokrajac et al. (2007) within the pores of a bed made of glass spheres using UVP in combination with PIV techniques. They found that momentum exchange occurs due to the balance between drag forces and gravity, and not due to the transport of momentum from the overlying flow. Thus, resulting in the lowest velocity near the overlying flow and high velocity toward the bed (Pokrajac et al. 2007).

A numerical study by Breugem et al. (2006) showed that for a highly permeable bed, flow velocity reduces exponentially within a gravel-bed with the decay controlled by the balance between turbulent diffusion of momentum into the bed and the removal of momentum due to Forchheimer drag. Turbulent motion into the bed is inactive, or in another word, they result from pressure fluctuation. The non-zero velocity (inside pore) effect on the overlying velocity profile and turbulent characteristics was not clarified that these types of beds need more researches to highlight the interaction between subsurface flow and surface flow (Breugem et al. 2006).

As discussed in this literature review, the interstitial flow features within gravel-beds themselves are difficult to measure with high accuracy due to the limitations of the measurement techniques. However, as this region is essential to aquatic ecosystems and dissolved oxygen levels, it is of the utmost importance that further research is conducted on this topic to expand our understanding and quantify turbulence in this region.

2.5 Velocity Measurement Instrumentation

Over the past 4 or 5 decades, many experiments have been conducted to study the mean velocity and turbulence characteristics of open-channel flow above rough-beds with different instruments and with varying degrees of accuracy and success.

Hot-wire anemometry is a technique that can be used to capture flow velocity. The hot wire sensor is a thin metallic wire which is electrically heated and event flow cooled, which works by effects of its temperature as well its mass flux during different influences, while forced convection is commonly dominant (Comte-Bellot 1976). Hot-film anemometry is a modification of hot-wire anemometry where convective cooling of a passing fluid alters the temperature of a heating film and, thus, its electrical resistance. The changing of this resistance can be exploited to acquire information about the flow velocity (Kuo et al. 2012; Saremi et al. 2014). The main advantages of hot-wire anemometry are that it is very cheap and has a small measurement volume, low signal-noise ratio, and good temporal and spatial resolution. However, the main disadvantages are that it is an intrusive method that can alter the regional flow field and pollution from the deposition of impurities on the sensor can significantly alter the reading. Equally, the probe can easily break and requires near-constant re-calibration (Osaro 2018). For many situations, hot-film anemometry is not appropriate, especially in the field or where sediments are suspended in the flow (Planchon et al. 2005).

Nowadays, many researchers use Large-Scale Particle Image Velocimetry (LSPIV) or PIV to measure 2D or 3D instantaneous velocity. For instance, PIV was applied to measure the 2D flow velocity of shear-driven flow bounded by a porous medium (Tachie et al. 2003). Similarly, researchers have also applied PIV to investigate 3D flow velocity above and through different arrangements of porous media to determine the slip velocity (Agelinchaab et al. 2006). Equally, PIV has been used to measure 2D velocity profiles in a pressure-driven flow over and through models of a porous medium where the main objective of the study was the investigation of the influence of three boundary conditions on a flow through a porous medium (Arthur et al. 2009).

Both LSPIV and PIV have the same measurement principle whereby 2D or 3D instantaneous velocity is extracted from images that capture the movement of some particle through a measurement domain acquired in a fast sequence using high-speed cameras (Jin and Liao 2019).

In the laboratory, PIV uses lasers to illuminate seed particles suspended within the flow to provide velocity data. However, in the field, LSPIV uses natural lighting conditions and tracks water surface shapes such as foams, floating debris, and surface deformation-produced glares to provide velocity measurements (Jin and Liao 2019). If LSPIV is used in the field, it cannot obtain water surface images from an orthogonal direction all the time. Consequently, images are taken from an oblique angle necessary to be orthorectified to a global coordinate before subsequent PIV interrogation (Jin and Liao 2019). The main advantages of PIV are that it is non-intrusive and can take velocity measurements at multiple points in the flow at high spatial resolution. However, the equipment is very high cost, and the size of the region under investigation, or the measurement domain, needs to be small for greater accuracy (Osaro 2018). LSPIV is also a non-intrusive technique. It can be used under extreme flow conditions or in places where traditional methods may not be appropriate because of safety and cost concerns (Ran et al. 2016). However, LSPIV also has several disadvantages; in particular, there are significant pitfalls in the system where ground reference positions and floating tracers are required, both of which are highly costly and hinder constant measurements in the field (Tauro et al. 2014).

From the perspective of this study, PIV techniques require a number of safety protocols due to the use of lasers and inherent radiation, and thus such instrumentation requires specialist laboratory setups obtained at great expense. Due to these reasons, the use of PIV or LSPIV techniques is beyond the scope of this study.

Endoscopic PIV (EPIV) techniques have also been used to measure flow fields, which measure the 2D of the flow field, which involves a digital video camera, a pulsed laser illumination and two borescopes that supplied optical entrance to the pore media. The laser endoscope directs laser light into the void, permitting an effective illumination of the pore media in the test section. Moreover, the camera endoscope transmitted the light dispersed through the seeding grains from the pore to the camera (Blois et al. 2012). Like LSPIV and PIV techniques, EPIV is a high-resolution technique that allows the measurement of instantaneous velocities under high Reynolds numbers. The main advantage of the EPIV technique is that it is less complex to set-up during experiments and is lower cost than other approaches such as RIM and magnetic resonance velocimetry techniques. This technique provides optical access to the normally inaccessible pore spaces within gravel-beds themselves, thus offering large advantages compared to external PIV techniques. However, the EPIV technique also has a significant drawback where disturbance of the pore-space flows is caused by the endoscopes and bubbles within the bed pores can greatly influence measurements due to the reflection of the light captured (Blois et al. 2012).

ADV has been used by many researchers to measure 3D velocity fluctuations in both the laboratory and the field, a full description of ADV techniques is provided in Chapter 3 Section 3.5.1. For instance, laboratory experiments were performed for a comparative study on the near-bed surface using ADV (Precht et al. 2006). The ADV results were compared with those obtained using Laser Doppler Anemometer (LDA) techniques, and it was found that great care and caution about the ADV settings and position had to be observed (Precht et al. 2006). The position of an ADV relative to a boundary is critical as echoes can bias velocity measurements. Such echoes can, however, be identified by sudden rises in the Signal Noise Ratio (SNR) dependant on the flow conditions and boundary material. In the main, velocity measurements should not be taken closer than 1.7-5 mm from a boundary due to the bed interference adversely affecting measurements with ADV within this region (Rusello 2012; Koca et al. 2017). This is because the reflected acoustic pulses echoing from solid boundaries suggest that velocity measurements for ADV could be high accuracy at positions approximately 0.75 cm above the bed (Voulgaris and Trowbridge 1998). Due to the presence of air bubbles, doppler noise aliasing, and higher turbulence intensities than the nominal scales to which the ADV is configured for measurement, ambiguous velocities can be created in ADV data (Voulgaris and Trowbridge 1998).

For ADV settings, users should define the sampling volume size for their specific device if they plan to take measurements near a wall. Accurate information about the ADV’s spatial resolution will also result in stronger conclusions about the nature of turbulent flows since the sample volume size also determines the scales of turbulence that can be resolved (Nikora and Goring 1998). ADV’s are easy relocated and deployed for 3D water velocity measurements in laboratories (Kraus et al. 1994). In addition, many streams, rocky shores, and estuaries have rough-beds that may pose greater challenges for positioning the sample volume compared to that above a smooth bed of a flume (Finelli et al. 1999). In addition, due to the presence probe of ADV in the flow, a small variation in local turbulence and streamlining occurs (Voulgaris and Trowbridge 1998; Hurther and Lemmin 2001; Oveici et al. 2020).

In this section, different instruments for the measurement of instantaneous velocity have been explored. The following Chapter 3 on Methods and Materials discusses ADV settings in greater detail.

2.6 Summary

This chapter has reviewed a body of literature exploring the statistical analysis of turbulent open-channel flow in the near-bed region through exploration of the logarithmic law parameters, velocity profiles, second-order statistical analysis, types of flow related to relative submergence, interstitial flow through gravel-bed, and velocity measurement instrumentation.

Several questions regarding these statistical analyses remain unclear. For example, there is uncertainty, due to inconsistent conclusions, about the physical mechanisms that drive variation in the von Karman constant from the traditional value of 0.41 and variations values of k_s in each study. Although many studies focus on the applicability of the logarithmic law for flows under intermediate and high relative submergence flow conditions above gravel-bed, it remains several gaps and shortcomings in the physical mechanisms of validation logarithmic law under these conditions. Determining the effects of the subsurface velocity of a gravel-bed on near-bed overlying turbulent flow is another substantial challenge. For example, the values of the empirical constants of the exponential decay equations vary for different studies and the reason for such variation is unclear. There is also a gap in the literature surrounding Reynolds shear stresses, Reynolds normal stresses and TKE above highly rough gravel-beds such as the influence of relative submergence and the effects of bed roughness on them. They are presented in the literature and are, at present, somewhat limited by the contradiction between different studies as well as a lack of directly comparable studies. At present, they are many studies about interstitial flow in open-channels, but quantification of this flow as natural riverbeds are lacking. The effect of pore velocity on the water column's velocity profile and turbulent properties is unexplained. Yet, this study area is crucial to our understanding of aquatic ecosystems, near-bed hydrodynamics, interstitial flows, and surface water/groundwater interactions. Consequently, quadrant analysis can be used in this thesis as a guide for expanding our understanding of the interaction between the overlying flow and subsurface flow and the hydrodynamic drivers behind them.

The study of turbulent flow near the gravel-bed and within gravel-bed itself appears the greatest challenge to experimental study alike presently because of limitations of measurement techniques. However, ADV techniques are relatively simple methods of measuring 3D velocity fluctuations in both the laboratory and the field.

Overall, this thesis will focus on these parameters and the applicability of the logarithmic law for turbulent velocities in the form of double averaged streamwise velocity profiles, turbulence intensity, Reynolds shear stress, the Reynolds normal stresses in three directions and TKE above highly porous gravel-beds under intermediate and high relative submergence flow conditions.

Chapter 3
Methods and Materials

CHAPTER 3
Methods and Materials

3.1 Introduction

In this chapter, six experimental data sets for three different bed surfaces and hydraulic conditions are introduced. For this purpose, the bed of the recirculating narrow flume in Cardiff University's Hydro-Laboratory was covered with natural gravel and an artificial bed. The particle diameters were chosen based on the grain size found in salmonid redds. To ensure the bed material remained stable and immobile, the experiments were undertaken such that the critical sediment shear stress for the applied particle size (according to Shields approach) was greater than the hydrodynamic bed shear stress arising from the applied fluid flow. Therefore, the flume bed layer represents a natural gravel-bed river with no bedload transport. The standard deviation of the bed surface elevations was defined in a similar fashion to Nikora et al. (2001); Stoesser (2010); Stubbs et al. (2018) and is outlined in this chapter. Two instruments were used to measure the velocity; an Acoustic Doppler Velocimeter (ADV) to take measurements above the bed surface and an endoscope to take measurements in the subsurface region. The velocity measurement procedure is explained in this chapter and the flow conditions for each experiment are presented (see Table 3.2).

3.2 Experimental Set up

The experiments were achieved using the 0.3 m wide, 0.3 m deep, and ten metres long, glass-walled recirculating narrow flume in Cardiff University's Hydro-Laboratory under uniform flow conditions with a bed slope of 1/1000, as shown in Figure 3.1. A tank is located at the flume outlet to direct the discharge and re-circulate the water back to the flume inlet via a pump and pipe network underneath the flume itself. The discharge is measured by a flowmeter located on the right-hand side of the flume. A weir is located at the flume end to control the longitudinal water surface.

The experiments conducted were carried out under uniform flow conditions. Uniform flow conditions were established by adjusting the tailgate weir for a given flow rate and by measuring the water surface every metre along the centreline of the flume using a point gauge to ensure it was parallel to the flume bed. Once the water surface slope was deemed the same as the flume bed, the flow was assumed uniform, as shown in Figure 3.2. The weir height relates to a measurement gauge on the wall of the flume outlet. The water depth is measured from the flume bed.

The two different natural gravel grain sizes used in these experiments have median diameters (d_{50}) of 20 mm and 35 mm within the test section. The test section for each experiment was approximately two metres in length. Natural gravel with a median diameter (d_{50}) of 28 mm was located upstream and downstream of the test section. Particle size distributions of the natural gravel were determined according to the British Standards method (British Standards Institution 1990), as shown in Figure 3.3. These grain sizes were chosen as they are representative of the bed grain sizes found in salmon redds in UK rivers. Female salmonids in southern England (Dorset), northeast England and south-west Wales prefer to spawn in median gravel of diameter between 20 mm and 30 mm (Crisp and Carling 1989). The experiments were carried out for discharge in the range 0.004to 0.009 m^3/s and Reynolds number (based on the flow depth) from 13,448 to 30,208.

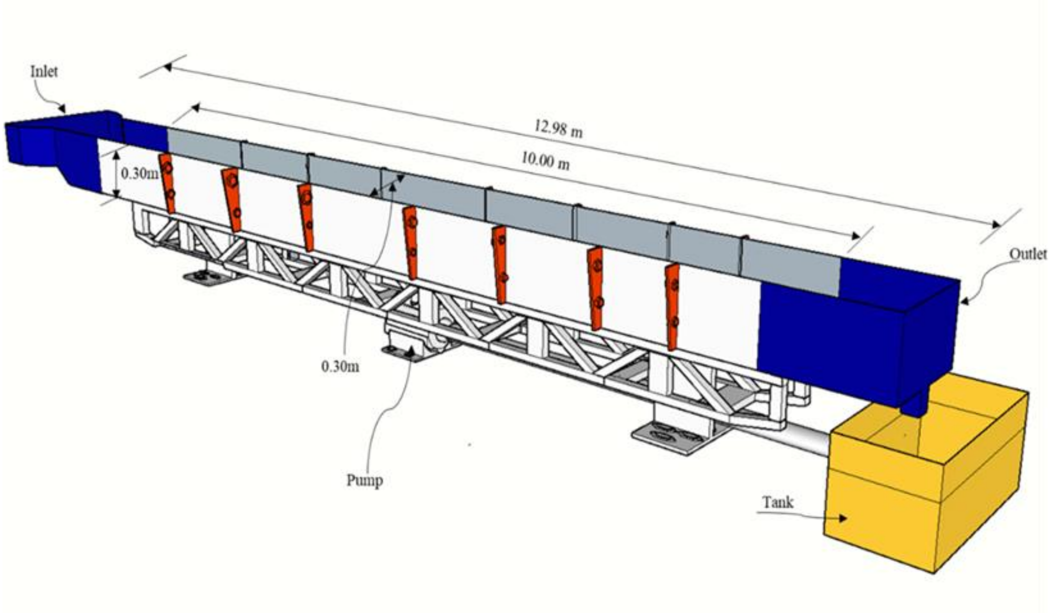

Figure 3.1. Three-dimensional view of the narrow flume, 0.30 m wide, 0.30 m deep, and 10 m long.

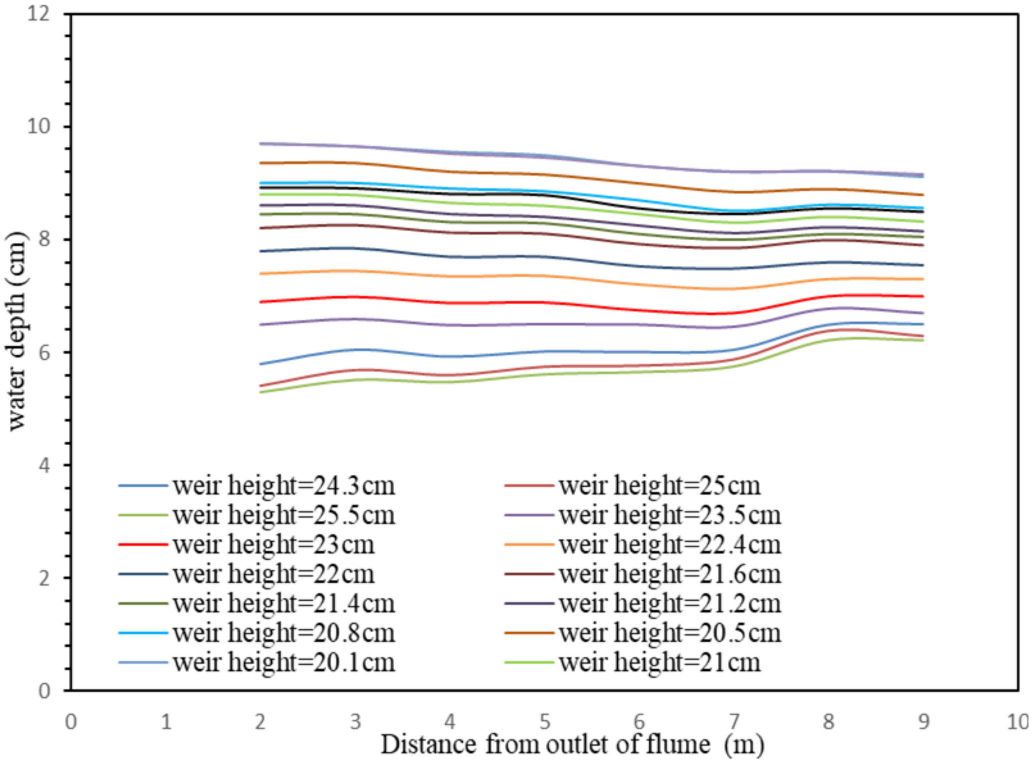

Figure 3.2. Water depth versus distance from the flume outlet was obtained for an experimental case above the artificial bed where k_s=0.2d, d_{50}=28 mm, Q=0.006 m^3/s.

The natural gravel-bed particle diameters (d_{50}= 20 mm and 35 mm) were also chosen so that the critical sediment shear stress (according to the Shields approach) was more than the hydrodynamic bed shear stress to ensure the sediment remained immobile under the experimental flow conditions.

For each experiment, the highest crest of the bed particles was found and used as a datum point where the point gauge was set to zero. The fluctuations in the bed surface elevations were then measured from this datum, which is given in (Section 3.4). This datum was used throughout each experiment to measure the water elevation and set the sampling volume elevation of the ADV. In addition, uniform depth and flow were maintained for all experiments by adjusting the outlet weir and the pump discharge.

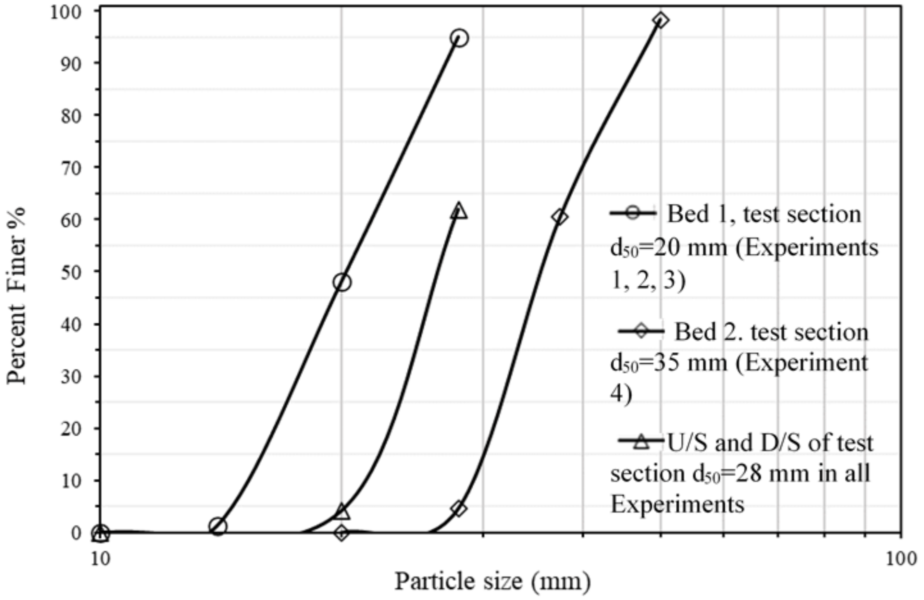

Figure 3.3. Particle size distribution curves for the natural gravel-beds used in experiments: Test bed 1 has a median particle diameter of d_{50}=20 mm; Test bed 2 has a median particle diameter of d_{50}=35 mm, and the median particle diameter of gravel placed upstream and downstream of the test bed section was d_{50}=28 mm for all experiments, including with the artificial bed.

3.3 Porosity

Porosity is a measure of the ratio between the volume of voids to the total volume Eq. (3.1) (Murthy 2002). To apply this relationship, total volume was measured using a container of known volume. The bulk Saturated Surface Dry (SSD) specific gravity of the natural gravel was measured to find solid volume using the method outlined by ASTM C127-15. (2015). The procedure starts with washing of the first gravel sample of known weight, before drying it to achieve a constant mass in an oven at 110°C. Secondly, the gravel sample was left at room temperature to achieve a comfortable handling temperature. Thirdly, the sample was immersed in water at room temperature for 15 to 19 hours. Fourthly, the sample was dried to a Saturated Surface Dry (SSD) condition by rolling the gravel on a towel. Finally, the sample was placed in a basket and weighed above water (B_1) and under water (C_1) after shaking the container to release any captured air when it was immersed. Thus, G_{SSD} could be calculated using Eq. (3.2).

$$n_p = \frac{V_v}{V_t} \tag{3.1}$$

$$G_{SSD} = \frac{B_1}{(B_1 - C_1)} \tag{3.2}$$

In addition, the solid volume was calculated using Eq. (3.3). Equation Eq. (3.4) was used to estimate the volume of voids for both gravel diameters and thus, porosity could be calculated using Equation (3.1).

$$V_s = \frac{W_s}{G_{SSD}\gamma_w} \tag{3.3}$$

$$V_v = V_t - V_s \tag{3.4}$$

where, n_p is porosity, V_v is the volume of voids, V_t is the total volume, G_{SSD} is bulk Saturated Surface Dry SSD specific gravity, B_1 is the mass of SSD sample in the air (g), C_1 is the mass of SSD sample in water (g) and the quantity (B_1-C_1) is the mass of water displaced by the SSD sample, Vs is the volume of solids, W_s is the weight of the gravel, and γ_w is the unit weight of water, which was assumed to be 1 N/m^3.

G_{SSD} of the 35 mm, 20 mm, and 28 mm diameter natural gravels was found to be 2.59, 2.62, and 2.57, respectively, as shown in Table 3.1.

The porosity of the 35 mm, 20 mm, and 28 mm diameter natural gravels was calculated as 34%, 38%, and 40%, respectively. However, Eq. (3.1) gives the porosity of an enclosed matrix with no account for a matrix with an open surface. In this study, the volume of the voids formed on the surface of the gravel-bed river is considered to be part of the channel and not the riverbed itself (Bridge and Bennett 1992; Nezu and Nakagawa 1993; Wu and Chou 2003). To account for the open surface layer, the porosity calculated using Eq. (3.1) was divided by a reduction factor. This reduction factor was found using a model of an artificial riverbed, which was generated using Computer-Aided Design (CAD) by Stubbs et al. (2018), whereby the porosity included a $0.25d_{50}$ surface volume allocation (Van Rijn 1984; Bridge and Bennett 1992; Nezu and Nakagawa 1993; Wu and Chou 2003) was divided by the porosity excluding a $0.25d_{50}$ allocation to give a reduction factor of 1.0619. It was assumed that a similar relationship existed for the porosity of the 20 mm, 28 mm, and 35 mm diameter natural gravels. Applying the reduction factor gave final porosity values of 36%, 38%, and 31% for the 20 mm, 28 mm, and 35 mm diameter natural gravels, respectively, as shown in Table 3.1.

Using Eq. (3.5), the void ratio, e of the natural gravel-beds was calculated as 0.61 for the gravel with a porosity of 38%, 0.56 for the gravel with a porosity of 36% and 0.46 for the gravel with a porosity of 31%, as shown in Table 3.1.

$$e = \frac{n_p}{1 - n_p} \tag{3.5}$$

It has been demonstrated that the void ratio decreases from 0.81 to 0.20 in gravel particles with increasing water content (Liao et al. 2013). It has also been shown that the void ratio reduces with increased depth into the bed due to compaction. The void ratios found here are generally comparable to the commonly accepted value of 0.60 (Scott 1960; Haynes et al. 2009) for a loose random packing arrangement of uniformly sized grains.

The artificial bed used in this study was designed to have similar attributes to a natural gravel-bed river. This type of bed has less surface protrusions than the natural gravel, thus, measurements above the artificial bed gathered within its vicinity are more convenient and less noisy than above the natural gravel-bed. The geometry of the pores within the artificial bed is highly idealised and somewhat dissimilar to natural gravel-beds, which leads to identifying characteristics of the interaction between the turbulent flow of the water column and the flow within pores with more convenient than in natural gravel-bed. However, the pores in a natural gravel-bed river have a variety of sizes and angles (Pokrajac and Manes 2009).

Table 3.1. Summary of the bed characteristics for natural gravel with a median diameter of 20 mm and 35 mm and artificial particles with a median diameter of 28 mm.

Bed type	n_p %	e (−)	G_{SSD}	σ_b (mm)	Sk_z (−)	Ku_z (−)
Natural gravel with a median diameter of 20 mm	36	0.56	2.62	7.83	−0.59	−0.30
Natural gravel with a median diameter of 35 mm	31	0.46	2.59	6.06	0.19	−0.72
Artificial bed with a median diameter of 28 mm by Stubbs et al. (2018)	32	0.47	-	3.81	−0.176	−1.012

Furthermore, the artificial bed was designed so that its surface bed roughness could be captured and reproduced in a computational grid for numerical simulation. The artificial bed was designed using CAD software and manufactured using Computer Numerical Control (CNC) machines (Stubbs et al 2018). The artificial bed in the test section was 2.048 m long, 0.12 m deep and 0.3 m wide, with a median particle diameter of 28 mm. The void ratio of the artificial bed was found to be 0.47 with a porosity of 32%, as shown in Table 3.1 (Stubbs et al. 2018). The porosity of the artificial bed is very similar to the porosity found for the natural gravel with a median diameter of 35 mm, also used in this study. The artificial bed was manufactured from 25 sheets of cast acrylic and divided into four sections, each with five layers, as shown in Figure 3.4.

This artificial bed was manufactured from sheets of cast acrylic and was transparent. The transparency enables video capture inside pores of the riverbed with high light levels and allows for the identification of turbulent flow features from outside of the flume (Stubbs et al. 2018). It is also low cost, has high thermal stability, and is lightweight/manoeuvrable.

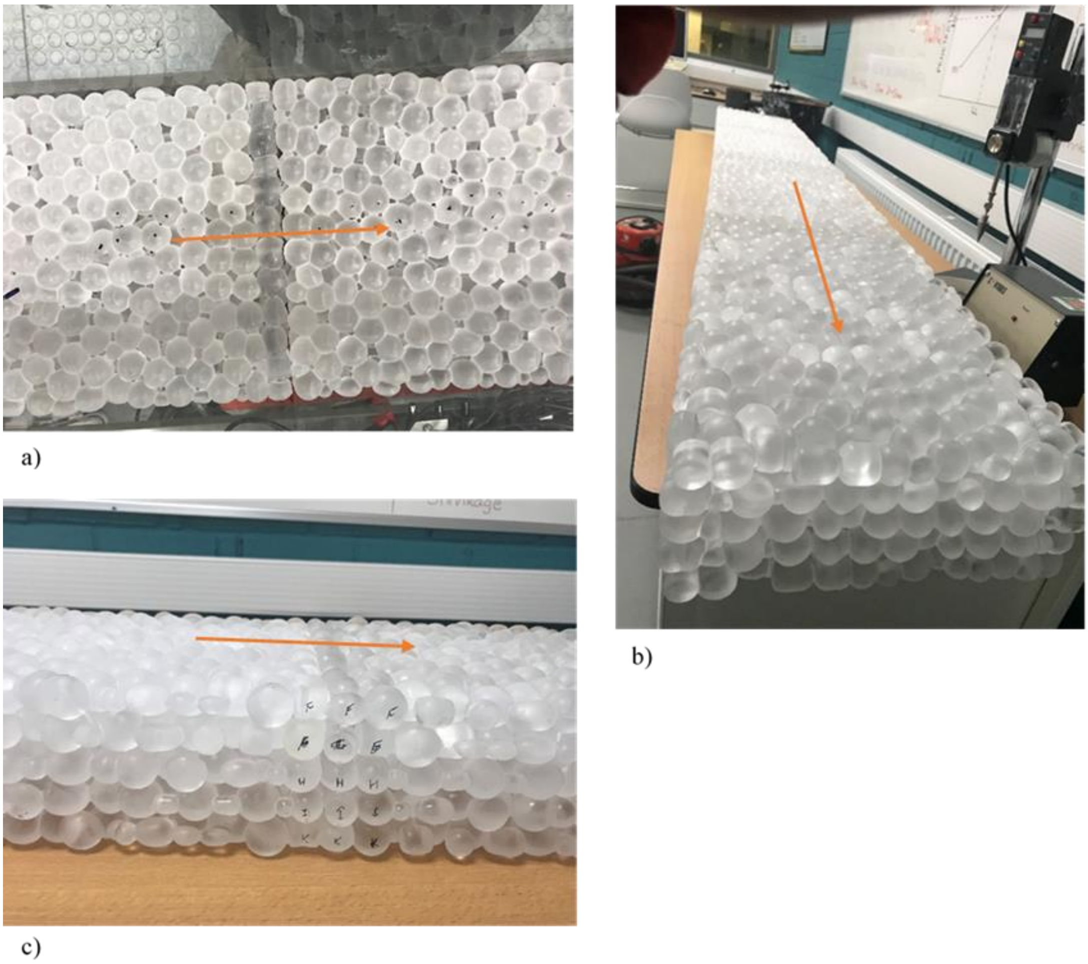

a)

b)

c)

Figure 3.4. The artificial bed a) a top-view sectional view in the x-y plane, b) a cross-sectional view in the z-y plane, and c) a streamwise sectional view in the x-z plane. The flow direction is indicated by the arrow in each figure.

3.4 Flume bed characteristics

Due to supplier constraints in purchasing the necessary amount of gravel needed to cover the entire ten-meter length of the flume, natural gravel with a median diameter of d_{50}=28 mm was used to cover the flume bed upstream and downstream of the test section in all experiments. The test section itself was then covered with natural gravel with a median diameter of 20 mm and 35 mm, as well as with the artificial bed with a median diameter of 28 mm and the depth of the bed was 12.00 cm in all experiments. This was in a similar fashion to Dancey et al. (2000), who covered the flume bed from the inlet to 2 m upstream of the test section with natural gravel with a median diameter of 25 mm.

In this study several experiments were conducted with each of the three beds types as follows:

1. Experiments 1, 2, and 3: 20 mm diameter natural gravel within the test section between 4 m and 6.8 m from the flume inlet and 28 mm diameter natural gravel between 0 m and 4 m and again from 6.8 m to 10 m from the flume inlet.
2. Experiment 4: 35 mm diameter natural gravel within the test section and again, 28 mm diameter natural gravel everywhere else within the flume.
3. Experiments 5 and 6: 28 mm diameter artificial bed within the test section and again, 28 mm diameter natural gravel everywhere else within the flume.

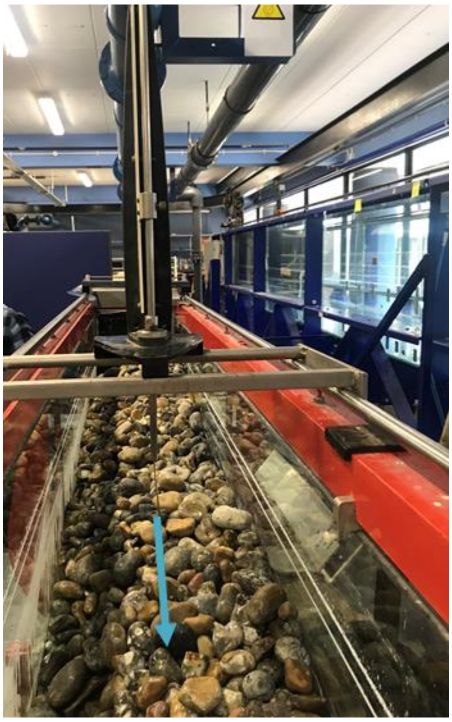

Figure 3.5. The flume bed was covered with 20 mm median diameter natural gravel within the test section of the narrow flume for experiments 1,2 and 3. The flow direction is indicated by the arrow.

The grain size distribution applied in this study is similar to that found in the surface layers upstream of the Wellington and Herrling bars in Fraser River, British

Columbia, Canada where the d_{50} of the gravel particle was found as 19.9 mm (on average 20.1 mm) and 34.7 mm (on average 32.0 mm), respectively (Rice and Church 2010). Similarly, in Oak Creek River, the median gravel size was found in the subsurface as 20 mm (Milhous 1973). In the Piave River, Eastern Alps, Italy the d_{50} was found to range from 13 mm to 83 mm on the surface but was mostly found to range from 17 mm to 47 mm on the surface (Surian 2002). Additionally, the grain sizes applied in this study were chosen as they are representative of the bed grain sizes found in salmonid redds in UK rivers such as Southern England (Dorset), Northeast England and South-West Wales, where the median gravel diameter ranges between 20 mm and 30 mm (Crisp and Carling 1989), as mentioned earlier in Section 3.2. Equally, the median gravel diameter ranges between 16 mm and 32 mm for smaller resident brown trout redds found in the River Daleelva, Norway (Barlaup et al. 2008). To be similar to the natural stable gravel river bed case, the natural bed diameter was chosen that critical sediment shear stress (according to Shields approach) is more than hydrodynamic bed shear stress to ensure sediments are immobile at the experiments' flow conditions. In the stable case, the roughness layer is unchanged in the natural gravel river bed (Carling 1988; Thorne et al. 1996; Dey and Ali 2019). With a porosity between 31% and 36%, the beds applied in this study can be classified as similar to a clean, open gravel-bed river as it exceeds the 20% requirement of such beds (Cary 1951; Carling and Reader 1982).

A point gauge was used to measure the surface topography within the measurement region with the highest particle crest of the gravel-bed chosen as the datum point where the point gauge was set to zero. For the natural gravel with a median diameter of 20 mm (experiments 1, 2 and 3), measurements were taken between 4 m and 6.8 m from the inlet, or between x=0 m and x=2.80 m in the flow direction every 0.1 m, and in the cross-streamwise direction between y=0.05 m and y=0.25 m every 0.025 m. Figure 3.7 demonstrates the bed surface topography for the 20 mm diameter natural gravel.

For the natural gravel with a median diameter of 35 mm (experiment 4), measurements were similarly taken between 4.25 m and 6.37 m from the inlet, or between x=0 m and x=2.12 m in flow direction every 0.1 m, and in the cross-streamwise direction between y=0.05 m and y=0.25 m every 0.025 m. Figure 3.8 demonstrates the bed surface topography for the 35 mm diameter natural gravel.

Figure 3.6. A novel artificial bed with a median particle diameter of 28 mm was placed within the test section for experiments 5 and 6.

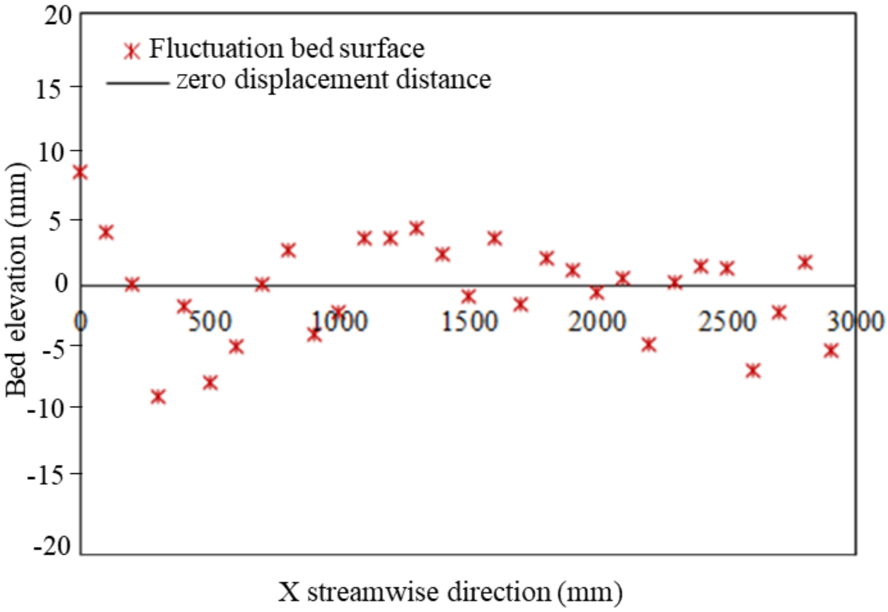

Figure 3.7. The topography of the bed surface elevations for d_{50}=20 mm diameter natural gravel within the test section for experiments 1, 2 and 3.

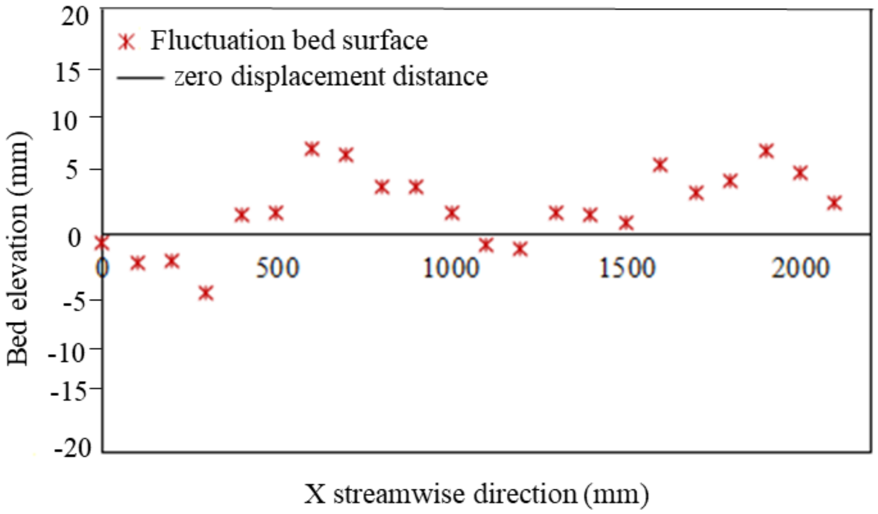

Figure 3.8. The topography of the bed surface elevations for d_{50}=35 mm diameter natural gravel within the test section for experiment 4.

Using the point gauge elevation data, the standard deviation of the surface elevations was calculated for both beds as:

$$\sigma_b = \sqrt{\frac{1}{N}\sum_{i=1}^{1=N}(z_i - \bar{z})^2} \tag{3.6}$$

where, N is the total number of bed elevation measurement points in the longitudinal direction, z_i is the bed surface elevation and $\bar{z}$ is the mean bed surface elevation. Table 3.1 shows the standard deviation for all beds as well as other bed characteristics.

The skewness coefficient was calculated to describe the general feature of the bed surface shape or form using Eq. (3.7). The kurtosis coefficient was also calculated, which gives a rate of bed homogeneity or intermittency, using Eq. (3.8) (Coleman et al. 2011; Stewart et al. 2019):

$$Sk_z = \frac{{}^{1}/_{N}\sum_{i=1}^{i=N}(z_i - \bar{z})^3}{\sigma_b^3} \tag{3.7}$$

$$Ku_z = \frac{{}^{1}/_{N}\sum_{i=1}^{i=N}(z_i - \bar{z})^4}{\sigma_b^4} \tag{3.8}$$

where, Sk_z is the skewness coefficient, and Ku_z is the kurtosis coefficient.

As shown in Table 3.1, Sk_z is negative for both the 20 mm diameter natural gravel-bed as well as the 28 mm diameter artificial bed, for which the skewness is also close to zero. Negative skewness values imply the median of negatively skewed is greater than the mean. However, the skewness is positive for the 35 mm diameter natural gravel-bed, where positive skewness values imply the median of positive skewness is less than the mean. A negative skewness coefficient was observed for an unworked gravel-bed, while a positive skewness coefficient was found for a water work gravel-bed (Nikora et al. 1998; Aberle and Nikora 2006). It means that the bed surface elevations for all beds have a normal distribution due to Sk_z is near zero.

The Kurtosis coefficient, Ku_z was found to be negative for all the beds, as shown in Table 3.1, meaning the bed surface elevations have a uniform distribution due to Ku_z is near zero, but the artificial bed has a large negative Ku_z. It can be seen from Table 3.1 that the Sk_z of the 35 mm diameter natural gravel-bed is 0.19 larger than the Sk_z of the 20 mm diameter natural gravel-bed and the 28 mm diameter artificial bed. The value of the skewness coefficient grows when particle size increases and changes with grain size which was found in field measurements (Carling and Reader 1982; Coleman et al. 2011).

To plot a roughness geometry function $A(z_b')$, the fluctuation in surface elevations, (z_b') was calculated from the formula below (Nikora et al. 2001):

$$z_b' = \frac{z_i - \bar{z}}{\sigma_b} \tag{3.9}$$

The roughness geometry function describes the cumulative probability distribution of the surface elevations and allows $A(z_b')$ to be plotted as a function of the fluctuations in surface elevation (z_b'), similarly to Nikora et al. (2001); Stoesser (2010); and Stubbs et al. (2018), as shown in Figure 3.9.

Figure 3.9 shows the roughness geometry function for the natural gravel-beds used here in this study agrees well with unworked gravel-bed and water-worked natural gravel-beds alike, such as river reaches found in New Zealand (Nikora et al. 1998; Nikora et al. 2001). Thus, the distribution of surface elevations of the gravel-beds used here is similar to that found in both experimental studies and nature. Additionally, the particle size, porosity, skewness coefficient, and kurtosis coefficient of the gravel-beds in this study are similar, or within range, to that found in natural gravel-bed rivers.

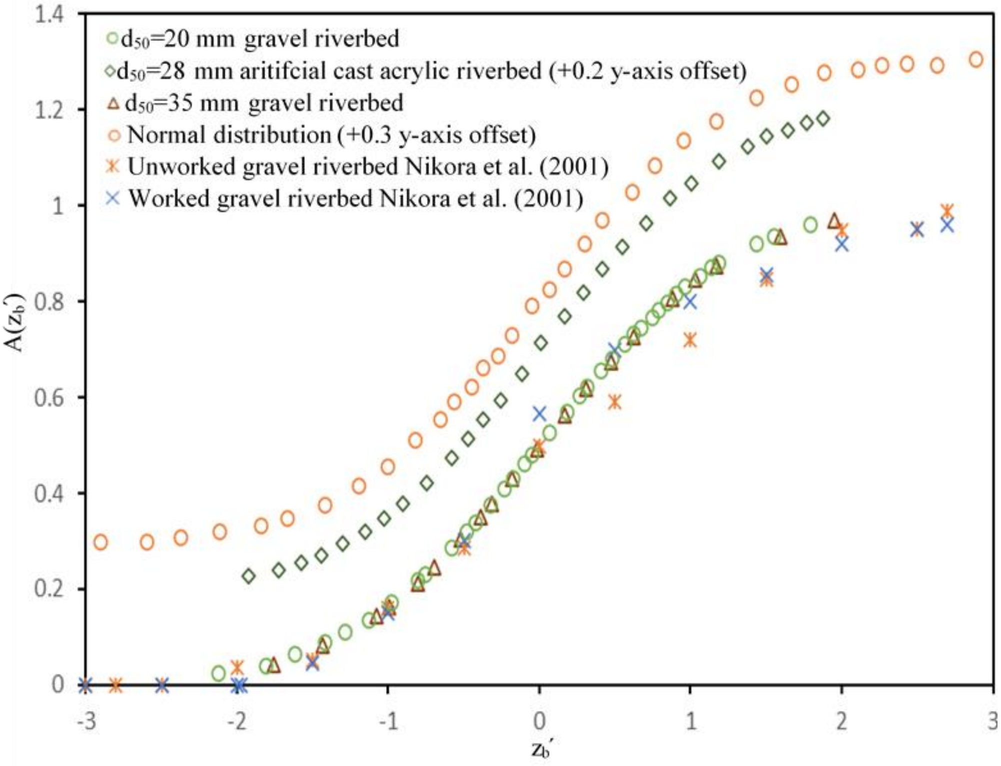

Figure 3.9. Roughness geometry function $A(z_b{}')$ plotted against the fluctuation in surface elevation ($z_b{}'$).

A single honeycomb lattice was placed at the flume inlet for the experiments conducted with a natural gravel-bed. Additionally, two honeycomb lattices were similarly positioned for the experiments using the artificial bed to achieve a more uniform flow and be similar fashion to Zeng et al. (2015). For all experiments, a single honeycomb lattice 12.00 cm in height was placed at the flume outlet to prevent any gravel from entering either the outlet tank or the pump pipework, as shown in Figure 3.10. The outlet lattice also helped to stabilise the gravel and the inlet lattice reduced any background turbulence or surface waves entering the flume from the header tank. Thus, helping to establish a uniform flow.

Figure 3.10. An image of the flume outlet looking in the upstream direction, showing the honeycomb lattice in place, preventing gravel particles from entering the outlet tank whilst allowing flow through the subsurface region. The flow direction is indicated by the arrow.

3.5 Flow Measurement Methods

3.5.1 Acoustic Doppler Velocimetry (ADV)

Nortek AS manufactured the Acoustic Doppler Velocimeter (ADV) or Vectrino Velocimeter that was used in this study to measure water velocity in the three-component directions above the various beds, as shown in Figure 3.11a. This measurement method utilises the doppler effect and involves the transmission of a short pulse of sound from the probe head, receiving the reflected sound, and measuring the relative frequency alteration, which can in turn be related to velocity (Nortek 2004). The sound does not only reflect due to the water itself, but also from particles suspended in the water (Nortek 2004).

In this study, spherical 110P8 hollow glass spheres with an average particle size of 11.7 μm and a density of 1.10 g/cc were suspended in the water flow. The hollow spheres are white in colour and hollow non-porous microspheres in shape. This seeding material was recommended by Nortek (2000) because hollow spheres have a density close to the density of water and will stay in suspension. The suggested seeding level is 10-50 g/m^3, or an ounce per ton of water. The size of the hollow spheres was chosen due to the relatively strong echo generated from particles of this size per unit of concentration.

For this study, a side-looking ADV was used with a sampling rate of 25 Hz and a sample volume 50 mm away from the probe head (Nortek 2004). The cylindrical sampling volume was set to 5.5 mm cylinder height and 6 mm diameter for all experiments, as shown in Figure 3.12. The ADV was vertically mounted on a carriage above the flume, which could be moved in the streamwise or the cross-streamwise directions. An automatic stepper motor was used to move the ADV vertically to each of the depth-wise measurement locations with an accuracy of ±0.02 mm per step, as shown in Figure 3.11b. For all experiments, the ADV was set to record for 5 minutes (300 s) at each z-coordinate measurement to obtain a time-independent average velocity for all experiments and provide an adequate time period to obtain a constant time series (Dey et al. 2011).

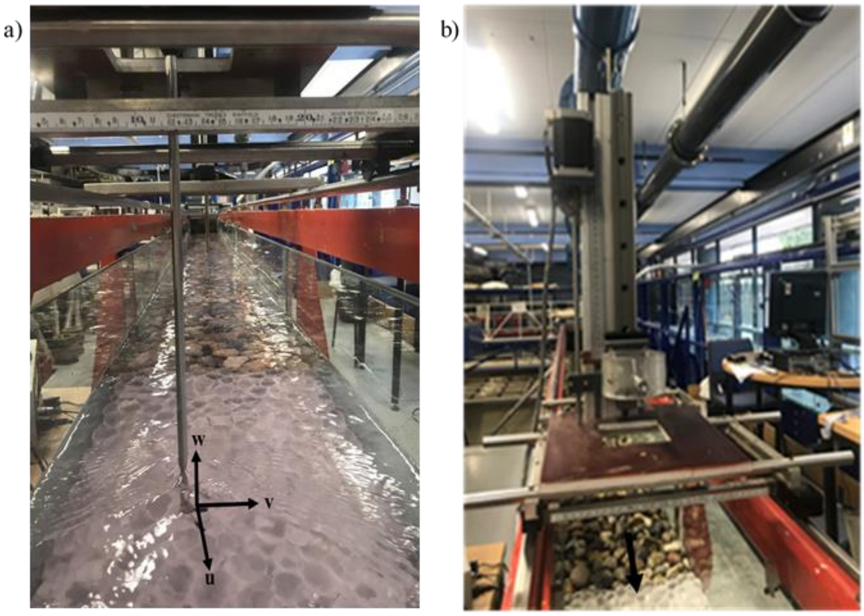

Figure 3.11. The ADV a) vertically mounted and positioned within the flow, as well as b) showing the carriage and automatic stepper motor rising mechanism the ADV was attached.

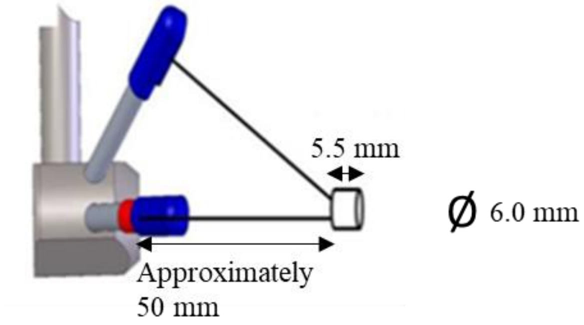

Figure 3.12. Diagrammatic layout of a side-looking ADV probe, adapted from Nortek (2018, p. 14).

Generally, errors during ADV data collection are typically due to velocity gradient errors or doppler noise. However, such errors have been shown to not have a significant impact on turbulence analysis (Lohrmann et al. 1994; Voulgaris and Trowbridge 1998). During the data collection process, it is best practice to decrease the noise energy level and thus, prevent any spikes in the signal and decrease noise energy levels overall (García et al. 2007). Such spikes occur due to the influences of high shear, the presence of a wall, high turbulence levels, and phase shifts in the doppler signal (Goring and Nikora 2002). Total noise increases in the velocity reading at higher sampling rates despite higher sampling frequencies being able to distinguish a larger range of turbulent frequencies (McLelland and Nicholas 2000). Also, doppler signals can become contaminated when previous pulses are reflected from complicated bed geometries, such as that used in this study, where the acquired velocity overtakes the set velocity range (Grams and Wilcock 2007). Therefore, the velocity range was set to between 0.300 m/s and 1.000 m/s for all experiments.

The time series gathered in each of the three component directions was inspected to distinguish likely problems such as trends, spikes, or abrupt discontinuities. This is particularly valuable for defining errors connected with large spikes resulting from the disconnection of the acoustic signal by large particles as they move through the sampling volume.

Further filtering of the ADV data by applying Phase-Space-Thresholding (PST) (Goring and Nikora 2002) detects and removes spurious spikes from the time series. This method assumes that the time derivatives of the component velocity fluctuations form an ellipsoid in 3D phase-space and that any data points lying outside of the ellipsoid can be considered spurious and can be removed (Goring and Nikor 2002). In this study, the PST technique was applied using MAJ's Velocity Signal Analyser (Jesson 2015).

MAJ's Velocity Signal Analyser (Jesson 2015) was also used to determine the mean velocity and the standard deviation, or the Root Mean Square (RMS), of the instantaneous velocity signal in the three-component directions (x, y and z) by applying the following equations:

$$\bar{u} = \frac{\sum_{i=1}^{i=N} u - u'}{N} \tag{3.10}$$

where, $\bar{u}$ is the mean velocity in the x-direction, u is the instantaneous velocity in the x-direction, and u′ is turbulent fluctuation from the mean velocity in the x-direction.

$$\bar{v} = \frac{\sum_{i=1}^{i=N} v - v'}{N} \tag{3.11}$$

where, $\bar{v}$ is the mean velocity in the y-direction, v is the instantaneous velocity in the y-direction, and v′ is turbulent fluctuation from the mean velocity in the y-direction.

$$\bar{w} = \frac{\sum_{i=1}^{i=N} w - w'}{N} \tag{3.12}$$

where, $\bar{w}$ is the mean velocity in the z-direction, w is the instantaneous velocity in the z-direction, and w′ is turbulent fluctuation from the mean velocity in the z-direction.

As mentioned earlier in Section 2.3.1, determining the standard deviation, or the Root Mean Square (RMS), of the velocity fluctuations, gives the turbulent strength in the three-component directions as:

$$U_{RMS} = \sqrt{\frac{\sum_{i=1}^{i=N} u'^2}{N}} \tag{3.13}$$

$$V_{RMS} = \sqrt{\frac{\sum_{i=1}^{i=N} v'^2}{N}} \tag{3.14}$$

where, V_{RMS} is the RMS of velocity fluctuation in the y-direction.

$$W_{RMS} = \sqrt{\frac{\sum_{i=1}^{i=N} w'^2}{N}} \tag{3.15}$$

where, W_{RMS} is the RMS of velocity fluctuation in the z-direction.

Moving on now to consider the hydraulic conditions for all experiments and the procedure of measurements above the natural gravel-beds and artificial bed. Table 3.2 provides the bulk hydraulic conditions for flow above the beds used in this study; where Q is the discharge, U_{bulk} is average bulk velocity, Fr is the Froude number, Re_R is the Reynolds number calculated using the hydraulic radius, Re_H is the Reynolds number calculated using flow depth, ks/H_{max} is the ratio of Nikuradse equivalent sand roughness to the water depth (H_{max}), n is the manning number, and B/H_{max} is the aspect ratio of flume width (B) to the water depth.

Table 3.2. Flow conditions for the experiments were conducted with natural gravel-beds with a median grain diameter of 20 mm and 35 mm, and an artificial bed with a median diameter of 28 mm. The longitudinal bed slope of the flume was fixed at 0.001.

Experiment No.	1	2	3	4	5	6
Gravel type	Natural	Natural	Natural	Natural	Artificial	Artificial
d_{50}(mm)	20	20	20	35	28	28
Q (m^3/s)	0.004	0.006	0.009	0.004	0.006	0.009
H_{max} (m)	0.082	0.098	0.118	0.093	0.075	0.094
u_{bulk} (m/s)	0.164	0.210	0.256	0.145	0.269	0.321
Fr (-)	0.183	0.214	0.238	0.152	0.314	0.334
Re_R (-)	8,695	12,448	16,907	8,324	13,450	18,550
Re_H (-)	13,448	20,580	30,208	13,485	20,175	30,174
k_s (mm)	55	35	26	61	6	5
K^+	1555	1085	898	1845	151	153
H_{max}/σ_b (-)	10.47	12.52	15.07	15.35	19.69	24.67
k_s/H_{max}	0.671	0.357	0.212	0.659	0.075	0.060
u_* (m/s)	0.028	0.031	0.034	0.030	0.027	0.030
n_p %	36	36	36	31	32	32
Manning n (-)	0.027	0.023	0.020	0.033	0.016	0.015
B/H_{max} (-)	3.659	3.061	2.542	3.226	4.000	3.191
R_{ek}	13.926	15.418	16.910	19.700	14.543	16.698
z_0 (mm)	6.5	6	7	7.5	5.6	5.6

In this study, the relative submergence was calculated as H_{max}/σ_b, where H_{max} is the maximum flow depth equal to $H_{measurement}+z_0$, in a similar fashion to Mohajeri et al. (2016). The shear velocity, u_* in Table 3.2 was found using water depth instead of the hydraulic radius (Shvidchenko and Pender 2000) as sidewall influences could be ignored since measurements were taken in sections where the sidewall had no effect (Koll 2006; Manes et al. 2007). Thus, Eq. (3.16) is not only convenient but appropriate for use in this study to obtain the shear velocity:

$$u_* = \sqrt{gH_{max}S} \tag{3.16}$$

Returning now to velocity measurements above rough surfaces, the greatest care was taken to guarantee the volume of sampling did not touch the gravel particles and to avoid any glass wall effects. Therefore, the computer monitor was observed to ensure the velocity fluctuations did not appear noisy, which would indicate the sampling volume touched the bed surface or glass caused reflection, whilst gathering all velocity measurements during all the experiments. The Signal Noise Ratio (SNR) should be ≥ 15 db and signal correlations between the received pair of pulses and that transmitted by the ADV should be ≥ 70%. If either value fell outside of the permitted ranges, data gathering was stopped and restarted. Therefore, all variables were adjusted until the best setup was found for the sample volume, sample height, sample rate, power level, and nominal velocity range as recommended by the Nortek support team (Nortek Group Support, personal communication, January 2018).

The measurements in the x- and y-directions were initially gathered in a grid pattern for experiments 2 and 3, following the systematic approach taken by Buffin-Bélanger et al. (2006), as shown in Figure 3.13. However, the wide range grid procedure did not have the spatial resolution necessary to apply the double average method to the gathered results and allow any meaningful conclusions to be drawn. Thus, the procedure was changed so that measurements in the x- and y-directions were taken randomly in experiments 1, 4, 5 and 6 similar to Nikora et al. (1998) and Nikora et al. (2001) and allowing the double average method to be appropriately applied, as shown in Figure 3.14. The difference between these two approaches to providing measurement gathering locations can also be explored.

Due to the restricted flow depth and the need to optimise the number of measurement points in the z-direction (flow depth direction), the velocity was measured every 0.003 m in depth in experiments 1 and 4 and 0.005 m in depth in experiments 2, 3, 5 and 6.

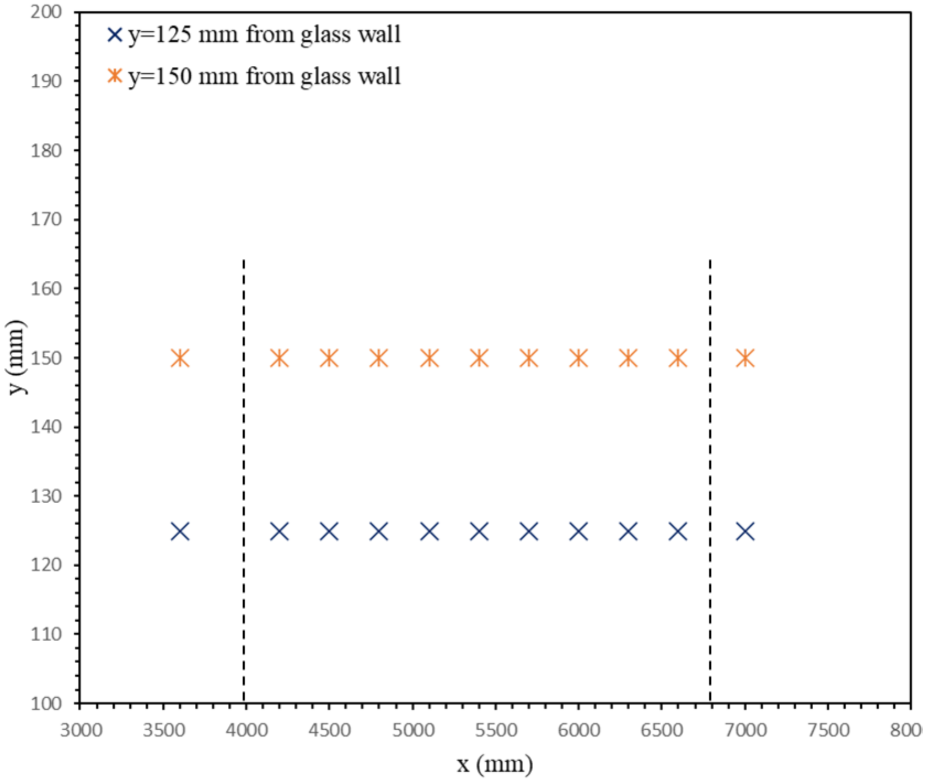

Figure 3.13. A sectional plan view in the x-y plane of measurement locations is arranged in a grid pattern, where x is the distance from the flume inlet and y is the distance from the glass wall.

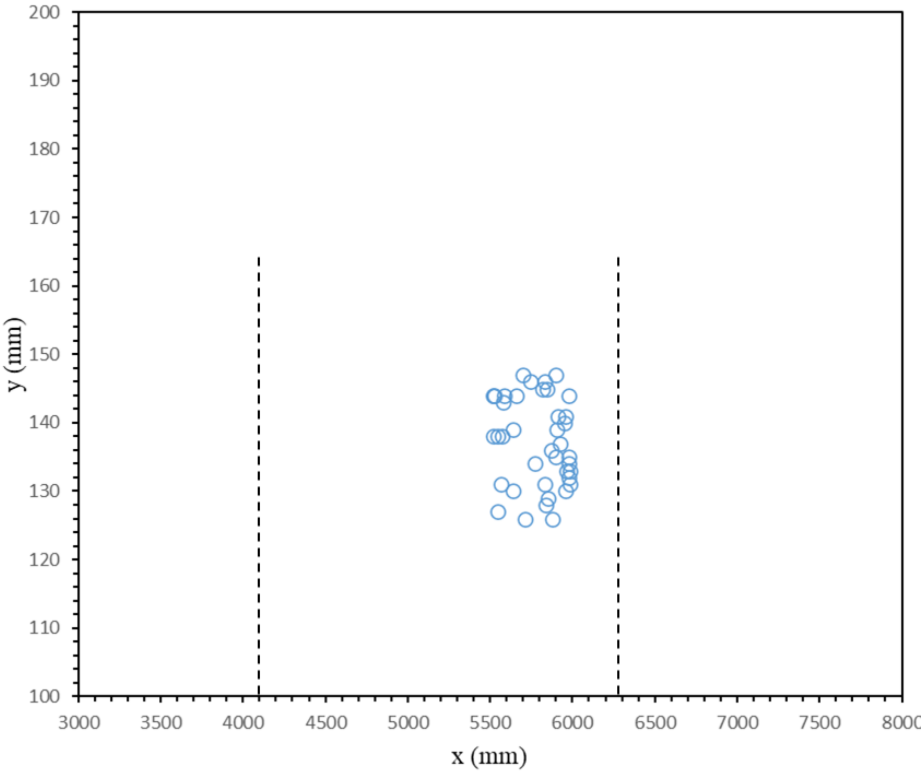

Figure 3.14. A sectional plan view in the x-y plane of measurement locations is arranged in a randomised pattern, where x is the distance from the flume inlet and y is the distance from the glass wall.

Different settings were used to find the best ADV setup for each experiment; the following details the experimental setups used to measure velocity above the natural gravel-bed and artificial beds in this study:

1. **Experiment 1:** The velocity profiles above a natural gravel-bed (d_{50} = 20 mm) were measured using an ADV at 40 randomly selected points within a test section 5.5 m to 6 m (±0.05 mm - ±1 mm) from the inlet of the flume and between 0.125 m and 0.150 m (±0.05 mm - ±1 mm) from the flume wall, where the flow was fully developed and unaffected by the influence of the flume sidewall. Six data points, each three millimetres apart were taken in the vertical direction (z-coordinate direction) for each of the 40 profiles. The ADV settings for this experiment are given in Table 3.3.

2. **Experiment's 2 and 3:** The velocity profiles above a natural gravel-bed (d_{50} = 20 mm) were measured using an ADV. Twenty-two velocity profiles were gathered in a grid-like fashion measuring 300 mm by 25 mm (x- and y-directions, respectively) within the test section, which was located between 4 m and 6.8 m (±0.05 mm - ±1 mm) from the upstream inlet. Again, to avoid any influence of

sidewall effects, measurements were taken between 0.125 m and 0.150 m (±0.05 mm - ±1 mm) from the flume wall. Velocity profiles are composed of seven points in the vertical direction for experiment 2 and eleven points in the vertical direction for experiment 3. Measurement points were five millimetres apart for each depth-wise measurement point. The first velocity profile was measured at a distance of 3.600 m from the flume inlet, as shown in Figure 3.15.

3. **Experiment 4:** The velocity profiles above a natural gravel-bed (d_{50} = 35 mm) were measured using an ADV at 40 randomly selected points within a test section 5.5 m to 6 m from the inlet of the flume and between 0.125 m and 0.150 m from the flume wall. Nine data points, each three millimetres apart, were taken in the vertical direction (z-direction).

4. **Experiment 5:** The velocity profiles above an artificial bed (d_{50} = 28 mm) were measured using an ADV at 40 randomly selected points within a test section 5.300 m to 5.795 m from the flume inlet and between 0.125 m and 0.150 m from the flume wall. In this experiment, two further sets of data were also measured. Firstly, five velocity profiles were measured between 0.130 m and 0.140 m from the flume wall upstream of the test section and between 4.878 m and 4.900 m from the inlet of the flume. Secondly, five velocity profiles were measured between 5.908 m and 5.928 m from the flume inlet and between 0.130 m and 0.140 m from the flume wall downstream of the test section, as shown in Figure 3.16. Seven data points, each five millimetres apart were taken in the vertical direction for each profile (z-coordinate direction) for all profiles.

5. **Experiment 6:** The velocity profiles above an artificial bed (d_{50} = 28 mm) were measured using an ADV at 40 randomly selected points within a test section 5.300 m to 5.795 m from the flume inlet and between 0.125 m and 0.150 m from the flume wall. Again, to ensure the approach flow was fully developed, five velocity profiles were measured upstream and downstream of the test section. Firstly between 4.870 m and 4.910 m from the flume inlet and between 0.130 m and 0.150 m from the flume wall upstream of the test section. Secondly, between 5.878 m and 5.928 m from the flume inlet and between 0.130 m and 0.150 m from the flume wall downstream of the test section, as shown in Figure 3.16. Eleven data

points, each five millimetres apart were taken in the vertical direction (z-direction) for each of the profiles.

Table 3.3. Acoustic Doppler Velocimeter (ADV) settings corresponding to each experiment to gather velocity measurements above natural gravel-beds with median particle diameters of 20 mm and 35 mm, as well as above an artificial bed with a median particle diameter of 28 mm.

	The diameter of the sampling volume (mm)	Nominal velocity range (m/s)	Sampling rate (Hz)
Experiment 1, 2, 3 and 5	5.5	0.3	25
Experiment 4	5.5	1.0	5
Experiment 6	5.5	1.0	25

The relative submergence was found to be 10.47, 12.52, 15.07, and 15.35 for experiments 1, 2, 3 and 4, respectively, above the natural gravel-bed, as shown in Table 3.2. The relative submergence was found to be 19.69 above the artificial bed, as shown in Table 3.2. Therefore, the flow was classified as under intermediate relative submergence conditions or flow Type 2 (Nikora et al. 2001; Nikora 2007) for experiments 1, 2, 3, 4, and 5. Whilst, for experiment 6, where the relative submergence was found to be 24.67 above the artificial bed, the flow was classified as under high relative submergence conditions or flow Type 1 (Nikora et al. 2001; Nikora 2007). Such submergence values are not dissimilar to other studies that have been conducted under high relative submergence conditions, for example: Mignot et al. (2009b) at 21.9; Sarkar and Dey (2010) at 25.6; and Dey and Das (2012) at 25.3.

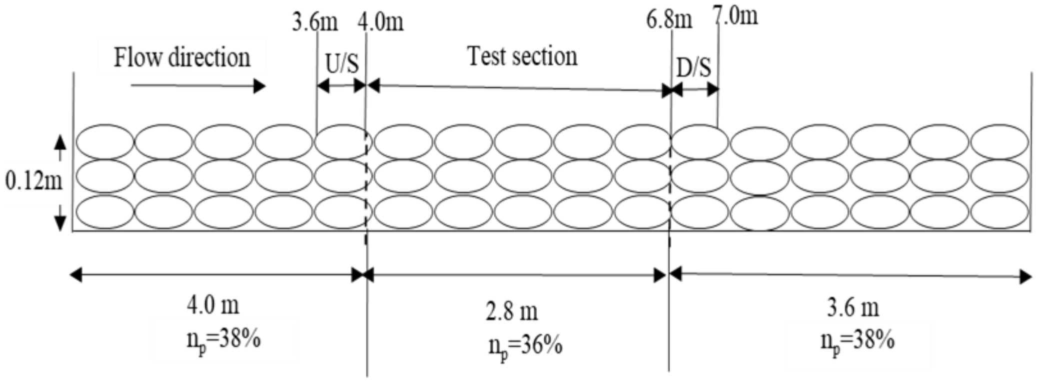

Figure 3.15. Diagrammatic view of the flume from the side showing the test section layout for experiments 2 and 3 with a natural gravel-bed with a median particle diameter of 20 mm.

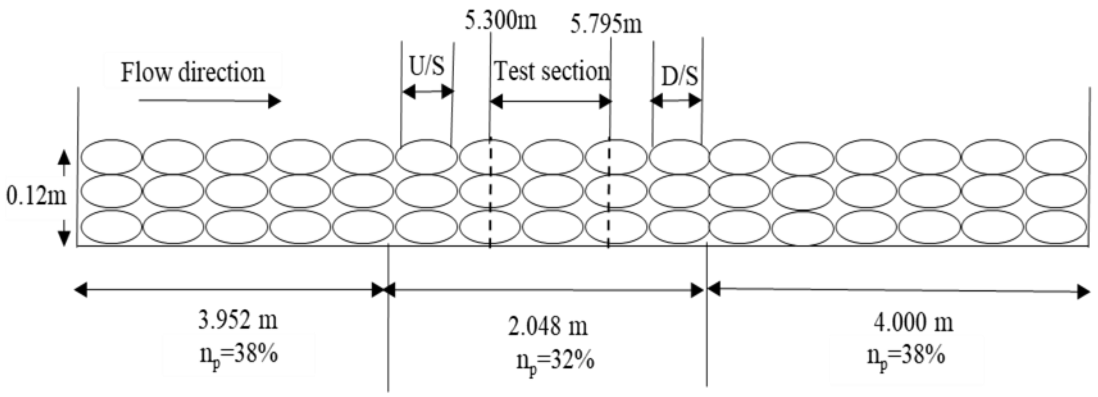

Figure 3.16. Diagrammatic view of the flume from the side showing the test section layout for experiments 5 and 6 with an artificial bed with a median particle diameter of 28 mm.

3.5.2 Endoscopic Cameras

Turning now to subsurface velocity measurements, the velocity through the bed in experiment's (1-3), (4), (5-6) was found to be 0.003 m/s, 0.004 m/s, and 0.005 m/s, respectively. Eq. (3.17) was used to calculate the discharge as (Pagliara et al. 2008):

$$Q_{sub} = U_{sub}BET \tag{3.17}$$

where, Q_{sub} is the flow rate through the gravel in m^3/s, B is flume width, and ET is the thickness of the bed material.

Total discharge in the flume, as shown in Table 3.2, was calculated as:

$$Q_{total} = Q_{sup} + Q_{sub} \tag{3.18}$$

where, Q_{sup} is the discharge above the bed.

The thickness of bed material, ET= (120 mm - z_0), needs to be calculated to obtain the discharge within the gravel-bed, as shown in Figure 3.17. Also shown in Figure 3.17, z_0 is the distance to the effective location where the flow velocity is theoretically zero (Pagliara et al. 2008). A range of values for z_0 has previously been applied indicating that the bed level is commonly taken as $0.15d_{50}$ to $0.3d_{50}$ below the crest of the sand-grain roughness (Bridge and Bennett 1992; Nezu and Nakagaw 1993), or is some distance between $0.2k_s$ and $k_s=d_{50}$ (Kironoto and Graf 1994).

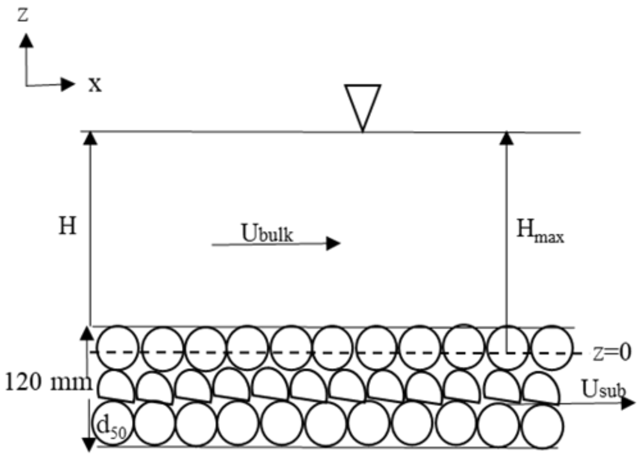

Figure 3.17. Streamwise sectional sketch in the (x-z) plane of the bed particles and the flow depth (H), where z_0 is zero-displacement, U_{bulk} is mean velocity, U_{sub} is subsurface velocity, d_{50} is the particle diameter of which 50% of the bed particle size distribution is finer, and the roughness thickness is 120 mm.

Due to the unfortunate issues with using a Particle Image Velocimetry (PIV) system, ten endoscopes were instead used to measure the instantaneous velocity field in the subsurface layers of the bed. Each endoscope had an 8.5 mm diameter lens and endoscopes were connected to four computers, as shown in Figure 3.18. The focal length of each endoscope was 30 mm, the video resolution was 640 x 480 pixels, and the frame capture frequency was 30 frames per second.

Additionally, Rhodamine WT was selected as a dye tracer for use with the endoscopes due to its high visibility, low eco-toxicity, low cost, and chemical stability (Smart and Laidlaw 1977; Field et al. 1995; Dierberg and DeBusk 2005). Rhodamine WT is a purple fluorescent dye and has a maximum fluorescence emission wavelength of 580 nm and a maximum excitation wavelength of 555 nm (Smart and Laidlaw 1977).

The dye tank, shown in Figure 3.19, was mounted vertically above the flume, and the flow of dye into the flume was controlled by a valve. A constant head was maintained to ensure the dye entered the flume at the same velocity as the fluid flow. The concentration was set at 10 ml of dye per 1000 ml of water (10 ppt concentration) for all experiments.

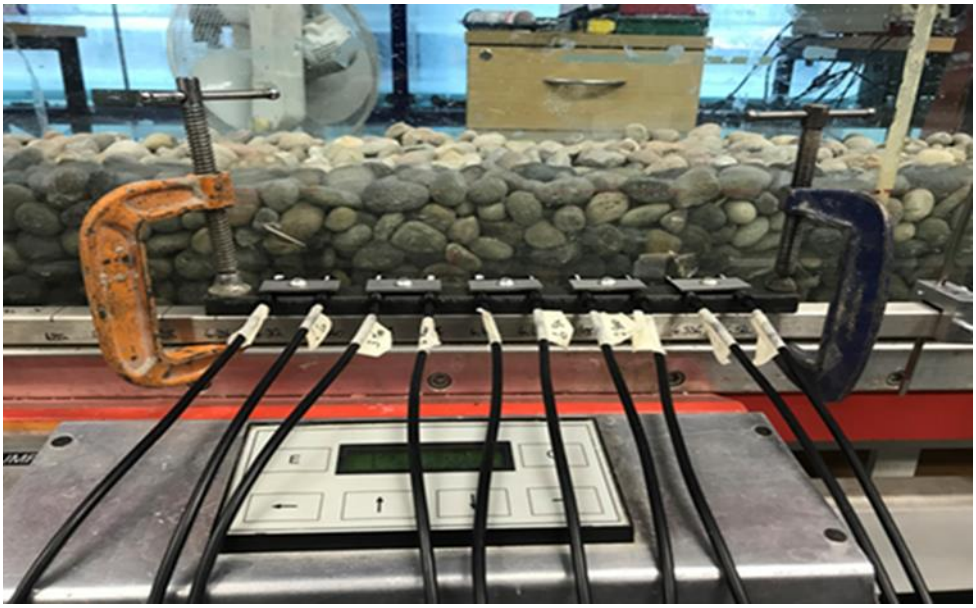

Figure 3.18. Endoscope setup to measure subsurface velocity between gravel viewed from the right-hand side of the flume when looking downstream from the inlet.

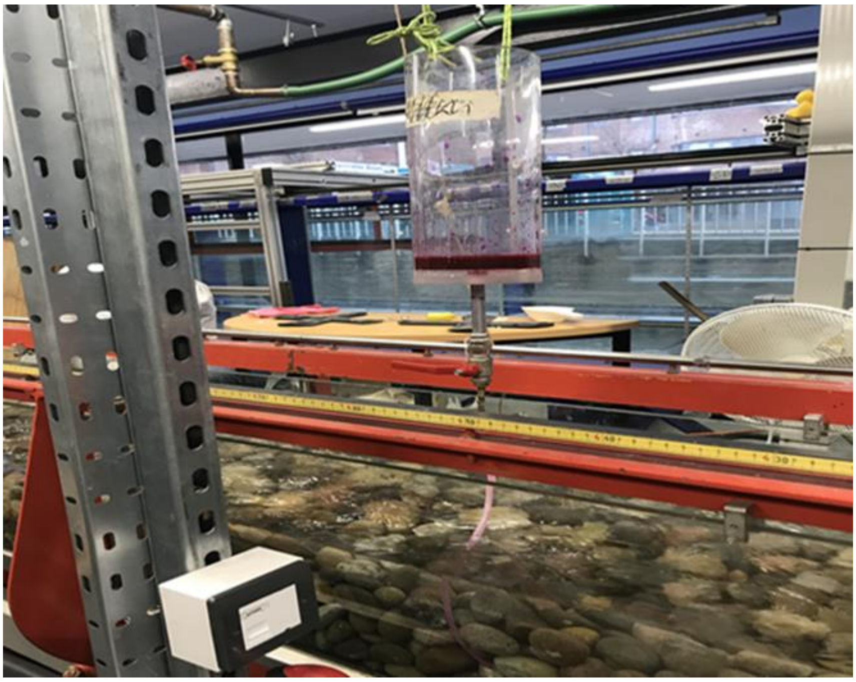

Figure 3.19. Constant head dye injection tank as well as a control valve.

The ten endoscopes were located on the right-hand side of the flume, as shown in Figure 3.18. The first endoscope was located 5.630 m from the inlet and 0.064 m from the flume bed for experiments 1 and 4, and 5.680 m from the inlet and 0.075 m from the flume bed for experiments 5 and 6. The distance between each endoscope was 0.027 m. The eighth and tenth endoscopes were positioned at 5.819 m and 5.873 m, respectively from the inlet for experiments 1 and 4, and positioned at 5.869 m and 5.923 m, respectively from the inlet for experiments 5 and 6. Video visualisation was used to record measurements of subsurface velocity using the endoscopes for all experiments over 256.4 s.

The obtained video data was converted to frames to allow the average velocity within the natural and artificial beds to be found. For this purpose, the image analysis code developed by Forughi (2014) was applied. The code procedure is diagrammatically explained by way of a flow chart in Figure 3.20.

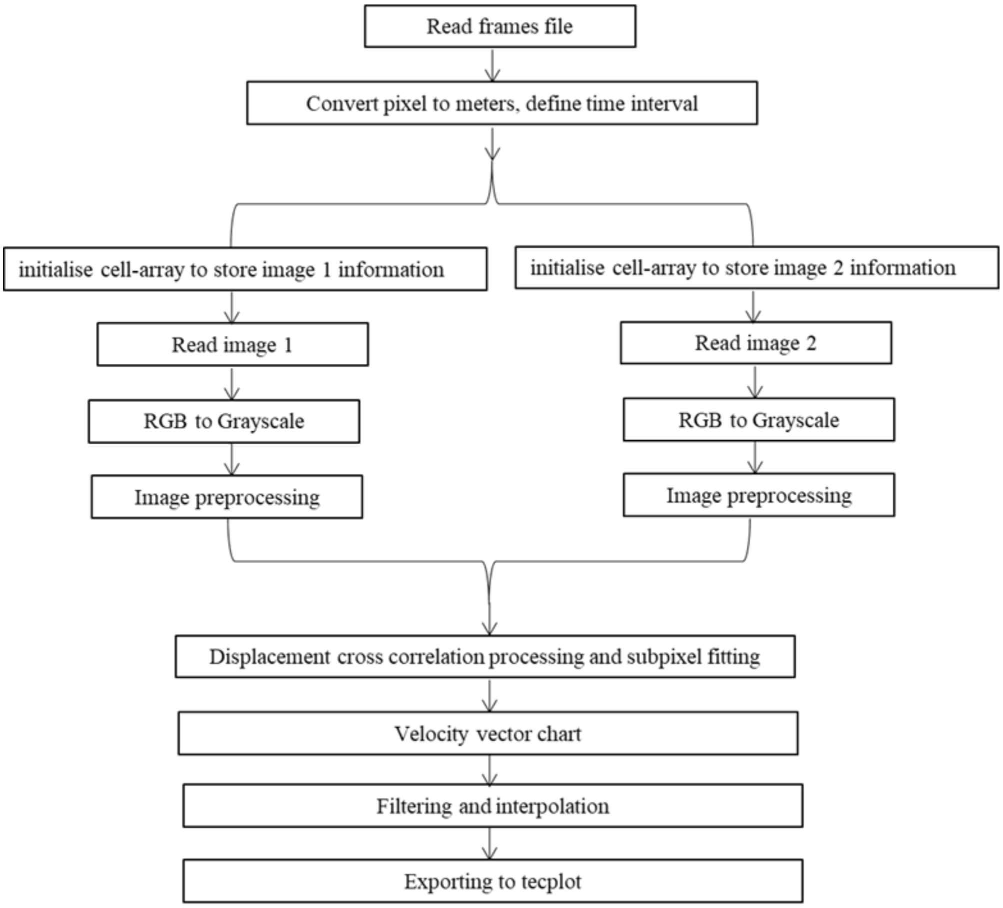

Figure 3.20. Code procedure for the image analysis software developed by Forughi (2014) and applied in this study to obtain subsurface velocity measurements from video captured using endoscopic cameras.

3.6 Summary

The experiments were carried out in a recirculating narrow flume under uniform flow conditions with a bed slope of 0.001. Uniform flow conditions were achieved for the different discharges by adjusting the tailgate weir height such that the water surface, when measured using a point gauge every metre along the flume centreline, was deemed parallel to the flume bed.

The flume bed was covered within the test section with two different natural gravel sizes, d_{50}=20 mm and d_{50}=35 mm, as well as by an artificial bed, d_{50}=28 mm. Natural gravel with d_{50}=28 mm was used to cover the flume bed upstream and downstream of the test section in all experiments due to supplier restrictions in obtaining the required amount of gravel necessary to cover the entire ten-meter length of the flume. The British Standard method (British Standards Institution 1990) was used to determine the particle size distributions of the natural gravel-bed, see Figure 3.3. The natural gravel-bed particle diameter was chosen so that the hydrodynamic bed shear stress was less than the critical sediment shear stress (according to Shield's approach), ensuring particles remained immobile during all experiments, whilst also being similar to that found in Salmonid Redds within UK rivers, as given in Section 3.2. The porosity of the natural gravel-beds was measured and calculated to be 36% and 31% for the beds with a median particle diameter of d_{50}=20 mm and d_{50}=35 mm, respectively. The porosity of the artificial bed with a median particle diameter of d_{50}=28 mm was found to be 32%.

To achieve naturalistic, open-channel flow conditions, the bed of a flume was configured similar to a riverbed (as shown in Figures 3.5 and 3.6) with similar porosity, particle size, and surface roughness. The bed surface topography was measured using a point gauge in the flow direction every 0.1 m, and in the cross-streamwise direction every 0.025 m for the natural gravel of d_{50}=20 mm (experiments 1, 2 and 3) as well as for the natural gravel of d_{50}=35 mm (experiment 4), as shown in Figures 3.7 and 3.8. After that, the standard deviation of the roughness surface was determined (as shown in Figure 3.9). An artificial bed measuring 2.048 m long, 0.12 m deep, and 0.3 m wide with a median particle diameter of 28 mm (Stubbs et al. 2018) was also used, as shown in Figure 3.4.

In this study, a side-looking ADV was found to be the most appropriate instrument to measure velocity above the natural and artificial beds with the available resources. The ADV settings and measurement locations for each experiment were reported in Section 3.5.1, Table 3.3. The hydraulic conditions and bed roughness parameters were calculated for the six different experiments. Endoscopes were also used, in conjunction with the injection of Rhodamine WT fluorescent dye, to measure velocity distributions within the subsurface region of each bed, as shown in Figures 3.18 and 3.19. The total discharge ranged from 0.004 m3/s to 0.009 m3/s across the experiments, as shown in Table 3.2.

Chapter 4

Flow Above Natural Gravel-Bed and Artificial-Bed

CHAPTER 4

Flow Above Natural Gravel- and Artificial-Bed

4.1 Introduction

In this chapter, the results of experiments collected using ADV above natural gravel and artificial beds are introduced. Results are compared with the theory and previous studies from the literature. Firstly, double averaged velocity profiles above natural gravel-beds and artificial beds for six experiments are explored to validate the logarithmic law. Secondly, the data set is compared with previous studies in the literature (Section 4.2). The turbulent stresses are presented in (Section 4.3) as turbulent intensities against the exponential decay functions reported by Nezu and Nakagawa (1993) and various other works found in the literature for the three coordinates directions: namely, the streamwise, cross-streamwise, and vertical directions (Section 4.3.1). In addition, Reynold shear stresses are explained (Section 4.3.2), streamwise, cross-streamwise, and vertical Reynolds normal stresses are discussed (Section 4.3.3). Finally, Turbulent Kinetic Energy is discussed for all six experiments (Section 4.3.4).

4.2 Velocity Profiles

Over the past three decades, there has been sustained research activity in the validation of velocity profiles against the logarithmic law above rough-beds. It is imperative to better understand the effects of intermediate and high relative submergence on the existence of the logarithmic law under such conditions, which, to date, remains questionable. Therefore, in this section, the analytical procedures and the results obtained from experiments conducted above natural gravel-beds and acrylic beds by ADV are described. A double-averaging (time-space averaging) procedure was used to study the velocity profile $\langle \bar{u} \rangle$ above natural gravel-beds and artificial beds under intermediate and high relative submergence and fully rough, turbulent flow conditions in a laboratory flume (unworked beds). The first, second and third experiments had 20 mm diameter natural gravel particles with a standard deviation of bed roughness heights of 7.83 mm and a porosity of 36%. The fourth experiment had a natural gravel-bed with a diameter of 35 mm, a standard deviation of bed roughness heights of 6.06 mm and a porosity of 31

%. The acrylic bed was composed of particles nominally 28 mm in diameter with a porosity of 32%, and a standard deviation, σ_b of the roughness heights of 3.81 mm in both experiments 5 and 6 (Stubbs et al. 2018) (see Section 3.3).

Table 4.1. Summary of hydraulic conditions for experimental flow behaviour above two natural gravel-beds with a median diameter of 20 mm and 35 mm, respectively and an artificial bed with a median diameter of 28 mm.

Experiment No.	1	2	3	4	5	6
Gravel type	Natural	Natural	Natural	Natural	Artificial	Artificial
d_{50}(mm)	20	20	20	35	28	28
k_s (mm)	55	35	26	61	6	5
Q (m^3/s)	0.004	0.006	0.009	0.004	0.006	0.009
H_{max} (m)	0.082	0.098	0.118	0.093	0.075	0.094
u_{bulk} (m/s)	0.164	0.210	0.256	0.145	0.269	0.321
Fr (-)	0.183	0.214	0.238	0.152	0.314	0.334
Re_R (-)	8,695	12,448	16,907	8,324	13,450	18,550
Re_H (-)	13,448	20,580	30,208	13,485	20,175	30,174
K^+	1555	1085	898	1845	151	153
H_{max}/σ_b (-)	10.47	12.52	15.07	15.35	19.69	24.67
k_s/H_{max}	0.671	0.357	0.220	0.656	0.08	0.053
u_* (m/s)	0.028	0.031	0.034	0.030	0.027	0.030
z_0 (mm)	6.5	6	7	7.5	5.6	5.6

The theoretical velocity profile calculated using Eq. (2.2) was used to find the best fit with measurements for experiment 1 at 5.579 m and 5.638 m from the inlet as well as the double averaged velocity profile with relative submergence of 10.47, as shown in Figure 4.1. The parameters of Eq. (2.2), as explained in Chapter 2 Section (2.2) were determined using a modified Clauser chart. The best fit procedure was achieved by assuming a small value of zero-displacement distance (z_0) at first, and then κ and k_s were determined in a similar fashion to Fang et al. (2018). Five iterations were used until the best fit with Eq. (2.2) and a maximum value of the regression coefficient, as shown in Table 4.2 was achieved. As shown by Figure 4.1, the measured velocity profiles agree well with Eq. (2.2) when κ, von Karman's constant, equals 0.38 and k_s, the Nikuradse equivalent sand roughness, equals $2.75d_{50}$, where d_{50}=20 mm and z_0 equals 6.5 m. Thus, κ is 0.03 less than that normally considered (0.41) for water without sediment. This is acceptable for validation of the logarithmic law, as will be discussed later in this section.

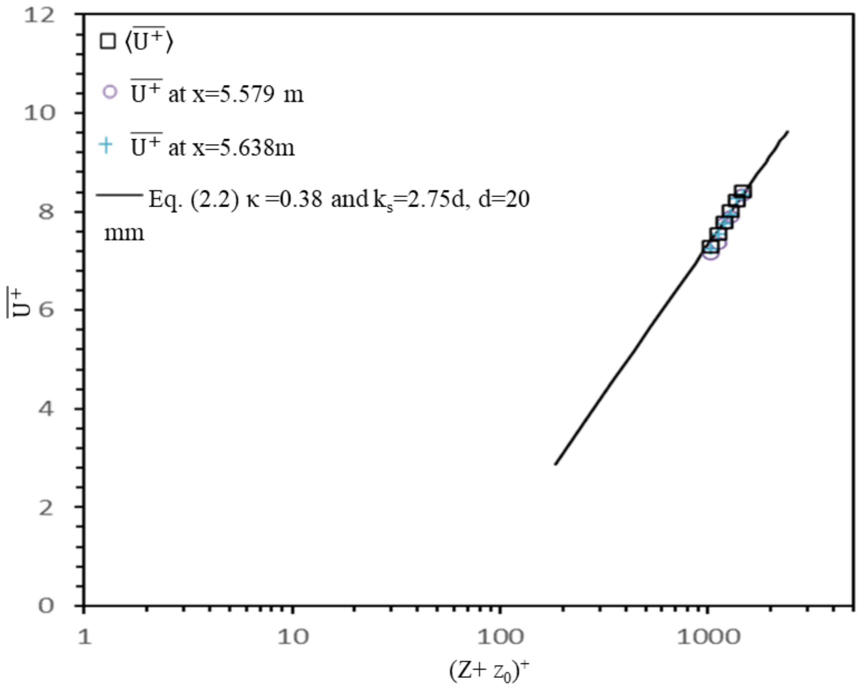

Figure 4.1. Double averaged and time-averaged streamwise velocity profiles were obtained from an experimental case above a natural gravel-bed with $k_s=2.75d_{50}$, d_{50}=20 mm, Q=0.004 m^3/s. $\overline{U^+} = \langle \bar{u} \rangle / u_*$ and $(Z + z_0)^+ = (Z + z_0)u_*/\upsilon$. Note: x is the distance from the flume inlet.

Table 4.2. The parameters of Eq. (2.2) were obtained after five iterations for experiment 1.

z_0 (mm)	κ	k_s	R^2	reason
2.50	0.34	$2.5d_{50}$	0.93	The measurements deviate from Eq. (2.2)
3.50	0.35	$2.55d_{50}$	0.93	The measurements deviate from Eq. (2.2)
4.50	0.36	$2.6d_{50}$	0.93	The measurements deviate from Eq. (2.2)
5.50	0.37	$2.7d_{50}$	0.93	The measurements deviate from Eq. (2.2)
6.50	0.38	$2.75d_{50}$	0.94	The best-fit measurements with Eq. (2.2)

In a similar fashion to experiment 1, the best fit procedure was also applied to all the other experiments; Table 4.3 shows the results of the iterations for experiment 2.

Figure 4.2 shows a Clauser plot of double averaged streamwise velocity normalised by u_* versus $(Z+z_0)^+$ for experiment 2.

Table 4.3. The parameters of Eq. (2.2) were obtained after five iterations for experiment 2.

z_0 (mm)	κ	k_s	R^2	reason
2.50	0.35	$1.4d_{50}$	0.92	The measurements deviate from Eq. (2.2)
3.50	0.36	$1.5d_{50}$	0.93	The measurements deviate from Eq. (2.2)
4.50	0.37	$1.6d_{50}$	0.93	The measurements deviate from Eq. (2.2)
5.50	0.38	$1.7d_{50}$	0.93	The measurements deviate from Eq. (2.2)
6.00	0.39	$1.75d_{50}$	0.94	The best-fit measurements with Eq. (2.2)

Figure 4.2 also shows time-averaged velocity profiles obtained at a distance x equal to 3.6 m, 4.8 m and 7.0 m, where x is the distance from the flume inlet (see Figure 3.15). As illustrated in Figure 4.2, the double averaged measurements agree well with Eq. (2.2), when κ and k_s equal 0.39 and $1.75d_{50}$, respectively, where d_{50}=20 mm under an intermediate relative submergence condition of 12.52. However, velocity measurements deviate from Eq. (2.2) when $(Z+z_0)^+ \leq 1271$ at x=3.6 m and x=7.0 m, but not at x=4.8 m. This trend was expected due to the effect of the irregular roughness particles which cause flow separation resulting in decreased velocity near the bed (e.g. Wiberg and Smith 1987; Afzalimehr and Rennie 2009). The deviation could also be due to the fact that the beds used in this study are highly porous, allowing flow to penetrate into the subsurface layers.

This phenomenon leads to the generation of turbulent eddies at the particle crests and results in an overall reduction in the average velocity near the bed (e.g. Ferguson 2007).

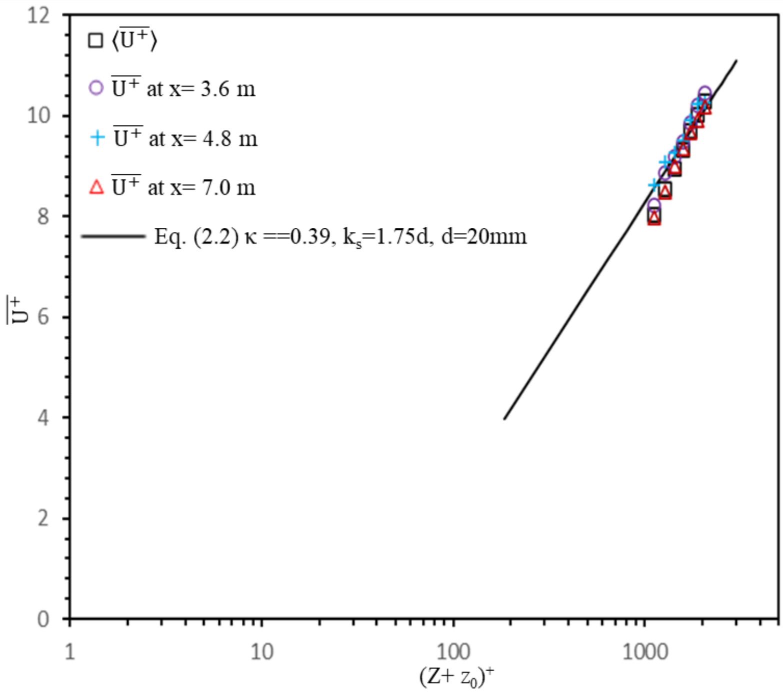

Figure 4.2. Double averaged and time-averaged streamwise velocity profiles were obtained from an experimental case above a natural gravel-bed with k_s=1.75d_{50}, d_{50}=20 mm, Q=0.006 m^3/s. $\overline{U^+} = \langle\bar{u}\rangle/u_*$ and $(Z + z_0)^+ = (Z + z_0)u_*/\upsilon$. Note: x is the distance from the flume inlet.

In addition, it should be pointed out that measurements were gathered in this experiment in a grid-like pattern with wide spacing between samples. Thus, it leads to interaction between sample location and the shear layer where the effect of individual bed particles on velocity results in a deviation from the logarithmic law near the bed. Therefore, it was recommended that measurements should be gathered at a high resolution for the application of the double average method (Buffin-Bélanger et al. 2006). This phenomenon does not occur in experiment 1 due to measurements being gathered over a higher-resolution, randomly located pattern.

The zero-displacement distance was found to be 6 mm through a best-fit approach in the same manner as experiment 1 (see Table 4.3). Figure 4.3 shows a Clauser plot of double averaged streamwise velocity normalised by u_* versus $(Z+z_0)^+$ for experiment 3 gathered in a grid-like pattern. Figure 4.3 also shows time-averaged velocity profiles measured at a distance from the flume inlet, x equal to 3.6 m, 4.8 m and 7.0 m. Figure 4.3 for experiment 3, where intermediate relative submergence was 15.07, shows that the velocity profiles are in close agreement with each other. Since both the double averaged, and time-averaged velocities remain constant along the flume, the flow in the test section was assumed to be approaching a fully developed condition. It should be noted that the logarithmic law constant of integration of 8.5 was applied for all experiments. This is because all experiments were carried out above highly rough hydraulically beds similar to (Nezu and Nakagawa 1993; Kironoto and Graf 1994). Clearly, Figure 4.3 shows that the velocities largely agree very well with the logarithmic law relationship when κ, k_s and z_0 are equal to 0.4, 1.32d_{50}, and 7 mm, respectively, for experiment 3 where d_{50}=20 mm (see Table 4.4).

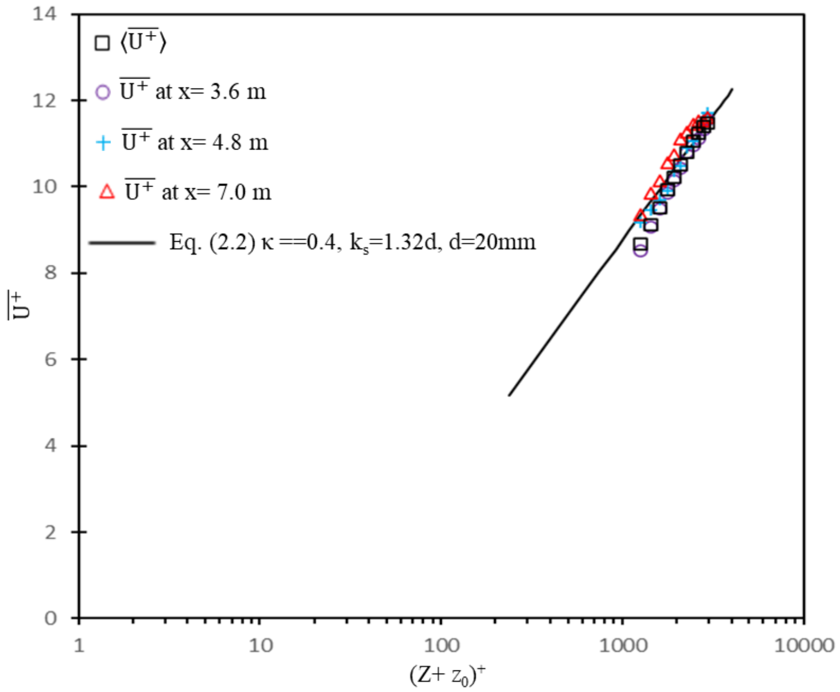

Figure 4.3. Double averaged and time-averaged streamwise velocity profiles were obtained from an experimental case above a natural gravel-bed of k_s=1.32d_{50}, d_{50}=20 mm, Q=0.009 m^3/s. $\overline{U^+} = \langle\bar{u}\rangle/u_*$ and $(Z + z_0)^+ = (Z + z_0)u_*/\upsilon$. Note: x is the distance from the flume inlet.

Table 4.4. The parameters of Eq. (2.2) were obtained after five iterations for experiment 3.

z_0 (mm)	κ	k_s	R^2	reason
3.00	0.36	0.50d_{50}	0.92	The measurements deviate from Eq. (2.2)
4.00	0.37	1.00d_{50}	0.92	The measurements deviate from Eq. (2.2)
5.00	0.38	1.10d_{50}	0.93	The measurements deviate from Eq. (2.2)
6.00	0.39	1.20d_{50}	0.93	The measurements deviate from Eq. (2.2)
7.00	0.40	1.32d_{50}	0.94	The best-fit measurements with Eq. (2.2)

However, the velocity measurements deviate from Eq. (2.2) when $(Z+z_0)^+ \leq 1598$ in the test section and when x=3.6 m. Experiment 3 was carried out under intermediate relative submergence conditions, where the outer flow layer does not exist, but both the logarithmic and roughness layers do. The velocity measurements might deviate from Eq. (2.2) as those sample locations in depth were located within the roughness layer. In this region, the effect of particles on flow is significant and results in the deviation shown in Figure 4.3 (Ferguson 2007).

It should also be noted that k_s values fluctuate between $1.32d_{50}$ and $2.75d_{50}$, although the bed features are the same in the three experiments 1, 2 and 3. However, the flow conditions are different in these experiments, resulting in different flow depths and average velocities and so on (see Table 3.2 and Table 4.1, as explained in Chapter 3 Section (3.5.1)). However, the velocities obtained at similar positions during experiments 2 and 3 highlight that the velocity remains unchanged throughout the test section. This is only achievable when the so-called boundary layer is fully developed (Te Chow 1959).

The results from this study and published data (e.g. Franca et al. 2008) support the assertion that the logarithmic law is valid even above rough-bed flows under relative intermediate submergence conditions.

Figure 4.4 shows a Clauser plot of double averaged streamwise velocity normalised by u_* versus $(Z+z_0)^+$ for experiment 4. The double averaged velocities gathered at 40 randomly selected sample locations are compared with Eq. (2.2) and time-averaged velocity profiles at distances from the flume inlet of x=5.696 m and x=5.985 m. This experiment was carried out under an intermediate relative submergence condition of 15.35 and $u_*=0.030$ m/s, as shown in Figure 4.4. The measurements agree well with Eq. (2.2) when κ and k_s are equal to 0.38 and $1.75d_{50}$, as shown in Table (4.5), as well as with the time-averaged measurements obtained at both x=5.696 m and x=5.985 m from the flume inlet. However, the time-averaged velocity profile at x=5.696 m somewhat deviates from the logarithmic law when $(Z + z_0)^+ \geq 1485$. This could be due to the uncertainty in velocity measurements obtained with ADV near the water surface. All velocity profiles somewhat deviate from the logarithmic law when $(Z + z_0)^+ \leq 1215$ even when the measurements were gathered in a randomised manner and at a higher spatial resolution similar to experiment 1. Such deviation could be due to the gravel particles in experiment 4 being larger in diameter than that in experiment 1 leading to higher k_s in experiment 4 compared to experiment 1 (see Table 3.2 and Table 4.1). Thus, indicating that a high level of bed friction occurs in experiment 4 which could result in the decrease in the obtained velocities near the bed.

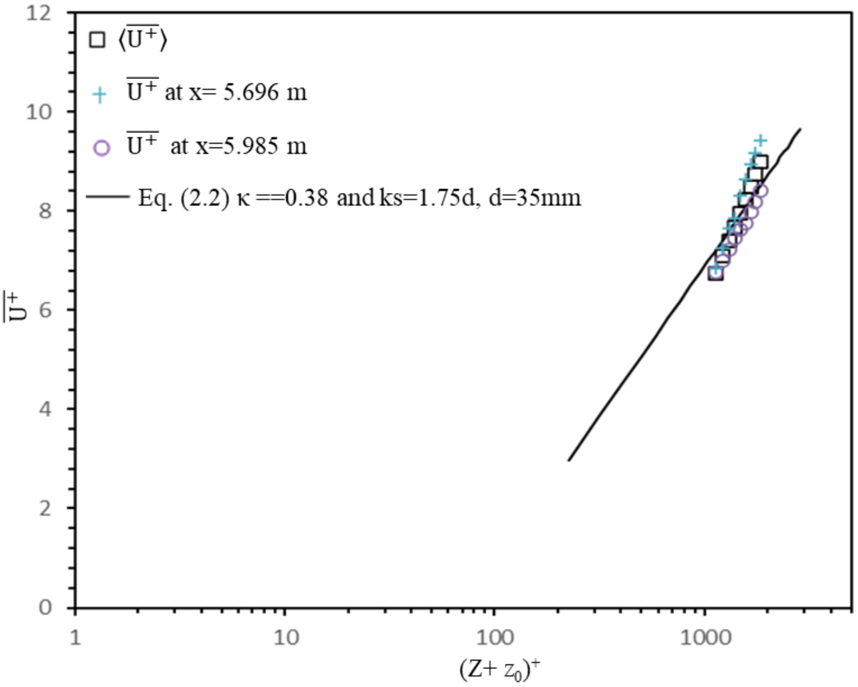

Figure 4.4. Double averaged and time-averaged streamwise velocity profiles were obtained from an experimental case above a natural gravel-bed of k_s=1.75d_{50}, d_{50}=35 mm, Q=0.004 m^3/s. $\overline{U^+} = \langle \bar{u} \rangle / u_*$ and $(Z + z_0)^+ = (Z + z_0)u_*/\upsilon$. Note: x is the distance from flume inlet.

Table 4.5. The parameters of Eq. (2.2) were obtained after five iterations for experiment 4.

z_0 (mm)	κ	k_s	R^2	reason
3.0	0.34	1.30d	0.93	The measurements deviate from Eq.(2.2)
4.00	0.35	1.40d	0.93	The measurements deviate from Eq.(2.2)
5.00	0.36	1.50d	0.93	The measurements deviate from Eq.(2.2)
6.00	0.37	1.60d	0.93	The measurements deviate from Eq.(2.2)
7.50	0.38	1.75d	0.94	The best-fit measurements with Eq.(2.2)

The double averaged velocity distributions and time-averaged velocity profiles agree well with each other and with Eq. (2.2) when κ changes from 0.38 to 0.4 and k_s varies between 1.32d_{50} and 2.75d_{50}, for all experiments conducted above natural gravel-beds.

Previously, it has been reported that κ tends to decrease as porosity increases (Nezu 1977). This appears at odds with that found here, where κ was found to be 0.38 for experiment 4 with a porosity of 31% and 0.38 to 0.4 for experiments 1, 2, 3 with a porosity of 36%. There is some uncertainty in the value of κ due to the number of velocity samples (6-11 points) measured in depth for each profile. Velocity profiles will be convenient to find parameters of logarithmic law when an increasing number of velocity samples in depth. However, velocity measurements obtained with ADV do have a higher resolution than that obtained with hot-film velocimeters as used by Nezu (1977). The relationship where κ decreases with increasing Re_k is consistent with that found by Fang et al. (2018).

Due to the limitations of ADV, measurements could not be gathered throughout the flow depth for the experiments discussed here, this is especially acute in the near-bed region. As illustrated in Table 3.2 and Table 4.1, all four experiments were carried out under intermediate relative submergence conditions ranging from 10.47 to 15.35. This means the flow includes both form-induced and interfacial sub-layers. It has been pointed out that the existence of a logarithmic layer is questionable above rough-bed open-channel flows with low and intermediate relative submergence (Nikora et al. 2001; Pokrajac et al. 2006). However, a well-described logarithmic layer was detected within the intermediate flow area, where Z/H is approximately between 0.20 and 0.80 (Franca et al. 2008). Such a conclusion agrees well with the present study, where it was found that the logarithmic law is valid when $(Z+ z_0)^+$ is in the range 421 to 2958, or Z/H is between 0.310 and 0.732 under intermediate relative submergence conditions.

According to the calculated roughness Reynolds number for experiments 1, 2 and 3 of 1555, 1085 and 898, respectively, the flow can be considered fully turbulent as the roughness Reynolds number is greater than 70. The variance in the roughness Reynolds number across these experiments may be the reason for the various k_s and κ values that were found here. Thus, it can be concluded that there are two important dimensionless factors that dominate the effect of the rough wall on turbulent boundary layers. The first parameter is the roughness Reynolds number K^+, which indicates the impact of the roughness on the buffer layer. The second factor is the ratio of the boundary layer thickness to the roughness height, which defines whether a logarithmic layer develops (Jimenez 2004).

The data presented in this study agree well with the logarithmic law velocity profile under intermediate relative submergence flow conditions. However, a previous study examining similar conditions above a gravel-bed highlighted the fact that there is some uncertainty as to whether a double averaged velocity distribution should follow the logarithmic equation (Mohajeri et al. 2015). Furthermore, studies have focused extensively on the validation of the logarithmic law under high relative submergence flow conditions. Indeed, the logarithmic law might be applicable to double averaged velocity profiles, as mentioned in a study by Nikora et al. (2001), but further work is clearly needed to elucidate this matter under intermediate relative submergence flow conditions.

There are some essential differences between experiment 4 and experiments 1, 2, and 3. The bed sediment in experiment 4 is larger than the three previous experiments and thus has a different standard deviation of bed elevations, porosity and zero-displacement distance. Even so, k_s was found to be similar to experiment 2 at $1.75d_{50}$ and κ was found to be 0.38, which is again similar to that found for experiment 2 at 0.39. However, k_s for experiment 4 differs from that found for experiments 1 and 3. A probable explanation is that both hydraulic conditions and roughness features govern the behaviour of the theoretical equation. Moreover, the measurement distance from the bed in experiment 4 is somewhat higher than in the three earlier experiments.

A previous study observed that the velocity distribution follows the logarithmic equation when the width/flow depth ratio (B/H_{max}) was less than 4.5 (Ferro 2003). When $B/H_{max}>4.5$, secondary flow effects reduce, flow in the open-channel becomes more 2D and thus the maximum velocity will occur at the free surface (Kironoto and Graf 1994). The ratio of maximum to surface flow velocity also decreases with an increasing B/H_{max} (Ferro 2003). The data reported here was carried out with B/H_{max} less than 3.660 and agrees with this finding.

The theoretical velocity profile calculated using Eq. (2.2) was compared with that measured for experiment 5 above an artificial bed with intermediate relative submergence of 19.69, in a similar manner to experiment 1, as shown in Table 4.6.

Table 4.6. The parameters of Eq. (2.2) were obtained after five iterations for experiment 5.

z_0 (mm)	κ	k_s	R^2	reason
1.50	0.36	$0.04d_{50}$	0.90	The measurements deviate from Eq. (2.2)
2.50	0.37	$0.05d_{50}$	0.91	The measurements deviate from Eq. (2.2)
3.50	0.38	$0.10d_{50}$	0.91	The measurements deviate from Eq. (2.2)
4.50	0.39	$0.15d_{50}$	0.92	The measurements deviate from Eq. (2.2)
5.60	0.41	$0.2d_{50}$	0.93	The best-fit measurements with Eq. (2.2)

Figure 4.5 displays a Clauser plot of double averaged streamwise velocity normalised by u_* versus $(Z+z0)^+$ for experiment 5. The double averaged velocities of the velocity profiles gathered within the test section at 40 randomly selected sample

locations, as well as velocities obtained at five randomly selected sample locations within the U/S and D/S regions of the flume are shown in Figure 4.5.

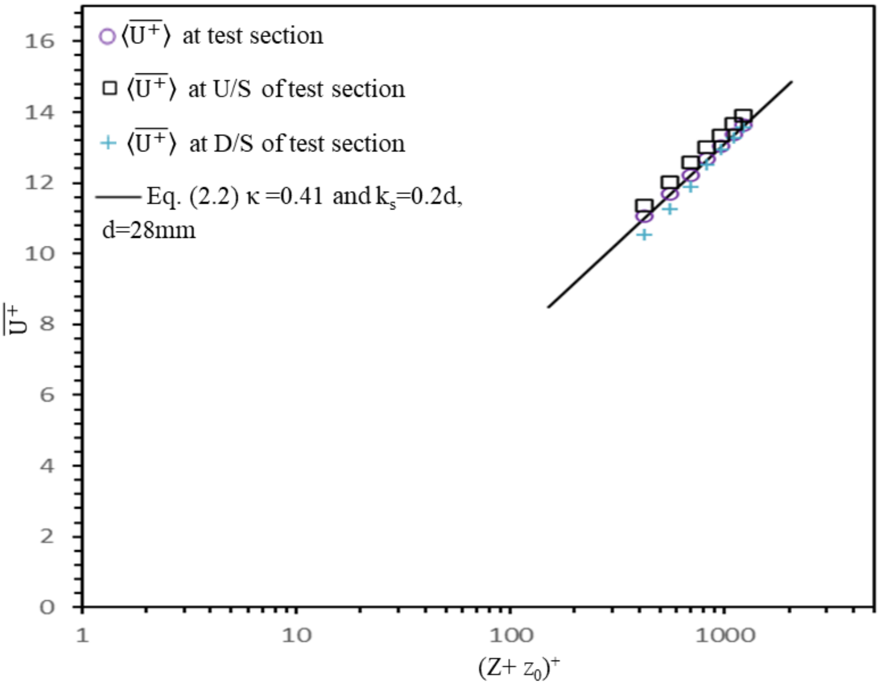

Figure 4.5. Double averaged and time-averaged streamwise velocity profiles were obtained from an experimental case above an artificial bed where k_s=0.2d_{50}, d_{50}=28 mm, Q=0.006 m^3/s in the test section as well as Up-Stream of the test section (U/S) and Down-Stream of the test section (D/S). $\overline{U^+} = \langle \bar{u} \rangle / u_*$ and $(Z + z_0)^+ = (Z + z_0)u_*/\upsilon$.

It can be clearly seen in Figure 4.5 that the velocity profiles in the test section region agree well with Eq. (2.2), but the velocity profiles in the U/S and D/S areas deviate somewhat from Eq. (2.2) when $(Z+z_0)^+ \leq 556.2$. The reason will be discussed later in this section. The best fit between measurements and that given by Eq. (2.2) was achieved when κ, von Karman's constant, equalled 0.41, k_s, the Nikuradse equivalent sand roughness, equalled 0.2d_{50}, and z_0, the zero-displacement distance equalled 5.6 mm.

Figure 4.6 shows a Clauser plot of double averaged streamwise velocity normalised by u_* versus $(Z+z_0)^+$ for experiment 6. It can be seen in Figure 4.6 that the double averaged velocities obtained from measurements gathered at 40 randomly selected sample locations within the test section are largely congruous with that obtained at five randomly selected sample locations within the U/S and D/S regions of the flume as well as Eq. (2.2).

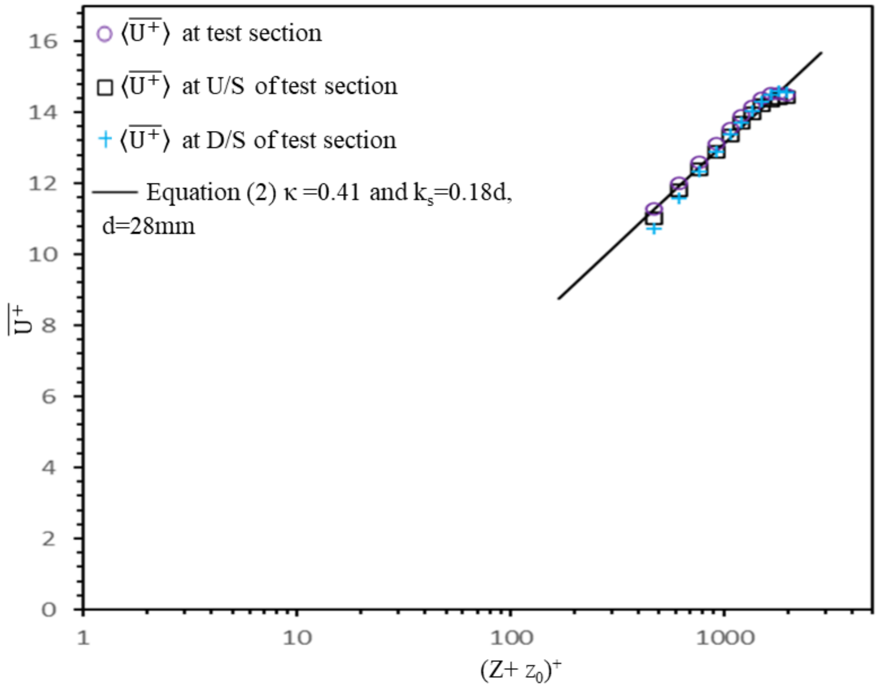

Figure 4.6. Double averaged and time-averaged streamwise velocity profiles were obtained from an experimental case above an artificial bed where d_{50}=28 mm, Q=0.009 m^3/s $k_s=0.18d_{50}$. $\overline{U^+} = \langle\bar{u}\rangle/u_*$ and $(Z + z_0)^+ = (Z + z_0)u_*/\upsilon$.

However, when $(Z+z_0)^+ \geq 1872.555$, velocity measurements deviate from Eq. (2.2). This occurs because experiment 6 was carried out under high relative submergence of 24.67 and might be indicative of the end of the logarithmic layer. This would appear to follow the velocity defect law. Wang et al. (2001) found similar results and explained that the velocity profile deviates from the logarithmic law due to the aspect ratio of the flume. In a similar trend to experiment 5, both velocity profiles in the U/S and D/S regions deviate from Eq. (2.2) when $(Z+z_0)^+ \leq 618.000$. This could be due to the porous beds being highly resistant to flow (Navaratnam et al. 2018). The best fit between measurements and the logarithmic law was found when κ, von Karman's constant was set to 0.41, and k_s equalled $0.18d_{50}$, as shown in Table (4.7).

Table 4.7. The parameters of Eq. (2.2) were obtained after five iterations for experiment 6.

z_0 (mm)	κ	k_s	R^2	reason
1.50	0.36	0.04d	0.89	The measurements deviate from Eq. (2.2)
2.50	0.37	0.05d	0.90	The measurements deviate from Eq. (2.2)
3.50	0.38	0.10d	0.90	The measurements deviate from Eq. (2.2)
4.50	0.39	0.15d	0.91	The measurements deviate from Eq. (2.2)
5.60	0.41	0.18d	0.92	The best-fit measurements with Eq. (2.2)

The artificial bed surface had a more uniform arrangement than the natural gravel-bed, and the zero-displacement distance was found to be 5.6 mm for both experiment´s 5 and 6, whereas the zero-displacement distance was found to vary for each experiment from 1 to 3. This could be due to the particles of the artificial bed protruding less into the flow than the particles of the natural gravel-bed. The zero-displacement distance varies across the six different experiments presented here by approximately 25% due to differences in the bed topography and by 14% due to differences in the hydraulic conditions.

Von Karman's constant κ was found to be 0.41 for both experiments 5 and 6. These findings contrast with the data reported by Han et al. (2017), who found κ to be equal to 0.286. The κ varies across the six different experiments presented here by approximately 5% due to differences in the hydraulic conditions and by 7% due to differences in the bed topography.

Again the value of k_s for both experiments 5 and 6 was found to be $0.18d_{50}$ and $0.2d_{50}$, respectively and this is in contrast with the findings of Wilson (1989) and Whiting and Dietrich (1990), who found k_s of $3d_{50}$. Even though velocity distributions in such flows diverge considerably from the logarithmic equation, it has also been demonstrated that k_s considerably varies with the concentration of bed roughness elements (Wiberg and Smith 1991). Both Figure 4.5 and Figure 4.6 show that average velocity is constant throughout the flume channel with velocity profiles in the test section and the U/S and D/S regions of the flume coinciding with each other for both experiments.

The zero-displacement distance for all experiments conducted here approximates the hydraulic roughness assumption equal to $((\sigma_b+d_{50})/2)$. Such assumption may be adequate to describe the hydraulic roughness of the boundary, as suggested by Smart (1999), based on the results of fitting the logarithmic law to measured data obtained in this study.

The data reported here also show that k_s decreases with increasing Reynolds number (see Table 3.2 and Table 4.1). The relationship between Re_R number and k_s could be related to the bed configuration, such as the size and shape of bed particles as well as the space between elements. It was found that the k_s changes linearly with the flow Reynolds number (Horoshenkov et al. 2013). The k_s varies across the six different experiments presented here by approximately 52% due to hydraulic conditions and by 91% due to differences in the bed topography.

Moving on now to compare streamwise velocity profiles above the natural and acrylic beds investigated here as well as that found in the literature, as shown in Figure 4.7. It is interesting in Figure 4.7 that the velocity profiles above the natural gravel-beds are significantly shifted downwards from the velocity profiles above the artificial bed as well as that found in the literature with the exception of Wang et al. (2012). Wang et al. (2012) carried out their experimental study with K^+=1432 and Fr=0.21 which approximate that conducted for experiments 1-3 in this study (see Table 3.2 and Table 4.1). Thus, this may be the reason experiments 1-3 agree with the velocity profile obtained by Wang et al. (2012).

It was found that the logarithmic velocity profile was valid under the subcritical flow in a boundary layer. However, a thin logarithmic layer appears when the flow is supercritical flow. Thus, k_s could be a function of Fr (Sumer et al. 1996; Smart 1999; Camenen et al. 2006). The k_s is known to play a role in shifting the velocity distribution up or down. However, the slope of the velocity profile obtained by Wang et al. (2012) differs from the slope of the velocity profiles in this study. This is could be due to the gravel particle size (40 mm) they used or the Reynolds number (42,012) the experiments were conducted under which are both larger than that in this study.

The double averaged streamwise velocity profiles for experiments 5 and 6 agree very well with each other; this is probably due to K^+ and Fr both being very similar at 151 and 0.314 for experiment 5, respectively and 153 and 0.334 for experiment 6, respectively. Such results somewhat agree with that found by Manes et al. (2007), who applied a similar flow depth to that used here in experiment 5. However, the results of the experimental studies by Grass (1971) (K^+=84.7), Grass et al. (1991) (K^+=79.2) and Dancey et al. (2000) (K^+=70) and a numerical study by Bomminayuni and Stoesser (2011) (K^+=95) and Yuan and Jouybari (2018) (K^+=78) are all significantly shifted upwards from the double averaged streamwise velocity profiles above the natural gravel-beds, yet only slightly shifted upwards from the double averaged velocity profiles above the artificial bed.

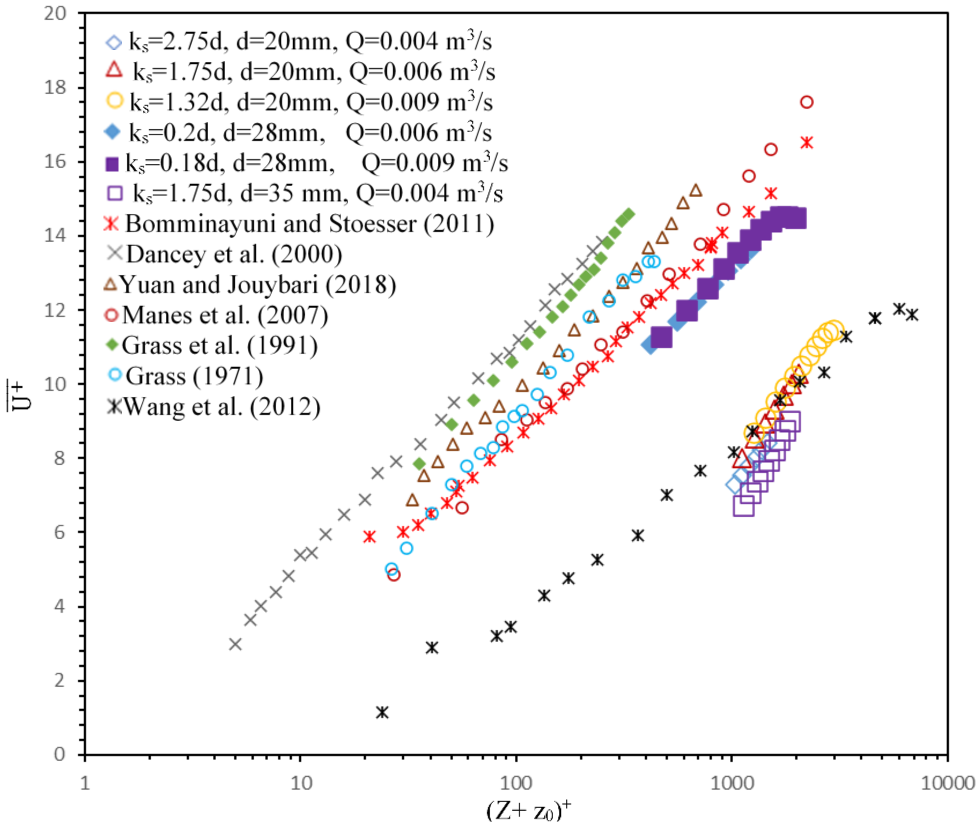

Figure 4.7. Double averaged streamwise velocity profiles were obtained from four experimental cases above natural gravel-bed (open symbols) and two experimental cases above artificial bed (filled symbols), as well as data points of previous experimental and numerical studies found in the literature, where $\langle \overline{U^+} \rangle = \langle \bar{u} \rangle / u_*$ and $(Z + z_0)^+ = (Z + z_0)u_*/\upsilon$.

This is because K^+ is considerably less in these studies than K^+ in experiments 1, 2, 3, and 4, yet somewhat similar to that found for experiments 5 and 6. It has been demonstrated numerically that increased K^+ results in a downwards shift in the average velocity distribution compared to velocity profiles above a smooth bed (Bomminayuni and Stoesser 2011).

Results show that the zero-displacement distance of 5.6 mm for both experiment's 5 and 6 and k_s of $0.2d_{50}$ and $0.18d_{50}$, respectively are lower than that for the natural gravel-beds where z_0 ranges from 6 mm to 7.5 mm and k_s ranges from $1.32d_{50}$ to $2.75d_{50}$ for experiments 1-4.

Furthermore, the significant difference between velocity profiles above the natural gravel-beds and the acrylic bed could be due to the differing relative submergence the experiments were conducted under. Experiment 5 was carried out under near high relative submergence conditions, while experiment 6 was conducted under high relative submergence conditions. However, all experiments above natural gravel-beds were performed under intermediate relative submergence conditions (see Table 3.2 and Table

4.1). Some differences could also be attributed to the particles of the natural gravel-beds protruding more into the flow than the particles of the artificial bed.

The results from this study, in comparison with the literature, support the conclusion that the so-called ‘constants’ of the logarithmic equation are highly significant and non-constant when fitting measured velocities with that obtained from the logarithmic law. These parameters were shown to be a function of bed geometry, such as sediment size, sediment arrangement, the standard deviation of the surface elevations, K^+, as well as the flow conditions, such as flow depth, Re, Fr and so on.

This section has reviewed the key aspects of the validation of the logarithmic law in flows under intermediate and high relative submergence conditions and the role that hydraulic conditions, bed surface geometry, and porosity play.

4.3 Turbulent Stresses

The earlier literature review highlighted that second-order turbulent statistics above the porous beds require further exploration in experimental studies. Therefore, in this section, the second-order turbulent statistics, such as turbulence intensity, Reynolds shear stresses, Reynolds normal stresses, and turbulence kinetic energy are presented. The results of the second-order turbulent statistics are also compared with that found in the wider literature.

4.3.1 Turbulence Intensity

The analytical procedure for obtaining the turbulent intensity from the fluctuations of the instantaneous velocity measurements above the natural gravel-beds and an acrylic bed is described in this section. The exponential decay functions, reported by Nezu and Nakagawa (1993) (see Section 2.3.1), were used to express turbulence intensity in the streamwise, cross-streamwise, and vertical directions, as explained in Chapter 3 Section (3.5.1) and were compared with that found in the literature.

Figure 4.8 presents the double averaged turbulence intensity of the velocity fluctuations in the streamwise direction normalised with shear velocity for all experiments as well as the exponential decay function expressed by Eq. (2.3). It also illustrates some comparisons with the experimental results of Nezu (1977). A least-squares fitting methodology was used to calculate the empirical constants D_1 and λ_1 in

Eq. (2.3) and were found to be 2.00 and 1.10, respectively, with a regression coefficient, R^2 of 0.981.

As Figure 4.8 highlights, $\langle\overline{U_{RMS}}\rangle/u_*$ for experiment 3 agrees particularly well with Eq. (2.3) when Z/H≤0.551, yet deviates by up to 4% when Z/H≥0.551. For experiment 2, $\langle\overline{U_{RMS}}\rangle/u_*$ is also shifted upwards from Eq. (2.3) by approximately 5%, as shown in Figure 4.8. The distribution of the double averaged streamwise turbulence intensity for experiment 6 is shifted downwards by approximately 6% from Eq. (2.3) when Z/H≤ 0.266, but is increasingly shifted downward by up to 10% when Z/H≥0.266. It can be noted from these experiments that turbulence intensity in the streamwise direction does not relate to k_s. This is because the profiles of $\langle\overline{U_{RMS}}\rangle/u_*$ in experiments 1, 4 and 5 agree well with each other even though these experiments have different k_s values.

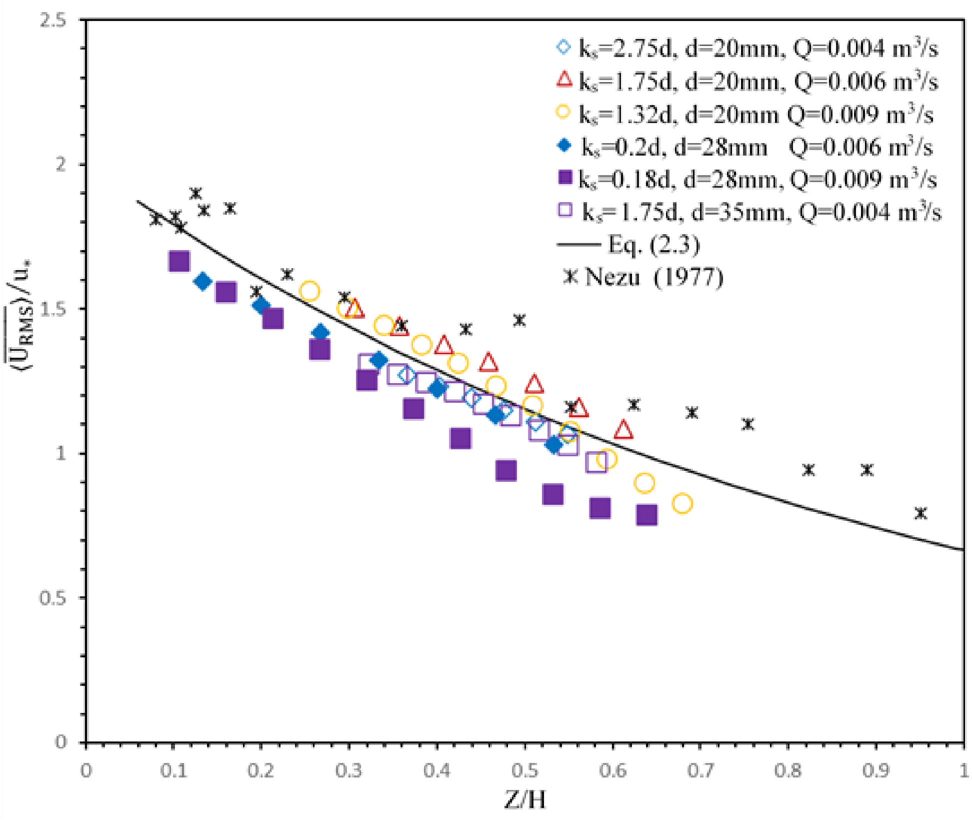

Figure 4.8. Distribution of double averaged streamwise turbulence intensity normalised with shear velocity versus normalised vertical distance for flow above natural gravel-beds obtained from four experimental cases (open symbols) and two experimental cases above an artificial bed (filled symbols) plotted with the exponential decay function as suggested by Nezu and Nakagawa (1993) (solid lines) and data points of previous studies found in the literature.

In addition, $\langle\overline{U_{RMS}}\rangle/u_*$ for both experiments 1 and 4 agree well with Eq. (2.3), but experiment 5 only agrees well with Eq. (2.3) when Z/H≥ 0.333. Overall, the differences between Eq. (2.3) and the turbulent intensity obtained here are acceptable and match the overall trend of linearly decreasing intensity with increased elevation within the water column towards the water surface.

$\langle\overline{U_{RMS}}\rangle/u_*$for both experiments 2 and 3 agree with the results reported by Nezu (1977). Overall, there is a good agreement between $\langle\overline{U_{RMS}}\rangle/u_*$ for all experiments and that reported by Nezu (1977), except for experiment 6, which is shifted downwards by approximately 6% when $Z/H \geq 0.213$. Although the Reynolds number for all experiments in this study (see Table 3.2 and Table 4.1) is higher than that presented by Nezu (1977) or 8,600, in general, the trend exhibited by this research agrees well with the former. A possible explanation for this might be that the Reynolds number does not influence $\langle\overline{U_{RMS}}\rangle/u_*$. The Froude number in the current study ranges from 0.152 and 0.334, as shown in (see Table 3.2 and Table 4.1), while Nezu (1977) had a Fr of 0.160.

The shifting down of the double averaged turbulence intensity in the streamwise direction in experiment 6 might be due to relative submergence. The observations also agree with the results reported by Cooper et al. (2013) and Mohajeri (2014).

The maximum turbulence intensity values are near the bed similar to Strom and Papanicolaou (2007), who stated that the maximum streamwise turbulence intensity occurs at the near-bed interface.

Figure 4.9 presents a comparison between measurements and the $\langle\overline{V_{RMS}}\rangle/u_*$values obtained from Eq. (2.4) versus normalised vertical elevation. Figure 4.9 shows that obtained $\langle\overline{V_{RMS}}\rangle/u_*$ values agree well with Eq. (2.4), when D_2 and λ_2 equal 1.18 and 1.00, respectively (see Table 4.8), with a regression coefficient R^2 of 0.984, for all experiments.

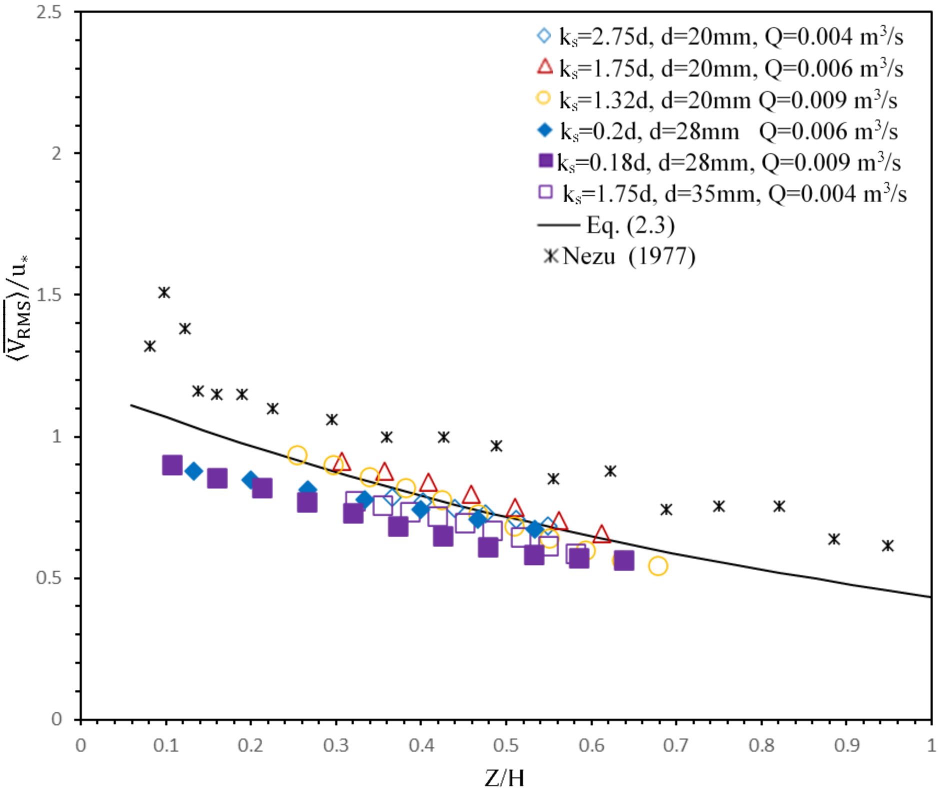

Figure 4.9. Distribution of double averaged cross-streamwise turbulence intensity normalised with shear velocity versus normalised vertical distance for flow above natural gravel-beds obtained from four experimental cases (open symbols) and two experimental cases above an artificial bed (filled symbols) plotted with the exponential decay function as suggested by Nezu and Nakagawa (1993) (solid lines) and data points of previous studies found in the literature.

Figure 4.9 shows that $\langle\overline{V_{RMS}}\rangle/u_*$ for experiment's 5 and 6 deviates from Eq. (2.4) when Z/H≤ 0.333 by approximately 6%, and then agrees well when Z/H≥0.333. Figure 4.9 also presents the findings of Nezu (1977). Similarly to the results of $\langle\overline{U_{RMS}}\rangle/u_*$, the results of $\langle\overline{V_{RMS}}\rangle/u_*$in this study are slightly less than the previous research presented by Nezu (1977). However, the general trend of $\langle\overline{V_{RMS}}\rangle/u_*$ for all experiments agrees well with that found in the literature (Nezu 1977).

The roughness impact might become relatively weak, and this phenomenon was noticed during the comparison of the experimental data with previous studies (for example Nezu 1977) with different $K^{+,}$ and it was found that they agree well with each other independent of the wall roughness. Overall, the study of the effect of K^+ on turbulence intensity is inconclusive. Moreover, the pattern of $\langle\overline{V_{RMS}}\rangle/u_*$ demonstrated in the same way as $\langle\overline{U_{RMS}}\rangle/u_*$coincides with that found in the literature.

Figure 4.10 presents the distribution of the double averaged vertical turbulence intensity compared with the exponential decay function as reported by Nezu and

Nakagawa (1993) and the findings of (Nezu 1977). As shown in Figure 4.10, the measurements of $\langle\overline{W_{RMS}}\rangle/u_*$ for all experiments agree well with values obtained from Eq. (2.5) when D_3 and λ_3 are equal to 0.70 and 1.00, respectively with a regression coefficient R^2 of 0.984, as shown in Table 4.8.

Even though the pattern of $\langle\overline{W_{RMS}}\rangle/u_*$ in both experiments 5 and 6 is similar, but shifted downwards from Eq. (2.3) by approximately 5% when $Z/H \leq 0.333$, they are all shifted downwards considerably compared to the results presented by Nezu (1977). This notable difference in $\langle\overline{W_{RMS}}\rangle/u_*$ could be due to the shear velocity which in this study ranges from 0.027 m/s to 0.034 m/s, which is higher than that of 0.013 m/s in the experimental study by Nezu (1977).

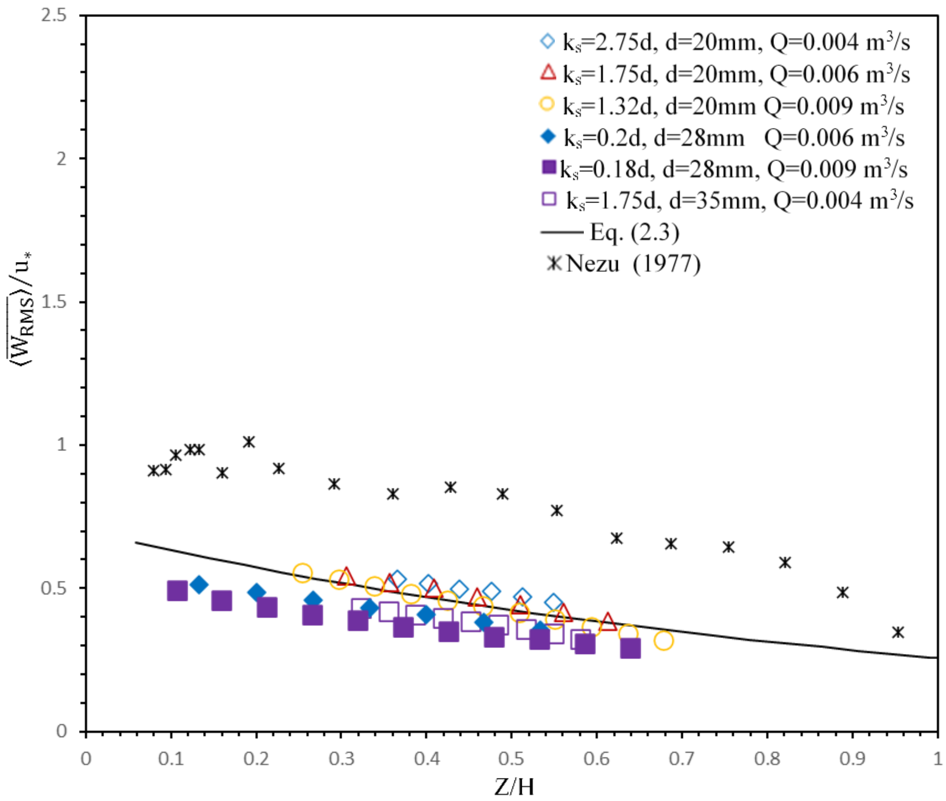

Figure 4.10. Distribution of double averaged vertical turbulence intensity normalised with shear velocity versus normalised vertical distance for flow above natural gravel-beds obtained from four experimental cases (open symbols) and two experimental cases above an artificial bed (filled symbols) plotted with the exponential decay functions as suggested by Nezu and Nakagawa (1993) (solid lines) and data points of previous studies found in the literature.

Table 4.8 shows that D_1 in the present study is slightly less than that obtained by Nezu and Rodi (1986), yet λ_1 is slightly higher than that proposed in most of the literature.

Nezu and Rodi (1986) carried out experiments above a smooth bed and compared their experiments with a database from Grass (1971)**;** an experiment with a spherical glass bed performed by Nakagawa et al. (1975); an experiment with both impermeable spherical rough and smooth open-channel beds by Nezu and Nakagawa (1993); a single layer impermeable rough-bed and a permeable natural gravel-bed by Kironoto and Graf (1994); and an impermeable single layer of spheres to create a rough open-channel bed by Manes et al. (2007).

The relatively small differences between the values obtained here and that found in the literature, as shown in Table 4.8, are likely to be due to the different gravel particle sizes and the degree of roughness employed by the various studies. This is confirmed by the findings of Nikora and Smart (1997).

Table 4.8. Empirical constants for the exponential decay functions of turbulent decay from the present study and various works found in the literature.

Sources	D_1 (−)	D_2 (−)	D_3 (−)	λ_1 (−)	λ_2 (−)	λ_3 (−)	Bed condition(s)
Present study	2.00	1.18	0.70	1.10	1.00	1.00	Rough
Nezu and Rodi (1986)	2.26	-	1.23	0.88	-	0.67	Rough and smooth
Kironoto and Graf (1994)	2.04	-	1.14	0.97	-	0.76	Rough
Manes et al. (2007)	2.2	-	1.14	0.88	-	0.76	Rough

Table 4.8 also shows that D_2 in the present study is slightly less than that obtained by Nezu and Nakagawa (1993), yet λ_2 is highly similar. The difference in D_2 could be because Nezu and Nakagawa (1993) derived the empirical constants of Eq. (2.4) above smooth and impermeable beds and not permeable rough-beds as utilised here. In addition, in Table 4.8, D_3 is clearly less than that found in the literature, yet λ_3 is similar to that found by Nezu and Nakagawa (1993), but higher than the values obtained by Nezu and Rodi (1986), Kironoto and Graf (1994), and (Manes et al. 2007). These constants were found by Nezu and Rodi (1986) during the comparison of turbulent intensities measured above the smooth and rough-bed, and this could be the reason for these differences, as mentioned earlier in this section. Moreover, the explanation of the difference between the present study and Manes et al. (2007), as seen in Table 4.8 could be due to H_{max}/d_{50} being less in this work compared to that obtained by Manes et al. (2007). Also, the present study was performed with highly porous beds, unlike much of the literature which employed impermeable or low permeability beds.

Manes et al. (2007) reported that Nezu and Nakagawa (1993) did not completely determine the behaviour of turbulent intensity close to the bed or the free surface, where turbulent generation and dissipation are not only related to conditions in the turbulent kinetic energy balance function. Variations in the exponential decay functions are especially evident for $\langle\overline{W_{RMS}}\rangle/u_*$, while they appear smaller for $\langle\overline{U_{RMS}}\rangle/u_*$ (Manes et al. 2007). This is consistent with the outcome of the present experimentation where deviations from the exponential decay functions in both $\langle\overline{U_{RMS}}\rangle/u_*$ and $\langle\overline{V_{RMS}}\rangle/u_*$ are less than $\langle\overline{W_{RMS}}\rangle/u_*$.

The general pattern of turbulence intensities for all experiments in the three-component directions decreases toward the water surface, with the highest values at the bed surface.

This section began by describing the pattern of double averaged turbulent intensity and comparing that with the exponential decay functions as well as the literature. It went on to suggest that the double averaged turbulent intensity in the streamwise direction could be reduced depending on the K^+ value. The influence of porosity and shear velocity possibly has a greater effect on the double averaged turbulence intensities, especially in the vertical direction. However, relative submergence might also affect the double averaged turbulence intensities, particularly in the streamwise direction. The results from this study confirm $\langle\overline{U_{RMS}}\rangle/u_*$ > $\langle\overline{V_{RMS}}\rangle/u_*$ > $\langle\overline{W_{RMS}}\rangle/u_*$ similar to Nezu and Nakagawa (1993).

4.3.2 Reynolds Shear Stress

In this section, the normalised double averaged Reynolds Shear Stress $\langle\overline{RSS}\rangle$ is presented as $\rho\langle\overline{u_{RMS}}\rangle\langle\overline{w_{RMS}}\rangle/u_*^2$ for experiments above both natural gravel-beds and an artificial bed conducted here as well as that found in the literature. Figure 4.11 presents $\rho\langle\overline{u_{RMS}}\rangle\langle\overline{w_{RMS}}\rangle/u_*^2$ against normalised vertical elevation from the bed surface obtained from this study as well as the results of Mohajeri et al. (2016) for comparison. It shows that $\langle\overline{RSS}\rangle$ for experiment's 1 and 2 is approximately 10% greater than that found in experiment's 4 and 5 and is approximately 15% greater than that found in experiment 6. Moreover, the $\langle\overline{RSS}\rangle$ profile for experiment 3 agrees with both experiment's 1 and 2 when $Z/H \leq 0.508$, but changes to agree more closely with experiment's 4 and 5 when $Z/H \geq 0.508$. The different patterns of the $\langle\overline{RSS}\rangle$ profile for experiment 3 could be due to the aspect ratio, which in experiment 3 is lower than in other experiments (see Table 3.2 and Table 4.1).

Even though experiment's 5 and 6 were carried out using the same bed, the $\langle\overline{RSS}\rangle$ values are approximately 8% less in experiment 6 than in experiment 5 and are likely due to being performed under high relative submergence flow conditions. Figure 4.11 also shows that profiles of $\rho\langle\overline{U_{RMS}W_{RMS}}\rangle/u_*^2$ for experiments’1, 2 and 3 agree well with the findings of Mohajeri et al. (2016) when Z/H≥0.336, as shown in Figure 4.11.

Furthermore, the observations of $\langle\overline{RSS}\rangle$ for experiments’ 4 and 5 agree well with that found by Mohajeri et al. (2016) when Z/H≥0.400, as demonstrated in Figure 4.11. $\rho\langle\overline{U_{RMS}W_{RMS}}\rangle/u_*^2$ for experiment 6 agrees with the published works (e.g. Mohajeri et al. 2016) when Z/H≤ 0.213 and then shifts downward by approximately 15% until Z/H≥ 0.585.

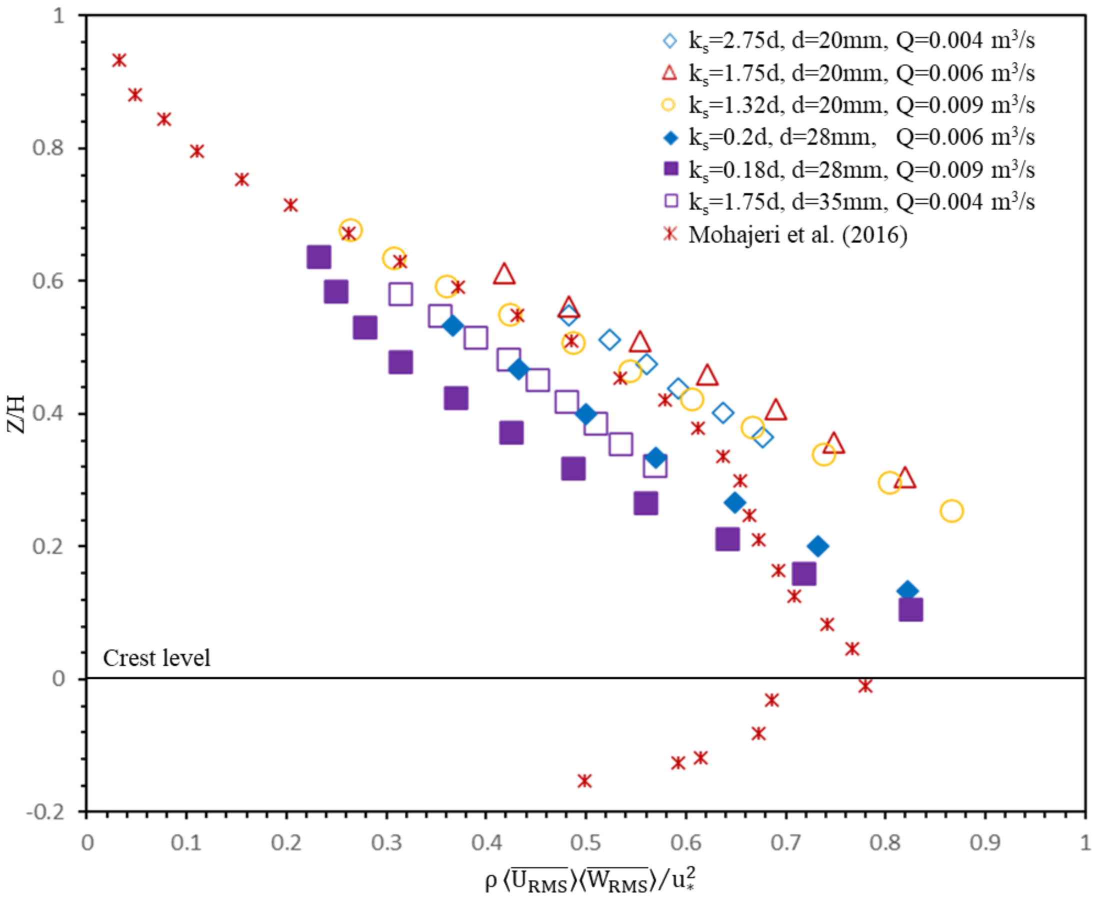

Figure 4.11. Vertical distribution of double averaged normalized Reynolds shear stress for flow above natural gravel-beds obtained from four experimental cases (open symbols) and above an artificial bed obtained from two experimental cases (filled symbols) as well as the data of Mohajeri et al. (2016).

The general trend where $\rho\langle\overline{U_{RMS}W_{RMS}}\rangle/u_*^2$ decreases linearly with increased elevation within the water column is evident for all experiments with the highest values near the bed when Z/H≤ 0.366 and the lowest values near the water surface as expected (Manes et al. 2007; Bomminayuni and Stoesser 2011; Mohajeri et al. 2016; Sarkar et al. 2016; Cameron et al. 2017; and Fang et al. 2018). As illustrated in Figure 4.11, the values of $\langle\overline{RSS}\rangle$ are increasingly shifted downwards as relative submergence increases.

Although the K^+ value in experiments 3-5 (see Table 3.2 and Table 4.1) is different to that found in the studies by Mohajeri et al. (2016) (K^+=250), the double averaged RSS for experiments 3, 4, and 5 are similar to these experiments. The analysis shows that relative submergence may affect the formation of $\langle\overline{\mathrm{RSS}}\rangle$. These findings are contrary to Krogstad and Antonia (1999), who showed experimentally that the bed surface geometry substantially influences the turbulent features of the flow, such as turbulent Reynolds stresses. It can be noted from Figure 4.11 that both experiments 4 and 5 agree well with each other even though they were carried out above different beds. It could be due to these experiments having the same porosity. It was found that the characteristics of porosity affects the Reynolds stresses of turbulent flow (Mendoza and Zhou 1992).

It should be pointed out that Mohajeri et al. (2016) performed three experiments above the same bed with different hydraulic conditions. In their third experiment, they found that $\langle\overline{\mathrm{RSS}}\rangle$ was approximately 2% less than their other two experiments near the bed and water surface. It is their third experiment that is shown in Figure 4.11.

Experiment's 5 and 6 were carried out with an almost constant Fr above the same bed, but the flow depth in experiment 5 is less than in experiment 6, resulting in the double averaged RSS for experiment 5 deviating from that found for experiment 6. The observations also agree with the results reported by Aberle et al. (2008), who found Reynolds stresses rely on water depth for fully turbulent flow conditions above rough-beds.

It should also be pointed out that for all the experiments in this study, measurements were only taken in 70% of the water column due to the limitations of the equipment used, whereby an ADV cannot collect data very close to a rough surface. In contrast, measurements in the literature cover the entire flow depth by employing PIV.

The outcome of the various experiments conducted here shows that relative submergence and porosity result in Reynolds shear stress variations, but the effects of varying K^+ is insignificant.

4.3.3 Reynolds Normal Stress

The streamwise, cross-streamwise, and vertical Reynolds normal stress $\langle\overline{\mathrm{RNS}}\rangle$, normalised with shear stress, are expressed as $\rho\langle\overline{\mathrm{U_{RMS}}}\rangle^2/\mathrm{u}_*^2$, $\rho\langle\overline{\mathrm{V_{RMS}}}\rangle^2/\mathrm{u}_*^2$, and $\rho\langle\overline{\mathrm{W_{RMS}}}\rangle^2/\mathrm{u}_*^2$, respectively.

The profiles of double averaged $\langle\overline{\mathrm{RNS}}\rangle$ in the streamwise direction are plotted against vertical distance above the natural gravel-beds and the artificial bed and are compared with the experimental results of Sarkar et al. (2016), as shown in Figure 4.12. The experimental study carried out by Sarkar et al. (2016) was conducted under uniform flow above a natural gravel-bed not dissimilar to that employed in this study.

In general, $\langle\overline{\mathrm{RNS}}\rangle$ is greatest for all experiments when $Z/H \leq 0.366$, i.e., near the gravel particle crests, and reduces towards the water surface. This behaviour is in agreement with Dey and Das (2012) and Sarkar et al. (2016). Figure 4.12 shows that experiment 1 is identical to experiment 4, even though their beds are different. This might be due to both experiments being conducted with approximately the same shear velocity and k_s/H_{max}. Experiment 3 agrees well with experiment 2 when $Z/H \leq 0.459$ and is also identical to that of experiment's 1, 4 and 5 when $Z/H \geq 0.484$. Additionally, the suddenly decreasing $\rho\langle\overline{U_{RMS}}\rangle^2/u_*^2$ in experiment 3 may be due to the aspect ratio.

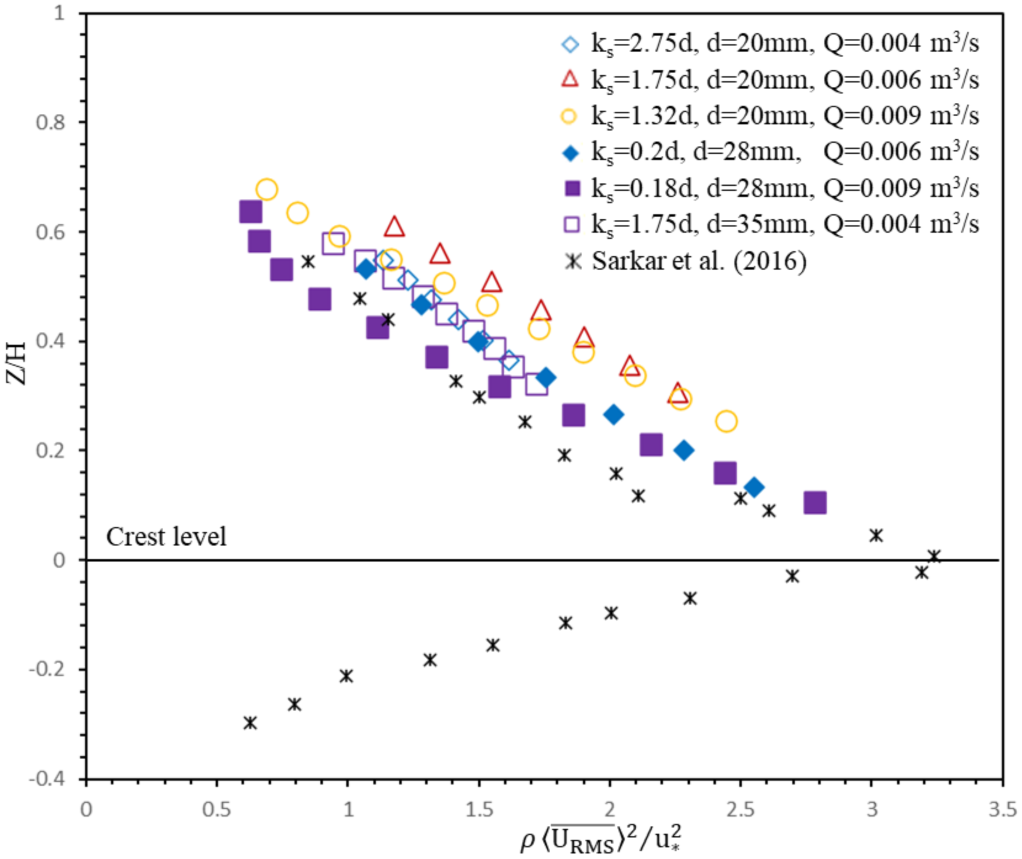

Figure 4.12. Vertical distribution of double averaged normalised streamwise Reynolds normal stress for flow above natural gravel-beds obtained from four experimental cases (open symbols) and above an artificial bed obtained from two experimental cases (filled symbols), as well as the data points of Sarkar et al. (2016).

In experiment 6, $\rho\langle\overline{U_{RMS}}\rangle^2/u_*^2$ suddenly increases near the water surface, but there may be several reasons for this phenomenon. For example, it has been shown (Auel et al. 2014) that this phenomenon can be attributed to the large flow fluctuations that occur near the free surface. It could also be the result of measurement uncertainties within the instantaneous velocity fluctuations found near the water surface due to the ADV instrument. In addition, experiment 6 was carried out under high relative submergence, and the water surface could affect turbulent stresses, i.e. in general, the spatial structure of the water surface waves is correlated with the energy dissipation by the turbulent flow above gravel-beds (Horoshenkov et al. 2013). Figure 4.12 also shows the profile of $\rho\langle\overline{U_{RMS}}\rangle^2/u_*^2$ obtained by Sarkar et al. (2016) is approximately 20% less than that found for experiment 2, and similarly for experiment 3 when $Z/H \le 0.593$. In addition, the profiles of $\rho\langle\overline{U_{RMS}}\rangle^2/u_*^2$ for experiments 1, 4, and 5 agree well with the findings of Sarkar et al. (2016) when $Z/H \le 0.113$, and they are approximately 5% higher than that of Sarkar et al. (2016) when $Z/H \ge 0.113$, as shown in Figure 4.12. In contrast, the profile of $\rho\langle\overline{U_{RMS}}\rangle^2/u_*^2$ for experiment 6 agrees well with the results of Sarkar et al. (2016).

Turning now to the profiles of double averaged $\langle\overline{RNS}\rangle$ in the cross-streamwise direction, Figure 4.13 shows that experiment 2 agrees somewhat with the findings of Sarkar et al. (2016). However, the results of Sarkar et al. (2016) are approximately 8% higher than the double averaged $\langle\overline{RNS}\rangle$ for all other experiments.

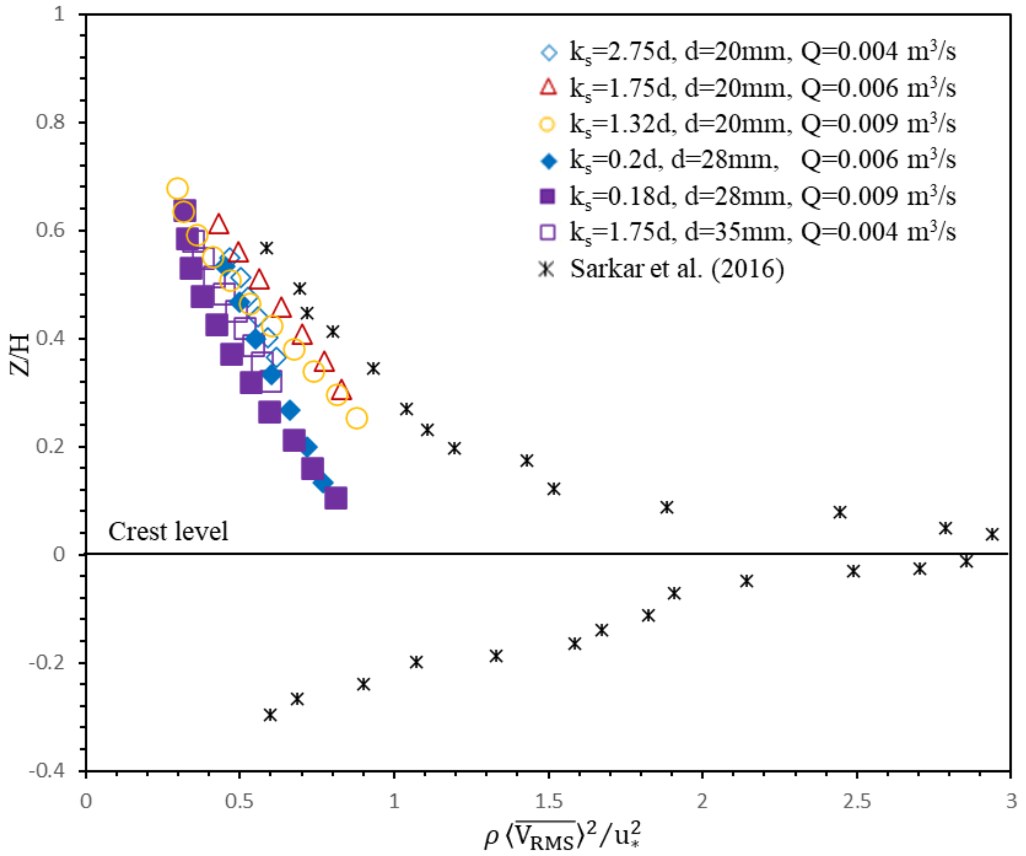

Figure 4.13. Vertical distribution of double averaged normalised cross-streamwise Reynolds normal stress for flow above natural gravel-beds obtained from four experimental cases (open symbols) and above an artificial bed obtained from two experimental cases (filled symbols), as well as the data points of Sarkar et al. (2016).

In general, the small differences in $\rho\langle\overline{U_{RMS}}\rangle^2/u_*^2$ and $\rho\langle\overline{V_{RMS}}\rangle^2/u_*^2$ among all the experiments are as expected since they were conducted above different beds and under different hydraulic conditions.

Figure 4.14 shows vertical $\langle\overline{RNS}\rangle$ against normalised vertical elevation from the bed surface above natural gravel-beds and an artificial bed in comparison with the experimental results of Sarkar et al. (2016). The profiles of $\rho\langle\overline{W_{RMS}}\rangle^2/u_*^2$ increase linearly towards the bed surface for all experiments similar to Sarkar et al. (2016), as illustrated in Figure 4.14. The same trend was found by Nikora et al.(2001), Mignot et al. (2009a), Dey and Das (2012), and Mohajeri et al. (2016). However, the profiles of $\rho\langle\overline{W_{RMS}}\rangle^2/u_*^2$ obtained by Sarkar et al. (2016) deviate significantly from that found in this study. $\rho\langle\overline{V_{RMS}}\rangle^2/u_*^2$ values obtained here are considerably less than that obtained by Sarkar et al. (2016) when Z/H≤0.196. This is likely due to the fact that the experiment performed by Sarkar et al. (2016) featured a range of obstacles on top of the rough-bed which led to flow separation in the wake of such elements. In addition, it was found that

$\rho\langle\overline{U_{RMS}}\rangle^2/u_*^2$, $\rho\langle\overline{V_{RMS}}\rangle^2/u_*^2$, and $\rho\langle\overline{W_{RMS}}\rangle^2/u_*^2$ reveal a tendency of growing variation in the near-bed zone with increasing submergence (Cameron et al. 2017).

The difference in the profiles of $\rho\langle\overline{W_{RMS}}\rangle^2/u_*^2$ for experiment's 4, 5-6 above the natural gravel-bed and the artificial bed, respectively is very small. This could be due to the porosity in experiment 4 of 31% approximating the porosity of both experiments 5 and 6 of 32%. The difference in the profiles of $\rho\langle\overline{W_{RMS}}\rangle^2/u_*^2$ for experiment's 1- 3 above natural gravel-beds with a d_{50}=20 mm particle diameter is also very small as they were all conducted above the same bed surface. It appears that vertical $\langle\overline{RNS}\rangle$ could be more sensitive to gravel size, porosity, and bed topography than in the other component directions. This could be related to the bed topography, as suggested by previous studies (Mohajeri et al. 2016). In general, the highest values of the vertical direction $\langle\overline{RNS}\rangle$ are when $Z/H \leq 0.366$ for all experiments.

In summary, it has been shown from this analysis that profiles of $\langle\overline{RNS}\rangle$ in the three component directions decrease linearly toward the water surface, and the findings of this study and published works (e.g. Dey and Das 2012) confirm $\rho\langle\overline{U_{RMS}}\rangle^2/u_*^2 > \rho\langle\overline{V_{RMS}}\rangle^2/u_*^2 > \rho\langle\overline{W_{RMS}}\rangle^2/u_*^2$. Thus, both $\rho\langle\overline{U_{RMS}}\rangle^2/u_*^2$ and $\rho\langle\overline{V_{RMS}}\rangle^2/u_*^2$ contribute to the total TKE more than $\rho\langle\overline{W_{RMS}}\rangle^2/u_*^2$ (Sarkar et al. 2016). The hydraulic conditions, such as k_s/H_{max}, shear velocity, and aspect ratio, are found to have little effect on the distribution of $\langle\overline{RNS}\rangle$. Moreover, the gravel particle size, bed topography, and porosity are shown to effect $\langle\overline{RNS}\rangle$, especially in the vertical direction.

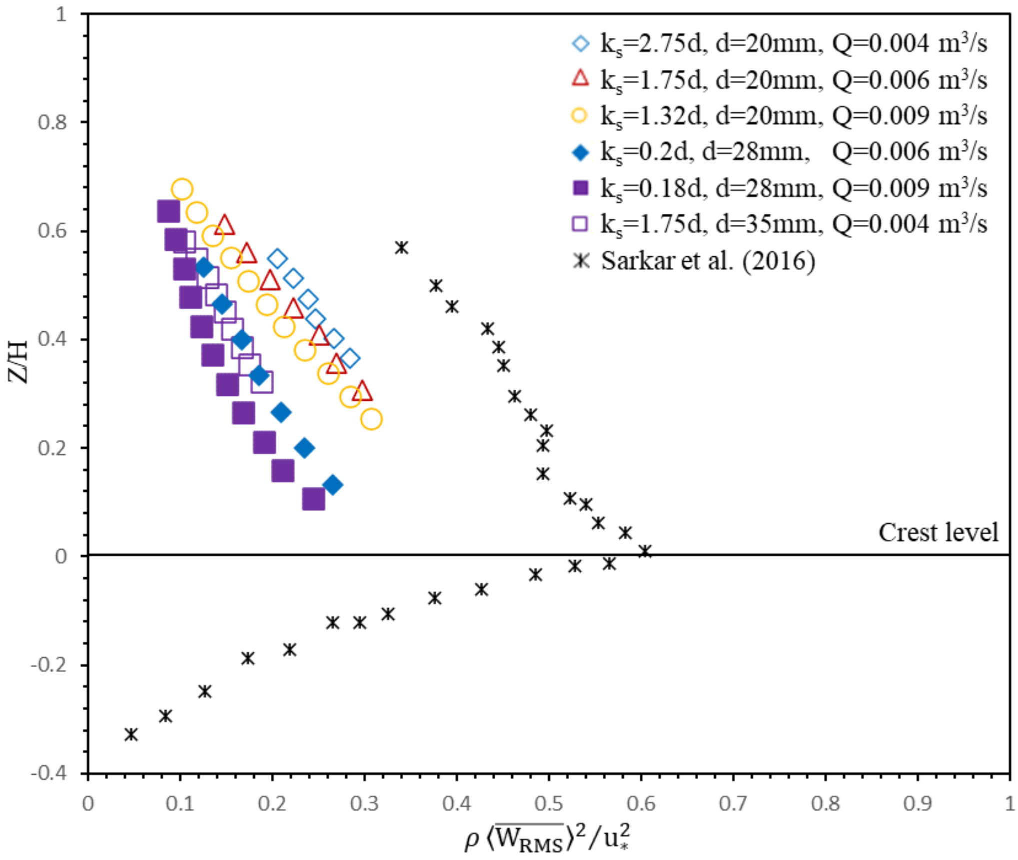

Figure 4.14. Vertical distribution of double averaged normalised vertical Reynolds normal stress for flow above natural gravel-beds obtained from four experimental cases (open symbols) and above an artificial bed obtained from two experimental cases (filled symbols), as well as the data points of Sarkar et al. (2016).

4.3.4 Turbulence Kinetic Energy (TKE)

The double averaged Turbulence Kinetic Energy $\langle \overline{TKE} \rangle$ for each experiment is presented and discussed in this section. Figure 4.15 shows $\langle \overline{TKE} \rangle$ for experiments above natural gravel-beds and an artificial bed against normalised elevation from the bed surface. The highest $\langle \overline{TKE} \rangle$ exists near the bed for all experiments, and measurements for experiment 2 coincide with measurements for experiment 3 within the near-bed region. However, when Z//H≥ 0.459, the results of experiment 2 then deviate from the measurements for experiment 3. The results for both experiments 1 and 3 coincide with each other but experiment 3 and 4 are notably different when Z/H≤ 0.459. The d_{50}=20 mm diameter gravel particle experiments have approximately 8% more $\langle \overline{TKE} \rangle$ than the artificial bed. Despite experiment's 1-3 being performed above the same roughness surface, the $\langle \overline{TKE} \rangle$ profiles shown in Figure 4.15 are distinctly different. The $\langle \overline{TKE} \rangle$ is markedly higher in experiment 5 than in experiment 6 when $Z/H \geq 0.319$, while they approximately agree when $Z/H \leq 0.319$, as shown in Figure 4.15. These differences among the profiles of $\langle \overline{\mathrm{TKE}} \rangle$ above the same bed might be due to the differences in relative submergence between each experiment.

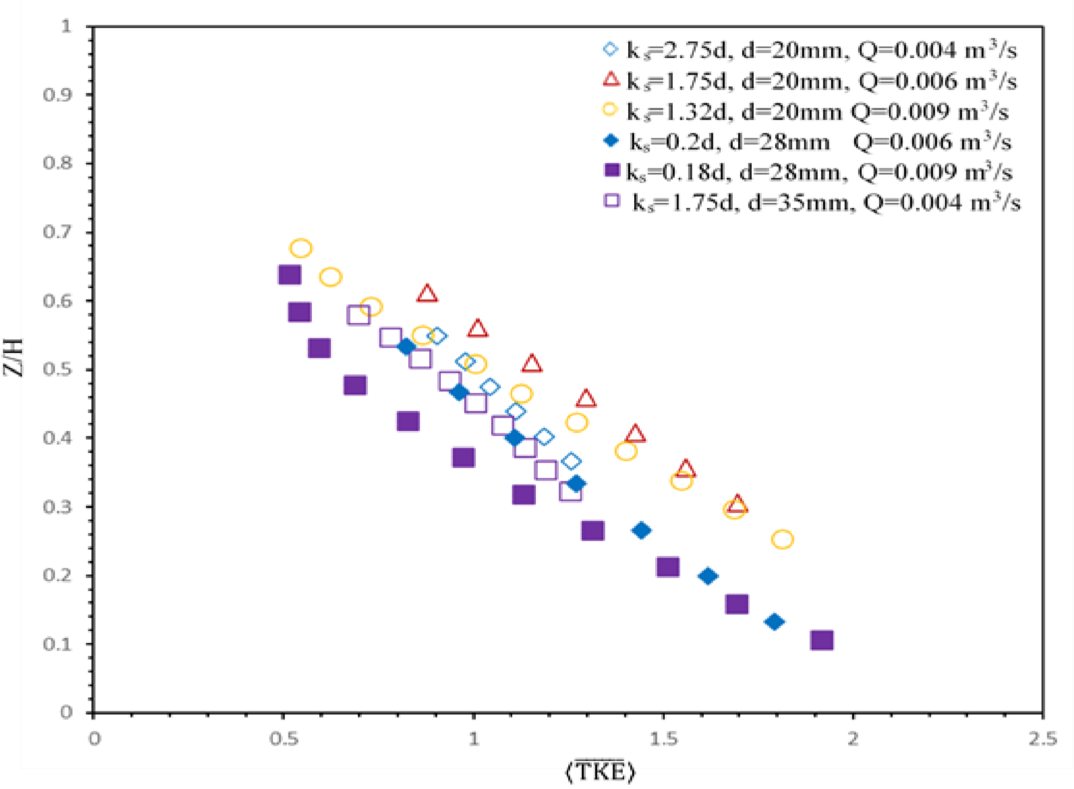

Figure 4.15. Vertical distribution of double averaged normalized turbulence kinetic energy for flow above natural gravel-beds obtained from four experimental cases (open symbols) and above an artificial bed obtained from two experimental cases (filled symbols).

In contrast to the findings of Qi et al. (2018), who found that values of $\langle \overline{\mathrm{TKE}} \rangle$ decrease with an increase in K^+, the $\langle \overline{\mathrm{TKE}} \rangle$ compares well for experiment's 4 and 5 even though they were conducted above different roughness surfaces and under different hydraulic conditions. The cause of such agreement is difficult to demonstrate but could be due to both experiments having very similar porosity, 31% and 32% for experiment's 4 and 5, respectively.

Experiment's 1-5 were conducted under intermediate relative submergence flow conditions but experiment 6 was carried out under high relative submergence flow conditions. This may be why experiment 6 exhibits less $\langle \overline{\mathrm{TKE}} \rangle$ than the other experiments shown in Figure 4.15. This observation agrees well with that reported by Monsalve et al. (2017), who found that spatially averaged turbulent kinetic energy reduces with increasing relative submergence.

In general, the $\langle\overline{\mathrm{TKE}}\rangle$ for all experiments decreases linearly towards the water surface in line with previous findings found in the literature (e.g. Tritico and Hotchkiss 2005; and Xu et al. 2020), as shown in Figure 4.15. As illustrated in Figure 4.15, the $\langle\overline{\mathrm{TKE}}\rangle$ calculated for experiment 6 is less than the other experiments, although it was conducted with a higher velocity (see Table 3.2 and Table 4.1). This could be due to decreasing temporal velocity fluctuations in experiment 6. Section 4.3.1 clearly shows that turbulence intensities in experiment 6 are less than in all other experiments. Thus, this is another possible explanation for the results of experiment 6 departing from the other experiments.

Previous studies have observed an inverse relationship between velocity and the development of coherent turbulent structures. For example, coherence is likely a function of the generation or decay of turbulent kinetic energy. Coherence might also be low at high discharge since new turbulence is being produced at more minor scales (MacVicar and Roy 2007). On the other hand, high TKE has been found within near-bed coherent structures, possibly produced in the shear area, while the TKE reduces with distance far away from the bed (Hardy et al. 2016).

In the turbulent boundary region, coherent structures are created by the flow of water above the porous bed, which can generate substantial flow through the gravel-bed. It can, in that way, promote mass (solute) transportation from the water column to the gravel-bed and vice versa (Higashino et al. 2009).

This section has presented and discussed the $\langle\overline{\mathrm{TKE}}\rangle$ above porous roughness surfaces with different particle diameters, porosity, and hydraulic conditions. It has been shown from this analysis that $\langle\overline{\mathrm{TKE}}\rangle$ decreases with increasing relative submergence and reducing instantaneous velocity fluctuations.

4.4 Summary

This chapter focused on the validation of the logarithmic law as reported by Nezu and Nakagawa (1993) using velocity measurements above natural gravel-beds (d_{50}=20 mm and d_{50}=35 mm particle diameters) and an acrylic bed (d_{50}=28 mm particle diameter). Velocity profiles were compared with those found in the literature (see Section 4.2). The theoretical logarithmic law was found to be valid above all beds under both intermediate and high relative submergence conditions when $(Z+ z_0)^+$ is in the range 421 to 2958. Such validation was achieved by finding the maximum value of the regression coefficient such that von Karman's constant κ was found to be 0.38, 0.39, 0.4, and 0.38 for experiment's 1, 2, 3 and 4, respectively; the zero-displacement distance (see Table 3.2 and Table 4.1); and k_s, the Nikuradse equivalent sand roughness, was found to be $2.75d_{50}$, $1.75d_{50}$, $1.32d_{50}$, and $1.75d_{50}$ for experiment's 1, 2, 3 and 4, respectively. Von Karman's constant was found to be 0.41 for both experiment's 5 and 6 above an artificial bed, and k_s was found to be $0.2d_{50}$ and $0.18d_{50}$, respectively (see Figures 4.5 and 4.6). There are expected differences between velocity profiles above natural gravel-beds and acrylic beds as well as with the literature (see Figure 4.7). This is because the roughness Reynolds number for experiments 1, 2, 3 and 4 is higher than in experiments 5 and 6 as well as that found in the literature. The variance in the roughness Reynolds number across these experiments may be the reason for the various k_s and κ that were previously found.

For experiments 1, 2 and 3, von Karman's constant and k_s range from 0.38 to 0.4 and from $2.75d_{50}$ to $1.75d_{50}$, respectively above a natural gravel-bed with a median diameter of 20 mm. The difference in the logarithmic parameters between these experiments could be due to the different flow conditions that were applied resulting in different flow depths and average velocities. Von Karman's constant could increase with increased porosity. The zero-displacement distance was found to be 5.6 mm for both experiments 5 and 6. This is likely due to the surface of the artificial bed being more uniform in arrangement than the natural gravel-beds. The same can likely be said for the value of von Karman's constant (0.41) which was also found to be the same between experiments 5 and 6.

In general, the zero-displacement distance found for all experiments in this study approximates the hydraulic roughness assumption equal to $((\sigma_b+d_{50})/2)$. It was also noted that k_s is negatively related to Re_R number, i.e., k_s decreases with increasing Reynolds number. The relationship between k_s and Re_R could be associated with the bed configuration, such as the size and shape of gravel particles, the bed porosity, as well as the space between elements. The key aspects of the validation of the logarithmic law in flows under intermediate and high relative submergence conditions are that both hydraulic conditions and roughness features play a significant role.

Furthermore, double averaged $\langle\overline{U_{RMS}}\rangle/u^*$, $\langle\overline{V_{RMS}}\rangle/u^*$, and $\langle\overline{W_{RMS}}\rangle/u^*$ above natural gravel-beds and an acrylic bed were presented and compared with the exponential decay functions (see Figures 4.8 to 4.10). The empirical constants of the exponential decay functions were found to differ from that of Nezu and Nakagawa (1993). It should be mentioned that these equations were derived above an impermeable bed, whereas the current experiments were carried out above highly porous beds. These parameters also are differed from that found in the literature. This could be because of the different gravel particle sizes and the degree of roughness employed by the various studies. Comparison between the turbulence intensity above natural gravel-beds and an acrylic bed, as well as the literature, showed the general trends agree well in the streamwise and cross-streamwise directions but significantly differs in the vertical direction, as explained in Section 4.3.1. However, the impact of relative submergence is notable on $\langle\overline{U_{RMS}}\rangle/u^*$, but has a lesser effect on K^+. For all experiments in the three-component directions, the general pattern of turbulence intensity distributions which decreases linearly with flow depth with the highest values at the bed surface is observed. It should be pointed out that the influence of porosity and shear velocity is probably greater on the double averaged turbulence intensities, especially in the vertical direction. It was confirmed that $\langle\overline{U_{RMS}}\rangle/u_* > \langle\overline{V_{RMS}}\rangle/u_* > \langle\overline{W_{RMS}}\rangle/u_*$ similar to Nezu and Nakagawa (1993).

The general trend that $\rho\langle\overline{U_{RMS}W_{RMS}}\rangle/u_*^2$ decreases linearly towards the water surface for all experiments with the highest values near the bed when $Z/H \leq 0.366$ (see Figure 4.11) was also observed. This agrees with the results reported in the literature. Due to the aspect ratio, the pattern of the $\langle\overline{RSS}\rangle$ profile for experiment 3 is different to all other experiments. As relative submergence increases, the profile of $\langle\overline{RSS}\rangle$ gradually shifts downwards. Thus, relative submergence, in addition to the roughness surface effects, may influence the pattern of $\langle\overline{RSS}\rangle$. The analysis of the various experiments in this study demonstrates that relative submergence affects Reynolds shear stress variations, but the effect of K^+ is insignificant.

The profiles of $\langle\overline{RNS}\rangle$ in the three-component directions decrease linearly with increased elevation within the water column. The analysis of the profiles of $\langle\overline{RNS}\rangle$ here in comparison to published data confirms that $\rho\langle\overline{U_{RMS}}\rangle^2/u_*^2 > \rho\langle\overline{V_{RMS}}\rangle^2/u_*^2 > \rho\langle\overline{W_{RMS}}\rangle^2/u_*^2$, as shown in Figures 4.12 to 4.14. The results highlight the impact of the hydraulic conditions, such as k_s/H_{max}, shear velocity, and aspect ratio, on the distribution of $\langle\overline{RNS}\rangle$. Moreover, gravel size, bed topography, and porosity were shown to affect $\langle\overline{RNS}\rangle$ profiles, especially in the vertical direction. Near the water surface, the profiles of $\rho\langle\overline{U_{RMS}}\rangle^2/u_*^2$ and $\rho\langle\overline{V_{RMS}}\rangle^2/u_*^2$ in experiment 6 suddenly increases. This could be the result of large flow fluctuations due to the propagation of a water surface wave as experiment 6 was carried out under high relative submergence. Equally, this could be due to the increased uncertainty in the measurement of instantaneous velocity fluctuations by

ADV instrumentation near the water surface. Findings also showed that the profile of vertical $\langle\overline{\mathrm{RNS}}\rangle$ might be more sensitive to gravel size, porosity, and bed topography than in the other two-component directions.

The main conclusion for all experiments, in terms of $\langle\overline{\mathrm{TKE}}\rangle$, is that it decreases linearly with increasing distance from the bed, similar to that found in the literature (see Figure 4.15). The analysis also showed that $\langle\overline{\mathrm{TKE}}\rangle$ decreases with increasing relative submergence and reducing instantaneous velocity fluctuations. It should be pointed out that the porosity also has some effect on $\langle\overline{\mathrm{TKE}}\rangle$ profiles.

To conclude, the first-order statistical analysis presented in this chapter shows that the velocity profiles are affected by bed features and K^{+}. However, second-order statistics such as turbulence intensities, $\langle\overline{\mathrm{RSS}}\rangle$, $\langle\overline{\mathrm{RNS}}\rangle$, and $\langle\overline{\mathrm{TKE}}\rangle$ are influenced by porosity and relative submergence. Both bed surface and hydraulic parameters play a role in the alteration of profiles of first- and second-order statistics.

Chapter 5

Near-Bed and Interstitial Flows

CHAPTER 5
Near-Bed and Interstitial Flows

5.1 Introduction

In this chapter, the interaction between the water column and subsurface flow is highlighted to clarify the effects of the surface flow on subsurface flow and vice versa Therefore, the results of experiments collected using ADV above natural gravel-beds and an artificial bed are introduced and double averaged quadrant analysis is applied for analysis in Section 5.2

In addition, preliminary results of subsurface velocity in natural gravel-beds and an artificial bed are presented to show the flow paths through the pore space. Four experiments were conducted with natural gravel-beds and an artificial bed using endoscopes to capture injected dye flow paths in videos which were then analysed using code developed by Forughi (2014). Firstly, for experiment 1, the interstitial flow through a natural gravel-bed with a median particle diameter of 20 mm under uniform flow conditions with intermediate relative submergence of 10.47 and bulk velocity of 0.164 m/s is presented in Section 5.3. Secondly, for experiment 4, the flow between natural gravel particles with a median diameter of 35 mm, with a bulk velocity of 0.145 m/s under uniform flow conditions, is also presented in Section 5.3. Finally, for experiment’s 5 and 6, the flow in the pore spaces of an artificial bed with a median particle diameter of 28 mm, with bulk velocities of 0.269 m/s and 0.321 m/s, respectively, under uniform conditions are also presented in Section 5.3.

5.2 Quadrant Analysis

The analytical procedure of quadrant analysis and the results obtained from experiments above both natural gravel-beds and an artificial bed are described in this section. Figure 5.1 shows double averaged Reynolds shear stress (u', w') components, as explained in Chapter 2 Section (2.3.5) and Chapter 3 Section (3.5.1) $\left|\langle\overline{S_{1,H}}\rangle\right|$ normalised with maximum shear stress in the streamwise direction against hole size (H) for experiment 1 at Z =30 mm near the bed surface and Z=45 mm near the water surface. Figure 5.2 also shows double averaged Reynolds shear stress in the streamwise direction against hole size (H) for experiment 2 at Z=30 mm near the bed surface and Z=60 mm near the water surface. What is evident in Figure 5.1 and Figure 5.2 is that the contribution of ejection events in Q2 to Reynolds shear stress is relatively large compared to the outward and inward interactions and sweep events in Q1, Q3 and Q4.

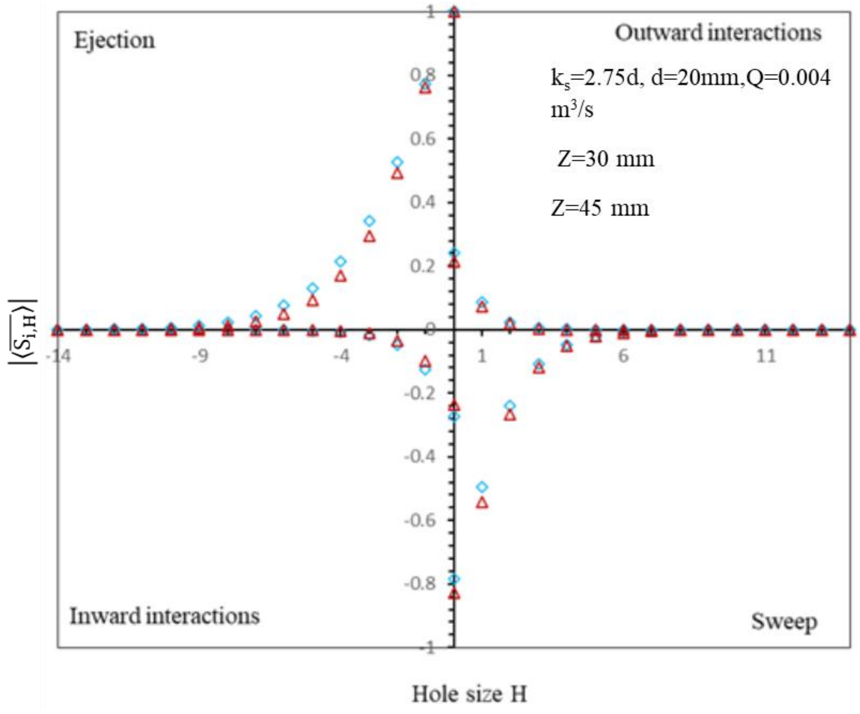

Figure 5.1. Double averaged quadrant analysis: variations of $\left|\langle \overline{S_{1,H}} \rangle\right|$ with H at two flow depth elevations from the natural gravel-bed surface for case $k_s=2.75d_{50}$, $d_{50}=20$ mm, Q=0.004 m^3/s.

However, the contribution of both outward and inward interactions to Reynolds shear stress in Q1 and Q3 events becomes negligible when $H \geq 3$, and $H \geq 4$, respectively, at the two different flow depth elevations from the bed surface for both experiments. However, the participation of both ejection and sweep events in Q2 and Q4 to Reynolds shear stress is still active for $H > 4$.

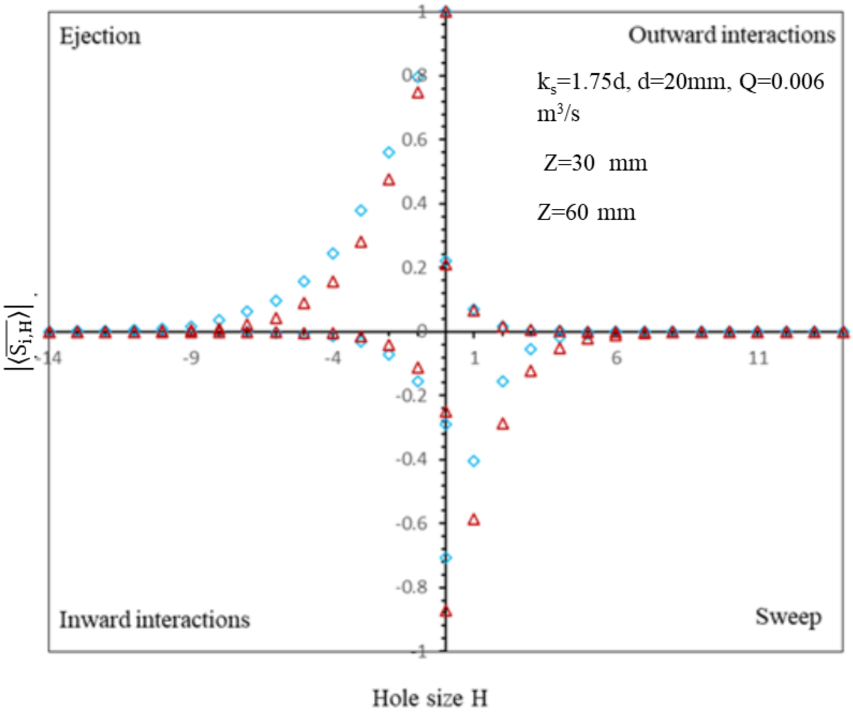

Figure 5.2. Double averaged quadrant analysis: variations of $|\langle\overline{S_{1,H}}\rangle|$with H at two flow depth elevations from the natural gravel-bed surface for case k_s=1.75d_{50}, d_{50}=20 mm, Q=0.006 m^3/s.

Figure 5.3 illustrates double averaged $|\langle\overline{S_{1,H}}\rangle|$ normalised with maximum shear stress in the streamwise direction against hole size (H) for experiment 3 at Z=30 mm near the bed surface and Z=80 mm near the water surface. Due to different water depths in each experiment, the elevation of the water surface is different in each experiment. Figure 5.4 presents double averaged $|\langle\overline{S_{1,H}}\rangle|$ in the streamwise direction against hole size (H) for experiment 4 at Z=30 mm near the bed surface and Z =54 mm near the water surface. In a similar fashion to experiment's 1 and 2, the contribution of ejection events in Q2 to Reynolds shear stress is somewhat higher than the outward and inward interactions and sweep events in Q1, Q3, and Q4 in experiments 3 and 4, as shown in Figure 5.3 and Figure 5.4. Otherwise, the contribution of both outward and inward interactions to Reynolds shear stress in Q1 and Q3 events becomes negligible when H ≥ 3, and H ≥ 4, respectively, at the two different flow depth elevations from the bed surface for experiment 3. The contribution of both outward and inward interactions to $|\langle\overline{S_{1,H}}\rangle|$ in Q1 and Q3 events are insignificant when H ≥ 2 and H ≥ 4, respectively, at the two different flow depth elevations from the bed surface for experiment 4. The contribution of both ejection and sweep events in Q2 and Q4 to Reynolds shear stress is effective for H > 4.

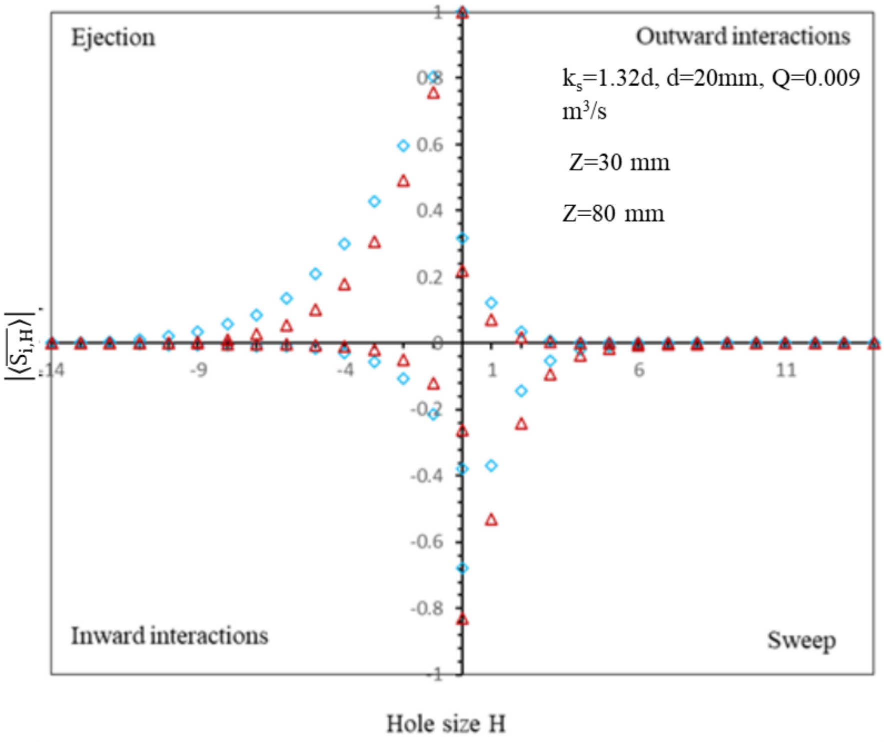

Figure 5.3. Double averaged quadrant analysis: variations of $|\langle\overline{S_{1,H}}\rangle|$ with H at two flow depth elevations from the natural gravel-bed surface for case k_s=1.32d_{50}, d_{50}=20 mm, Q=0.009 m^3/s.

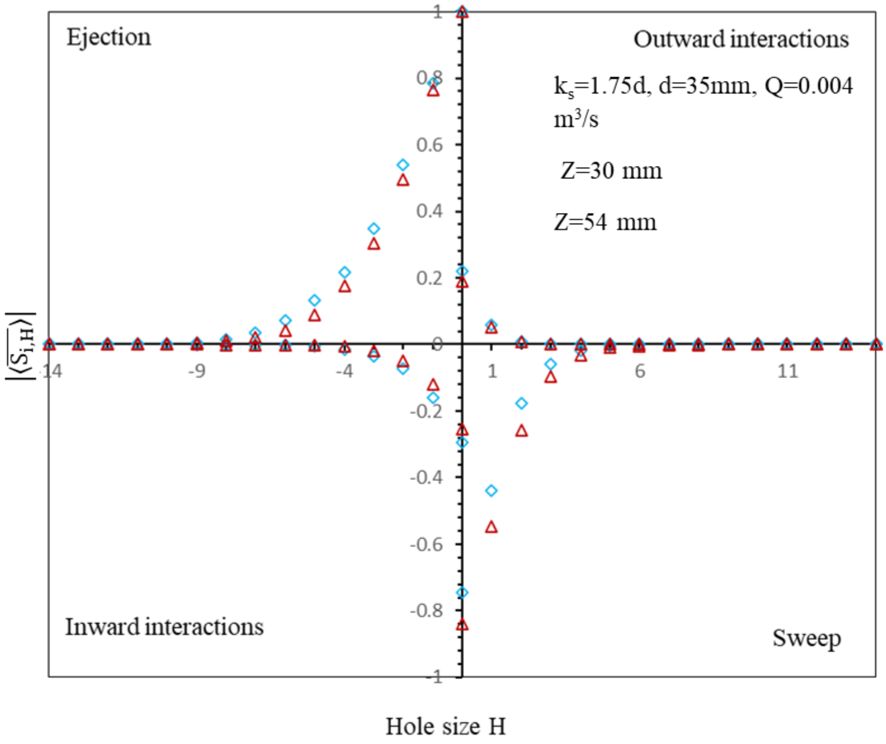

Figure 5.4. Double averaged quadrant analysis: variations of $|\langle\overline{S_{1,H}}\rangle|$ with H at two flow depth elevations from the natural gravel-bed surface for case k_s=1.75d_{50}, d_{50}=35 mm, Q=0.004 m^3/s.

Overall, the contribution to Reynolds shear stress of Q1 and Q3 events is smaller than the contribution of Q2 and Q4 events. As shown in Figure's 5.1 to 5.4, the contribution of ejection events to Reynolds shear stress near the water surface for all experiments is slightly larger than the ejection events near the bed. This is clearest in experiment 3, where ejection events remain effective until $H\approx12$ at $Z=80$ mm, as shown in Figure 5.3. Thus, the ejection events might increase with increasing velocity. This is because experiment 3 was carried out with a higher velocity than in the other experiments above natural gravel-beds.

The general trend for the four events is similar to that found in the literature, (e.g. Mignot et al. 2009b; Dey and Das 2012). In the quadrant analysis, sweeps and ejections dominate, especially in the near-bed and the equilibrium zone. For example, with an increase in distance from the bed, the ejection events become largest, but the sweep events are the controlling mechanism in the near-bed flow area (Grass 1971; Nezu and Nakagawa 1993; Sarkar et al. 2016; Qi et al. 2018; Bagherimiyab and Lemmin 2018). The analysis conducted here shows that the high ejection and sweep events occur above both experimental gravel-beds used in this study. At the same time, both outward and inward interactions occur less than ejection and sweep events. The observations also agree with the results reported by Mohajeri (2014), who found both sweep and ejection bursts are common above gravel-beds, while they are not exceeding each other.

Figure 5.5 shows double averaged Reynolds shear stress $\left|\langle\overline{S_{1,H}}\rangle\right|$ normalised with maximum shear stress in the streamwise direction against hole size (H) for experiment 5 at $Z=10$ mm near the bed surface and $Z=40$ mm near the water surface. What stands out in Figure 5.5 is that the general pattern of $\left|\langle\overline{S_{1,H}}\rangle\right|$ is similar to experiments above natural gravel-bed as well as with the literature (e.g. Raupach et al. 1991). As seen in Figure 5.5, the contribution of both ejection and sweep events to $\left|\langle\overline{S_{1,H}}\rangle\right|$ dominate more than both outward and inward interaction events. This is similar to that found in the literature, e.g. Dey and Nath (2010), who concluded that sweep and ejection events are the main contributors to total Reynolds shear stress generation.

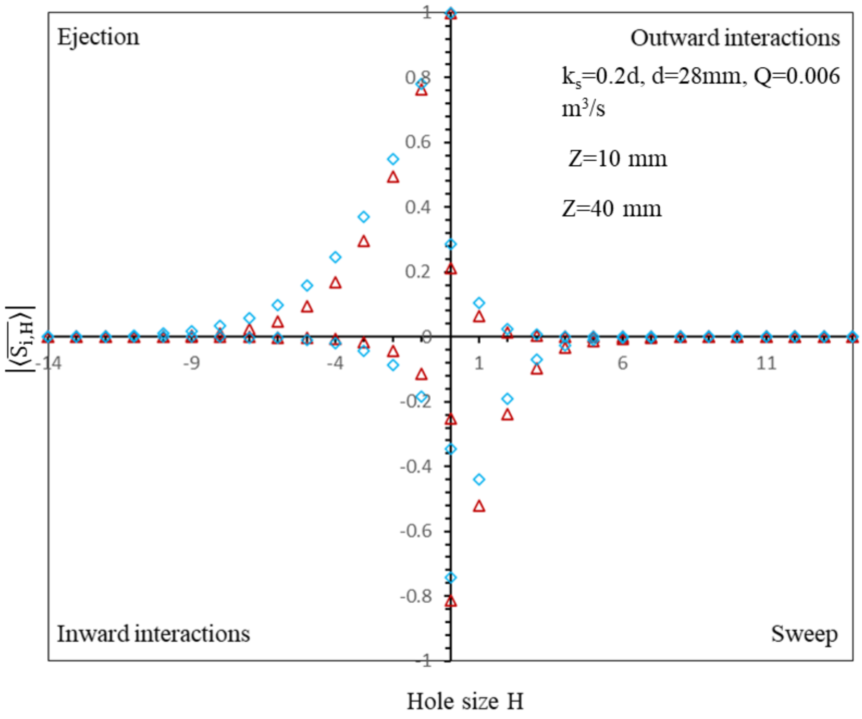

Figure 5.5. Double averaged quadrant analysis: variations of $\left|\langle\overline{S_{1,H}}\rangle\right|$ with H at two flow depth elevations from the artificial bed surface for case k_s=0.2d_{50}, d_{50}=28 mm, Q=0.006 m^3/s.

The contribution of both outward and inward interactions to Reynolds shear stress in Q1 and Q3 events disappear when H ≥ 3, and H ≥ 4, respectively, at the two different flow depth elevations from the bed surface. However, the contribution of both ejection and sweep events in Q2 and Q4 to Reynolds shear stress is still active when H>4. As illustrated in Figure 5.5, the contribution of ejection events to Reynolds shear stress near the bed in experiment 5 is slightly less than the ejection events near the water surface. The contribution of sweep events to Reynolds shear stress near the water surface is somewhat less than sweep events near the bed.

Figure 5.6 shows double averaged $\left|\langle\overline{S_{1,H}}\rangle\right|$ normalised with maximum shear stress in the flow direction versus hole size (H) for experiment 6 at Z=10 mm near the bed surface and Z=60 mm near the water surface. Figure 5.6 shows that the contribution of outward and inward interactions events to $\left|\langle\overline{S_{1,H}}\rangle\right|$ near the water surface in experiment 6 is marginally larger than such events near the bed. Outward interaction events near the water and bed surfaces become inactive when H>4 and H>3, respectively, at the two different flow depth elevations from the bed surface for experiment 6. Similarly, inward interaction events near both the water and bed surfaces become negligible when H>4. In addition, both ejection and sweep events contribute to $\left|\langle\overline{S_{1,H}}\rangle\right|$ more than either outward or inward interaction events. However, these events remain effective when H>4.

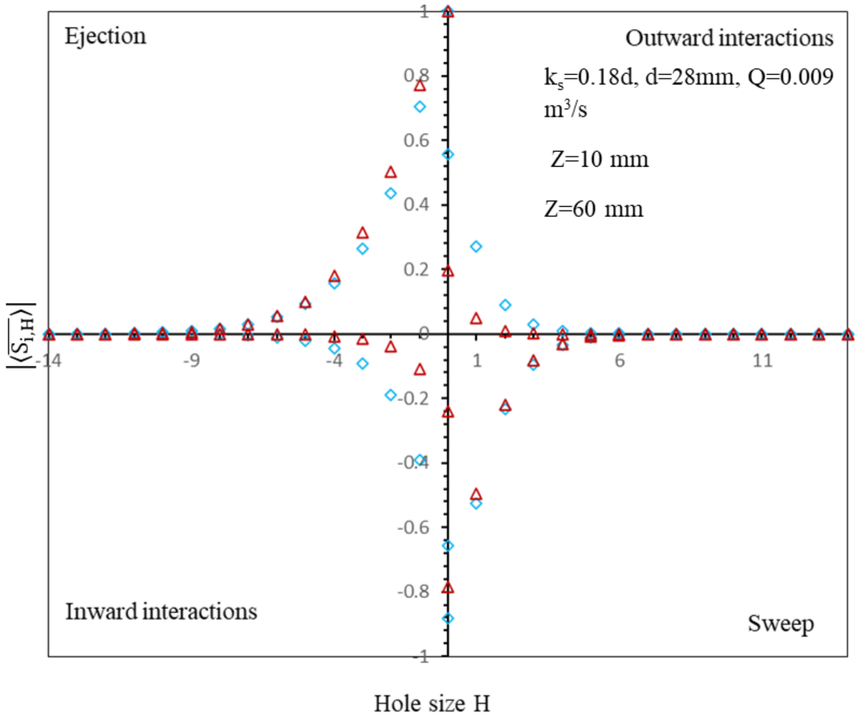

Figure 5.6. Double averaged quadrant analysis: variations of $|\langle \overline{S_{i,H}} \rangle|$ with H at two flow depth elevations from the artificial bed surface for case k_s=0.18d_{50}, d_{50}=28 mm, Q=0.009 m^3/s.

It should be pointed out that slight differences were found in the contribution of ejection and sweep events to Reynolds shear stress near the bed surface and close to the water surface for experiment 6. These findings contrast with the data reported for experiment 5, as well as all the experiments above the natural gravel-beds, and that found in the literature. This could be attributed to the fact that experiment 6 was carried out under high relative submergence conditions, unlike all the other experiments which were carried out under intermediate relative submergence conditions.

Generally, all events completely disappear when H>10 in both experiments 5 and 6 unlike that found in experiment 3 where events continue until H≈12. However, the bulk velocity in experiment 3 was lower than that applied in experiments 5 and 6. Equally, experiment 3 was carried out above a natural gravel-bed with k_s= 26 mm, which is higher than that in experiment's 5 (k_s= 6 mm) and 6 (k_s= 5 mm). The roughness effect also was noticed by Nakagawa and Nezu (1977). Overall, all events are insignificant when H=14. It has been experimentally demonstrated that all events are negligible when H > 15 regardless of the flow depth (Sarkar et al. 2016).

It can be clearly seen from Figure's 5.5 and 5.6 that both ejection events in the second quadrant (u' <0 and w' >0) and sweep events in the fourth quadrant (u'>0 and w'<0) dominate. This means there are more low-speed, outward-moving fluid structures as well as more high-speed, inward-moving fluid structures in both experiments above the artificial bed compared with any other turbulent events. Due to the sweep events towards the bed and the ejection events away from the bed, there are many upward and downward flows in all experiments above all bed types. These events lead to the exchange of fluid between the subsurface and the water column. Such event phenomena also play a role essential for the resuspension of fine particles from permeable rough-beds.

5.3 Interstitial Flow in Natural Gravel-Bed and Artificial-Bed

Interaction between surface and subsurface flow is essential because it plays a role in controlling the exchange of dissolved oxygen, nutrients and pollutants between the subsurface and the water column of gravel-bed rivers, which in turn, affects the water quality of riverine ecosystems (Packman et al. 2004; Manes et al. 2009; Higashino et al. 2009).

In this section, a preliminary study of interstitial flows through natural gravel-beds (experiments 1 and 4) and an artificial bed (experiments 5 and 6) are presented. All experiments were conducted under uniform flow conditions and intermediate or high relative submergence (H_{max}/σ_b=10.47, 15.35, 19.69 and 24.67, for experiments 1, 4, 5, and 6 respectively), as shown in Table 3.2 and Table 4.1. The theoretical subsurface velocity for experiments 1, 4, and 5-6 was found to be 0.003 m/s, 0.004 m/s, and 0.005 m/s, respectively.

The reason for the investigation of interstitial velocity through different beds is to clarify the effects of overlying flow on pore space flow and vice versa. To this end, the dye was injected at approximately half the depth of the bed from the surface to help identify flow paths within the bed. To further understand the interaction between the water column and pore water, the dye also was injected at approximately the first layer of the bed surface in both experiments 5 and 6.

Figure 5.7Figure 5.7 shows a contour map of the subsurface velocity in mm/s (U_{sub}) collected by endoscope's 1, 4, and 8 at 5.630 m, 5.711 m, and 5.819 m, respectively, from the flume inlet for both experiments 1 and 4. As shown in Figure 5.7, there are many vectors of average subsurface velocity in different directions as well as recirculating flow, such as upwelling and downwelling flow due to the turbulent flows above the bed. The maximum value of the subsurface velocity at 5.630 m and 5.819 m is 9 mm/s and 5 mm/s, respectively, for experiment 1, as shown in Figure’s 5.7a and 5.7c, and approximately 10 mm/s and 6.5 mm/s for experiment 4, as shown in Figure’s 5.7d and 5.7f. Thus, there is slightly more flow through the pores of the 35 mm diameter gravel particle bed (experiment 4) compared to that through the 20 mm diameter gravel particle bed (experiment 1).

Figure 5.7e illustrates the value of U_{sub} is approximately 9.5 mm/s for experiment 4 collected by endoscope 4 at 5.711 m from the flume inlet in the streamwise direction. The subsurface velocity remains slightly higher than that found in experiment 1 at the same location, as shown in Figure 5.7b.

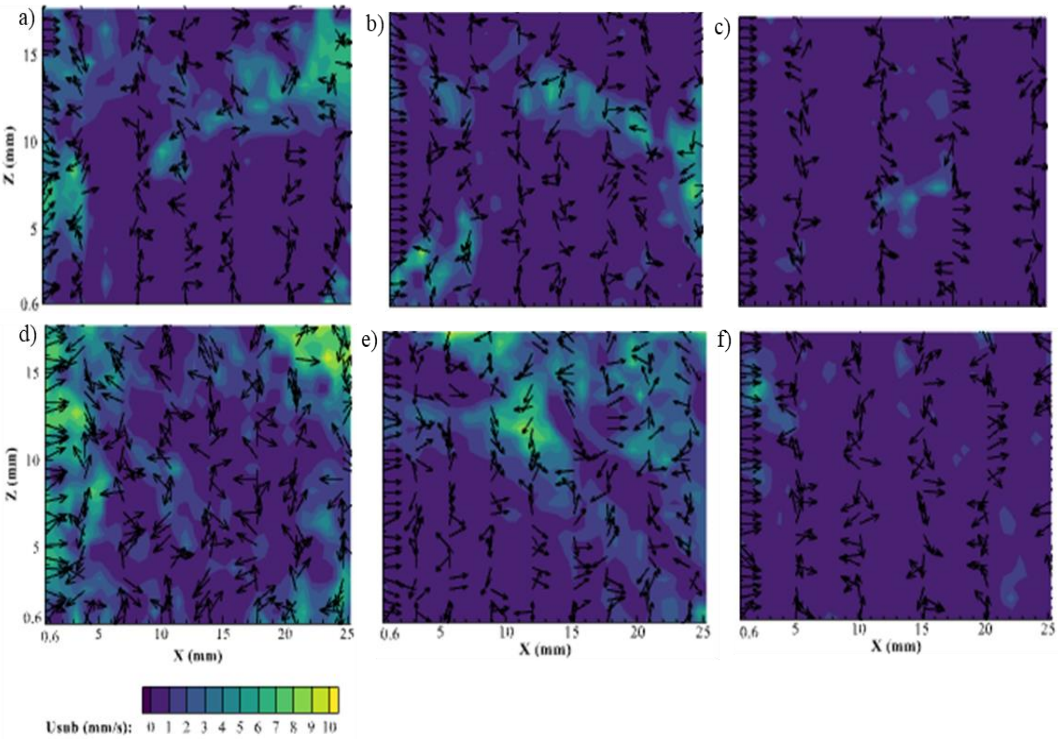

Figure 5.7. Contour map of subsurface velocity (mm/s) through natural gravel-beds: (a-c) $k_s=2.75d_{50}$, $d_{50}=20$ mm, and $Q=0.004$ m^3/s (experiment 1), and (d-f) $k_s=1.75d_{50}$, $d_{50}=35$ mm, and $Q=0.004$ m^3/s (experiment 4) at 5.630 m, 5.711 m and 5.819 m, respectively from the flume inlet in the streamwise direction for both experiments. Dye was injected at approximately half the depth of the gravel-bed from the surface for both experiments.

Figure’s 5.8 and 5.9 show a contour map of the subsurface velocity in mm/s (U_{sub}) collected by endoscope’s 1, 5 and 10 at 5.680 m, 5.788 m and 5.923 m from the inlet in the streamwise direction for both experiments 5 and 6 (artificial bed with 28 mm diameter particles). The maximum value of U_{sub} for both experiments is 10 mm/s at a distance of 5.680 m from the inlet in the streamwise direction, as shown in Figure’s 5.8 and 5.9 regardless of the elevation of the dye injection.

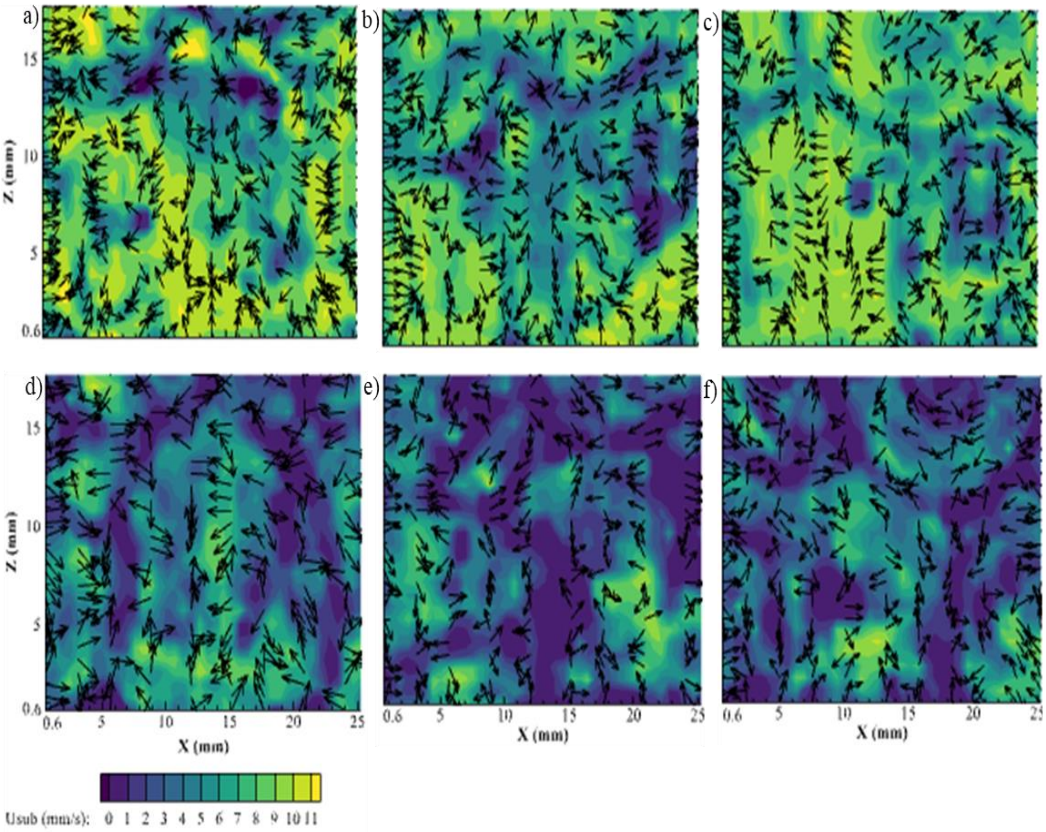

Figure 5.8. Contour map of subsurface velocity (mm/s) through an artificial bed at 5.680 m, 5.788 m, and 5.923 m, respectively from the flume inlet in the streamwise direction: (a-c) where the dye was injected at approximately half the depth of the gravel-bed from the surface, and (d-f) dye was injected at approximately the first layer of the gravel-bed surface. All panels are of experiment 5 where k_s=0.2d_{50}, d_{50}=28 mm, and Q=0.006 m^3/s.

Moving on now to consider a general comparison of subsurface velocity through 20 mm gravel particles in experiment 1, through 35 mm gravel particles in experiment 4, and through 28 mm particles in experiments 5 and 6. Figure's 5.7a to 5.7c show that, for experiment 1, there is a decrease in subsurface velocity between 5.630 m to 5.819 m from the flume inlet in the streamwise direction. Figure's 5.7d to 5.7f show that for experiment 4, although Re_k (19.700) is higher than that for experiment 1 (13.926), the migration of dye through the pore spaces is slower in experiment 4 compared to experiment 1. This could be due to the bulk velocity in experiment 1 (0.164) being higher than the bulk velocity in experiment 4 (0.145), which enhances the exchange between the water column and subsurface flow.

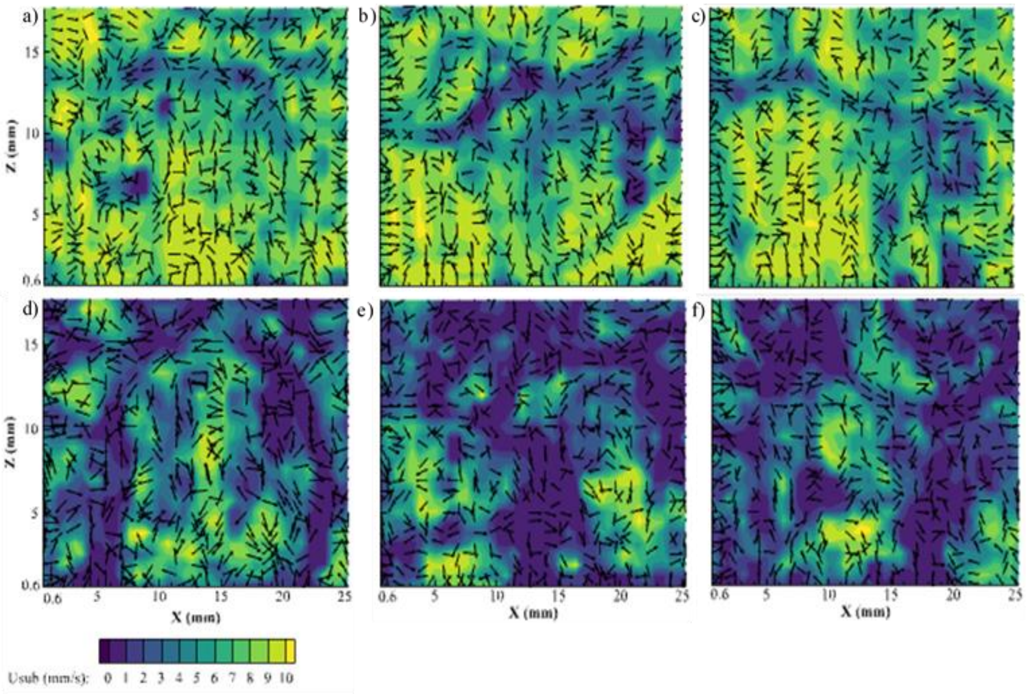

Figure 5.9. Contour map of subsurface velocity (mm/s) through an artificial bed at 5.680 m, 5.788 m, and 5.923 m, respectively from the flume inlet in the streamwise direction: (a-c) where dye was injected at approximately half the depth of the gravel-bed from the surface, and (d-f) dye was injected at approximately the first layer of the gravel-bed surface. All panels are of experiment 6 where k_s=0.18d_{50}, d_{50}=28 mm, and Q=0.009 m^3/s.

Additionally, Re_k in experiment 4 (19.700) is higher than that in experiments 5 and 6, (14.543 and 16.698, respectively), yet the migration of dye through the artificial bed is slower than both the 20 mm and 35 mm natural gravel-beds. The higher residence time of the dye in experiments 5 and 6 (time≈243.000s) compared to both experiment's 1 (time≈47.250s) and 4 (time≈54.00s) may be due to the lower porosity of the artificial bed as well as the hydraulic conditions of experiments 5 and 6, as shown in Table 3.2 and Table 4.1. It should also be pointed out that the roughness Reynolds number in both experiments 1 and 4 is higher than in both experiments 5 and 6, which could affect the exchange of flow between the surface and the subsurface. The transfer of mass above a flatbed has been shown to be a function of K^+ (Reidenbach et al. 2010). Increasing bed roughness, such as bed particles that protrude into the overlying flow, has also been shown to result in increasing exchange between surface and subsurface flow (Reidenbach et al. 2010).

There are also more recirculating flows occurring in experiments 5 and 6 as well as experiment 4 than the equivalent in experiment 1, as shown in Figures 5.7 to 5.9. This could be due to the void ratio and porosity, which are higher for the 20 mm particle diameter gravel-bed in experiment 1 less than the 35 mm particle diameter gravel-bed in experiment 4 and the 28 mm particle diameter artificial bed in both experiments 5 and 6. A review of the wider literature found that subsurface and surface flow in an open-channel can be affected by bed permeability, bedforms, and grain roughness (Han et al. 2019).

It has been demonstrated experimentally that an impermeable bed results in lower flow resistance than a permeable bed by Manes et al. (2009) who measured velocities above one layer of an impermeable bed as well as above and within five layers of a permeable bed of spherical elements. Flow resistance increases with rising Reynolds number as the flow can penetrate the bed and interact with the subsurface flow (Manes et al. 2009). Large-scale eddies within the surface flow have been shown to influence the subsurface flow and might be related to pressure fluctuations (Manes et al. 2009). Such pressure fluctuations could arise due to the roughness of the bed. Here, roughness is indicated by the standard deviation of the bed elevations where the artificial bed, with a value of 3.81 mm, is significantly less rough than the natural gravel-beds of experiment 1, with a value of 7.83 mm, and experiment 4, with a value of 6.06 mm. This topic is widely reported and extensively explored in the literature by Vollmer et al. (2002), who considered highly turbulent pressure fluctuations in the near-bed region and concluded that the impact of the resulting pressure gradients likely scales with roughness. Pressure variations occurring in the boundary layer are expected to result in the exchange of water and mass between the overlying and pore flows. This exchange may be the reason for the short dye residence times observed in-between pores of the natural gravel-bed in this study.

The subsurface velocity in the artificial bed (experiments 5 and 6) was found to be higher than that in the natural gravel-beds (experiments 1 and 4). This could be due to the dye path being easier for the endoscopes to capture through the artificial bed than the natural gravel-bed, as shown in Figure’s 5.10 and 5.11. Although the investigation of subsurface velocity in this study is a preliminary study, the artificial bed was chosen to measure interstitial flow through the bed as much as possible.

Figure 5.10. Dye distribution after measurements were taken for a natural gravel-bed.

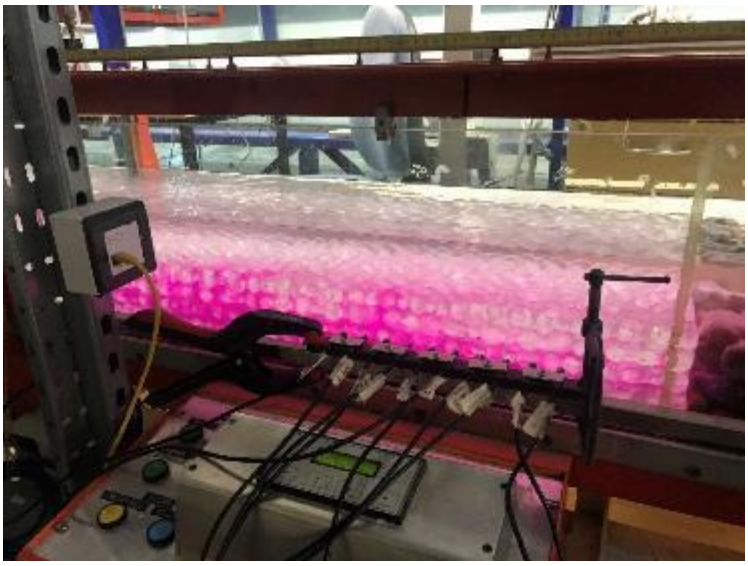

Figure 5.11. Dye distribution within the acrylic bed.

The dye injected at approximately half the depth of the bed from the surface migrated slowly within the pore space of both experiments 5 and 6 compared and the dye injected in the first layer of the bed from the surface, as shown in Figure 5.8 and Figure 5.9. This is likely due to the rapid exchange of water and mass between the water column and subsurface due to pressure variations and the hydraulic gradient. A previous study found in the literature demonstrated a close link between dye migration and the boundary layer conditions whereby the dye penetrated deeper into the bed due to the development of preferential flow paths resulting in a degree of pulsating of the flow within the bed (Packman et al. 2004). Additionally, because of the interaction of the turbulent surface flow with the channel bed, there could be temporal fluctuations in the void water flow field (Packman et al. 2004). The dye distribution could also depend on local velocity and local conditions, such as a high hydraulic gradient ($v^2/2g$) in the boundary layer, which plays a role in increasing the velocity of water exchanging between the water column and pore water. For example, near the boundary layer, flow is controlled by hydraulic conditions such as bulk velocity, Reynolds number, and bed surface topography. Where turbulent characteristics in the channel can be characterised by Reynolds number, and variations in boundary conditions lead to subsurface exchange flux, as well as momentum moves to the channel bed (Packman et al. 2004; Janssen et al. 2012). The channel velocity and size of the bed particles employ first-order controls on the subsurface exchange (Packman et al. 2004).

There are more upwelling and downwelling flows in the natural gravel-beds than in the artificial bed. As explained earlier in Section 5.25.2, this could be related to the contribution of both ejection and sweep events in Q2 and Q4 to Reynolds shear stress, which is relatively large compared to the outward and inward interaction events in Q1 and Q3 during these experiments. This could lead to upward and downward flows that increase the exchange between the water column and the pore flows. The interstitial flow in gravel-beds may affect the overlying turbulent flow characteristics, as observed earlier in Section 4.3.1 when comparing the root mean square of velocity fluctuations of each experiment with the decay function (Nezu and Nakagawa 1993). It can be seen from Figures 5.7 to 5.11 that there are many upwelling and downwelling flows due to the highly porous bed that was employed. These types of flow are significant in the hydrodynamics of a gravel-bed river and contribute to the maintenance of a healthy environment for aquatic organisms to live in. The effects of porosity and bed particle arrangement contribute the most to increasing interstitial velocity in Salmonid Redds beyond any effects of bed topography (Tonina and Buffington 2009).

5.4 Summary

In this chapter, quadrant analysis was presented, the contribution of ejection events in the second quadrant ($u' < 0$ and $w' > 0$) and sweep events in the fourth quadrant ($u' > 0$ and $w' < 0$) to Reynolds shear stress predominate more than outward interactions in the first quadrant ($u' > 0$ and $w' > 0$) and inward interactions in the third quadrant ($u' < 0$ and $w' < 0$) (as shown in Figures 5.1 to 5. 6 in Section 5.2). The contribution of ejection events to Reynolds shear stress near the bed for all experiments is slightly smaller than the ejection events near the water surface. However, the contribution of sweep events to Reynolds shear stress near the bed for all experiments is slightly larger than the sweep events near the water surface. This general pattern for the four events is similar to that found in the literature (e.g. Mignot et al. 2009b; Dey and Das 2012). Small differences were observed in the contribution of ejection and sweep events to Reynolds shear stress near the bed surface and close to the water surface for experiment 6. Inward and outward interaction events in experiment 6 were observed near the water surface, contrary to the other experiments. These results differ from the data reported for experiment 5, all experiments above natural gravel-beds, and that found in the literature. This could be due to the relative submergence as experiment 6 was carried out under high relative submergence flow conditions, all the other experiments were carried out under intermediate relative submergence conditions.

Moreover, for all experiments, outward and inward interaction events near the water and bed surfaces become ineffective when H>4, and H>3, respectively. Besides, both outward and inward interaction events contribute to $\left|\langle S_{i,H}\rangle\right|$ less than either ejection or sweep events. However, ejection and sweep events remain active when H>4. Thus, there are more low-speed, outward-moving fluid structures as well as more high-speed, inward-moving fluid structures in experiments above the natural and artificial beds alike compared with any other turbulent events. There are many upward and downward flows in experiments above natural and artificial beds because of the sweep events towards the bed and the ejection events away from the bed. These events result in the exchange of fluid between the bed and the overlying flow.

Overall, when H>10, all events totally disappear in all experiments except for experiment 3 where events continue until H≈12. Thus, the occurrence of ejection events might increase with an increasing bulk velocity above permeable beds. In conclusion, sweep and ejection events are the main contributors to total Reynolds shear stress generation.

This chapter has also described the methods used for a preliminary investigation of interstitial flows through measurements of subsurface velocity for four experiments performed under uniform flow conditions, and intermediate and high relative submergence using endoscopes and dye path tracking. Firstly, the highest subsurface velocity was found through the 20 mm diameter gravel particles of experiment 1 at 9 mm/s, which is approximately 6% of the bulk velocity (see Section 5.3 and Figures 5.7a to c). Secondly, subsurface velocity through the 35 mm diameter particles of experiment 4 with a total discharge of 0.004 m^3/s was found to be 10 mm/s (see Section 5.3 and Figure 5.7d to f). Finally, the subsurface velocity was shown with two different dye injection locations in the pores of an artificial bed composed of particles with a median diameter of 28 mm in experiments 5 and 6 to equal 0.006 m^3/s and 0.009 m^3/s, respectively. The faster dye migration in the boundary layer at the point of injection were observed in the second method compared to the first methodology in both experiments 5 and 6 due to high interaction between the water column and subsurface flow near gravel-bed (see Section 5.3, Figure 5.8 and Figure 5.9).

Chapter 6

Conclusions and Recommendations

CHAPTER 6
Conclusions and Recommendations

6.1 Conclusions

The objective of the investigation presented in this thesis was to improve the understanding of the complexities of open-channel flow over rough, porous surfaces such as that found in river systems and the effect of roughness characteristics on turbulent flow phenomena. This thesis focuses on the validation of the velocity profile logarithmic law above highly porous beds. The primary outcomes of each chapter are summarised in the following sections.

6.1.1 Flume Bed Characteristics

Six experiments were undertaken in a narrow recirculating flume ten metres long, 0.3.m wide, and 0.3 m deep under uniform flow conditions. Natural gravel 28 mm in diameter was placed upstream and downstream of the test section. Within the test section (approximately two metres in length), three different bed types were investigated: two natural gravel-beds, one with particles 20 mm in diameter and the other with particles 35 mm in diameter, and one artificial bed, with particles 28 mm in diameter. A gauge-point was used to collect water depth and gravel-bed surface topography measurements. The standard deviation of the natural gravel-bed surface elevations with 20 mm particle diameter was found to be 7.83 mm and with 35 mm particle diameter was found to be 6.06 mm. This agrees well with previous studies for unworked and water-worked gravel-bed rivers (Nikora et al. 2001). However, the standard deviation of the artificial bed surface elevations within the test area was calculated numerically by Stubbs et al. (2018), and it was found to be 3.81 mm, which is half of that found for the natural gravel-beds. The standard deviation of the artificial bed surface elevations is lower than that expected for natural gravel-bed rivers (Stubbs et al. 2018) and, thus, is not as rough as the natural gravel-beds used in this study. The grain size and porosity of the three-bed types investigated here are all in good agreement with that found in previous studies and are hence comparable with natural gravel-bed rivers (Stubbs et al. 2018). It was found that the porosity affects turbulent stresses such as turbulence intensity and Reynolds normal stress, especially in the vertical direction. Porosity is an essential parameter for a permeable rough bed, and it plays a role in exchange processes between overlying flow and subsurface flow. The exchange of flow between the free surface and the rough bed could affect turbulence intensity above the pore bed and so on. Similar to Nikora et al. (2001), Stoesser (2010) and Stubbs et al. (2018), a roughness geometry function A(z_b') was also applied to further determine the roughness characteristics of each bed type, as explained in Chapter 3 Section (3.4). This showed that all the beds investigated here exhibit a normally distributed surface roughness like gravel-bed rivers found in nature. Since the characteristics of turbulent flow over a boundary are directly related to the roughness of that boundary, it was determined that the turbulence observed in this study would be like that found in nature.

6.1.2 Flow above Natural Gravel and Artificial Beds

Whether the velocity profile above a porous gravel-bed obeys the logarithmic law, the exponential decay functions of turbulent intensities and other turbulent stresses under intermediate and high relative submergence is a subject matter of debate. Therefore, velocity data were gathered above the natural gravel-beds and acrylic bed using ADV instruments under uniform, intermediate, and high relative submergence flow conditions. In addition, this thesis concentrated on the analysis of the overlying turbulent flow by applying a time-space averaging methodology to the Navier-Stokes equations to elucidate flow behavior from profiles of streamwise velocity, turbulence intensities, Reynolds shear stress, turbulence kinetic energy, Reynolds normal stress, and quadrant analysis. Validation of the logarithmic law using double-averaged velocity statistics, as reported by Nezu and Nakagawa (1993) and Nikora et al. (2001), has been undertaken for three different beds. Root mean square velocity fluctuations were used to describe turbulence strength. Turbulence intensity was compared to the exponential decay functions reported by Nezu and Nakagawa (1993) in the three-component directions.

The main conclusions of this thesis are, firstly, that the theoretical logarithmic law is valid above all beds for intermediate and high relative submergences when the von Karman's constant, κ equals 0.38, 0.39, 0.4 and 0.38 for experiments 1, 2, 3 and 4, respectively. κ may increase with increasing bed porosity for flow above a natural gravel-bed. The variation in von Karman's constant may be due to the variation in flow conditions and different beds. The effect of different beds (approximately 7%) on κ was found to be higher than the effect of hydraulic conditions (approximately 5%).

These experiments showed different values for von Karman's constant ranging from 0.38 and 0.41 and that the mixing length increases as von Karman's constant increases. Von Karman's constant is an important parameter when considering both fish and riverine habitats in general. Bed particle mobility is determined by the relationship between the hydrodynamic Reynolds shear stress and the sediment shear stress (according to the Shields approach). This study showed that as von Karman's constant increases, Reynolds shear stress decreases, thus reducing the ability of the fluid flow to move bed particles. Such a scenario occurring in a natural river would provide an area suitable for both adult and juvenile fish populations, as well as redds of eggs. This study also showed that increasing shear stress results in a reduction in the overlying mean channel velocity. Thus implying that colmation processes, in a natural river, would occur resulting in reduced dissolved oxygen exchange between the channel flow and the inter-particle bed flow which could negatively impact fish eggs.

Due to the increased protrusion of particles from the natural gravel-beds in comparison with the artificial bed, the Nikuradse equivalent sand roughness, k_s was found to be higher in value for the natural gravel-beds than that for the artificial bed. Different values for k_s were obtained above the same bed surface and this was interpreted to be due to the different hydraulic conditions. Therefore, the differences found in k_s are approximately 52% and 91% due to hydraulic conditions and bed characteristics, respectively.

In addition, there are expected differences between the velocity profiles above the acrylic bed and those above natural gravel-beds. This may be a result of K^+, where increasing K^+ shifts the velocity profiles increasingly downwards. It is clear from this study that the normally considered constant parameters of the logarithmic law change with bed characteristics such as porosity, sediment size, sediment arrangement, bed roughness, K^+, as well as flow conditions such as flow depth. It should also be pointed out that k_s is inversely linked to the Re_R number, where k_s decreases with increasing Reynolds number.

The estimation of the zero-displacement distance requires precise measurement of the hydraulic parameters, such as flow depth. These hydraulic parameters, bed geometry, and relative submergence all influence the determination of the velocity profile fitting. The acrylic bed surface is more uniform in arrangement than the natural gravel-beds leading to a von Karman's constant of 0.41, obtaining the same z_0, and approximately the same k_s ($0.2d_{50}$ and $0.18d_{50}$) for both experiment's 5 and 6. Overall, the zero-displacement distance for all experiments of this investigation is approximated to be as the assumption (($(\sigma_b+d_{50})/2$). The most significant observation of this study is that the validation of the logarithmic law in flows under intermediate and high relative submergence conditions is that both hydraulic condition and roughness features play a role. Therefore, the effect of hydraulic conditions (approximately 14%) on zero-displacement distance is less than the effect of the bed characteristics (approximately 25%).

Furthermore, normalised double averaged turbulent intensity in the three-component directions above natural gravel-beds and acrylic bed were presented and compared with the exponential decay functions. It was found that the values of the empirical constants of the exponential decay functions of double averaged turbulent intensity in the streamwise direction somewhat compared to that obtained in the literature. However, the values of the empirical constants of the exponential decay functions of double averaged turbulent intensity in both cross-streamwise and vertical directions were found to be dissimilar to that obtained in the literature. It should be noted that the exponential decay functions from the previous studies were derived above impermeable beds, whereas the current experiments were carried out above highly porous beds. Thus, the velocity is non-zero close to the bed and causes recirculated flow such as upwelling and downwelling flow in the near-bed region. This leads to the exchange of flows between the subsurface and the water column. This phenomenon could affect overlaying instantaneous velocity fluctuations and thus decrease turbulence intensity.

The difference between the empirical constants of the exponential decay functions in the current study and previous studies could be due to the presence of bed particles in natural riverbeds that are noticeably larger than the viscous sublayer so that their roughness can be described by some feature sizes of bed grains (Nikora and Smart 1997). It is likely that the constants of the exponential decay functions depend on the experimental situation. Comparison between the turbulence intensity profiles above the acrylic bed and the natural gravel-beds showed that the relative submergence affects the streamwise turbulence intensity more than K^+. However, the relative submergence might affect the turbulence intensity in the vertical direction to a lesser degree. The key findings of this investigation are that, in general, turbulent intensity distributions in the three-component directions decrease linearly with flow depth with the highest values at the bed surface. This study also confirmed the magnitudes of $\langle\overline{U_{RMS}}\rangle/u_* > \langle\overline{V_{RMS}}\rangle/u_* > \langle\overline{W_{RMS}}\rangle/u_*$. The influence of porosity and shear velocity is probably greater on the double averaged values of turbulence intensities, especially in the vertical direction. Otherwise, the relative submergence is likely to affect the streamwise turbulence intensity.

Analysis of the double averaged Reynolds Shear Stress $\langle\overline{\mathrm{RSS}}\rangle$ shows, in general, that it decreases linearly with flow depth, with the highest value near the bed for all experiments. The profile of $\langle\overline{\mathrm{RSS}}\rangle$ could be influenced by the relative submergence, roughness surface, and aspect ratio, but the effect of K^+ is insignificant.

The double averaged Reynolds Normal Stress $\langle\overline{\mathrm{RNS}}\rangle$, was shown to decrease linearly with increased distance from the bed surface in all three-component directions. The profiles of $\langle\overline{\mathrm{RNS}}\rangle$ depend upon the hydraulic conditions, aspect ratio, k_s/H_{max}, and shear velocity. In addition, the streamwise and cross-streamwise velocity fluctuations are affected by the relative submergence more than the vertical velocity fluctuation. While the bed characteristics such as gravel size and porosity had a greater effect on $\langle\overline{\mathrm{RNS}}\rangle$ in the vertical direction than in the other two-component directions. The results of this study showed that $\rho\langle\overline{U_{RMS}}\rangle^2/u_*^2 > \rho\langle\overline{V_{RMS}}\rangle^2/u_*^2 > \rho\langle\overline{W_{RMS}}\rangle^2/u_*^2$, like that found in the literature. Therefore, both $\rho\langle\overline{U_{RMS}}\rangle^2/u_*^2$ and $\rho\langle\overline{V_{RMS}}\rangle^2/u_*^2$ contribute to total TKE more than $\rho\langle\overline{W_{RMS}}\rangle^2/u_*^2$.

The highest values of $\langle\overline{\mathrm{TKE}}\rangle$ are near the bed which then decreases linearly towards the water surface. There is a variation in the profiles of the double averaged turbulence kinetic energy due to the different hydraulic conditions and bed types. The porosity and relative submergence affect the behaviour of $\langle\overline{\mathrm{TKE}}\rangle$.

In summary, the first-order statistical analysis in this thesis shows that the bed structure and K+ are the most influential on the velocity profile. However, porosity and relative submergence are the most influential on the turbulence intensity, $\langle\overline{\mathrm{RSS}}\rangle$, $\langle\overline{\mathrm{RNS}}\rangle$, and $\langle\overline{\mathrm{TKE}}\rangle$. In general, both flow conditions and bed characteristics play a role in affecting the first- and second-order statistics.

6.1.3 Near-Bed and Interstitial Flows

In this study, quadrant analysis was presented and showed that the contribution of ejection and sweep events to Reynolds shear stress dominates more than outward and inward interactions. In addition, due to relative submergence, the pattern of double averaged quadrant analysis in experiment 6 is different to the other experiments. It can be concluded that relative submergence affects Reynolds shear stress as observed through quadrant analysis.

Generally, the occurrence of ejection events could increase with an increasing bulk velocity above natural gravel-beds. It can be pointed out that upward and downward flows occur in experiments above natural gravel-beds and an artificial bed alike due to the ejection events away from the bed and the sweep events towards the bed. Thus, there are more low-speed, outward-moving fluid structures as well as more high-speed, inward-moving fluid structures in the experiments. Such events enhance the turbulent exchange between interstitial and overlying flows. It can be concluded that sweep and ejection events are the main contributors to the generation of Reynolds shear stress.

The study presented here investigates subsurface average velocity in natural gavel-beds and an artificial bed as well as the effects of both overlying turbulent flow and characteristics of the bed on subsurface flow and vice versa. In this study, preliminary measurements of pore space velocity were collected. The outcome of this study leads to the conclusion that bed characteristics such as bed permeability, porosity, void space size, and bed surface features affect average interstitial velocity within the riverbed itself. Hydraulic conditions and the overlying turbulent flow characteristics, such as the root mean square of velocity fluctuations, result in reduced dye residence times in the pore spaces. The bed configuration is likely to influence upwelling and downwelling flows. For example, particles of the natural gravel-beds protruded more into the near-bed flow than that of the artificial bed. Equally, the k_s for the natural gravel-beds was higher than that of the artificial bed. The flow enters into pore space as vertical inwards and outward events and horizontal flow although contribution sweep events to Reynolds shear stress dominate near the beds. The contribution of both ejection and sweep events in Q2 and Q4 to Reynolds shear stress in the overlying flow results in the exchange of flow between the surface and subsurface.

From this study's point of view, the local version of velocity and hydraulic conditions as well as bulk flow conditions in open-channel flow have a considerable effect on exchange flow between overlying flow and subsurface flow the gravel-bed rivers such as momentum transport to bed and vice versa. In addition, this study increases insight into the interaction between surface and subsurface flows and furthers our understanding of the effects bed characteristics, turbulent features, and hydraulic conditions have on subsurface flow. This interaction plays a significant role in near-bed hydrodynamics of gravel-bed rivers, such as driving colmation and decolmation processes as well as the transport of important solutes for fishes during their hatching and alevin periods.

6.2 Contributions

The contributions of this study to the research topic of turbulence above highly porous beds and in subsurface flow are as follows:

1. The dependence of von Karman's constant on relative submergence is still not clear (Gaudio et al. 2010; Rouzes et al. 2019). This study provides evidence that with increasing relative submergence, von Karman's constant approaches the traditional value of 0.41.
2. These experiments showed that von Karman's constant ranges from 0.38 to 0.41 and increasing von Karman's constant leads to a decrease in Reynolds shear stress from the fluid. Due to the use of different bed surfaces and hydraulic conditions in this study, distinctions between the effects of such differences on turbulent flow above rough, porous beds can be made. The effects of changing bed surface characteristics on turbulent flow both within and above gravel-beds are more significant than the effects of changing hydraulic flow conditions. Clarification was required about whether the zero-displacement distance varies with bed configuration or hydraulic conditions (Mohajeri 2014) or other parameters (Gaudio et al. 2010; Antico et al. 2019). Therefore, this study provides evidence that bed configuration affects the logarithmic law parameters, such as zero-displacement distance, von Karman's constant, and the Nikuradse equivalent sand roughness more than hydraulic conditions.
3. Zero-displacement distance is as the assumption ($(\sigma_b + d_{50})/2$) convenient to find other parameters of logarithmic law, and κ increase with increasing bed porosity for flow above a natural gravel-beds.
4. The bed structure and roughness Reynolds number are the most significant on the velocity profile. However, relative submergence, aspect ratio, k_s/H_{max}, and shear velocity are the most significant on the turbulence intensity, Reynolds shear stress, Reynolds normal stress and turbulence kinetic energy.
5. This study qualified the quantification of turbulent intensity in flows above a porous bed compared to that above a smooth and impermeable beds flow. It was noticed that subsurface velocity affects velocity fluctuations near gravel-beds and vice versa.

6. The results of this study can be used as a database for future numerical and experimental studies.

6.3 Recommendations and future research

It was impossible to examine all probable areas of interest during this study due to limitations on equipment, time, and facilities. Consequently, the following are recommendations proposed for further research:

1. In this study, the logarithmic law was validated at intermediate and high relative submergence flow conditions above highly porous beds. In order to further understand the streamwise velocity distributions, more investigations are needed under low relative submergence flow conditions and above various beds of different porosity.

2. This study used different porous bed configurations with different flow depths to investigate the logarithmic law parameters. However, further investigation of such parameters is needed with a constant flow depth above different bed configurations.

3. This study distinguished between the effects of bed configurations and hydraulic conditions on the logarithmic law parameters in clear water. However, the investigations need to be expanded for unclear water, ie: containing suspended sediments, to provide a complete picture of the behaviour of the logarithmic layer above porous beds in an open-channel.

4. This study used different gravel sizes and materials outside of the test section compared to that within to cover the entire flume during each experiment. Therefore, future experiments need to expand by using the same particle size throughout the flume for each experiment. This is to guarantee the same hydraulic characteristics occur above and within the bed from the inlet to the outlet of the flume.
5. Further investigations are required using piezometers to give more insight into the effect of the bed on the water surface and the interaction between interstitial flow and the water surface.

6. The velocity statistics presented in Chapter 4 were obtained using an ADV instrument. There are, however, other measurement techniques that have a higher temporal and spatial resolution such as Particle Image Velocimetry (PIV) or Laser Doppler Anemometer (LDA), that could be employed for future work.

7. Interstitial flow could be measured using high-resolution PIV systems founded upon endoscopy, such as Endoscopic Particle Image Velocimetry (EPIV) (Blois et al. 2012).

References

Aberle, J., Koll, K. and Dittrich, A. 2008. Form induced stresses over rough gravel-beds. *Acta Geophysica* 56(3), pp. 584–600.

Aberle, J. and Nikora, V. 2006. Statistical properties of armored gravel bed surfaces. *Water Resources Research* 42(11), p. W11414/1-11.

Aberle, J. and Smart, G.M. 2003. The influence of roughness structure on flow resistance on steep slopes. *Journal of Hydraulic Research* 41(3), pp. 259–269.

Adak, A. 2018. Turbulent Flow Characterization over the Gravel Bed. *IOP Conference Series: Materials Science and Engineering* 377(1), pp. 012090/1–13.

Adrian, R.J., Meinhart, C.D. and Tomkins, C.D. 2000. Vortex organization in the outer region of the turbulent boundary layer. *Journal of Fluid Mechanics* 422, pp. 1–54. Available at: http://www.journals.cambridge.org/abstract_S0022112000001580.

Adrian, R.J. and Marusic, I. 2012. Coherent structures in flow over hydraulic engineering surfaces. *Journal of Hydraulic Research* 50(5), pp. 451–464.

Afzalimehr, H. 2010. Effect of non-uniformity of flow on velocity and turbulence intensities over a cobble-bed. *Hydrological Processes* 24(3), pp. 331–341.

Afzalimehr, H. and Anctil, F. 2000. Accelerating shear velocity in gravel-bed channels. *Hydrological sciences journal* 45(1), pp. 113–124.

Afzalimehr, H. and Rennie, C.D. 2009. Determination of bed shear stress in gravel-bed rivers using boundary-layer parameters. *Hydrological Sciences Journal* 54(1), pp. 147–159.

Agelinchaab, M., Tachie, M.F. and Ruth, D.W. 2006. Velocity measurement of flow through a model three-dimensional porous medium. *Physics of Fluids* 18(1), pp. 017105/1–11.

Albayrak, I. and Lemmin, U. 2011. Secondary currents and corresponding surface velocity patterns in a turbulent open-channel flow over a rough bed. *Journal of Hydraulic Engineering* 137(11), pp. 1318–1334.

Antico, F., Ricardo, A.M. and Ferreira, R.M.L. 2019. The logarithmic law of the wall in flows over mobile lattice-arranged granular beds. *Water* 11(6), pp. 1166/1–15.

Arthur, J.K., Ruth, D.W. and Tachie, M.F. 2009. PIV measurements of flow through a model porous medium with varying boundary conditions. *Journal of Fluid Mechanics* 629, pp. 343–374.

Ashley, G.M. 1990. Classification of large-scale subaqueous bedforms: a new look at an old problem-SEPM bedforms and bedding structures. *Journal of Sedimentary Petrology* 60(1), pp. 160–172.

ASTM C127-15. 2015. Standard test method for relative density (specific gravity) and absorption of coarse aggregate.

Auel, C., Albayrak, I. and Boes, R.M. 2014. Turbulence Characteristics in Supercritical Open Channel Flows: Effects of Froude Number and Aspect Ratio. *Journal of Hydraulic Engineering* 140(4), p. 04014004.

Baas, J.H. 1978. Ripple, ripple mark, ripple structure. In: *Sedimentology*. pp. 921–925.

Bagherimiyab, F. and Lemmin, U. 2018. Large-scale coherent flow structures in rough-bed open-channel flow observed in fluctuations of three-dimensional velocity, skin friction and bed pressure. *Journal of Hydraulic Research* 56(6), pp. 806–824. Available at: https://www.tandfonline.com/doi/full/10.1080/00221686.2017.1416686.

Bailey, S.C.C., Vallikivi, M., Hultmark, M. and Smits, A.J. 2014. Estimating the value of von Kármán ' s constant in turbulent pipe flow. *Journal of Fluid Mechanics* 749, pp. 79–98.

Balachandar, R. and Bhuiyan, F. 2007. Higher-Order Moments of Velocity Fluctuations in an Open-Channel Flow with Large Bottom Roughness. *Journal of Hydraulic Engineering* 133(1), pp. 77–87.

Barila, T.Y., Williams, R.D. and Stauffer, J.R. 1981. The influence of stream order and selected stream bed parameters on fish diversity in Raystown Branch, Susquehanna River drainage, Pennsylvania. *Journal of Applied Ecology* 18(1), pp. 125–131.

Barlaup, B.T., Gabrielsen, S.E., Skoglund, H. and Wiers, T. 2008. Addition of spawning gravel - A means to restore spawning habitat of Atlantic Salmon (salmo salar L.), and anadromous and resident brown trout (Salmo Trutta L.) in regulated rivers. *River Research and Applications* 24(5), pp. 543–550.

Barros, J.M. and Christensen, K.T. 2014. Observations of turbulent secondary flows in a rough-wall boundary layer. *Journal of Fluid Mechanics* 748(2), p. R1/1-13.

Bartram, J., Ballance, R. and Eds. 1996. *Water quality monitoring: a practical guide to the design and implementation of freshwater quality studies and monitoring programmes*.

Bennett, S.J. and Bridge, J.S. 1995. The geometry and dynamics of low-relief bed forms in heterogeneous sediment in a laboratory channel, and their relationship to water flow and sediment transport. *Journal of Sedimentary Research* A65(1), pp. 29–39.

Best, J., Bennett, S., Bridge, J. and Leeder, M. 1997. Turbulence modulation and particle velocities over flat sand beds at low transport rates. *Journal of Hydraulic Engineering* 123(12), pp. 1118–1128.

Best, J.L. and Brayshaw, A.C. 1985. Flow separation—a physical process for the concentration of heavy minerals within alluvial channels. *Journal of the Geological Society* 142(5), pp. 747–755.

Blaschke, A.P., Steiner, K.H., Schmalfuss, R., Gutknecht, D. and Sengschmitt, D. 2003. Clogging processes in hyporheic interstices of an impounded river, the Danube at Vienna, Austria. *International Review of Hydrobiology* 88(3–4), pp. 397–413. Available at:

http://www.scopus.com/inward/record.url?eid=2-s2.0-0042709521&partnerID=40&md5=1a95e332f3626f82b169afaa06cd31c2.

Blois, G., Sambrook Smith, G.H., Best, J.L., Hardy, R.J. and Lead, J.R. 2012. Quantifying the dynamics of flow within a permeable bed using time-resolved endoscopic particle imaging velocimetry (EPIV). *Experiments in Fluids* 53(1), pp. 51–76.

Bomminayuni, S. and Stoesser, T. 2011. Turbulence Statistics in an Open-Channel Flow over a Rough Bed. *Journal of Hydraulic Engineering* 137(11), pp. 1347–1358.

Boulton, A.J., Findlay, S., Marmonier, P., Stanley, E.H. and Valett, H.M. 1998. the Functional Significance of the Hyporheic Zone in Streams and Rivers. *Annual Review of Ecology and Systematics* 29(1), pp. 59–81. Available at: http://www.annualreviews.org/doi/10.1146/annurev.ecolsys.29.1.59.

Boulton, A.J., Datry, T., Kasahara, T., Mutz, M. and Stanford, J.A. 2010. Ecology and management of the hyporheic zone: stream–groundwater interactions of running waters and their floodplains. *Journal of the North American Benthological Society* 29(1), pp. 26–40. Available at: http://www.journals.uchicago.edu/doi/10.1899/08-017.1.

Breugem, W.P., Boersma, B.J. and Uittenbogaard, R.E. 2006. The influence of wall permeability on turbulent channel flow. *Journal of Fluid Mechanics* 562, pp. 35–72.

Bridge, J.S. and Bennett, S.J. 1992. A model for the entrainment and transport of sediment grains of mixed sizes, shapes, and densities. *Water Resources Research* 28(2), pp. 337–363.

British Standards Institution 1990. *Methods of test for soils for civil engineering purposes. Classification tests.* London: BSI.

Brunke, M. and Gonser, T. 1997. The ecological significance of exchange processes between rivers and groundwater. *Freshwater Biology* 37(1), pp. 1–33.

Buffin-Bélanger, T., Rice, S., Reid, I. and Lancaster, J. 2006. Spatial heterogeneity of near-bed hydraulics above a patch of river gravel. *Water Resources Research* 42(4), p. W04413/1-12.

Buffington, J.M. and Montgomery, D.R. 1999a. A Procedure for classifying textural facies in gravel-bed rivers. *Water Resource Research* 35(6), pp. 1903–1914.

Buffington, J.M. and Montgomery, D.R. 1999b. Effects of hydraulic roughness on surface textures of gravel-bed rivers. *Water Resources Research* 35(11), pp. 3507–3521.

Camenen, B., Bayram, A. and Larson, M. 2006. Equivalent roughness height for plane bed under Steady flow. *Journal of Hydraulic Egineering* 132(11), pp. 1146–1158.

Cameron, S.M., Nikora, V.I. and Stewart, M.T. 2017. Very-large-scale motions in rough-bed open-channel flow. *Journal of Fluid Mechanics* 814, pp. 416–429.

Campbell, L., McEwan, I., Nikora, V., Pokrajac, D., Gallagher, M. and Manes, C. 2005. Bed-Load Effects on Hydrodynamics of Rough-Bed Open-Channel Flows. *Journal of Hydraulic Engineering* 131(7), pp. 576–585. Available at:

http://ascelibrary.org/doi/10.1061/%28ASCE%290733-9429%282005%29131%3A7%28576%29.

Cao, H., Ye, C., Yan, X.-F., Liu, X.-N. and Wang, X.-K. 2020. Experimental investigation of turbulent flows through a boulder array placed on a permeable bed. *Water Supply*, pp. 1–13.

Capra, H., Plichard, L., Bergé, J., Pella, H., Ovidio, M., McNeil, E. and Lamouroux, N. 2017. Fish habitat selection in a large hydropeaking river: Strong individual and temporal variations revealed by telemetry. *Science of the Total Environment* 578, pp. 109–120. Available at: http://dx.doi.org/10.1016/j.scitotenv.2016.10.155.

Carling, p. A. and Reader, N.A. 1982. Structure, composition and bulk properties of upland stream gravels. *Earth Surface Processes and Landforms* 7(4), pp. 349–365.

Carling, P. 1988. The concept of dominant discharge applied to two gravel-bed streams in relation to channel stability thresholds. *Earth surface processes and landforms* 13(4), pp. 355–367.

Carling, P.A. 1989. Bedload transport in two gravel-bedded streams. *Earth Surface Processes and Landforms* 14(1), pp. 27–39.

Carling, P.A., Gölz, E., Orr, H.G. and Radecki-Pawlik, A. 2000. The morphodynamics of fluvial sand dunes in the River Rhine, near Mainz, Germany. I. Sedimentology and morphology. *Sedimentology* 47(1), pp. 227–252.

Carling, P.A. and Orr, H.. 2000. Morphology of Riffle-Pool Sequences in the River Severn, England. *Earth Surface Processes and Landforms* 25(4), pp. 369–384.

Cary, A.S. 1951. Origin and significance of open work gravel. *Transactions of the American Society of Civil Engineers* 116(1), pp. 1296–1308.

Cecchetto, M., Tregnaghi, M., Bottacin-busolin, A., Tait, S. and Marion, A. 2017. Statistical Description on the Role of Turbulence and Grain Interference on Particle Entrainment from Gravel Beds. *Journal of Hydraulic Engineering* 143(1), pp. 06016021/1–9.

Cellino, M. and Lemmin, U. 2004. Influence of Coherent Flow Structures on the Dynamics of Suspended Sediment Transport in Open-Channel Flow. *Journal of Hydraulic Engineering* 130(11), pp. 1077–1088.

Chan, L., Macdonald, M., Chung, D., Hutchins, N. and Ooi, A. 2015. A systematic investigation of roughness height and wavelength in turbulent pipe flow in the transitionally rough regime. *Journal of Fluid Mechanics* 771, pp. 743–777.

Te Chow, V. 1959. *Open-channel hydraulics*. McGraw-Hill New York.

Clauser, F.H. 1956. The Turbulent Boundary Layer. *Advances in Applied Mechanics* 4(C), pp. 1-51. Elsevier.

Coleman, S.E., Nikora, V.I. and Aberle, J. 2011. Interpretation of alluvial beds through bed-elevation distribution moments. *Water Resources Research* 47(11), p. W11505/1-14.

Comte-Bellot, G. 1976. Hot-wire anemometry. *Annual review of fluid mechanics* 8(1), pp. 209–231.

Cooper, J.R. 2006. *Spatially-induced momentum transfer over water-worked gravel beds*. Doctoral dissertation, University of Sheffield.

Cooper, J.R., Aberle, J., Koll, K. and Tait, S.J. 2013. Influence of relative submergence on spatial variance and form-induced stress of gravel-bed flows. *Water Resources Research* 49(9), pp. 5765–5777.

Cooper, J.R., Ockleford, A., Rice, S.P. and Powell, D.M. 2018. Does the permeability of gravel river beds affect near-bed hydrodynamics? *Earth Surface Processes and Landforms* 43(5), pp. 943–955.

Corino, E.R. and Brodkey, R.S. 1969. A visual investigation of the wall region in turbulent flow. *Journal of Fluid Mechanics* 37(1), pp. 1–30.

Crisp, D.T. and Carling, P.A. 1989. Observations on siting, dimensions and structure of salmonid redds. *Journal of Fish Biology* 34(1), pp. 119–134.

Crowley, K.D. 1983. Large-scale bed configurations (macroforms), Platte River Basin , Colorado and Nebraska : Primary structures and formative processes. *Geological Society of America Bulletin* 94(1), pp. 117–133.

Dade, W.B. and Friend, P.F. 1998. Grain-size, sediment-transport regime, and channel slope in alluvial rivers. *Journal of Geology* 106(6), pp. 661–675.

Dancey, C.L., Balakrishnan, M., Diplas, P. and Papanicolaou, A.N. 2000. The spatial inhomogeneity of turbulence above a fully rough, packed bed in open channel flow. *Experiments in Fluids* 29(4), pp. 402–410.

Detert, M., Weitbrecht, V. and Jirka, G.H. 2010. Laboratory measurements on turbulent pressure fluctuations in and above gravel beds. *Journal of Hydraulic Engineering* 136(10), pp. 779–789.

Dey, S., Sarkar, S., Bose, S.K., Tait, S. and Castro-Orgaz, O. 2011. Wall-wake flows downstream of a sphere placed on a plane rough wall. *Journal of Hydraulic Engineering* 137(10), pp. 1173–1189.

Dey, S., Das, R., Gaudio, R. and Bose, S.K. 2012. Turbulence in mobile-bed streams. *Acta Geophysica* 60(6), pp. 1547–1588.

Dey, S. and Ali, S.Z. 2019. Bed sediment entrainment by streamflow: State of the science. *International Association of Sedimentologist* 66(5), pp. 1449–1485.

Dey, S. and Das, R. 2012. Gravel-Bed Hydrodynamics: Double-Averaging Approach. *Journal of Hydraulic Engineering* 138(8), pp. 707–725.

Dey, S. and Nath, T.K. 2010. Turbulence Characteristics in Flows Subjected to Boundary Injection and Suction. *Journal of Engineering Mechanics* 136(7), pp. 877–888.

Dierberg, F.E. and DeBusk, T.A. 2005. An evaluation of two tracers in surface-flow wetlands: Rhodamine-WT and lithium. *Wetlands* 25(1), pp. 8–25.

Dietrich, W.E., Smith, J.D. and Dunne, T. 1984. Boundary shear stress, sediment transport and bed morphology in a sand-bedded river meander during high and low flow. *In River Meandering*, pp. 622–639.

Dijksman, J.A., Rietz, F., Lorincz, K.., Hecke, M.L. van and Losert, W. 2012. Refractive index matched scanning of dense granular materials. *Review of Scientific Instruments* 83(1), pp. 011301/1–12.

Dinehart, R.L. 1992. Gravel-bed deposition and erosion by bedform migration observed ultrasonically during storm flow, North Fork Toutle River, Washington. *Journal of Hydrology* 136(1–4), pp. 51–71.

Drake, T.G., Shreve, R.L., Dietrich, W.E., Whiting, P.J. and Leopold, L.B. 1988. Bedload transport of fine gravel observed by motion-picture photography. *Journal of Fluid Mechanics* 192, pp. 193–217.

Fang, H., Han, X., He, G. and Dey, S. 2018. Influence of permeable beds on hydraulically macro-rough flow. *Journal of Fluid Mechanics* 847, pp. 552–590.

Ferguson, R. 2007. Flow resistance equations for gravel- and boulder-bed streams. *Water Resources Research* 43(5), p. W05427/1-12.

Ferguson, R.I. 1993. Understanding braiding processes in gravel-bed rivers: Progress and unsolved problems. *Geological Society, London, Special Publications* 75(1), pp. 73–87.

Ferraro, D., Servidio, S., Carbone, V., Dey, S. and Gaudio, R. 2016. Turbulence laws in natural bed flows. *Journal of Fluid Mechanics* 798, pp. 540–571.

Ferreira, R.M.L., Franca, M.J., Leal, J.G.A.B. and Cardoso, A.H. 2012. Flow over rough mobile beds: Friction factor and vertical distribution of the longitudinal mean velocity. *Water Resources Research* 48(5), p. W05529/1-14.

Ferreira, R.M.L. 2015. The von Kármán constant for flows over rough mobile beds. Lessons learned from dimensional analysis and similarity. *Advances in Water Resources* 81, pp. 19–32. Available at: http://dx.doi.org/10.1016/j.advwatres.2014.10.004.

Ferro, V. 2003. ADV measurements of velocity distributions in a gravel-bed flume. *Earth Surface Processes and Landforms* 28(7), pp. 707–722.

Field, M.S., Wilhelm, R.G., Quinlan, J.F. and Aley, T.J. 1995. An assessment of the potential adverse properties of fluorescent tracer dyes used for groundwater tracing. *Environmental Monitoring and Assessment* 38(1), pp. 75–96.

Finelli, C.M., Hart, D.D. and Fonseca, D.M. 1999. Evaluating the spatial resolution of an acoustic Doppler velocimeter and the consequences for measuring near-bed flows. *Limnology and Oceanography* 44(7), pp. 1793–1801.

Finnigan, J. 2000. Turbulence in plant canopies. *Annual review of fluid mechanics* 32(1), pp. 519–571.

Flodmark, L.E.W., Urke, H.A., Halleraker, J.H., Arnekleiv, J. V., Vøllestad, L.A. and Poléo, A.B.S. 2002. Cortisol and glucose responses in juvenile brown trout subjected to a fluctuating flow regime in an artificial stream. *Journal of Fish Biology* 60(1), pp. 238–248.

Foroughi, A. F. 2014 [online]. Available at : https://github.com/foroughi/PIV/blob/master/Matlab_Code.m [Accessed: 16 July 2022].

Franca, M.J., Ferreira, R.M.L. and Lemmin, U. 2008. Parameterization of the logarithmic layer of double-averaged streamwise velocity profiles in gravel-bed river flows. *Advances in Water Resources* 31(6), pp. 915–925.

Frenzen, P. and Vogel, C.A. 1995. On the magnitude and apparent range of variation of the von Karman constant in the atmospheric surface layer. *Boundary-Layer Meteorology* 72(4), pp. 371–392.

Frings, R.M. 2008. Downstream fining in large sand-bed rivers. *Earth-Science Reviews* 87(1–2), pp. 39–60.

Gaeuman, D., Schmidt, J.C. and Wilcock, P.R. 2005. Complex channel responses to changes in stream flow and sediment supply on the lower Duchesne River, Utah. *Geomorphology* 64(3–4), pp. 185–206.

García, C.M., Cantero, M.I., Niño, Y. and García, M.H. 2007. Closure to “Turbulence Measurements with Acoustic Doppler Velocimeters”. *Journal of Hydraulic Engineering* 133(11), pp. 1289–1292. Available at: doi: 10.1061/(ASCE)0733-9429(2007)133:11(1289).

Gaudio, R., Miglio, A. and Dey, S. 2010. Non-universality of von Kármán’s κ in fluvial streams. *Journal of Hydraulic Research* 48(5), pp. 658–663.

Gilvear D.J. 1999. Fluvial geomorphology and river engineering: future roles utilizing a fluvial hydrosystems framework. *Geomorphology* 31, pp. 229–245.

Gomez, B. 1983. Temporal Variations in the Particle Size Distribution of Surficial Bed Material : The Effect of Progressive Bed Armouring. *Geografiska Annaler: Series A, Physical Geography* 65(3/4), pp. 183–192.

Gomez, B. 1991. Bedload transport. *Earth Science Reviews* 31(2), pp. 89–132.

Gomez, B. 1993. Roughness of Stable , Armored Gravel Beds. *Water Resource Research* 29(11), pp. 3631–3642.

Goring, D.G. and Nikora, V.I. 2002. Despiking Acoustic Doppler Velocimeter Data. *Journal of hydraulic engineering* 128(1), pp. 117–126.

Grams, P.E. and Wilcock, P.R. 2007. Equilibrium entrainment of fine sediment over a coarse immobile bed. *Water Resources Research* 43(10), p. W10420/1-14.

Grant, G.E. 2012. The Geomorphic Response of Gravel-Bed Rivers to Dams: Perspectives and Prospects. *In: Church, M.; Biron, PM; Roy, AG, eds. Gravel-bed rivers: processes, tools, environments. Chichester, UK: John Wiley & Sons, Ltd*, pp. 165–181.

Grass, A.J. 1971. Structural features of turbulent flow over smooth and rough boundaries. *Journal of Fluid Mechanics* 50(2), pp. 233–255.

Grass, A.J., Stuart, R.J. and Mansour-Tehrani, M. 1991. Vortical Structures and Coherent Motion in Turbulent Flow over Smooth and Rough Boundaries. *Philosophical Transactions of the Royal Society of London. Series A: Physical and Engineering Sciences* 336(1640), pp. 35–65. Available at: http://rsta.royalsocietypublishing.org/cgi/doi/10.1098/rsta.1991.0065.

Gregory, K.J., Gurnell, A.M., Hill, C.T. and Tooth, S. 1994. Stability of the pool-riffle sequence in changing river channels. *Regulated Rivers: Research & Management* 9(1), pp. 35–43.

Gupta, A.D. and Paudyal, G.N. 1985. Characteristics of Free Surface Flow Over Gravel Bed. *Journal of Irrigation and Drainage Engineering* 111(4), pp. 299–318.

Han, X., He, G.J. and Fang, H.W. 2017. Double-averaging analysis of turbulent kinetic energy fluxes and budget based on large-eddy simulation. *Journal of Hydrodynamics* 29(4), pp. 567–574. Available at: http://dx.doi.org/10.1016/S1001-6058(16)60769-2.

Han, X., Fang, H.W., Johnson, M.F. and Rice, S.P. 2019. The Impact of Biological Bedforms on Near-Bed and Subsurface Flow: A Laboratory-Evaluated Numerical Study of Flow in the Vicinity of Pits and Mounds. *Journal of Geophysical Research: Earth Surface* 124(7), pp. 1939–1957.

Hanmaiahgari, P.R., Roussinova, V. and Balachandar, R. 2017. Turbulence characteristics of flow in an open channel with temporally varying mobile bedforms. *Journal of Hydrology and Hydromechanics* 65(1), pp. 35–48.

Harby, A. and Halleraker, J.H. 2001. Ecological impacts of hydro peaking in rivers. *International Journal on Hydropower and Dams* 8(4), pp. 132–135.

Harby, A. and Noack, M. 2013. 19 Rapid Flow Fluctuations and Impacts on Fish and the Aquatic Ecosystem. *Ecohydraulics: An Integrated Approach*, pp. 323–335.

Hardy, R.J., Best, J.L., Parsons, D.R. and Marjoribanks, T.I. 2016. On the evolution and form of coherent flow structures over a gravel bed: Insights from whole flow field visualization and measurement. *Journal of geophysical research: earth surface* 121(8), pp. 1472–1493.

Harper, D.M., Smith, C.D. and Barham, P.J. 1992. Habitats as the building blocks for river conservation assessment. *River conservation and management*, pp. 311–319.

Harvey, J.W. and Fuller, C.C. 1998. Effect of enhanced manganese oxidation in the hyporheic zone on basin-scale geochemical mass balance. *Water Resources Research* 34(4), pp. 623–636.

Haschenburger, J.K. 2016. Cross-channel patterns of bed material transport in a poorly sorted sand-bed channel. *Geomorphology* 273, pp. 374–384. Available at: http://dx.doi.org/10.1016/j.geomorph.2016.08.029.

Haynes, H., Vignaga, E. and Holmes, W.M. 2009. Using magnetic resonance imaging for experimental analysis of fine-sediment infiltration into gravel beds. *Sedimentology* 56(7), pp. 1961–1975.

Heathershaw, A.D. 1981. Comparisons of measured and predicted sediment transport rates in tidal currents. *Marine Geology* 42(1–4), pp. 75–104.

Hey, R.D. 1988. Bar form resistance in gravel-bed rivers. *Journal of Hydraulic Engineerin* 114(12), pp. 1498–1508.

Hey, R.D. and Thorne, C.R. 1986. Stable channels with mobile gravel beds. *Journal of Hydraulic engineering* 112(8), pp. 671–689.

Heywood, M.J.T. and Walling, D.E. 2007. The sedimentation of salmonid spawning gravels in the Hampshire Avon catchment , UK : implications for the dissolved oxygen content of intragravel water and embryo survival. *Hydrological Processes* 21, pp. 770–788.

Higashino, M., Clark, J.J. and Stefan, H.G. 2009. Pore water flow due to near-bed turbulence and associated solute transfer in a stream or lake sediment bed. *Water Resources Research* 45(12), p. W12414/1-17.

Higashino, M. and Stefan, H.G. 2011. Dissolved oxygen demand at the sediment-water interface of a stream: Near-bed turbulence and pore water flow effects. *Journal of Environmental Engineering* 137(7), pp. 531–540.

Hlushkou, D. and Tallarek, U. 2006. Transition from creeping via viscous-inertial to turbulent flow in fixed beds. *Journal of Chromatography A* 1126, pp. 70–85.

Horoshenkov, K. V., Nichols, A., Tait, S.J. and Maximov, G.A. 2013. The pattern of surface waves in a shallow free surface flow. *Journal of Geophysical Research: Earth Surface* 118(3), pp. 1864–1876.

Hosseini, S.A. and Hajibabaei, E. 2020. The effect of grain roughness and bed-load transport on the friction resistance of erodible beds in steep slopes. *Environmental Earth Sciences* 79(181), pp. 1–18. Available at: https://doi.org/10.1007/s12665-020-08922-7.

Hsu, T.-J., Sakakiyama, T. and Liu, P.L.-F. 2002. A numerical model for wave motions and turbulent flows in front of a composite break-water. *Coastal Engineering* 46(1), pp. 25–50.

Huang, A.Y.L., Huang, M.Y.F., Capart, H. and Chen, R.H. 2008. Optical measurements of pore geometry and fluid velocity in a bed of irregularly packed spheres. *Experiments in Fluids* 45(2), pp. 309–321.

Huffman, G.D. and Bradshaw, P. 1972. A note on von Kármán’s constant in low Reynolds number turbulent flows. *Journal of Fluid Mechanics* 53(1), pp. 45–60.

Hupp, C.R., Demas, C.R., Kroes, D.E., Day, R.H. and Doyle, T.W. 2008. Recent sedimentation patterns within the central Atchafalaya Basin, Louisiana. *Wetlands* 28(1), pp. 125–140.

Hupp, C.R., Pierce, A.R. and Noe, G.B. 2009. Floodplain geomorphic processes and environmental impacts of human alteration along coastal plain rivers, USA. *Wetlands* 29(2), pp. 413–429.

Hurther, D. and Lemmin, U. 2001. A Correction Method for Turbulence Measurements with a 3D Acoustic Doppler Velocity Profiler. *Journal of Atmospheric and Oceanic Technology* 18, pp. 446–458.

Hutchins, N. and Marusic, I. 2007. Evidence of very long meandering features in the logarithmic region of turbulent boundary layers. *Journal of Fluid Mechanics* 579, pp. 1–28.

Hwang, H.G. and Lee, J.H. 2018. Secondary flows in turbulent boundary layers over longitudinal surface roughness. *Physical Review Fluids* 3(1), pp. 014608/1–25.

Iseya, F. and Ikeda, H. 1987. Pulsations in Bedload Transport Rates Induced by a Longitudinal Sediment Sorting : A Flume Study Using Sand and Gravel Mixtures. *Geografiska Annaler. Series A, Physical Geography* 69(1), pp. 15–27.

Jackson, P.S. 1981. On the displacement height in the logarithmic velocity profile. *Journal of fluid mechanics* 111, pp. 15–25.

Jackson, R.G. 1976. Sedimentological and fluid-dynamic implications of the turbulent bursting phenomenon in geophysical flows. *Journal of Fluid Mechanics* 77(3), pp. 531–560.

Jain, P. and Ghoshal, K. 2020. An explicit expression for velocity profile in presence of secondary current and sediment in an open channel turbulent flow. *Canadian Journal of Civil Engineering* 48(1), pp. 1–26.

Janssen, F., Cardenas, M.B., Sawyer, A.H., Dammrich, T., Krietsch, J. and de Beer, D. 2012. A comparative experimental and multiphysics computational fluid dynamics study of coupled surface – subsurface flow in bed forms. *Water Resources Research* 48(8), p. W08514/1-16.

Jay Lacey, R.W. and Roy, A.G. 2007. A comparative study of the turbulent flow field with and without a pebble cluster in a gravel bed river. *Water Resources Research* 43(5), p. W05502/1-7.

Jay Lacey, R.W. and Roy, A.G. 2008. Fine-scale characterization of the turbulent shear layer of an instream pebble cluster. *Journal of Hydraulic Engineering* 134(7), pp. 925–936. Available at: http://ascelibrary.org/doi/10.1061/%28ASCE%290733-9429%282008%29134%3A7%28925%29.

Jesson, M. 2015. *MAJ's Velocity Signal Analyser. Installation and User Guide v1.5.63*.

Jimenez, J. 2004. Turbulent Flows Over Rough Walls. *Annual Review of Fluid Mechanics* 36(1), pp. 173–196.

Jin, T. and Liao, Q. 2019. Application of large scale PIV in river surface turbulence measurements and water depth estimation. *Flow Measurement and Instrumentation* 67, pp. 142–152. Available at: https://doi.org/10.1016/j.flowmeasinst.2019.03.001.

Judes, C., Gouraud, V., Capra, H., Maire, A., Barillier, A. and Lamouroux, N. 2020. Consistent but secondary influence of hydropeaking on stream fish assemblages in space and time. *Journal of Ecohydraulics*, pp. 1–15. Available at: https://doi.org/10.1080/24705357.2020.1790047.

Von Karman, T. 1930. Mechanische änlichkeit und turbulenz. *Nachrichten von der Gesellschaft der Wissenschaften zu Göttingen, Mathematisch-Physikalische Klasse*, pp. 58–76.

Keirsbulck, L., Labraga, L., Mazouz, A. and Tournier, C. 2002. Surface roughness effects on turbulent boundary layer structures. *Journal of Fluids Engineering* 124(1), pp. 127–135.

Keller, E.A. 1971. Areal sorting of bed-load material: The hypothesis of velocity reversal. *Geological Society of America Bulletin* 82(3), pp. 753–756.

Kennedy, J.F. 1969. The formation of sediment ripples, dunes, and antidunes. *Annual review of fluid mechanics* 1(1), pp. 147–168.

Kim, H. and Lee, K.K. 2018. A comparison of the water environment policy of Europe and South Korea in response to climate change. *Sustainability* 10(2), pp. 384/1–9.

Kim, K.C. and Adrian, R.J. 1999. Very large-scale motion in the outer layer. *Physics of Fluids* 11(2), pp. 417–422.

Kim, T., Blois, G., Best, J.L. and Christensen, K.T. 2018. Experimental study of turbulent flow over and within cubically packed walls of spheres: Effects of topography, permeability and wall thickness. *International Journal of Heat and Fluid Flow* 73, pp. 16–29. Available at: https://doi.org/10.1016/j.ijheatfluidflow.2018.06.004.

Kim, T., Blois, G., Best, J.L. and Christensen, K.T. 2019. PIV measurements of turbulent flow overlying large, cubic- and hexagonally-packed hemisphere arrays. *Journal of Hydraulic Research* 58(2), pp. 363–383.

Kirchner, J.W., Dietrich, W.E., Iseya, F. and Ikeda, H. 1990. The variability of critical shear stress, friction angle, and grain protrusion in water-worked sediments. *Sedimentology* 37(4), pp. 647–672.

Kirkbride, A.D. 1993. Observations of the influence of bed roughness on turbulence structure in depth limited flows over gravel beds. *Turbulence: perspectives on flow and sediment transport*, pp. 185–196.

Kirkbride, A.D. and Ferguson, R. 1995. Turbulent flow structure in a gravel-bed river: Markov chain analysis of the fluctuating velocity profile. *Earth Surface Processes and Landforms* 20, pp. 721–733.

Kirkbride, A.D. and McLelland, S.J. 1994. Visualization of the turbulent flow structure in a gravel-bed river. *Earth Surface Processes and Landforms* 19(9), pp. 819–825.

Kironoto, B.A. and Graf, W.H. 1994. Turbulence Characteristics in Rough Uniform Open-Channel Flow. *Proceedings of the Institution of Civil Engineers - Water Maritime and Energy* 106(4), pp. 333–344. Available at:

http://www.icevirtuallibrary.com/doi/10.1680/iwtme.1995.28114.

Kline, S.J., Reynolds, W.C., Schraub, F.A. and Runstadler, P.W. 1967. The structure of turbulent boundary layers. *Journal of Fluid Mechanics* 30(4), pp. 741–773.

Knopp, T., Eisfeld, B. and Calvo, J.B. 2009. A new extension for k-ω turbulence models to account for wall roughness. *International Journal of Heat and Fluid Flow* 30(1), pp. 54–65. Available at: http://dx.doi.org/10.1016/j.ijheatfluidflow.2008.09.009.

Koca, K., Noss, C., Anlanger, C., Brand, A. and Lorke, A. 2017. Performance of the Vectrino Profiler at the sediment--water interface. *Journal of Hydraulic Research* 55(4), pp. 573–581.

Koll, K. 2002. *Feststofftransport und geschwindigkeitsverteilung in raugerinnen*. Diss., Univ. Karlsruhe, Fak. f. Bauingenieur- und Vermessungswesen.

Koll, K. 2006. Parameterisation of the vertical velocity profile in the wall region over rough surfaces. In: *Proceedings of the International Conference on Fluvial Hydraulics, River Flow,edited by R. M. L. Ferreira et al.Taylor and Francis, London.* pp. 163–172.

Kondolf, G.M. and Schmitt, R.J. 2018. Dams , Sediment Discontinuity , and Management Responses. *hydrolink. Reservoir sedimentation* (3), pp. 68–71.

Kondolf, G.M. and Wolman, M.G. 1993. The sizes of salmonid spawning gravels. *Water Resources Research* 29(7), pp. 2275–2285.

Kraus, N.C., Lohrmann, A. and Cabrera, R. 1994. New Acoustic Meter for Measuring 3D Laboratory Flows. *Journal of Hydraulic Engineering* 120(3), pp. 406–412. Available at: http://ascelibrary.org/doi/10.1061/%28ASCE%290733-9429%281994%29120%3A3%28406%29.

Krogstad, P.Å. and Antonia, R.A. 1999. Surface roughness effects in turbulent boundary layers. *Experiments in Fluids* 27(5), pp. 450–460.

Kuo, J.T.W., Yu, L. and Meng, E. 2012. Micromachined Thermal Flow Sensors — A Review. *Micromachines* 3(3), pp. 550–573.

Lamouroux, N., Capra, H., Pouilly, M. and Souchon, Y. 1999. Fish habitat preferences in large streams of southern France. *Freshwater Biology* 42(4), pp. 673–687.

Lanzoni, S. 2000a. Experiments on bar formation in a straight flume 1. Uniform sediment. *Water Resources Research* 36(11), pp. 3337–3349.

Lanzoni, S. 2000b. Experiments on bar formation in a straight flume 2. Graded sediment. *Water Resources Research* 36(11), pp. 3351–3363.

Lapointe, M. 1992. Burst-like sediment suspension events in a sand bed river. *Earth Surface Processes and Landforms* 17(3), pp. 253–270.

Leonardi, A., Pokrajac, D., Roman, F., Zanello, F. and Armenio, V. 2018. Surface and subsurface contributions to the buildup of forces on bed particles. *Journal of Fluid Mechanics* 851, pp. 558–572.

Leopold, L., Wolman, M.G. and Miller, J.P. 1964. Fluvial processes in geomorphology: San Francisco.

Liao, T., Massoudi, N., McHood, M., Stokoe, K.H., Jung, M.J. and Menq, F.Y. 2013. Normalized shear modulus of compacted gravel. In: *Proceedings of the 18th International Conference on Soil Mechanics and Geotechnical Engineering, Paris*. pp. 1535–1538.

Liu, D., Liu, X., Fu, X. and Wang, G. 2016. Quantification of the bed load effects on turbulent open-channel flows. *Journal of Geophysical Research: Earth Surface* 121(4), pp. 767–789.

Lo, T.S., L'vov, V.S., Pomyalov, A. and Procaccia, I. 2005. Estimating von Kármán's constant from homogeneous turbulence. *Europhysics Letters* 72(6), pp. 943–949.

Lohrmann, A., Cabrera, R. and Kraus, N.C. 1994. Acoustic-Doppler velocimeter (ADV) for laboratory use. In: *Fundamentals and advancements in hydraulic measurements and experimentation*. pp. 351–365.

Lorke, A., Müller, B., Maerki, M. and Wüest, A. 2003. Breathing sediments: The control of diffusive transport across the sediment-water interface by periodic boundary-layer turbulence. *Limnology and Oceanography* 48(6), pp. 2077–2085.

MacVicar, B.J. and Roy, A.G. 2007. Hydrodynamics of a forced riffle pool in a gravel bed river: 2. Scale and structure of coherent turbulent events. *Water Resources Research* 43(12), p. W12402/1-17.

Maddock, I. and Hill, G. 2007. *The Rivers of Worcestershire: a Baseline Geomorphological Survey*. Report undertaken for Herefordshire and Worcestershire Earth Heritage Trust and Worcestershire County Council.

Maddux, T.B., Nelson, J.M. and McLean, S.R. 2003. Turbulent flow over three-dimensional dunes: 1. Free surface and flow response. *Journal of Geophysical Research* 108(F1), pp. 10/1-20.

Madej, M.A. 2001. Development of channel organization and roughness following sediment pulses in single-thread, gravel bed rivers. *Water Resources Research* 37(8), pp. 2259–2272.

Manes, C., Pokrajac, D. and McEwan, I. 2007. Double-Averaged Open-Channel Flows with Small Relative Submergence. *Journal of Hydraulic Engineering* 133(8), pp. 896–904. Available at: http://ascelibrary.org/doi/10.1061/(ASCE)0733-9429(2007)133:8(896).

Manes, C., Pokrajac, D., Mcewan, I. and Nikora, V. 2009. Turbulent structure of open channel flows over permeable and impermeable beds : A comparative study. *Physics of Fluids* 21(12), p. 125109.

Marusic, I., McKeon, B.J., Monkewitz, P.A., Nagib, H.M., Smits, A.J. and Sreenivasan, K.R. 2010. Wall-bounded turbulent flows at high Reynolds numbers: Recent advances and key issues. *Physics of Fluids* 22(6), pp. 065103/1–24.

Matthes, G.H. 1947. Macroturbulence in natural stream flow. *Eos, Transactions*

American Geophysical Union 28(2), pp. 255–265.

McLean, S.R., Nikora, V.I. and Coleman, S.E. 2008. Double-averaged velocity profiles over fixed dune shapes. *Acta Geophysica* 56(3), pp. 669–697.

McLelland, S.J. and Nicholas, A.P. 2000. A new method for evaluating errors in high-frequency ADV measurements. *Hydrological processes* 14(2), pp. 351–366.

Mendoza, C. and Zhou, D. 1992. Effects of porous bed on turbulent stream flow above bed. *Journal of Hydraulic Engineering* 118(9), pp. 1222–1240.

Mignot, E., Bartherelemy, E. and Hurther, D. 2009. Double-averaging analysis and local flow characterization of near-bed turbulence in gravel-bed channel flows. *Journal of Fluid Mechanics* 618, pp. 279–303.

Mignot, E., Hurther, D. and Barthelemy, E. 2009. On the structure of shear stress and turbulent kinetic energy flux across the roughness layer of a gravel-bed channel flow. *Journal of Fluid Mechanics* 638, pp. 423–452.

Milhous, R.T. 1973. *Sediment transport in a gravel-bottomed stream*. PhD thesis, Dept. of Civil Engineering, Oregon State University, U.S.A.

Mohajeri, S.H. 2014. *Hydrodynamics of Gravel Bed Flows (Implication on Colmation)*. Doctoral dissertation, Queen Mary University of London.

Mohajeri, S.H., Grizzi, S., Righetti, M., Romano, G.P. and Nikora, V. 2015. The structure of gravel-bed flow with intermediate submergence: A laboratory study. *Water Resources Research* 51(11), pp. 9232–9255.

Mohajeri, S.H., Righetti, M., Wharton, G. and Romano, G.P. 2016. On the structure of turbulent gravel bed flow: Implications for sediment transport. *Advances in Water Resources* 92, pp. 90–104. Available at: http://dx.doi.org/10.1016/j.advwatres.2016.04.001.

Monsalve, A., Yager, E.M. and Schmeeckle, M.W. 2017. Effects of Bed Forms and Large Protruding Grains on Near-Bed Flow Hydraulics in Low Relative Submergence Conditions. *Journal of Geophysical Research: Earth Surface* 122(10), pp. 1845–1866.

Montgomery, D.R. and Buffington, J.M. 1997. Channel-reach morphology in mountain drainage basins. *Geological Society of America Bulletin* 109(5), pp. 596–611.

Monty, J.P., Hutchins, N., Ng, H.C.H., Marusic, I. and Chong, M.S. 2009. A comparison of turbulent pipe, channel and boundary layer flows. *Journal of Fluid Mechanics* 632, pp. 431–442.

Morris, H.M. 1955. Flow in rough conduits. *Transactions of the American Society of Civil Engineers* 120(1), pp. 373–398.

Mortensen, N.G., Larsen, S.E., Troen, I. and Mikkelsen, T. 1987. Two-years-worth of turbulence data recorded by a sonic-anemometer-based data acquisition system. *In 6. Symposium: Meteorological observations and instrumentation*, pp. 393–396.

Murthy, V.N.S. 2002. *Geotechnical engineering: principles and practices of soil mechanics and foundation engineering*. Boca Raton: CRC press.

Nakagawa, H., Nezu, I. and Ueda, H. 1975. Turbulence of open channel flow over smooth and rough beds. In: *Proceedings of the Japan Society of Civil Engineers*. pp. 155–168.

Nakagawa, H. and Nezu, I. 1977. Prediction of the contributions to the Reynolds stress from bursting events in open-channel flows. *Journal of Fluid Mechanics* 80(1), pp. 99–128.

Nakagawa, H. and Nezu, I. 1980. Turbulent behaviours of open channel flow with permeable beds'. In: *Proceedings of the International Conference on Water Re- sources Developme*. pp. 661–670.

Naot, D. and Rodi, W. 1982. Calculation of secondary currents in channel flow. *Journal of the Hydraulics Division* 108(8), pp. 948–968.

Navaratnam, A.C.U. and Aberle, J. 2017. The effect of bed porosity on near-bed turbulent flow characteristics in gravel-bed rivers. *Vann* 2, pp. 181–190.

Navaratnam, C.U., Aberle, J., Qin, J. and Henry, P.Y. 2018. Influence of gravel-bed porosity and grain orientation on bulk flow resistance. *Water* 10(5), pp. 561/1–16.

Neave, M. 2014. Gravel-bed rivers : processes , tools , environments. *Australian Geographer* 45(4), pp. 565–567.

Nelson, J.M., McLean, S.R. and Wolfe, S.R. 1993. Mean flow and turbulence fields over two-dimensional bed forms. *Water Resources Research* 29(12), pp. 3935–3953.

Nelson, J.M., Shreve, R.L., McLean, S.R. and Drake, T.G. 1995. Role of Near-Bed Turbulence Structure in Bed Load Transport and Bed Form Mechanics. *Water Resources Research* 31(8), pp. 2071–2086.

Nezu, I. 1977. *Turbulent structure in open-channel flows*. English translation of the Japanese dissertation of Iehisa Nezu.

Nezu, I. 2005. Open-Channel Flow Turbulence and Its Research Prospect in the 21st Century. *Journal of Hydraulic Engineering* 131(4), pp. 229–246.

Nezu, I. and Nakagawa, H. 1984. Cellular secondary currents in straight conduit. *Journal of Hydraulic Engineering* 110(2), pp. 173–193.

Nezu, I. and Nakagawa, H. 1993. Turbulence in open channels. *IAHR/AIRH Monograph. Balkema, Rotterdam, The Netherlands*.

Nezu, I. and Rodi, W. 1986. Open-channel flow measurements with a laser Doppler anemometer. *Journal of Hydraulic Engineering* 112(5), pp. 335–355.

Nguyen, C. 2012. Basics of Turbulent Flow. *Mit*, pp. 1–10.

Nikora;, V., McLean, S., Coleman, S., Pokrajac, D., McEwan, I., Campbell, L., Aberle, J., Clunie, D. and Koll, K. 2007. Double-Averaging Concept for Rough-Bed Open-Channel and Overland Flows: Applications. *Journal of Hydraulic Engineering* 133(8), pp. 884–895.

Nikora, V., Goring, D., McEwan, I. and Griffiths, G. 2001. Spatially averaged open-channel flow over rough bed. *Journal of Hydraulic engineering* 127(2), pp. 123–133.

Nikora, V., Koll, K., McEwan, I., McLean, S. and Dittrich, A. 2004. Velocity Distribution in the Roughness Layer of Rough-Bed Flows. *Journal of Hydraulic Engineering* 130(10), pp. 1036–1042. Available at: http://ascelibrary.org/doi/10.1061/%28ASCE%290733-9429%282004%29130%3A10%281036%29.

Nikora, V. 2007. 3 Hydrodynamics of gravel-bed rivers: scale issues. *Developments in Earth Surface Processes* 11, pp. 61–81.

Nikora, V., Mcewan, I., Mclean, S., Coleman, S., Pokrajac, D. and Walters, R. 2007. Double-Averaging Concept for Rough-Bed Open-Channel and Overland Flows : Theoretical Background. *Journal of Hydraulic Engineering* 133(8), pp. 873–883.

Nikora, V. and Goring, D. 2000. Flow turbulence over fixed and weakly mobile gravel beds. *Journal of Hydraulic Engineering* 126(9), pp. 679–690.

Nikora, V. and Roy, A.. 2012. Secondary Flows in Rivers : Theoretical Framework , Recent Advances , and Current Challenges. *Gravel bed rivers: Processes, tools, environments* (3–22).

Nikora, V.I., Goring, D.G. and Biggs, B.J.F. 1998. On gravel-bed roughness characterization. *Water Resources Research* 34(3), pp. 517–527.

Nikora, V.I., Koll, K., McLean, S.R., Ditrich, A. and Aberle, J. 2002. Zero-plane displacement for rough-bed open-channel flows. In: *International Conference on Fluvial Hydraulics River Flow, 2002, September 4–6, 2002, Louvain-la-Neuve, Belgium*. pp. 83–92.

Nikora, V.I. and Goring, D.G. 1998. ADV measurements of turbulence: Can we improve their interpretation? *Journal of hydraulic engineering ASCE* 124(6), pp. 630–634.

Nikora, V.I. and Rowiński, P.M. 2008. Rough-bed flows in geophysical, environmental, and engineering systems: Double-Averaging Approach and its applications. *Acta Geophysica* 56(3), pp. 529–533.

Nikora, V.I. and Smart, G.M. 1997. Turbulence characteristics of New Zealand gravel-bed rivers. *Journal of Hydraulic Engineering* 123(9), pp. 764–773.

Nikuradse, J. 1933. Stromungsgesetze in rauhen Rohren. *VDI-Forschungsheft* 361.

Nilsson, C., Reidy, C.A., Dynesius, M. and Revenga, C. 2005. Fragmentation and flow regulation of the world’s large river systems. *Science* 308(5720), pp. 405–408.

Noack, M., Ortlepp, J. and Wieprecht, S. 2016. An Approach to Simulate Interstitial Habitat Conditions During the Incubation Phase of Gravel-Spawning Fish. *River Research and Applications* 33(2), pp. 192–201.

Nortek 2018. The Comprehensive Manual for Velocimeters. *Nortek AS*.

Nortek, A.S. 2000. Nortek 10 MHz Velocimeter Operations Manual. *Nortek AS*, pp. 1–30.

Nortek, A.S. 2004. Vectrino Velocimeter User Guide (Rev. C). *Nortek AS: Vangkroken 2, Norway*.

Osaro, I.L. 2018. *Turbulent Suspension and Sediment Grains Transport in Natural Flows*. Doctoral dissertation, Royal Holloway, University of London.

Oveici, E., Tayari, O. and Jalalkamali, N. 2020. Experimental (ADV & PIV) and Numerical (CFD) Comparisons of 3D Flow Pattern around Intact and Damaged Bridge Piers. *Journal of Science & Technology* 28(2), pp. 523–544.

Packman, A.I., Salehin, M. and Zaramella, M. 2004. Hyporheic Exchange with Gravel Beds: Basic Hydrodynamic Interactions and Bedform-Induced Advective Flows. *Journal of Hydraulic Engineering* 130(7), pp. 647–656.

Padhi, E., Penna, N., Dey, S. and Gaudio, R. 2018a. Hydrodynamics of water-worked and screeded gravel beds: A comparative study. *Physics of Fluids* 30(8), p. 085105.

Padhi, E., Penna, N., Dey, S. and Gaudio, R. 2018b. Spatially averaged dissipation rate in flows over water-worked and screeded gravel beds. *Physics of Fluids* 30(12), pp. 125106/1–14.

Padhi, E., Dey, S., Penna, N. and Gaudio, R. 2020. Conditional Turbulence Characteristics in Water-Worked and Screeded Gravel-Bed Flows. *Journal of Hydraulic Engineering* 146(2), pp. 04019052/1–13.

Pagliara, S., Das, R. and Carnacina, I. 2008. Flow resistance in large-scale roughness condition. *Canadian Journal of Civil Engineering* 35(11), pp. 1285–1293. Available at: http://www.nrcresearchpress.com/doi/10.1139/L08-068.

Pan, W.H., Liu, S.H. and Huang, L. 2018. Coupled three-layer model for turbulent flow over large-scale roughness: On the hydrodynamics of boulder-bed streams. *Geomorphology* 303, pp. 122–132. Available at: https://doi.org/10.1016/j.geomorph.2017.11.022.

Parker, G., Dhamotharan, S. and Stefan, H. 1982. Model experiments on mobile, paved gravel bed streams. *Water Resources Research* 18(5), pp. 1395–1408.

Parker, G. and Klingeman, P.C. 1982. On why gravel bed streams are paved. *Water Resources Research* 18(5), pp. 1409–1423.

Parker, G. and Peterson, A.W. 1980. Bar resistance of gravel-bed streams. *Journal of the Hydraulics Division* 106(10), pp. 1559–1575.

Peloutier, V. 1998. Flume study of the deposition of fine sediment into river gravel. University of Glasgow.

Perry, A.E. and Li, J.D. 1990. Experimental support for the attached-eddy hypothesis in zero-pressure-gradient turbulent boundary layers. *Journal of Fluid Mechanics* 218, pp. 405–438.

Planchon, O., Silvera, N., Gimenez, R., Favis-Mortlock, D., Wainwright, J., Le Bissonnais, Y. and Govers, G. 2005. An automated salt-tracing gauge for flow-velocity measurement. *Earth Surface Processes and Landforms* 30(7), pp. 833–844.

Pokrajac, D., Finnigan, J.J., Manes, C., McEwan, I. and Nikora, V. 2006. On the definition of the shear velocity in rough bed open channel flows. *Proceedings of the International Conference on Fluvial Hydraulics - River Flow* 1, pp. 89–98.

Pokrajac, D., Manes, C. and McEwan, I. 2007. Peculiar mean velocity profiles within a porous bed of an open channel. *Physics of Fluids* 19(9), pp. 098109/1–4.

Pokrajac, D. and Manes, C. 2009. Velocity measurements of a free-surface turbulent flow penetrating a porous medium composed of uniform-size spheres. *Transport in Porous Media* 78(3), pp. 367–383.

Powell, D.M. 1998. Patterns and processes of sediment sorting in gravel-bed rivers. *Progress in Physical Geography* 22(1), pp. 1–32. Available at: http://ppg.sagepub.com/cgi/doi/10.1177/030913339802200101.

Powell, D.M., Reid, I. and Laronne, J.B. 2001. Evolution of bed load grain size distribution with increasing flow strength and the effect of flow duration on the caliber of bed load sediment yield in ephemeral gravel bed rivers. *Water Resources Research* 37(5), pp. 1463–1474.

Prandtl, L. 1925. ericht über Untersuchungen zur ausgebildeten Turbulenz. *ZAMM-Journal of Applied Mathematics and Mechanics/Zeitschrift für Angewandte Mathematik und Mechanik* 5(2), pp. 136–139.

Precht, E., Janssen, F. and Huettel, M. 2006. Near-bottom performance of the Acoustic Doppler Velocimeter (ADV) - A comparative study. *Aquatic Ecology* 40(4), pp. 481–492.

Prestegaard, K.L. 1983. Bar resistance in gravel bed streams at bankfull stage. *Water Resources Research* 19(2), pp. 472–476.

Prinos, P., Sofialidis, D. and Keramaris, E. 2003. Turbulent flow over and within a porous bed. *Journal of Hydraulic Engineering* 129(9), pp. 720–733.

Pu, J.H., Tait, S., Guo, Y., Huang, Y. and Hanmaiahgari, P.R. 2018. Dominant features in three-dimensional turbulence structure: comparison of non-uniform accelerating and decelerating flows. *Environmental Fluid Mechanics* 18(2), pp. 395–416.

Qi, M., Li, J., Chen, Q. and Zhang, Q. 2018. Roughness effects on near-wall turbulence modelling for open-channel flows. *Journal of Hydraulic Research* 56(5), pp. 648–661. Available at: https://www.tandfonline.com/doi/full/10.1080/00221686.2017.1399931.

Radecki-pawlik, A., Carling, P.A., Słowik-Opoka, E., Leszek, K. and Breakspeare, R. 2006. Field investigations of sand-gravel bed forms within the Raba River, Poland. *River Flow2006 – Ferreira, Alves, Leal & Cardoso (eds)*, pp. 979–984.

Ran, Q.H., Li, W., Liao, Q., Tang, H.L. and Wang, M.Y. 2016. Application of an automated LSPIV system in a mountainous stream for continuous flood flow measurements. *Hydrological Processes* 30(17), pp. 3014–3029.

Raupach, M.R., Antonia, R.A. and Rajagopalan, S. 1991. Rough-wall turbulent boundary layers. *Applied Mechanics Reviews* 44(1), pp. 1–25.

Raven, P.J., Holmes, N.T.H., Dawson, F.H., Fox, P.J.A., Everard, M., Fozzard, I.R. and Rouen, K.J. 1998. *River Habitat Quality the physical character of rivers and streams in the UK and Isle of Man*. Bristol: Environment Agency.

Reidenbach, M.A., Limm, M., Hondzo, M. and Stacey, M.T. 2010. Effects of bed roughness on boundary layer mixing and mass flux across the sediment-water interface. *Water Resources Research* 46(7), p. W07530/ 1-15.

Rice, S.P. and Church, M. 2010. Grain-size sorting within river bars in relation to downstraming along a wandering channel. *Sedimentology* 57, pp. 232–251.

Richmond, M.C., Deng, Z., Guensch, G.R., Tritico, H. and Pearson, W.H. 2007. Mean flow and turbulence characteristics of a full-scale spiral corrugated culvert with implications for fish passage. *Ecological Engineering* 30(4), pp. 333–340.

Rifflart, R., Carrel, G., Le Coarer, Y. and Fontez, B.N.T. 2009. Spatio-temporal patterns of fish assemblages in a large regulated alluvial river. *Freshwater Biology* 54(7), pp. 1544–1559.

Van Rijn, L.C. 1984. Sediment transport, PART I: bed load transport. *Journal of Hydraulic Engineering-* 110(10), pp. 1431–1456.

Van Rijn, L.C. 1993. *Principles of sediment transport in rivers, Estuaries and coastal seas*. Aqua publications Blokzijl.

Robert, A. 2003. *River processes-An introduction to fluvial dynamics*. London: Hodder Education.

Robinson, S.K. 1991. Coherent motions in the turbulent boundary layer. *Annual Review of Fluid Mechanics* 23(1), pp. 601–639.

Rosport, M. 1997. Fließwiderstand und Sohlstabilität steiler Fließgewässer unter Berücksichtigung gebirgsbachtypischer Sohlstrukturen. Mitt. des Instituts für Wasserwirtschaft und Kulturtechnik, Univ. Karlsruhe, Heft 196.

Rouzes, M., Moulin, F.Y., Florens, E. and Eiff, O. 2019. Low relative-submergence effects in a rough-bed open-channel flow. *Journal of Hydraulic Research* 57(2), pp. 139–166.

Roy, A.G., Buffin-Belanger, T. and Deland, S. 1996. Scales of turbulent coherent flow structures in a gravel-bed river. *In Coherent flow structures in open channels* (ed. P. J. Ashworth, S. J. Bennett, J. L. Best & S. J. Mclelland), pp. 147–164. John Wiley.

Roy, A.G., Biron, P.M., Buffin-banger, T. and Levasseu, M. 1999. Combined visual and quantitative techniques in the study of natural turbulent flows. *Water Resources Research* 35(3), pp. 871–877.

Roy, A.G., Buffin-Bélanger, T., Lamarre, H. and Kirkbride, A.D. 2004. Size, shape and dynamics of large-scale turbulent flow structures in a gravel-bed river. *Journal of Fluid Mechanics* (500), pp. 1–27.

Rusello, P.J. 2012. Near boundary measurements with a profiling acoustic Doppler velocimeter. *In Hydraulic Measurement and Experimental Methods Conference*.

Salehin, M., Packman, A.I. and Paradis, M. 2004. Hyporheic exchange with heterogeneous streambeds: Laboratory experiments and modeling. *Water Resources Research* 40(11), p. W11504/1-16.

Saltveit, S.J., Halleraker, J.H., Arnekleiv, J. V. and Harby, A. 2001. Field experiments on stranding in juvenile atlantic salmon (Salmo Salar) and brown trout (Salmo Trutta) during rapid flow decreases caused by hydropeaking. *Regulated Rivers: Research & Management* 17(4–5), pp. 609–622.

Saremi, S., Alyari, A., Feili, D. and Seidel, H. 2014. A MEMS-based hot-film thermal anemometer with wide dynamic measurement range. *In Sensors 2014 IEEE*, pp. 420–423.

Sarkar, S., Papanicolaou, A.N. and Dey, S. 2016. Turbulence in a Gravel-Bed Stream with an Array of Large Gravel Obstacles. *Journal of Hydraulic Egineering* 142(11), pp. 04016052/1–16.

Sarkar, S., Ali, S.Z. and Dey, S. 2019. Turbulence in wall-wake flow downstream of an isolated dunal bedform. *Water* 11(10), pp. 1975/1–18.

Sarkar, S. and Dey, S. 2010. Double-averaging turbulence characteristics in flows over a gravel bed. *Journal of Hydraulic Research* 48(6), pp. 801–809.

Sayre, W.W. and Albertson, M.L. 1963. Roughness spacing in rigid open channels. *Transactions of the American Society of Civil Engineers* 128(1), pp. 343–372.

Schalchli, U. 1992. The Clogging of Coarse Gravel River Beds by Fine Sediment. *Hydrobiologia* 235(236), pp. 189–197. Available at: http://search.proquest.com/docview/19159373?accountid=29008.

Schälchli, U. 1995. Basic equations for siltation of riverbeds. *Journal of Hydraulic Engineering* 121(3), pp. 274–287.

Schlichting, H. 1936. Experimentelle untersuchungen zum rauhigkeitsproblem. *Archive of Applied Mechanics* 7(1), pp. 1–34.

Scott, G.D. 1960. Packing of spheres: Packing of equal spheres. *Nature* 188(4754), pp. 908–909.

Sear, D.A. and Newson, M.D. 2004. The hydraulic impact and performance of a lowland rehabilitation scheme based on pool-riffle installation: The River Waveney, Scole, Suffolk, UK. *River Research and Applications* 20(7), pp. 847–863.

Shvidchenko, A.B. and Pender, G. 2000. Initial motion of streambeds composed of coarse uniform sediments. *Proceedings of the Institution of Civil Engineers-Water and Maritime*

Engineering 142(4), pp. 217–227.

Silva, A.T., Santos, J.M., Ferreira, M.T., Pinheiro, A.N. and Katopodis, C. 2011. Effects of water velocity and turbulence on the behaviour of Iberian barbel (Luciobarbus bocagei, Steindachner 1864) in an experimental pool-type fishway. *River Research and Applications* 27(3), pp. 360–373.

Simpson, S.C. and Meixner, T. 2012. Modeling effects of floods on streambed hydraulic conductivity and groundwater-surface water interactions. *Water Resources Research* 48(2), p. W02515/1-13.

Singh, A., Lanzoni, S., Wilcock, P.R. and Foufoula-Georgiou, E. 2011. Multiscale statistical characterization of migrating bed forms in gravel and sand bed rivers. *Water Resources Research* 47(12), p. W12526/1-26.

Singh, K.M., Sandham, N.D. and Williams, J.J.R. 2007. Numerical Simulation of Flow over a Rough Bed. *Journal of Hydraulic Engineering* 133(4), pp. 386–398.

Sirovlch, L. and Karlsson, S. 1997. Turbulent drag reduction by passive mechanisms. *Nature* 388(6644), pp. 753–755.

Smart, G.M. 1999. Turbulent velocity profiles and boundary shear in gravel bed rivers. *Journal of Hydraulic Engineering* 125(2), pp. 106–116.

Smart, P.L. and Laidlaw, I.M.S. 1977. An evaluation of some fluorescent dyes for water tracing. *Water Resources Research* 13(1), pp. 15–33. Available at: http://www.agu.org/pubs/crossref/1977/WR013i001p00015.shtml.

Smith, D.L., Brannon, E.L., Shafii, B. and Odeh, M. 2006. Use of the Average and Fluctuating Velocity Components for Estimation of Volitional Rainbow Trout Density. *Transactions of the American Fisheries Society* 135(2), pp. 431–441.

Smith, N.D. 1971. Transverse Bars and Braiding in the Lower Platte River, Nebraska. *Geological Society of America Bulletin* 82(12), pp. 3407–3420.

Smith, N.D. 1974. Sedimentology and Bar Formation in the Upper Kicking Horse River , a Braided Outwash Stream. *The Journal of Geology* 82(2), pp. 205–223.

Soulsby, C., Youngson, A.F., Moir, H.J. and Malcolm, I.A. 2001. Fine sediment influence on salmonid spawning habitat in a lowland agricultural stream: A preliminary assessment. *The Science of the Total Environment* 265(1–3), pp. 295–307.

Spiller, S.M., Rüther, N. and Baumann, B. 2015. Form-induced stress in non-uniform steady and unsteady open channel flow over a static rough bed. *International Journal of Sediment Research* 30(4), pp. 297–305. Available at: http://dx.doi.org/10.1016/j.ijsrc.2014.10.002.

Steffler, P.M., Rajaratnam, N. and Peterson, A.W. 1985. LDA measurements in open channel. *Journal of Hydraulic Engineering* 111(1), pp. 119–130.

Stephenson, D.J. 1979. *Rockfill in hydraulic engineering*. Elsevier.

Stewart, M.T., Cameron, S.M., Nikora, V.I., Zampiron, A. and Marusic, I. 2019. Hydraulic resistance in open-channel flows over self-affine rough beds. *Journal of Hydraulic Research* 57(2), pp. 183–196. Available at: https://doi.org/10.1080/00221686.2018.1473296.

Stoesser, T., Fröhlich, J. and Rodi, W. 2007. Turbulent Open-Channel Flow Over a Permeable Bed. *32th IAHR Congress* 32(1), p. 189. Available at: https://tu-dresden.de/ing/maschinenwesen/ism/psm/ressourcen/dateien/mitarbeiter/froehlich/publications/Stoesser_Froehlich_Rodi_IAHR_07.pdf?lang=en.

Stoesser, T. 2010. Physically realistic roughness closure scheme to simulate turbulent channel flow over rough beds within the framework of LES. *Journal of Hydraulic Engineering* 136(10), pp. 812–819.

Strom, K.B. and Papanicolaou, A.N. 2007. ADV Measurements around a Cluster Microform in a Shallow Mountain Stream. *Journal of Hydraulic Engineering* 133(12), pp. 1379–1389.

Stubbs, A., Stoesser, T. and Bockelmann-evans, B. 2018. Developing an Approximation of a Natural , Rough Gravel Riverbed Both Physically and Numerically. *Geosciences* 8(12), pp. 449/1–14.

Sulaiman, M.S., Sinnakaudan, S.K. and Shukor, M.R. 2013. Near bed turbulence measurement with acoustic doppler velocimeter (ADV). *KSCE Journal of Civil Engineering* 17(6), pp. 1515–1528.

Sumer, B.M., Kozakiewicz, A., Fredsøe, J. and Deigaard, R. 1996. Velocity and concentration profiles in sheet-flow layer of movable bed. *Journal of Hydraulic Engineering* 122(10), pp. 549–558.

Surian, N. 2002. Downstream variation in grain size along an Alpine river: analysis of controls and processes. *Geomorphology* 43(1–2), pp. 137–149.

Sutherland, A.J. 1967. Proposed mechanism for sediment entrainment by turbulent flows. *Journal of Geophysical Research* 72(24), pp. 6183–6194.

Tachie, M.F., James, D.F. and Currie, I.G. 2003. Velocity measurements of a shear flow penetrating a porous medium. *Journal of Fluid Mechanics* 493, pp. 319–343.

Tan, L. and Curran, J.C. 2012. Comparison of turbulent flows over clusters of varying density. *Journal of Hydraulic Engineering* 138(12), pp. 1031–1044.

Tauro, F., Porfiri, M. and Grimaldi, S. 2014. Orienting the camera and firing lasers to enhance large scale particle image velocimetry for streamflow monitoring. *Water Resources Research* 50(9), pp. 7470–7483.

Tenzin, R.Y., Ricardo, A.M. and Ferreira, R.M.L. 2019. Hydrodynamic Characterization of Gravel River Flows: Influence of Bed Hydraulic Conductivity. *E-proceedings of the 38th IAHR World Congress* 38, pp. 1839–1849.

Thompson, D.M., Nelson, J.M. and Wohl, E.E. 1998. Interactions between pool geometry and hydraulics. *Water Resources Research* 34(12), pp. 3673–3681.

Thompson, D.M. 2018. Pool–Riffle Sequences. *Reference Module in Earth Systems and Environmental Sciences; Elsevier: Amsterdam, The Netherlands*.

Thompson, D.M. and Hoffman, K.S. 2001. Equilibrium pool dimensions and sediment-sorting patterns in coarse-grained, New England channels. *Geomorphology* 38(3–4), pp. 301–316.

Thompson, L.C. 2011. Hydropower-related pulsed-flow impacts on stream fishes : a brief review, conceptual model , knowledge gaps , and research needs. *Reviews in Fish Biology and Fisheries* 21(4), pp. 713–731.

Thomson, J.R., Taylor, M.P., Fryirs, K.A. and Brierley, G.J. 2001. A geomorphological framework for river characterization and habitat assessment. *Aquatic Conservation: Marine and Freshwater Ecosystems* 11(5), pp. 373–389.

Thorne, C.R., Allen, R.G. and Simon, A. 1996. Geomorphological river channel reconnaissance for river analysis , engineering and management. *Transactions of the Institute of British Geographers* 21(3), pp. 469–483.

Thorne, P.D., Williams, J.J. and Heathershaw, A.D. 1989. In situ acoustic measurements of marine gravel threshold and transport. *Sedimentology* 36(1), pp. 61–74.

Tominaga, A. and Nezu, lehisa 1992. Velocity Profiles in Steep Open-Channel Flows. *Journal of Hydraulic Engineering* 118(1), pp. 73–90.

Tonina, D. and Buffington, J.M. 2009. A three-dimensional model for analyzing the effects of salmon redds on hyporheic exchange and egg pocket habitat. *Canadian Journal of Fisheries and Aquatic Sciences* 66(12), pp. 2157–2173.

Triska, F.J., Kennedy, V.C., Avanzino, R.J., Zellweger, G.W. and Bencala, K.E. 1989. Retention and Transport of Nutrients in a Third-Order Stream in Northwestern California : Hyporheic Processes. *Ecology* 70(6), pp. 1893–1905.

Tritico, H.M. and Hotchkiss, R.H. 2005. Unobstructed and obstructed turbulent flow in gravel bed rivers. *Journal of Hydraulic Engineering* 131(8), pp. 635–645.

Tuhtan, J.A., Noack, M. and Wieprecht, S. 2012. Estimating stranding risk due to hydropeaking for juvenile European grayling considering river morphology. *KSCE Journal of Civil Engineering* 16(2), pp. 197–206.

Vanoni, V.A. 1946. Transportation of suspended sediment by water. *Transactions of the American Society of Civil Engineers* 111(1), pp. 67–102.

Vanoni, V.A. 1953. Some effects of suspended sediment on flow characteristics. *Proceedings Of The Fifth Hydraulics Conference Bulletin 34, State University of Iowa Studies in Engineering*.

Veras, T.B., Cabral, J.J. da S.P., Paiva, A.L.R. de, Barcellos, R.L. and Santos, L.L. dos 2016. Vertical hydraulic gradient research in hyporheic zone of Beberibe river in Pernambuco State (Brazil). *Brazilian Journal of Water Resources* 21(4), pp. 674–684.

Verheijen, F.G.A., Jones, R.J.A., Rickson, R.J. and Smith, C.J. 2009. Tolerable versus actual soil erosion rates in Europe. *Earth-Science Reviews* 94(1–4), pp. 23–38. Available at: http://dx.doi.org/10.1016/j.earscirev.2009.02.003.

Versteeg, H.K. and Malalasekra, W. 1995. An Introduction to Computational Fluid Dynamics: The Finite Volume Method.

Voermans, J., Ghisalberti, M. and Ivey, G.N. 2016. The Structure of Turbulence Across the Sediment-Water-Interface. *20th Australasian Fluid Mechanics Conference*, pp. 8–11.

Vollmer, S., de los Santos Ramos, F., Daebel, H. and Kühn, G. 2002. Micro scale exchange processes between surface and subsurface water. *Journal of Hydrology* 269(1–2), pp. 3–10.

Voulgaris, G. and Trowbridge, J.H. 1998. Evaluation of the acoustic Doppler velocimeter (ADV) for turbulence measurements. *Journal of Atmospheric and Oceanic Technology* 15(1), pp. 272–289.

Wallace, J.M. 2016. Quadrant Analysis in Turbulence Research: History and Evolution. *Annual Review of Fluid Mechanics* 48(1), pp. 131–158.

Wang, J., Dong, Z., Chen, C. and Xia, Z. 1993. The effects of bed roughness on the distribution of turbulent intensities in open-channel flow. *Journal of Hydraulic Research* 31(1), pp. 89–98.

Wang, X., Wang, Z.Y., Yu, M. and Li, D. 2001. Velocity profile of sediment suspensions and comparison of log-law and wake-law. *Journal of Hydraulic Research* 39(2), pp. 211–217.

Wang, X.Y., Yang, Q.Y., Lu, W.Z. and Wang, X.K. 2012. Experimental study of near-wall turbulent characteristics in an open-channel with gravel bed using an acoustic Doppler velocimeter. *Experiments in Fluids* 52(1), pp. 85–94.

Weill, P., Mouazé, D., Tessier, B. and Brun-Cottan, J.C. 2010. Hydrodynamic behaviour of coarse bioclastic sand from shelly cheniers. *Earth Surface Processes and Landforms* 35(14), pp. 1642–1654.

Wharton, G., Mohajeri, S.H. and Righetti, M. 2017. The pernicious problem of streambed colmation: a multi-disciplinary reflection on the mechanisms, causes, impacts, and management challenges. *Wiley Interdisciplinary Reviews: Water* 4(5), p. e1231/1-17.

Whiting, P.J., Dietrich, W.E., Leopold, L.B., Drake, T.G. and Shreve, R.L. 1988. Bedload sheets in heterogeneous sediment. *Geology* 16(2), pp. 105–108.

Whiting, P.J. and Dietrich, W.E. 1990. Boundary shear stress and roughness over mobile alluvial beds. *Journal of Hydraulic Engineering* 116(12), pp. 1495–1511.

Wiberg, P.L. and Smith, J.D. 1987. Calculations of the Critical Shear Stress for Motion of Uniform and Heterogeneous Sediments. *Water resources research* 23(8), pp. 1471–1480.

Wiberg, P.L. and Smith, J.D. 1991. Velocity distribution and bed roughness in high-gradient streams. *Water Resources Research* 27(5), pp. 825–838.

Wilkes, M., Gittins, J., Mathers, K., Mason, R., Casas-Mulet, R., Vanzo, D., Mckenzie, M., Murray-Bligh, J., England, J., Gurnell, A. and Jones, J.I. 2019. Physical and biological controls on fine sediment transport and storage in rivers. *Wires Water* 6(2), pp. 1-51/ e1331.

Wilkinson, S.N., Keller, R.J. and Rutherfurd, I.D. 2004. Phase-shifts in shear stress as an explanation for the maintenance of pool-riffle sequences. *Earth Surface Processes and Landforms* 29(6), pp. 737–753.

Williams, G.P. and Wolman, M.G. 1984. *Downstream effects of dams on alluvial rivers.* US Geological Survey Professional Paper 1286, p. 83.

Wilson, I.G. 1973. Equilibrium cross-section of meandering and braided rivers. *Nature* 241(5389), pp. 393–394.

Wilson, K.C. 1989. Mobile-bed friction at high shear stress. *Journal of Hydraulic Engineering* 115(6), pp. 825–830.

Wooster, J.K., Dusterhoff, S.R., Cui, Y., Sklar, L.S., Dietrich, W.E. and Malko, M. 2008. Sediment supply and relative size distribution effects on fine sediment infiltration into immobile gravels. *Water Resources Research* 44(3), p. W03424/1-18.

Wu, F.C. and Chou, Y.J. 2003. Rolling and Lifting Probabilities for Sediment Entrainment. *Journal of Hydraulic Engineering* 129(2), pp. 110–119.

Xu, Z., Chenling, Z., Qiang, Y., Xiekang, W. and Xufeng, Y. 2020. Hydrodynamics and bed morphological characteristics around a boulder in a gravel stream. *Water Supply* 20(2), pp. 395–407.

Yanda, R., Harada, M. and Tamagawa, I. 2018. Study on Double-Averaged Velocity Profile for Rough Beds and Low-Flow Conditions. *Journal of Japan Society of Civil Engineers, Ser. B1 (Hydraulic Engineering)* 74(4), p. I_619-I_624.

Yuan, J. and Jouybari, M.A. 2018. Topographical effects of roughness on turbulence statistics in roughness sublayer. *Physical Review Fluids* 3(11), pp. 114603/1–19. Available at: https://doi.org/10.1103/PhysRevFluids.3.114603.

Yue, W., Meneveau, C., Parlange, M.B., Zhu, W., Van Hout, R. and Katz, J. 2007. A comparative quadrant analysis of turbulence in a plant canopy. *Water Resources Research* 43(5), p. W05422/1-14.

Zagarola, M. V. and Smits, A.J. 1998. Mean-flow scaling of turbulent pipe flow. *Journal of Fluid Mechanics* 373, pp. 33–79.

Zampiron, A., Cameron, S. and Nikora, V. 2020. Secondary currents and very-large-scale motions in open-channel flow over streamwise ridges. *Journal of Fluid Mechanics* 887, p. A17/1-25.

Zeng, C., Li, C., Tang, H., Wang, L. and Mao, J. 2015. Experimental study of depth-limited open-channel flows over a gravel bed. *International Journal of Sediment Research* 30(2), pp. 160–166. Available at: http://dx.doi.org/10.1016/j.ijsrc.2015.04.001.

Appendix A

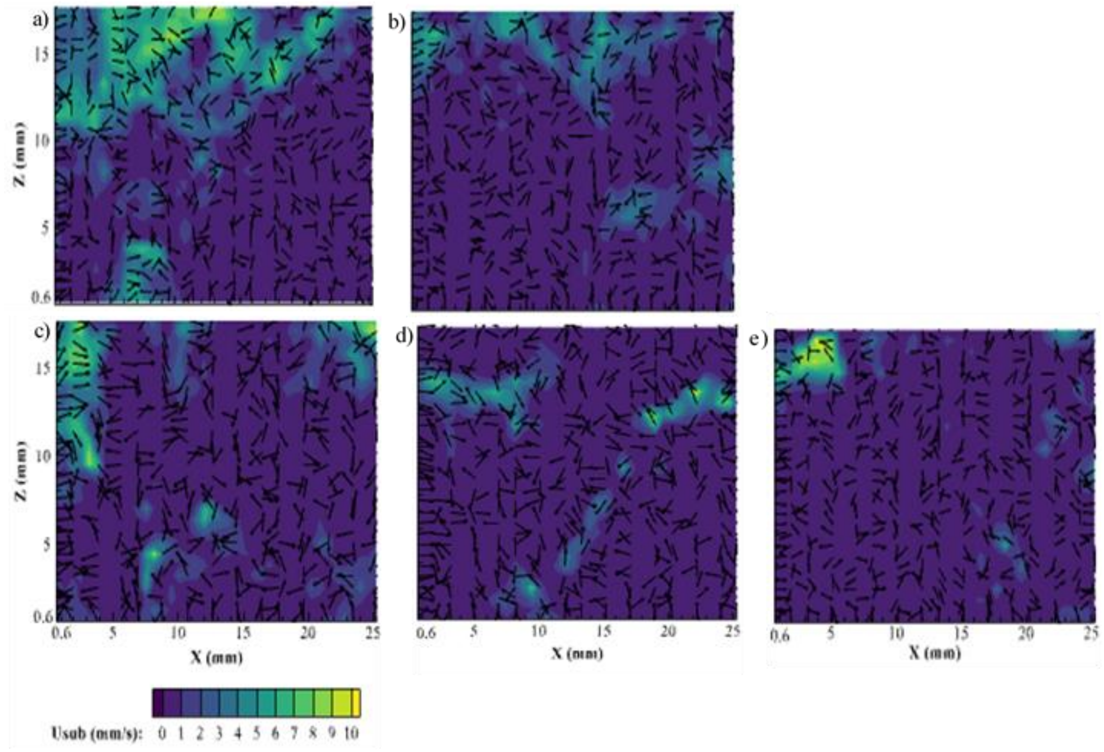

Figure A.1. Contour map of subsurface velocity (mm/s) through natural gravel-bed from (a) to (e) for an experiment of k_s=2.75d_{50}, d_{50}=20 mm, Q=0.004 m^3/s (experiment 1) at a distance 5.657 m, 5.684 m, 5.738 m, 5.765 m and 5.792 m, respectively from the inlet of the flume in streamwise direction for both natural gravel-bed experiments and dye was injected at approximately half the depth of the gravel-bed from the surface.

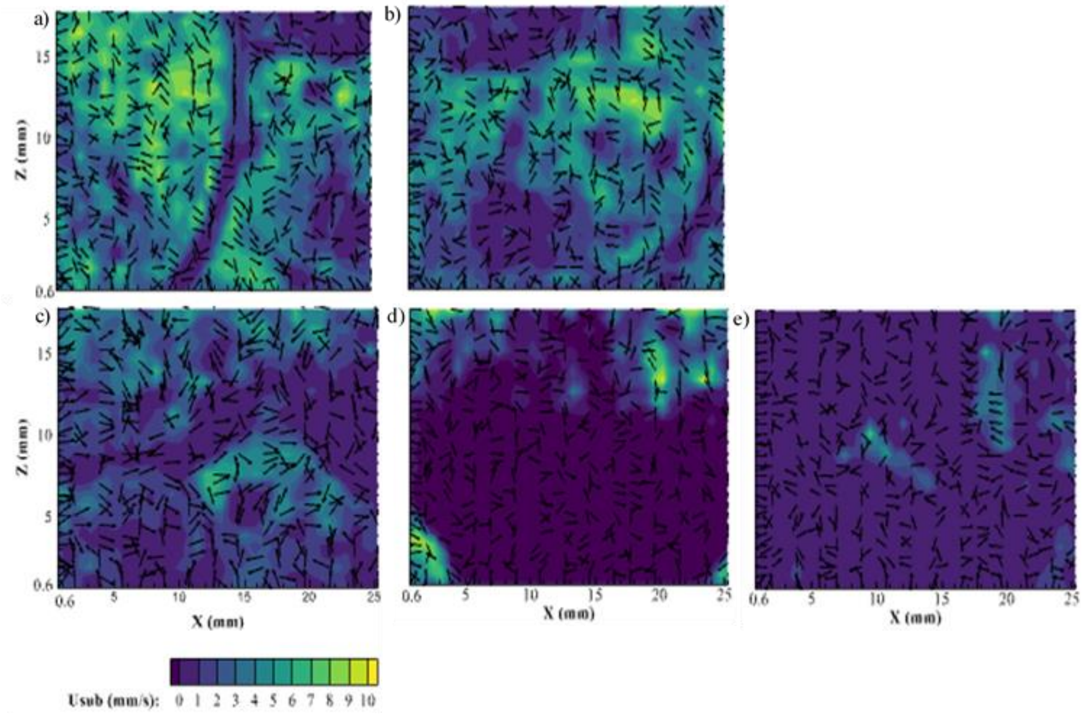

Figure A.2. Contour map of subsurface velocity (mm/s) through natural gravel-bed from (a) to (e) for an experiment of k_s=1.75d_{50}, d_{50}=35 mm, Q=0.004 m^3/s (experiment 4) at a distance 5.657 m, 5.684 m, 5.738 m, 5.765 m and 5.792 m, respectively from the inlet of the flume in streamwise direction for both natural gravel-bed experiments and dye was injected at approximately half the depth of the gravel-bed from the surface.

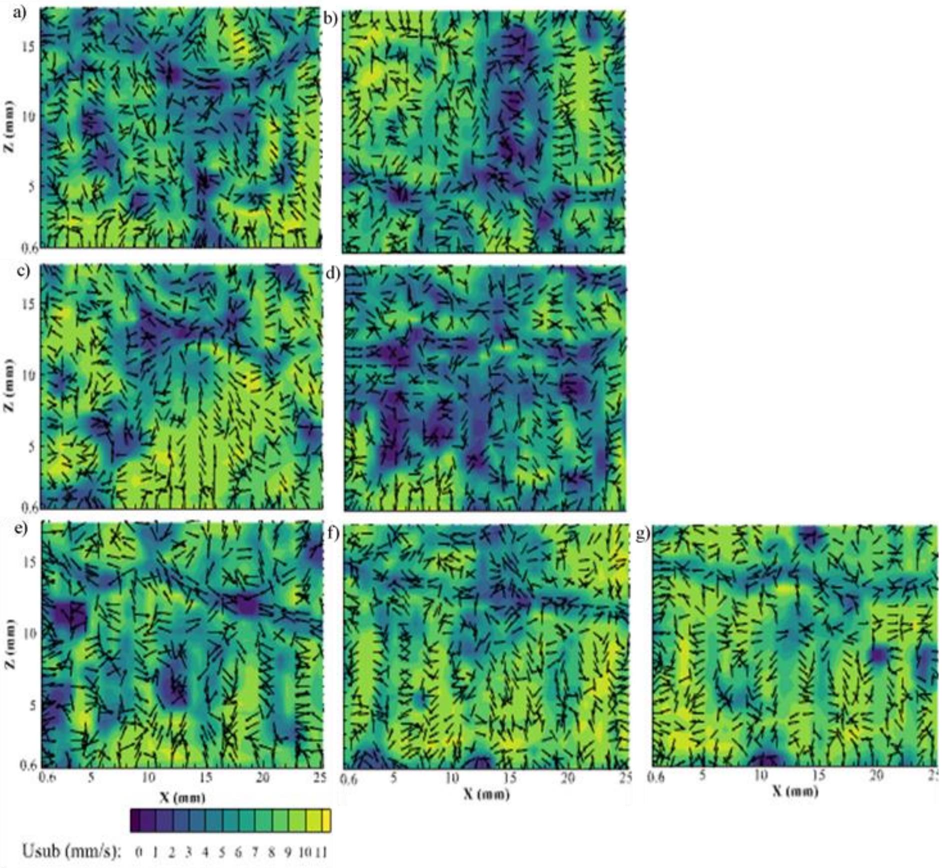

Figure A.3. Contour map of subsurface velocity (mm/s) through the artificial bed from (a) to (g) dye was injected at approximately half the depth of the gravel-bed from the surface for an experiment of k_s=0.2d_{50}, d_{50}=28 mm, Q=0.006 m^3/s (experiment 5) at a distance 5.707 m, 5.734 m, 5.761 m, 5.815 m, 5.842 m, 5.869 m and 5.896 m, respectively from the inlet of the flume in a streamwise direction in artificial bed experiments.

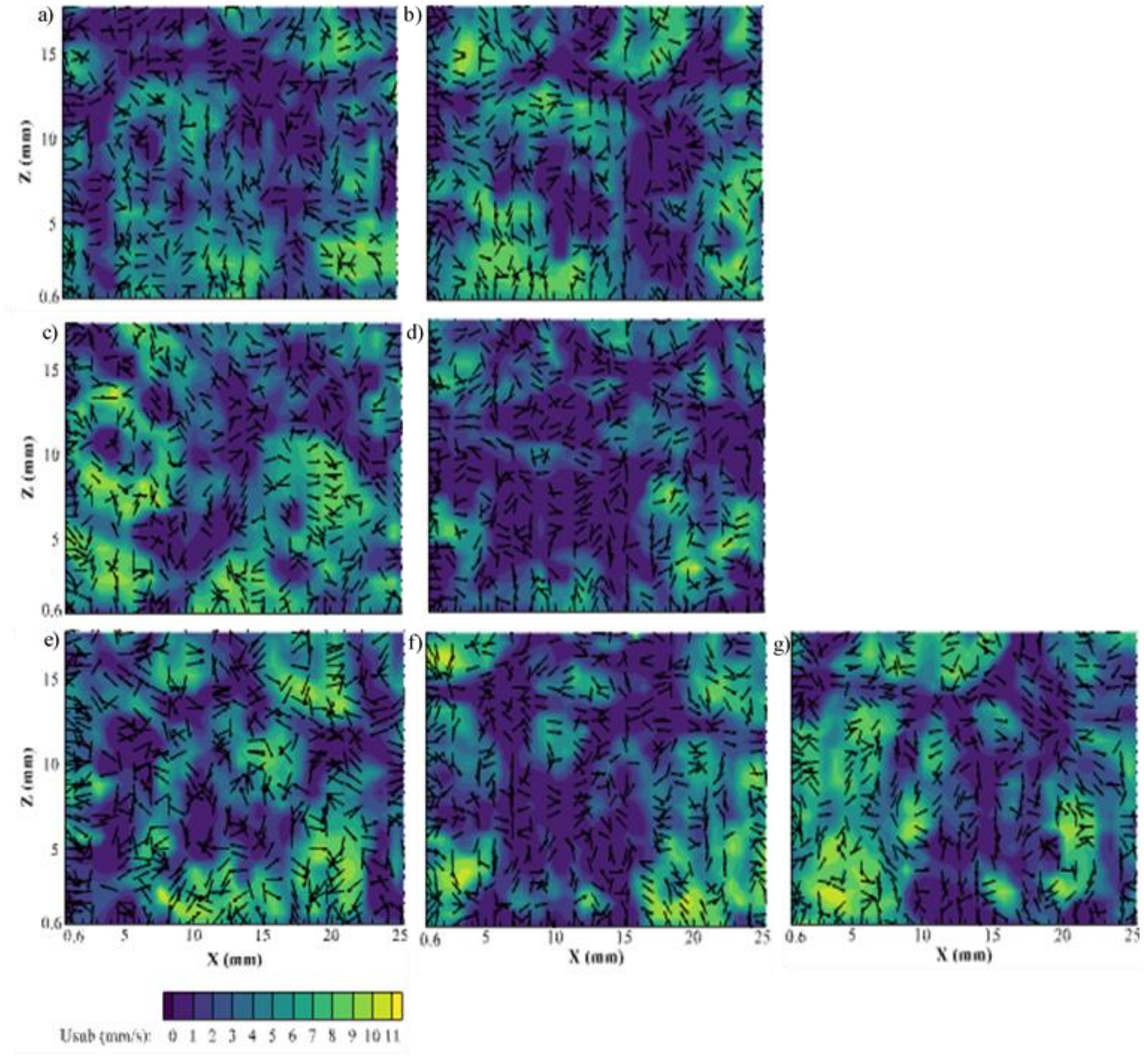

Figure A.4. Contour map of subsurface velocity (mm/s) through the artificial bed from (a) to (g) dye was injected at approximately the first layer of the gravel-bed surface for an experiment of ks=0.2d_{50}, d_{50}=28 mm, Q=0.006 m^3/s (experiment 5) at a distance 5.707 m, 5.734 m, 5.761 m, 5.815 m, 5.842 m, 5.869 m and 5.896 m, respectively from the inlet of the flume in a streamwise direction in artificial bed experiments.

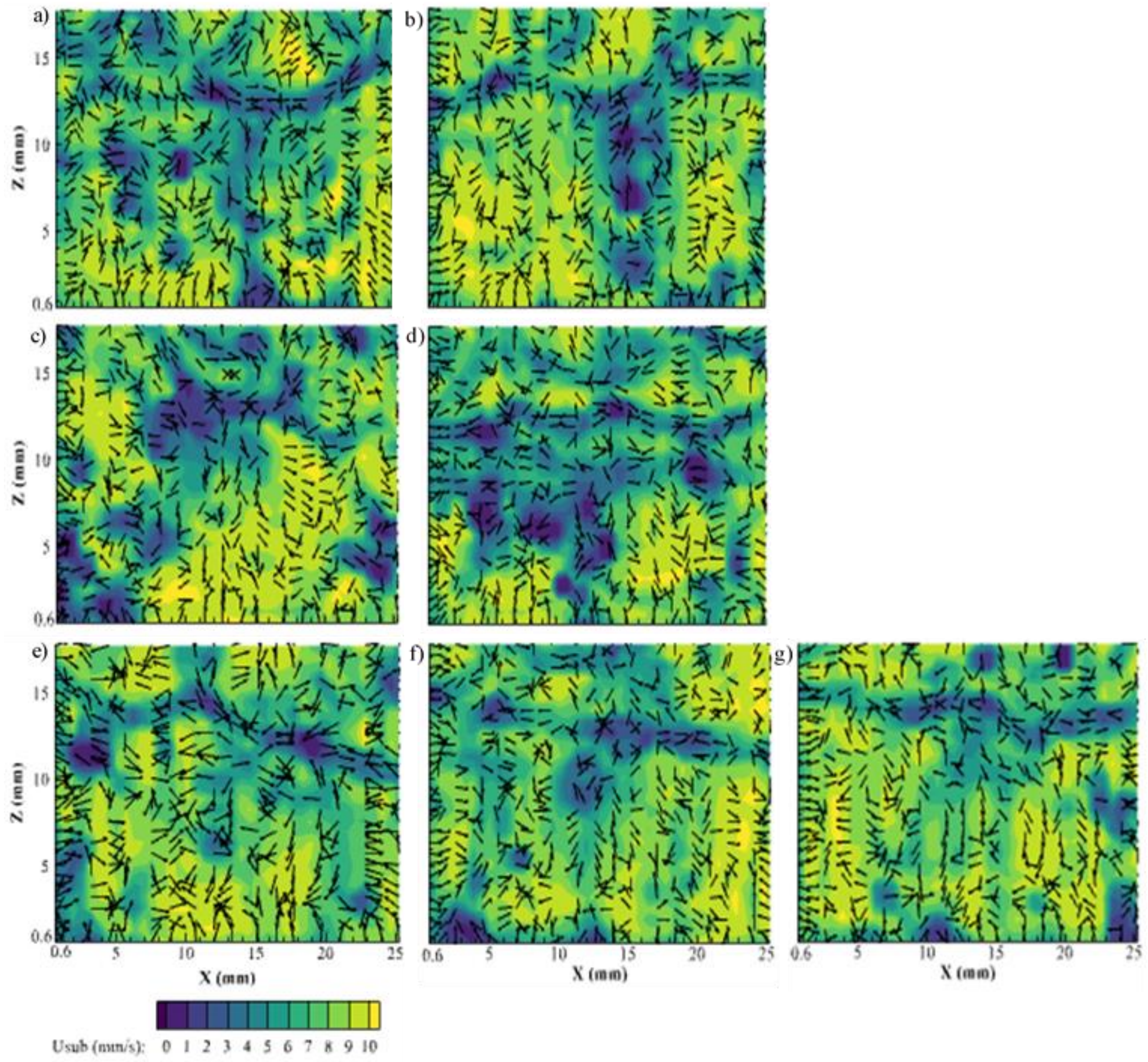

Figure A.5. Contour map of subsurface velocity (mm/s) through the artificial bed from (a) to (g) dye was injected at approximately half the depth of the gravel-bed from the surface for an experiment of ks=0.18d_{50}, d_{50}=28 mm, Q=0.009 m^3/s (experiment 6) at a distance 5.707 m, 5.734 m, 5.761 m, 5.815 m, 5.842 m, 5.869 m and 5.896 m, respectively from the inlet of the flume in a streamwise direction in artificial bed experiments.

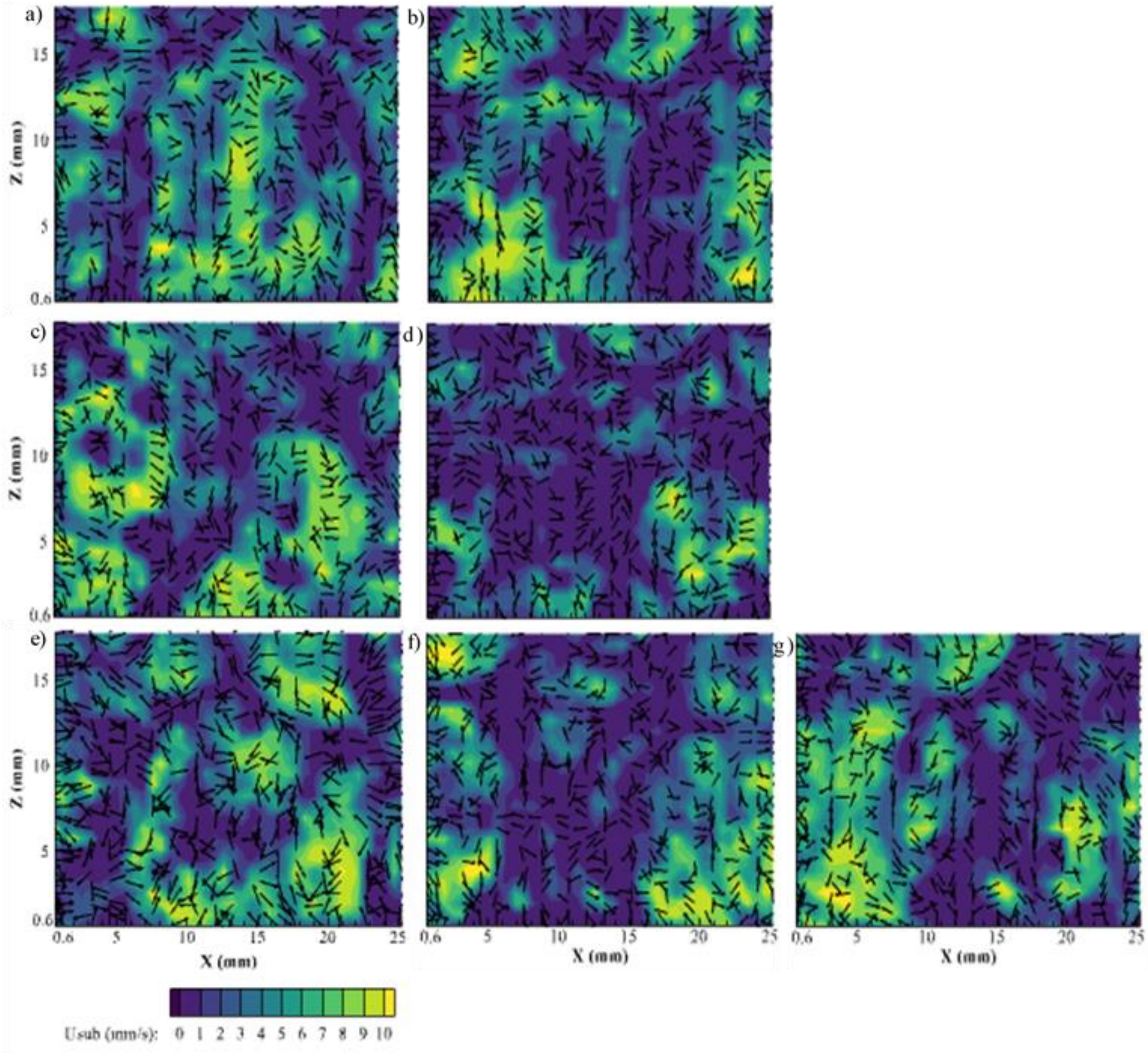

Figure A.6. Contour map of subsurface velocity (mm/s) through the artificial bed from (a) to (g) injected at approximately the first layer of the gravel-bed surface for an experiment of ks=0.18d_{50}, d_{50}=28 mm, Q=0.009 m^3/s (experiment 6) at a distance 5.680 m, 5.788 m and 5.923 m, respectively from the inlet of the flume in a streamwise direction in artificial bed experiments.